

## INFORMATION TO USERS

This manuscript has been reproduced from the microfilm master. UMI films the text directly from the original or copy submitted. Thus, some thesis and dissertation copies are in typewriter face, while others may be from any type of computer printer.

**The quality of this reproduction is dependent upon the quality of the copy submitted.** Broken or indistinct print, colored or poor quality illustrations and photographs, print bleedthrough, substandard margins, and improper alignment can adversely affect reproduction.

In the unlikely event that the author did not send UMI a complete manuscript and there are missing pages, these will be noted. Also, if unauthorized copyright material had to be removed, a note will indicate the deletion.

Oversize materials (e.g., maps, drawings, charts) are reproduced by sectioning the original, beginning at the upper left-hand corner and continuing from left to right in equal sections with small overlaps. Each original is also photographed in one exposure and is included in reduced form at the back of the book.

Photographs included in the original manuscript have been reproduced xerographically in this copy. Higher quality 6" x 9" black and white photographic prints are available for any photographs or illustrations appearing in this copy for an additional charge. Contact UMI directly to order.

# UMI

A Bell & Howell Information Company  
300 North Zeeb Road, Ann Arbor MI 48106-1346 USA  
313/761-4700 800/521-0600



University of Alberta

# Nonlinear Analyses of Cracked Bodies

by

Jianhua Wu



A thesis submitted to the Faculty of Graduate Studies and Research in partial  
fulfilment of the requirements for the degree of Doctor of Philosophy

Department of Mechanical Engineering

Edmonton, Alberta  
Fall 1995



National Library  
of Canada

Acquisitions and  
Bibliographic Services

395 Wellington Street  
Ottawa ON K1A 0N4  
Canada

Bibliothèque nationale  
du Canada

Acquisitions et  
services bibliographiques

395, rue Wellington  
Ottawa ON K1A 0N4  
Canada

*Your file Votre référence*

*Our file Notre référence*

The author has granted a non-exclusive licence allowing the National Library of Canada to reproduce, loan, distribute or sell copies of this thesis in microform, paper or electronic formats.

The author retains ownership of the copyright in this thesis. Neither the thesis nor substantial extracts from it may be printed or otherwise reproduced without the author's permission.

L'auteur a accordé une licence non exclusive permettant à la Bibliothèque nationale du Canada de reproduire, prêter, distribuer ou vendre des copies de cette thèse sous la forme de microfiche/film, de reproduction sur papier ou sur format électronique.

L'auteur conserve la propriété du droit d'auteur qui protège cette thèse. Ni la thèse ni des extraits substantiels de celle-ci ne doivent être imprimés ou autrement reproduits sans son autorisation.

0-612-22157-1

**University of Alberta**

**Library Release Form**

**Name of Author:**

**Jianhua Wu**

**Title of Thesis:**

**Nonlinear Analyses of Cracked Bodies**

**Degree:**

**Doctor of Philosophy**

**Year this Degree Granted:**

**1995**

Permission is hereby granted to the University of Alberta Library to reproduce single copies of this thesis and to lend or sell such copies for private, scholarly, or scientific research purposes only.

The author reserves all other publication and other rights in association with the copyright in the thesis, and except as hereinbefore provided, neither the thesis nor any substantial portion thereof may be printed or otherwise reproduced in any material form whatever without the author's prior written permission.



---

8532 82 Ave.

Edmonton, Alberta

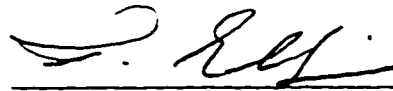
Canada T6C 0Y1

Date: *July 27, 1995*

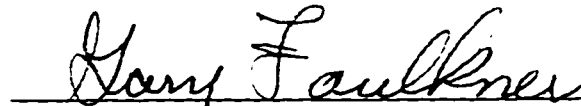
**University of Alberta**

**Faculty of Graduate Studies and Research**


The undersigned certify that they have read, and recommend to the Faculty of Graduate Studies and Research for acceptance, a thesis entitled **Nonlinear Analyses of Cracked Bodies** submitted by **Jianhua Wu** in partial fulfilment of the requirements for the degree of **Doctor of Philosophy**.



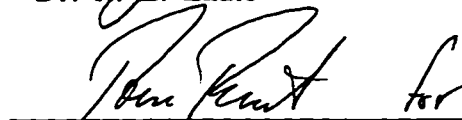
Dr. F. Ellyin ( Supervisor )



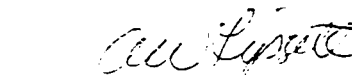
Dr. M. G. Faulkner



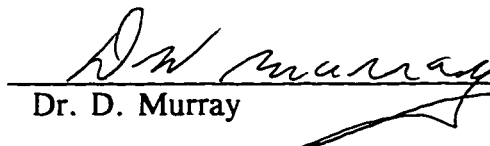
Dr. R. L. Eadie



Dr. H. Schitoglu ( External Examiner )



Dr. A. W. Lipsett



Dr. D. Murray

Date: 95-07-18

谨献给我的父亲和母亲

## **Abstract**

The purpose of this work is to demonstrate the use of numerical analyses in solving fracture problems. However, the numerical results are highly dependent on the material model used. A constitutive model is presented first. This model is sufficiently simple to be implemented in computer programs and it can match the essential features of the time-independent inelastic behaviour of materials fairly well for complex non-proportional loading paths including cyclic loading. Two practical fracture problems, namely delayed hydride cracking and crack closure, are investigated by elastic-plastic finite element analysis using the proposed constitutive model.

To find the effect of hydride on the elastic-plastic stress field near a crack tip, a modelling procedure is outlined which simulates the precipitation and expansion of the hydride. The results of the analysis show that the hydride formation causes an elastic unloading in the crack tip (reduction of the peak stress) and appearance of a peak stress at the front end of the hydride. Effects of the hydride length, its location with respect to the crack tip, and geometry of the front end extremity of the hydride, are also investigated.

In the second problem, a simple and efficient node release scheme is proposed to simulate crack growth under cyclic loading. Crack opening and closing stresses are calculated under constant and variable amplitude loadings. An attempt is made to explain the results in terms of the physical phenomenon. In general, the results obtained are in good agreement with the experimental observations.



## **Acknowledgement**

I am very pleased to acknowledge my deepest gratitude to Professor F. Ellyin for his invaluable guidance and great encouragement at various stages of my graduate studies, especially for his remarkable tolerance and patience throughout the years, and for providing a conducive environment which made it possible for me to complete the this research work at the University of Alberta.

I would like to thank Professors M. G. Faulkner and A. W. Lipsett of the department of Mechanical Engineering and Professor R. L. Eadie of the Department of Mining, Metallurgical & Petroleum Engineering for their advice and guidance.

Finally, I thank my wife Ruodi for much needed support in many ways throughout these years. The completion of the thesis would not have been possible without her understanding and daily care.

# Contents

Chapter 1	Introduction	1
1.1	Review of non-linear analysis in solid mechanics . . . . .	1
1.2	Mechanics of cracked bodies . . . . .	9
Chapter 2	An Elastic-Plastic Constitutive Relation	13
2.1	Background and review . . . . .	13
2.1.1	A general form of constitutive relation for a work-hardening material . . . . .	13
2.1.2	An overview of elastic-plastic constitutive models commonly used . . . . .	18
2.2	Evolution of the yield surface . . . . .	23
2.2.1	Review . . . . .	23
2.2.2	Limit memory surface . . . . .	26
2.2.3	Two examples to compare the proposed motion rule with Ziegler's rule . . . . .	28
2.3	Change in size of the yield surface during monotonic and cyclic loadings	30
2.3.1	Review . . . . .	30
2.3.2	Treatment of the radius of the yield surface . . . . .	32
2.4	Formulation in the matrix form . . . . .	36

2.4.1 Plane stress condition . . . . .	37
2.4.2 Plane strain condition . . . . .	38
2.4.3 Three dimension . . . . .	40
2.5 Brief summary . . . . .	42

### Chapter 3 Effect of Hydride Precipitation on the Elastic-

#### Plastic Stress Field Near a Crack Tip 55

3.1 Introduction . . . . .	55
3.2 Modelling and loading procedure . . . . .	57
3.3 The analysis under plane stress condition . . . . .	60
3.3.1 Finite element mesh and material properties . . . . .	60
3.3.2 Loading steps . . . . .	61
3.3.3 Results and discussion . . . . .	61
3.3.4 Conclusions . . . . .	63
3.4 The analysis under plane strain condition . . . . .	63
3.4.1 Finite element mesh and material properties . . . . .	63
3.4.2 Loading steps . . . . .	65
3.4.3 Results and discussion . . . . .	66
3.4.4 Conclusions . . . . .	71
3.5 The analysis using a finite deformation model . . . . .	72
3.5.1 A comparison of results between a small deformation model and a finite deformation model . . . . .	74
3.5.2 The effect of the crack length . . . . .	77

3.5.3 The effect of the start location of the hydride precipitation . . . .	78
3.5.4 Conclusions . . . . .	79

## Chapter 4 Study of the Crack Closure Under Cyclic Loading

by Elastic-Plastic Finite Element Analysis	115
4.1 Introduction . . . . .	115
4.2 Finite element modelling . . . . .	119
4.2.1 Elastic-plastic material model . . . . .	119
4.2.2 Mesh and material properties . . . . .	120
4.2.3 A new crack-tip node release scheme . . . . .	121
4.3 Analysis of crack extension under a constant-amplitude loading and releasing crack-tip node at the top of each loading cycle . . . . .	124
4.3.1 Crack opening and closing stresses . . . . .	124
4.3.2 A new definition of crack opening and closing stresses . . . . .	125
4.3.3 Applied load vs displacement . . . . .	127
4.3.4 Plastic zone . . . . .	129
4.3.5 Crack profile and CTOD . . . . .	130
4.3.6 Stress distribution . . . . .	133
4.3.7 Strain distribution . . . . .	136
4.3.8 Stress-strain history . . . . .	137
4.3.9 Energy release . . . . .	139
4.4 Analysis of crack extension under a constant-amplitude loading and releasing crack-tip node at the bottom of each loading cycle . . . . .	143

4.4.1	Crack opening and closing stresses	144
4.4.2	Crack profile	145
4.4.3	Stress distribution	145
4.4.4	Strain distribution	148
4.4.5	Crack opening stress vs closing stress	148
4.5	Analysis for a stationary crack	150
4.5.1	Crack opening and closing stresses	150
4.5.2	Crack profiles	151
4.6	Analysis of a single overload	151
4.6.1	Review of the experimental results	151
4.6.2	Simulation procedure	153
4.6.3	Crack opening and closing stresses	154
4.6.4	Crack profiles	156
4.6.5	Stress distribution	158
4.6.6	Strain distribution	161
4.7	Analysis of a single underload	163
4.7.1	Introduction	163
4.7.2	Crack opening and closing stresses	164
4.7.3	Crack profiles	165
4.7.4	Stress distribution	166
4.7.5	Strain distribution	166
4.8	Analysis of compression-compression cyclic loading	167
4.8.1	Introduction	167

4.8.2 Numerical simulation . . . . .	168
4.8.3 Crack opening and closing stresses . . . . .	170
4.8.4 Stress distribution . . . . .	171
4.8.5 Strain distribution . . . . .	173
4.9 Conclusions . . . . .	174
 Chapter 5 Summary and Suggestion for Further Research	 216
 References	 220

## List of Figures

Fig.(2-1) A schematic representation of the motion of yield surface for monotonically proportional loading. . . . .	44
Fig.(2-2) A schematic representation of the motion of yield surface for monotonically nonproportional loading. . . . .	45
Fig.(2-3) The motion of the centre of yield surface by Ziegler's rule under loading path $0 \rightarrow A \rightarrow B \rightarrow C \rightarrow D \rightarrow E$ in tension-torsion space. . . . .	46
Fig.(2-4) The motion of the centre of yield surface by the proposed rule under loading path $0 \rightarrow A \rightarrow B \rightarrow C \rightarrow D \rightarrow E$ in tension-torsion space. . . . .	47
Fig.(2-5) The motion of the centre of yield surface by Ziegler's rule under loading path $0 \rightarrow A \rightarrow B \rightarrow C \rightarrow D \rightarrow E$ in tension-torsion space. . . . .	48
Fig.(2-6) The motion of the centre of yield surface by the proposed rule under loading path $0 \rightarrow A \rightarrow B \rightarrow C \rightarrow D \rightarrow E$ in tension-torsion space. . . . .	49
Fig.(2-7) (a) Stress-strain hysteresis loops showing Masing behaviour[2-13]. (b) Stress-strain hysteresis loops showing Non Masing behaviour[2-14].	50
Fig.(2-8) Effect of the yield stress $\sigma_0$ on the stress-strain curve described by Ramberg-Osgood relation. . . . .	51
Fig.(2-9) Effect of the material constant $\alpha$ on the stress-strain curve described by Ramberg-Osgood relation. . . . .	52
Fig.(2-10) Effect of the material constant $n$ on the stress-strain curve described by Ramberg-Osgood relation. . . . .	53
Fig.(2-11) The stress-strain curves (Dashed lines), which are described by the Ramberg-Osgood relation and followed by the material points in different strain ranges, are in good agreement with the experimental curves (Solid lines)[2-14] during a cyclic loading in steady state. . . . .	54
Fig.(3-1) A schematic of a crack with its coordinate system, far field applied stress, and precipitated hydride. Details of stepwise modelling of hydride formation and expansion are given in the inset. . . . .	81
Fig.(3-2) Finite element mesh of a quarter cracked panel with 189 element and 517 nodes. The width of the half-panel is 42 mm, the half-crack	

length is 10 mm. . . . .	82
Fig.(3-3) A stress-strain curve of Zr-2.5% Nb at room temperature. . . . .	83
Fig.(3-4) Distributions of stress component normal to the crack plane for several specific loading steps. . . . .	84
Fig.(3-5) Distributions of strain component normal to the crack plane for several specific loading steps. . . . .	85
Fig.(3-6) The plastic zone in front of the crack tip at loading step 27(load=80 MPa) and the elastic zone caused by displacing nodes ahead the crack tip at loading step 36 (load=80 MPa, displacement=2.5 $\mu$ m). . . . .	86
Fig.(3-7) Accumulated strain energy density for the applied load history. . . . .	87
Fig.(3-8) Finite element mesh of a quarter cracked panel, denoted as section I. The crack is located in the bottom left corner and the indentation represents crack tip region which is enlarged in Fig.(3-9). . . . .	88
Fig.(3-9) Finite element mesh of crack tip region (b) which fits into the indentation of section II(a) which in turn fits into the indentation of Fig.(3-8). . . . .	89
Fig.(3-10) The stress-strain curve for Zr-2.5% Nb at 250 $^{\circ}$ c. . . . .	90
Fig.(3-11) Increments of applied far field stress (filled circles) with the left scale, and stepwise increase of hydride expansion (empty circles) with the right scale. Numbers in abscissa correspond to the progression of the loading process. . . . .	91
Fig.(3-12) Distribution of stress component normal to the crack plane for various stress intensity factors, $X_1 = 0$ indicates the crack tip. . . . .	92
Fig.(3-13) Plastic zone size in front of the crack as a function of stress intensity factor. . . . .	93
Fig.(3-14) Hydrostatic stress contours for the cracked panel, in the absence of hydride. . . . .	94
Fig.(3-15) Distribution of stress component normal to the crack plane due to hydride expansion. (Length of hydride platelet $L=10\ \mu$ m, $X_1=0$ denotes the crack tip.) . . . . .	95
Fig.(3-16) Distribution of strain component normal to the crack plane due to	



hydride expansion. (Length of hydride platelet $L=10\ \mu\text{m}$ . $X_1=0$ denotes the crack tip.) . . . . .	96
Fig.(3-17) Hydrostatic stress contours after expansion of a hydride platelet of length $L=10\ \mu\text{m}$ by $D=0.25\ \mu\text{m}$ . . . . .	97
Fig.(3-18) Crack opening profile before and after hydride expansion. (Length of hydride platelet $L=10\ \mu\text{m}$ . and note that the coordinates are non-dimensionalized by different quantities, see text.) . . . . .	98
Fig.(3-19) Effect of different hydride length on the normal stress distribution. (Expansion of hydride platelet $D=0.1\ \mu\text{m}$ for all three cases.) . . . .	99
Fig.(3-20) Effect of hydride front end geometry on the normal stress distribution for a hydride platelet of length $L=10\ \mu\text{m}$ expanding by $D=0.1\ \mu\text{m}$ . . . . .	100
Fig.(3-21) Effect of hydride front end geometry on the plastic zone size for a hydride platelet of length $L=10\ \mu\text{m}$ and expansion of $D=0.1\ \mu\text{m}$ . . . . .	101
Fig.(3-22) Effect of location of the hydride from the crack tip on the normal stress distribution. (Hydride length $L=10\ \mu\text{m}$ and its expansion $D=0.1\ \mu\text{m}$ .) . . . . .	102
Fig.(3-23) Distributions of stress component normal to the crack plane for various stress intensity factors by von Mises isotropic hardening small deformation model. . . . .	103
Fig.(3-24) Distributions of stress component normal to the crack plane for various stress intensity factor by von Mises isotropic hardening finite deformation model. . . . .	104
Fig.(3-25) Distributions of strain component normal to the crack plane for various stress intensity factor by von Mises isotropic hardening small deformation model. . . . .	105
Fig.(3-26) Distributions of strain component normal to the crack plane for various stress intensity factors by von Mises isotropic hardening finite deformation model. . . . .	106
Fig.(3-27) Crack opening profiles at $K_I=9\ \text{MPa}\sqrt{\text{m}}$ in the dimensionless coordinates by von Mises isotropic hardening small deformation model(dashed line) and finite deformation model(solid line). . . . .	107
Fig.(3-28) Crack opening profiles at $K_I=6, 9, 12\ \text{MPa}\sqrt{\text{m}}$ in millimetre unit by von Mises isotropic hardening small deformation model	

(dashed lines) and finite deformation model(solid lines). . . . .	108
Fig.(3-29) The plastic zone at the stress intensity factor of $9 \text{ MPa}\sqrt{\text{m}}$ by von Mises isotropic hardening small deformation model. . . . .	109
Fig.(3-30) The plastic zone at the stress intensity factor of $9 \text{ MPa}\sqrt{\text{m}}$ by von Mises isotropic hardening finite deformation model. . . . .	110
Fig.(3-31) Distributions of stress component normal to the crack plane for a crack length $a=0.8 \text{ mm}$ under various applied stress by von Mises isotropic hardening finite deformation model. . . . .	111
Fig.(3-32) Distributions of stress component normal to the crack plane for a crack length $a=2.08 \text{ mm}$ under various applied stress by von Mises isotropic hardening finite deformation model. . . . .	112
Fig.(3-33) Distributions of stress component normal to the crack plane for a crack length $a=4.0 \text{ mm}$ under various applied stress by von Mises isotropic hardening finite deformation model. . . . .	113
Fig.(3-34) The stress distributions before (solid line) and after (dashed line) precipitating the hydride at the peak stress. . . . .	114
Fig.(4-1) Finite element mesh of one-quarter of a centre-cracked panel used in this study. . . . .	177
Fig.(4-2) Monotonic and cyclic stress-strain curves for a typical structure steel. . . . .	178
Fig.(4-3) A schematic of truss elements connected to boundary nodes and a pair of contact surfaces set up on the crack line. . . . .	179
Fig.(4-4) Crack opening stresses and closing stresses for constant- amplitude cyclic loading with $S_{\max}=0.3\sigma_{0c}$ and $R=0$ under releasing node at the top of the cycles. . . . .	180
Fig.(4-5) A comparison between the new and old definitions for crack opening stress and closing stress. . . . .	181
Fig.(4-6) Applied load-displacement relationship without the effect of artificial releasing node. . . . .	182
Fig.(4-7) Plastic zones for the first, second and tenth cycle and reversed plastic zone for the first cycle identified by cross symbols. . . . .	183

Fig.(4-8) Crack profiles under constant-amplitude crack extension with $S_{\max}=0.3\sigma_{0c}$ and $R=0$ . . . . .	184
Fig.(4-9a) Stress distributions for special points on a typical loading cycle under releasing node at the top of loading cycles, Part 1. . . . .	185
Fig.(4-9b) Stress distributions for special points on a typical loading cycle under releasing node at the top of loading cycles, Part 2. . . . .	186
Fig.(4-10a) Strain distributions for special points on a typical loading cycle under releasing node at the top of loading cycles, Part 1. . . . .	187
Fig.(4-10b) Strain distributions for special points on a typical loading cycle under releasing node at the top of loading cycles, Part 2. . . . .	188
Fig.(4-11) Cyclic stress-strain history at a point along the crack as the crack tip approaches and passes. . . . .	189
Fig.(4-12) Crack opening stresses and closing stresses by the new and old definitions under releasing node at the bottom of the loading cycles. . . . .	190
Fig.(4-13) A comparison between crack profiles for releasing node at the top or the bottom of loading cycles. . . . .	191
Fig.(4-14a) Stress distributions for special points on a typical loading cycle under releasing node at the bottom of loading cycles, Part 1. . . . .	192
Fig.(4-14b) Stress distributions for special points on a typical loading cycle under releasing node at the bottom of loading cycles, Part 2. . . . .	193
Fig.(4-15a) Strain distributions for special points on a typical loading cycle under releasing node at the bottom of loading cycles, Part 1. . . . .	194
Fig.(4-15b) Strain distributions for special points on a typical loading cycle under releasing node at the bottom of loading cycles, Part 2. . . . .	195
Fig.(4-16) Stress opening stresses and closing stresses of a stationary crack by new definition. . . . .	196
Fig.(4-17) Crack profiles of a stationary crack for each constant-amplitude loading cycle. . . . .	197
Fig.(4-18) Crack opening stresses and closing stresses under constant-amplitude cyclic loading with a single 100% overload by new definition. . . . .	198
Fig.(4-19) Crack opening stresses and closing stresses under constant-amplitude	

cyclic loading with a single 100% overload by old definition. . . . .	199
Fig.(4-20) Crack profiles under constant-amplitude cyclic loading with a single 100% overload. . . . .	200
Fig.(4-21a) Stress distributions for special points near the overload cycle. . . . .	201
Fig.(4-21b) Residual stress distributions for the cycle before overload cycle, overload cycle and the cycle after 12 cycles from overload cycle. . . .	202
Fig.(4-22a) Strain distributions for special points near the overload cycle. . . . .	203
Fig.(4-22b) Residual strain distributions for the cycle before overload cycle, overload cycle and the cycle after 12 cycles from overload cycle. . . .	204
Fig.(4-23) Crack opening stresses and closing stresses under constant-amplitude cyclic loading with a single 200% underload or 300% underload. . . .	205
Fig.(4-24) Crack profiles under constant-amplitude cyclic loading with a single 200% underload. . . . .	206
Fig.(4-25) Stress distributions for special points near the underload. . . . .	207
Fig.(4-26) Strain distributions for special points near the underload. . . . .	208
Fig.(4-27) The mesh for a centre region near the notch root. . . . .	209
Fig.(4-28) Normal stress distributions and plastic zones for the maximum compressive stress of $0.4\sigma_{0c}$ (dashed lines) and $0.5\sigma_{0c}$ (solid lines). . .	210
Fig.(4-29) Crack opening and closing stresses during compressive cyclic loading using the proposed definition. . . . .	211
Fig.(4-30) A comparison of the crack opening and closing stresses between the newly proposed and the old definition. . . . .	212
Fig.(4-31) Normal stress distributions for the first cycle (dashed lines) and the 8 <sup>th</sup> cycle (solid lines), and the stresses at the notch root and each advancing crack tip for each loading cycle (individual solid dots). . .	213
Fig.(4-32) Normal strain distributions for the first cycle (dashed lines) and the 8 <sup>th</sup> cycle (solid lines), and the strains at the notch root and each advancing crack tip for each loading cycle (individual solid dots). . .	214
Table(4-1) Crack opening stress, maximum stress, maximum strain and CTOD for each cycle during constant-amplitude cyclic loading. . . . .	215

# CHAPTER 1

## INTRODUCTION

### 1.1 Review of non-linear analysis in solid mechanics

Before the middle of this century, most studies and investigations of solid mechanics were generally restricted to a linear category, i.e. the elastic response. Applications of solid mechanics were aimed at finding solutions of boundary value problems in elastic deformable bodies. The major governing equations are:

equilibrium equations:

$$\sigma_{ij,j} + F_i = 0 \quad (i, j = 1, 2, 3) \quad (1-1)$$

geometric equations:

$$\epsilon_{ij} = \frac{1}{2}(u_{i,j} + u_{j,i}) \quad (i, j = 1, 2, 3) \quad (1-2)$$

and physical equations:

$$\epsilon_{ij} = \frac{1+\nu}{E} \sigma_{ij} - \frac{\nu}{E} \delta_{ij} \sigma_{kk} \quad (i, j = 1, 2, 3) \quad (1-3)$$

Fifteen equations are used to solve 15 unknowns including 6 stress components  $\sigma_{ij}$ , 6 strain components  $\epsilon_{ij}$ , and 3 displacement components  $u_i$  under appropriate boundary and initial conditions. The boundary conditions that occur are usually one of two kinds: (i)

specified surface tractions and (ii) specified displacements. The reason for calling it a linear theory is that the relationship between strains and displacement gradients, Eq.(1-2), as well as the relationship between the stress and strain components, Eq.(1-3), are linear. The linear theory has existed for a long time and has been widely used in engineering. This is because the behaviour of most practical structures and machines can be described by the linear theory, also because the deformation of engineering structures is too small to be detected by the naked eye under operating loads. Therefore, when the constitutive relation of commonly used materials, such as steel and aluminum, is considered to be linear, there will not be appreciable errors under the conditions of small deformation and room temperature.

However, the situation has changed considerably since the 1950's. Nonlinear mechanics has gained an important position for the following reasons. A great deal of new engineering materials, such as high molecular materials, synthetic rubbers and solid fuels of rockets, have emerged and their nonlinear behaviours cannot be described by the classical linear constitutive relations. Also, flexible structures and large deformation structures have been increasingly adopted in engineering. In these instances, the linear geometric relations are clearly inadequate. The development of some fields, such as fracture mechanics and metal plastic forming, requires that the effect of large displacements be considered. The effect of displacements can have different meanings: (i) the displacements themselves are larger and thus, the deformation of materials has entered the plastic range; (ii) the strains caused by the displacement are large and therefore, the relationship between strains and displacement gradients does not remain

linear; (iii) the strains caused by the displacements are small, but the rotation of materials must be considered in calculation. When solving a specific engineering problem, it is convenient that the above nonlinear factors be classified as physical nonlinearity (or material nonlinearity) and geometric nonlinearity.

For physically nonlinear problems within the range of plastic deformation, the relationship between stress and strain components is no longer elastic but elastic-plastic. A plastic strain part will have to be added to equation (1-3) but in an incremental form:

$$\dot{\epsilon}_{ij} = \dot{\epsilon}_{ij}^e + \dot{\epsilon}_{ij}^p \quad (1-4)$$

The plastic strain term involves three fundamental constituents: (i) an initial yield criterion which specifies the states of stress corresponding to the start of plastic flow; (ii) an associated flow law, obtained from a plastic potential postulate, indicating the relationship between plastic strain increments and the current stresses as well as the stress increments after yielding; and (iii) a hardening rule which specifies the movement and the change of the yield surface in the stress space. Using different constituents will result in distinct constitutive relations of materials.

For geometrically nonlinear problems, in general, the relationship between strains and displacements is established by either Lagrangian or Eulerian description. The description of motion or deformation expressed by equations in which the material coordinates are independent variables is known as the Lagrangian description. On the other hand, the motion or deformation given through equations in which the spatial coordinates are independent variables, is known as the Eulerian description. In the geometric equations

obtained. the quadratic term of  $u_{ij}$  can not be neglected, or more definitely, the effect of rotation on deformations can not be neglected.

It is well known that, even for linear structures, finding the solutions of boundary value problems by the analytical approach is difficult due to the irregularity of structure shapes. Therefore, the linear analysis of practical structures has been attempted either by simplifying the geometry of structures and loading patterns or by finding an approximate solution. Often both methods have been employed at the same time.

In the past, the main methods of finding approximate solutions were the finite difference method and the variational calculus. The finite difference method uses difference equations to approach to the partial differential equations, as a physical approximation. The variational calculus derives the discrete equations (algebraic equations) from the partial differential equations by finding the extreme value of the functionals.

In the late 1950's and early 1960's, the finite element method was applied in aeronautical engineering. The finite element method utilizes the advantages of both the finite difference method and variational calculus, and thus, has flourished considerably. In the finite element method, the actual continuum or deformable body is represented as an assemblage of subdivisions called finite elements. The relationship between strains and displacements for elements is:

$$\{\epsilon^e\} = [B] \{u^e\}, \quad (1-5)$$

where  $\{\epsilon^e\}$  and  $\{u^e\}$ , of element "e", are the strain vector and the displacement vector



respectively, and  $[B]$  is strain-displacement matrix. The relationship between stresses and strains can be expressed as:

$$\{\sigma^e\} = [D] \{\epsilon^e\}, \quad (1-6)$$

where  $\{\sigma^e\}$  is the stress vector of element "e" and  $[D]$  is stress-strain matrix. The stiffness matrix of element "e" is:

$$[K^e] = \int_{V^e} [B]^T [D] [B] dV \quad (1-7)$$

The equilibrium equations are formulated as

$$[K^e] \{u^e\} = \{P^e\} \quad (1-8)$$

where  $\{P^e\}$  is the load vector acting on the nodes of the element.

For the linear elastic materials, the  $[D]$  matrix in Eq.(1-6) and (1-7) does not change following the variation of strain  $\{\epsilon\}$ . For nonlinear elastic or elastic-plastic materials, the  $[D]$  matrix is a function of strain  $\{\epsilon\}$ , and thus, is a function of displacement  $\{u\}$  as well. The matrix  $[B]$  in Eq.(1-5) and (1-7) is related to the partial derivative of an interpolation model which is an assumed solution of displacements within an element. If the displacements of the assemblage of finite elements are infinitesimal, it can be assumed that the interpolation model has no relation to the displacements; the matrix  $[B]$  is not a function of displacement  $\{u\}$ . Otherwise, the interpolation model will vary with the

displacements: matrices  $[B]$  and  $[K]$  will be functions of the displacements  $\{u\}$ . Moreover, the integral region,  $V^e$  (the volume of element) in Eq.(1-7) will change when the displacements are not infinitesimal.

While the nonlinear solid mechanics made considerable advances in theory, its application to practical problems did not advance enough until high powered digital computers became available. When compared with the analytical procedures of a couple of decades ago, it is evident that a revolution has taken place.

Developments in the computer software have tended to parallel those in computer hardware. Many large finite element programs for linear or nonlinear analysis, such as ADINA [1-1] and ANSYS [1-2], have matured gradually. The principal advantage of these commercial programs is that they are easy to operate and avoid a vast amount of repetitious work which is the same but necessary in any finite element program. The results obtained by these commercial codes are reliable because hundreds of person-years have been dedicated to their development and improvement.

The finite element program, Automatic Dynamic Incremental Nonlinear Analysis (ADINA), includes a number of constitutive relations, from the isotropic linear elastic to the rate-dependent, thermal and creep plastic. User-supplied constitutive relations are allowed through an interface. Physical nonlinearity can be achieved by using an appropriate nonlinear constitutive relation. ADINA also provides two different solutions methods: the total Lagrangian (T.L.) and Updated Lagrangian (U.L.) formulations. The T.L. formulation has also been referred to as Lagrangian formulation. In the solution scheme, all static and kinematic variables are referred to the initial configuration at time

0. The U.L. formulation is based on the same procedures that are used in the T.L. formulation, but in the solution, all static and kinematic variables are referred to the configuration at time  $t$ . Both the T.L. and U.L. formulations include all kinematic nonlinear effects due to large displacements, large rotations, and large strains, but whether the large strain behaviour is modeled appropriately depends on the specified constitutive relations. In ADINA, finally, several equilibrium iteration algorithms for nonlinear analysis can be selected using the incremental solution scheme.

It is apparent that the establishment of appropriate constitutive relations is a key link in the nonlinear analysis. In general, the derivation of constitutive relations is taken from one of three approaches. One approach deals with microscopic plasticity through dislocation theory or crystallography. The constitutive behaviour of a single crystal is investigated, and then it is extended to polycrystalline solids. A statistical or averaging treatment is used in the process of its development. This approach seems preferable and practical at present, and some specific plastic stress-strain relationships have been obtained. The second approach is based on the thermodynamics of an irreversible process. The change of internal state of materials is represented by an internal variable, while the history of deformation is described through the internal variables. The constitutive relation of a material established by this approach is one of the state equations in thermodynamics. This approach is probably the most universal and fundamental one, but it is not fully developed. The third approach, and the most popular approach, is based on macroscopic continuum mechanics. This type of theory generally starts from hypotheses and assumptions of a phenomenological character based on certain

experimental observations. Mathematical simplicity allows for it to be readily applied to practical analysis and design situations. As mentioned before, an initial yield criterion, an associated flow law and a hardening rule are fundamental constituents of the constitutive relations.

In the author's master thesis [1-3], a nonlinear anisotropic hardening constitutive model was studied. Two types of surfaces were defined, a memory surface associated with the loading, and a yield surface indicating the boundary of the elastic plastic deformation. The description of the motion of the subsequent yield surfaces was verified and a hardening modulus curve was proposed which related the change in size of these surface to the tangent modulus of the material [1-4]. Thus a simple rate-independent constitutive model was derived, which later was extended to a hierarchy of constitutive models by Ellyin and Xia [1-5]~[1-8]. It should be pointed out that the establishment of a constitutive model by analyzing the experimental results, is essential, however its application to practical engineering problems must be the *raison d'être* for such an endeavour. Frequently, a constitutive model will be refined and improved during its application.

Chapter 2 in this thesis presents a refined rate-independent constitutive model based on the Ellyin-Xia constitutive relations. The description of the evolution of the subsequent yield surfaces is completed under two loading types: Monotonically increasing load (ML) and reversed loading (RL) by newly defining a limit memory surface. The radius  $q$  of the yield surface is treated for Masing and non-Masing materials under the stable cyclic

loading. The formulations in a matrix form appropriate for the numerical analysis, are given. Computer programs of the constitutive model are prepared and then inserted into the ADINA code.

## **1.2 Mechanics of cracked bodies**

Fracture mechanics became a recognized discipline after World War II because of the inability of continuum-mechanics theories to address failure by unexpected fracture. The need for methods to quantify the effect of cracks on a material's performance led to the development and evolution of the theory of fracture mechanics. Cracks are present to some degree in all structures. They may exist as basic defects in the constituent material or they may be induced in construction or during service life. Therefore, a fundamental requirement of fracture mechanics theory is to assess the stability of such cracks. In this respect, the first successful analysis of a fracture-dominant problem was that of Griffith in 1920, who stated the now well-known concept that crack propagation will occur if the energy released upon crack growth is sufficient to provide all the energy that is required for crack growth. The total energy absorbed during crack growth per unit length and per unit thickness,  $G$ , was defined as a material property, called the "energy release rate". Another major advance was the introduction of the stress intensity factor,  $K$ , as a parameter for categorising the onset of crack propagation. Demonstration of the equivalence of  $G$  and  $K$  provided the basis for development of the discipline of Linear Elastic Fracture Mechanics (LEFM). For Elastic-Plastic Fracture Mechanics (EPFM) one of the earliest fracture parameters was the crack tip opening displacement (CTOD)

introduced by Wells in 1961. A more fundamentally based fracture criterion for non-linear problems was subsequently proposed by Rice through the concept of the J-contour integral. The use of these fracture parameters:  $G$ ,  $K$ , CTOD and  $J$  in examining crack stability requires an accurate knowledge of the stress field in the vicinity of the crack tip for the structural geometry, loading and boundary conditions in question. Unfortunately, analytical solutions only exist for selected, relatively simple, cases. It is in the determination of the stress and displacement fields for complex practical situations that numerical techniques such as finite element and boundary integral methods play an important role.

Chapter 3 and Chapter 4 in this thesis present the elastic-plastic finite element analyses applied to practical fracture problems. In addition, the constitutive model described in Chapter 2 is employed in these finite element analyses.

Delayed hydride cracking has been explained as a process involving the diffusion of hydrogen up the stress gradient resulting from the presence of a stress raiser in material containing hydrides, precipitation and subsequent cracking of hydride at the stress raiser. The process repeats until the component fails. This phenomenon came into prominence in the 1970's when it caused some leakages in the pressure tubes of early CANDU (CANadian Deuterium Uranium) nuclear reactors. Experimental investigation in the next decade indicated the mechanism of delayed hydride cracking. Despite the fact that several models have been proposed to calculate the flux of hydrogen and the rate of hydride growth, the effect of the hydride precipitation on stresses at the crack tip has not been

clearly understood. In order to find a relationship between the change of stress field with hydride precipitation, a finite element analysis using the proposed constitutive model is performed in Chapter 3.

It is shown that hydride formation causes an elastic unloading ahead of the crack tip along the hydride platelet (reduction of the peak stress) and the appearance of a peak stress at the front end of hydride. This gives a pertinent explanation of the hydride growth. Effects of the hydride length, its location with respect to the crack tip, and geometry of the front end extremity of the hydride, are also investigated.

In addition, the crack tip blunting can influence the stress distribution in front of the crack tip. Thus, a finite deformation constitutive model is also employed to investigate the change in the crack tip stress and strain fields due to hydride growth. As well a comparison of the results between the small and finite deformation models is made.

Since the discovery of the crack closure phenomenon by Elber, the study of closure in fatigue crack growth problems has been actively investigated through experimental, analytical and numerical studies. Many publications on the subject have been produced in the past twenty years. As a numerical method, the finite element analysis has played an important role.

In a finite element analysis, different material properties, load histories, or geometries can be easily accommodated. The crack opening stress levels, the stress and strain distribution; and the crack profiles can be obtained directly for every step during a cyclic loading. This allows the effects of stresses, strains, residual stresses, and plastic

deformations on the crack opening level to be analyzed in great detail. However, the published finite element analyses have two major shortcomings: (i) the constitutive models used in them are relatively simple (most of the researchers have employed an elastic-perfect plastic model or a bi-linear model with small strain hardening); and (ii) the simulation of crack growth is relatively crude. Simulating the crack growth in a finite element analysis is a challenging task, which cannot be evaded because of mathematic difficulty. In Chapter 4 the crack closure under constant and variable amplitude cyclic loading is investigated by an elastic-plastic finite element analysis using the proposed constitutive model and a new crack-tip node release scheme. Special attention is given to some basic concepts of fatigue crack growth and crack closure behaviour. An attempt has been made to explain the crack opening levels through changes of stresses and strains in the area of the crack-tip. In general, the results obtained are in good agreement with the experimental observations. Some contentious results are given appropriate explanations.



## CHAPTER 2

# AN ELASTIC-PLASTIC CONSTITUTIVE RELATION

### 2.1 Background and Review

#### 2.1.1 A general form of constitutive relation for a work-hardening material

A constitutive relation of an incremental form relates the increment of plastic strain components  $d\epsilon_{ij}^p$  to the state of stress,  $\sigma_{ij}$ , and the stress increment,  $d\sigma_{ij}$ . Such a constitutive relation is based on the three ingredients: an initial yield surface, a flow law and a hardening rule as mentioned in Chapter 1.

A general form of the yield function for a work-hardening material can be written as

$$\phi_y = f_y(\sigma_{ij} - \alpha_{ij}) - q^2 = 0 \quad (2-1)$$

in which the function  $f_y(\sigma_{ij} - \alpha_{ij})$  defines the shape of the yield surface, the  $\alpha_{ij}$ , back stress tensor, specifies the location of surface centre, while the hardening parameter  $q$  represents the size of the yield surface. Here, the parameter  $q$  can be a function of plastic work or cumulative plastic strain or other scalars. When  $\alpha_{ij}$  are zero and  $q$  is the yield stress of the material,  $\phi_y$  represents the initial yield surface of the material.

Various yield criteria were reviewed in reference [1-3]. Two popular yield criteria for structural materials are those attributed to von Mises and to Tresca. Experiments have shown that test data generally fall closer to the von Mises' yield condition than to

Tresca's.

In 1928, von Mises proposed the concept of the plastic potential function, which is a scalar function of the stresses,  $g(\sigma_{ij})$ . Analogous to the elastic potential function, the plastic flow equations can be written in the form

$$d\epsilon_{ij}^p = d\lambda \frac{\partial g(\sigma_{ij})}{\partial \sigma_{ij}} \quad (2-2)$$

where  $d\lambda$  is a positive scalar factor of proportionality. The equation  $g(\sigma_{ij}) = \text{constant}$  defines the surface (hypersurface) of the plastic potential in a nine-dimensional stress space. Since the direction cosines of the normal vector at the point on the surface,  $\sigma_{ij}$ , are proportional to the gradient  $\partial g(\sigma_{ij})/\partial \sigma_{ij}$ , the relation (2-2) implies that the plastic flow vector,  $d\epsilon_{ij}^p$ , is directed along the normal to the surface of the plastic potential.

Drucker, 1951, postulated that for a stable material, the initial and each subsequent yield surfaces are convex, and at regular points of the yield surface  $f_y = 0$ , the plastic strain increment vector is always directed along the normal to the yield surface. Thus, the normality of the plastic strain increment vector at regular regimes of the yield surface requires that,

$$d\epsilon_{ij}^p = d\lambda \frac{\partial f_y}{\partial \sigma_{ij}} \quad (2-3)$$

where  $d\lambda$  can be any scalar function of stress, strain and loading history.

Comparing Equations (2-2) and (2-3), a possible outcome is that  $g(\sigma_{ij})$  is equal to  $f_y(\sigma_{ij})$ .

i.e. the yield function is the plastic potential function. This is the simplest case and is of great importance. Apart from its simplicity, this case enables the derivation of a uniqueness theorem and extremum principles, which give the theory a certain completeness.

Thus, Equation (2-3) is called the associated flow law, because the plastic flow is connected or associated with the yield criterion. When  $g \neq f$  Eq.(2-2) is called a non-associated flow rule. For some materials like soil, when a dilatation of volume is considered the non-associated flow rule will be used.

Drucker, 1952, utilizing loading criterion, rewrites Equation (2-3) in the form

$$d\epsilon_{ij}^p = H \frac{\partial f_y}{\partial \sigma_{ij}} \frac{\partial f_y}{\partial \sigma_{kl}} d\sigma_{kl} \quad (2-4)$$

where  $H$  is also a scalar function of stress, strain and history, and independent of  $d\sigma_{ij}$ , although it can be expressed as a homogeneous function of order zero in  $d\sigma_{ij}$ .

The total strain increment tensor is assumed to be the sum of the elastic and plastic strain increment tensors:

$$d\epsilon_{ij} = d\epsilon_{ij}^e + d\epsilon_{ij}^p \quad (2-5)$$

The elastic strain increment can be obtained from the generalized Hooke's Law:

$$d\epsilon_{ij}^e = \frac{1}{E} [(1+\nu) \delta_{ik} \delta_{jl} - \nu \delta_{ij} \delta_{kl}] d\sigma_{kl} = C_{ijkl} d\sigma_{kl} \quad (2-6)$$

where  $\delta_{ij}$  is the Kronecker delta equal to unity when  $i=j$ , otherwise zero.

By substituting Eq.(2-4) and (2-6) into (2-5), the complete strain-stress relations for a work-hardening material are expressed as:

$$d\epsilon_{ij} = \left\{ \frac{1}{E} [(1+\nu) \delta_{ik} \delta_{jl} - \nu \delta_{ij} \delta_{kl}] + H \frac{\partial f_y}{\partial \sigma_{ij}} \frac{\partial f_y}{\partial \sigma_{kl}} \right\} d\sigma_{kl} \quad (2-7)$$

In certain instance, such as a finite element analysis, it is more convenient to use the inverse form of Eq. (2-7). After the existence and uniqueness of the inverse form are proved, the stress increment tensor is determined as

$$d\sigma_{ij} = \left\{ \frac{E}{1-\nu} \left[ (\delta_{ik} \delta_{jl} - \frac{\nu}{1-2\nu} \delta_{ij} \delta_{kl}) - c h \frac{\frac{\partial f_y}{\partial \sigma_{ij}} \frac{\partial f_y}{\partial \sigma_{kl}}}{\frac{1+\nu}{E} + h \frac{\partial f_y}{\partial \sigma_{mn}} \frac{\partial f_y}{\partial \sigma_{mn}}} \right] \right\} d\epsilon_{kl} \quad (2-8)$$

where  $c=1$  when  $f_y=0$  and  $(\partial f_y / \partial \sigma_{ij}) d\epsilon_{ij} > 0$  (plastic loading)

$c=0$  when  $f_y < 0$  or  $f_y=0$  and  $(\partial f_y / \partial \sigma_{ij}) d\epsilon_{ij} \leq 0$  (elastic or neutral loading)

and  $E$  is the elastic modulus,  $\nu$  is the Poisson's ratio, the hardening modulus  $h$  can be obtained through specializing Eq.(2-4) to the uniaxial case after specifying a particular form of the yield function.

When an initial yield surface is known, the rule of work hardening defines its evolution during the process of plastic flow. The most widely used rules are those of isotropic hardening, kinematic hardening and combined hardening.

When the yield function is assumed to remain unchanged, i.e. the yield surface is fixed

in stress space, the  $\alpha_{ij}$  and  $q$  in Eq.(2-1) are zero and a constant, respectively. Eq.(2-8) represents a constitutive relation for the elastic-perfectly plastic material.

The isotropic hardening rule is based on the assumption that the initial yield surface expands uniformly without distortion and translation as plastic flow occurs. The  $\alpha_{ij}$  in Eq.(2-1) are equal to zero, and  $q$  changes as a function of a certain internal variable. The kinematic hardening rule assume that during plastic deformation, the subsequent yield surface translates as a rigid body in stress space, maintaining the size, shape, and orientation of the initial yield surface. In Eq.(2-1)  $q$  is constant and  $\alpha_{ij}$  changes following a certain rule. A combination of isotropic and kinematic hardening would lead to the combined hardening rule. In this case, the subsequent yield surface experiences a translation defined by  $\alpha_{ij}$  and a uniform expansion measured by  $q$ ; but it still retains its original shape.

A number of hardening rules were reviewed in reference [1-3]. Two well known hardening rules are due to Prager [2-1] and Ziegler [2-2] for kinematic hardening. It should be pointed out that some researchers use a single surface to describe the hardening rule. This is relatively simple and more suitable to uncomplicated loading paths. Some researchers employ two- or multi-surfaces which predict results more accurately than those of single-surface for non-proportional cyclic loading paths.

Thus, Eqs.(2-8), (2-1) and suitable expressions for  $\alpha_{ij}$  and  $q$  would comprise the constitutive relation for various materials. Different yield criteria will result in different constitutive relations, or further, different hardening expressions will lead to different constitutive relations.

### 2.1.2. A overview of elastic-plastic constitutive models commonly used

It is a common belief that there is no universally accepted model for the plastic behaviour that can describe all aspects of nonlinear material behaviour. There are, however, some models which are better suited for particular applications than the others, and they combine mathematical and computational simplicity with a proper representation of experimentally observed behaviour.

#### i) Prandtl-Reuss material model

In 1924, Prandtl extended Saint Venant's theory that the principal axes of the strain increment coincide with the principal axes of stress, for plane problem to include the elastic component of the strain, and Reuss in 1930 carried out its extension to three dimensional solids. That is

$$d\epsilon_{ij} = d\epsilon_{ij}^e + d\lambda \frac{\partial f}{\partial \sigma_{ij}} \quad (2-9)$$

Then, by choosing the von Mises' yield criterion as  $f$

$$f = J_2 - K^2 = 0 \quad (2-10)$$

where  $J_2 = S_{ij}S_{ij}/2$ , they obtained

$$d\epsilon_{ij} = C_{ijkl} d\sigma_{kl} + \frac{dw_p}{2K^2} S_{ij} \quad (2-11)$$

where the first term represents Hooke's Law,  $dw_p$  is the rate of plastic work and  $s_{ij}$  is the stress deviator tensor.

Perhaps this model is the most widely used and simplest elastic-perfectly plastic material model. The material does not strain harden.

ii) von Mises material model

When von Mises' yield function is employed, Eq. (2-1) is rewritten as

$$\phi_y = \frac{3}{2} \bar{S}_{ij} \bar{S}_{ij} - q^2 = 0 \quad (2-12)$$

where  $\bar{s}_{ij} = \bar{\sigma}_{ij} - \bar{\sigma}_{kk}\delta_{ij}/3$  and  $\bar{\sigma}_{ij} = \sigma_{ij} - \alpha_{ij}$ .

For an isotropic hardening model, the simplest way to choose  $q$  is to make it equal to the maximum effective stress,  $\sigma_{\text{eff.max}}$ , reached during the loading process. For the kinematic hardening,  $q$  is a constant, usually replaced by the yield stress of the material.  $\sigma_0$ , and  $\alpha_{ij}$  are expressed by Ziegler's hardening rule

$$d\alpha_{ij} = d\mu (\sigma_{ij} - \alpha_{ij}) \quad (2-13)$$

where  $d\mu$  is a positive proportionality factor determined by the condition that the stress point remains on the yield surface during the plastic flow. The hardening modulus  $h$  in Eq.(2-8) can be found through substituting Eq.(2-12) into Eq.(2-4) and specializing it to the uniaxial case:

$$h = \frac{1}{4q^2} \left( \frac{1}{E_t} - \frac{1}{E} \right) \quad (2-14)$$

where  $E$  is the elastic modulus and  $E_t$  is the instantaneous tangent modulus. It is evident

that when  $q$  and  $\alpha_{ij}$  are expressed by different functions, respectively, Eqs.(2-8), (2-12) and (2-13) will indicate varying types of von Mises material models.

### iii) Drucker-Prager material model

The Drucker-Prager yield criterion was proposed in 1952 [2-3] as a simple modification of the von Mises yield criterion for rocks and soils. The influence of a hydrostatic stress component on failure was introduced by an additional term in von Mises yield function:

$$\phi_y = \alpha I_1 + \sqrt{J_2} - K = 0 \quad (2-15)$$

where  $\alpha$  and  $K$  are material constants.  $I_1 = \sigma_{kk}$  and  $J_2 = S_{ij}S_{ij}/2$ . Following increasing of hydrostatic stress ( $I_1 < 0$ ), the radius of von Mises' yield circle will grow. The yield surface or failure surface of Eq.(2-15) is a circular cone in the principal stress space. By using the associated flow, the total strain increment can be obtained from

$$d\epsilon_{ij} = C_{ijkl} d\sigma_{kl} + d\lambda \left[ \alpha \delta_{ij} + \frac{S_{ij}}{2\sqrt{J_2}} \right] \quad (2-16)$$

After some algebraic manipulation, the Drucker-Prager material model can be written as

$$d\sigma_{ij} = 2G\{\delta_{ik}\delta_{jl} - [A(\sigma_{kl}\delta_{ij} + \sigma_{ij}\delta_{kl}) + B\delta_{kl}\delta_{ij} + C\sigma_{ij}\sigma_{kl}]\}d\epsilon_{kl} \quad (2-17)$$

where  $A = h/\beta k$

$$B = (\alpha - I_1/6\sqrt{J_2})(\beta - 1)/3\alpha\beta - \nu/(1 - 2\nu)/\beta$$

$$C = 1/k\beta\sqrt{J_2}$$

$$\beta = \sqrt{J_2}/k\{1 + 6(1 + \nu)\alpha^2/(1 - 2\nu)\}$$



$$h = \alpha(1 + \nu)/(1 - 2\nu) - I_1/6\sqrt{J_2}$$

When considering a dilatation of volume a non-associated flow rule will be adopted.

iv) Mroz material model

Since mid 60's. Mroz and co-workers have devoted themselves to the study of constitutive models. In 1967, Mroz [2-4] introduced a concept of a "field of work hardening moduli". which was defined by a configuration of surfaces of constant work hardening moduli in the stress space, to determine the translation and expansion or contraction of the yield surfaces. These surfaces  $f_0, f_1, \dots$  are similar and concentric, enclosing the origin. And it is assumed that the surfaces cannot intersect but consecutively contact and push each other during the loading process. A typical description for the motion of surfaces is that when the stress point P lies on the surface  $f_L$ , the instantaneous translation of  $f_L$  will occur along PR where R is a point on  $f_{L-1}$  corresponding to the same direction of outward normal. Meanwhile, it was generally assumed that the radii of surfaces are not constants but functions of a scalar parameter  $\lambda$  monotonically increasing in the course of plastic flow.

Based on the above-mentioned concepts Mroz et al. developed their model[2-5][2-6]. They still chose von Mises yield condition represented by a sphere in the deviatoric stress space. So that

$$S_{ij} - \alpha_{ij} = n_{ij} R(H) \quad (2-18)$$

where  $n_{ij}$  denotes the unit normal vector to the yield surface,  $S_{ij}$  is the stress deviator, the back stress  $\alpha_{ij}$  specifies the centre position of the yield surface.  $R(H)$  denotes its radius.

and  $H$  is a history parameter. The associated flow law now takes the form

$$\dot{\epsilon}_{ij}^p = \frac{1}{h} n_{ij} (n_{kl} \dot{s}_{kl}), \quad n_{ij} = \frac{s_{ij} - \alpha_{ij}}{[(s_{kl} - \alpha_{kl})(s_{kl} - \alpha_{kl})]^{1/2}} \quad (2-19)$$

where  $h$  denotes the hardening modulus.

For the evolution of the back stress,  $\alpha_{ij}$ , a scalar function (or norm) of  $\alpha_{ij}$  was first introduced

$$\alpha_e = \left( \frac{3}{2} \alpha_{ij} \alpha_{ij} \right)^{1/2} \quad (2-20)$$

Thus, the maximal value of  $\alpha_e$  reached during the plastic deformation process is denoted by

$$\alpha_m = \sup \alpha_e(t-s) \quad 0 < s < t \quad (2-21)$$

When the material element is partially unloaded, the norm  $\alpha_e$  decreases and the maximal value  $\alpha_m$  is kept in the material memory.

The back stress rate can be decomposed into two portions, one associated with the back stress loading process, the other with the back stress reorientation process.

$$\dot{\alpha}_{ij} = \dot{\alpha}_{ij}^{(L)} + \dot{\alpha}_{ij}^{(r)} = c^{(L)} \dot{\epsilon}_{ij}^p + c^{(r)} \dot{\lambda}_p \beta_{ij}^r \quad (2-22)$$

where  $c^{(L)} = c[(\alpha_r - \alpha_m)/(3/2)^{1/2} R_0]^m$

$$c^{(r)} = D(s_d^*/(3/2)^{1/2} R_0)^n$$

$$s_d^* = [3/2(\alpha_{ij}^* - \alpha_{ij})(\alpha_{ij}^* - \alpha_{ij})]^{1/2}$$

$$\alpha_{ij}^* = (2/3)^{1/2} \alpha_m n_{ij}$$

$$\lambda_p = (2/3 \dot{\epsilon}_{ij}^p \dot{\epsilon}_{ij}^p)^{1/2}$$

$$\beta_{ij}^r = (\alpha_{ij}^* - \alpha_{ij}) / [(\alpha_{kl}^* - \alpha_{kl})(\alpha_{kl}^* - \alpha_{kl})]^{1/2}$$

The loading term  $\alpha_{ij}^{(L)}$  evolves with the plastic strain rate until  $\alpha_m$  reaches the saturation value  $\alpha_f$ . When  $\alpha_m = \alpha_f$ ,  $c^{(L)}$  vanishes. The back stress reorientation term  $\alpha_{ij}^{(r)}$  is assumed to evolve towards the image stress  $\alpha_{ij}^*$  on the memory surface corresponding to the same normal direction as that of the plastic strain rate.

The evolution rule of the radius  $R(H)$  is assumed in the form

$$\dot{R} = A [(R_s - R)/R_0]^k \dot{\lambda}_p \quad (2-23)$$

where  $A$  and  $K$  are assumed to be the material parameters,  $R_s$  denotes the saturation value of isotropic hardening and  $R_0$  is the initial radius.

These four models are a sample of representative constitutive models in common use. The first one is a simple elastic-perfectly plastic model; the second one uses a single surface to describe the elastic-plastic responses of materials; the third one considers the influence of the hydrostatic stress; and the last one adopts multi-surfaces in description of the evolution rules. From these four models, an outline of constitutive models in the present use can be seen.

## 2.2 Evolution of the yield surface

### 2.2.1 Review

In Prager's hardening rule [2-1] the motion of the yield surface is assumed along the

direction of the exterior normal of the yield surface. so that.

$$d\alpha_{ij} = d\mu \frac{\partial f_y}{\partial \sigma_{ij}} \quad (2-24)$$

In the modified Parger's rule due to Ziegler [2-2], the yield surface is assumed to translate in the direction of the vector connecting the centre of the yield surface with the stress point which remains on the yield surface during the plastic flow. i.e.

$$d\alpha_{ij} = d\mu (\sigma_{ij} - \alpha_{ij}) \quad (2-25)$$

After a series of experiments. Phillips and Lee [2-7] claimed that the motion of the yield surface is between the direction of stress increment vector and that of the normal to the yield surface. The influence of stress increment vector is a predominant one and sometimes the influence of the normal is completely missing. Therefore as a good approximation, they assumed that the centre of the yield surface moves in the direction of stress increment vector:

$$d\alpha_{ij} = \mu d\sigma_{ij} \quad (2-26)$$

Ellyin [2-8] and Ellyin and Wu [2-9] defined two types of stress hypersurface: a yield and a memory surface to describe the evolution of the yield locus (back-stress) in the stress space. The memory surface memorizes the maximum stress experienced by the material in its loading history, and indicates the isotropic hardening extent of the material. The yield surface always remains inside the memory surface and portrays the

locus of the elastic region. The combination of the yield and memory surfaces can model complex loading situations, including cyclic loading.

The memory and yield surfaces are expressed by

$$\phi_m = f_m(\sigma_{ij}) - \sigma_{eff,max}^2 = 0 \quad (2-27)$$

$$\phi_y = f_y(\sigma_{ij} - \alpha_{ij}) - q^2 = 0 \quad (2-28)$$

where  $f(\sigma_{ij})$  is the yield function, for a von Mises material  $f(\sigma_{ij}) = 3S_{ij}S_{ij}/2$  and  $f(\sigma_{ij} - \alpha_{ij}) = 3\bar{S}_{ij}\bar{S}_{ij}/2$ .  $\sigma_{eff,max}$  is the maximum effective stress achieved by the function  $f(\sigma_{ij})$  during the plastic deformation,  $\alpha_{ij}$ 's are the coordinates of the centres of the subsequent yield surface (back-stress), and  $q$  is a measure of the yield surface radius.

For the stress path inside the current memory surface, the direction of motion of the yield surface centre is parallel to the direction of the vector connecting the starting point of the stress path on the instantaneous yield surface,  $(\sigma_{ij})_y$ , to the point on the memory surface,  $(\sigma_{ij})_m$ , whose exterior normal is parallel to the outward normal of the yield surface at the starting point, see Fig.4 of [2-9]. This motion can be written as

$$d\alpha_{ij} = d\mu [(\sigma_{ij})_m - (\sigma_{ij})_y] \quad (2-29)$$

where  $d\mu$  is a scalar function which is determined from the consistency condition:

$$d\mu = \frac{(\partial f_y / \partial \sigma_{ij}) d\sigma_{ij} - 2q dq}{[(\sigma_{kl})_m - (\sigma_{kl})_y] (\partial f_y / \partial \sigma_{kl})} \quad (2-30)$$

Here, the monotonic loading path and reloading path exceeding the current memory

surface are not referred. Therefore, the concept of a limit memory surface will be introduced.

### 2.2.2 Limit memory surface

According to the earlier definition, the memory surface will originally coincide with the initial yield surface, expand uniformly in the stress space during the loading process with its centre fixed. Thus, there should be a maximum memory surface for any given material. The radius of the maximum memory surface is the ultimate strength of the material. Corresponding to the yield strength of the material under the uniaxial stress state, there exists a yield surface in six dimensional stress space. Also, corresponding to the ultimate strength of the material under the uniaxial stress state, there exists a maximum memory surface, which will be called "limit memory surface" in the six dimensional stress space. Thus, the limit memory surface is a real surface, it characterizes a certain property of the material. The limit memory surface can be constructed experimentally in a manner similar to that of a yield surface, see [2-8].

The limit memory surface can be written as

$$\phi_L = f_L(\sigma_{ij}) - R_L^2 = 0 \quad (2-31)$$

where  $f(\sigma_{ij})$  is the yield function,  $R_L$  is a constant equal to the ultimate strength of the material.

Thus, two loading paths in the plastic range are distinguished: (a) Monotonically increasing loading after the loading point touches the initial yield surface or the loading

exceeding the current memory surface in the reversed direction, they are attributed to the monotonic loading (ML). (b) Reversed loading after the loading point touches the current yield surface during the unloading and before it reaches the current memory surface. this is termed reloading (RL). For RL, as mentioned in §2.2.1., the evolution of the centre of the yield surface is defined with respect to the current memory surface which is not change during RL. The mathematical expression for this type of motion is given by Eq.(2-29). For ML, the direction of motion of the yield surface centre is parallel to the direction of the vector connecting the loading point on the current yield surface  $(\sigma_{ij})_j$  to the point on the limit memory surface  $(\sigma_{ij})_L$ , whose exterior normal is parallel to the outward normal of the yield surface at the loading point. see Fig.(2-1) for a monotonically proportional loading and Fig.(2-2) for a monotonically nonproportional loading. In Fig.(2-1) the yield surface centre moves just along the direction of the vector connecting the loading point B on the current yield surface to the point C on the limit memory surface; the outward normals of both points,  $\bar{n}_B$  and  $\bar{n}_C$ , are parallel. Note that the current yield surface is tangent to the current memory surface at the loading point during ML. In this case, the yield surface moves and the memory surface expands. Figure(2-2) shows that for a monotonically nonproportional loading, loading history is  $O \rightarrow A \rightarrow B \rightarrow C \rightarrow D$ , the direction of motion of the yield surface centre gradually changes according to the vectors which connect the loading point on the current yield surface to the corresponding point on the limit memory surface i.e. the direction of centre O is parallel to  $\overline{BB'}$ ; the direction of  $O_1$  is parallel to  $\overline{CC'}$  and the direction of  $O_2$  is parallel to  $\overline{DD'}$ . Thus, the centre of yield surface moves in the loading direction for the

proportional loading whereas it gradually moves towards the loading direction for the nonproportional loading. A mathematical expression similar to Eq.(2-29) is employed to describe the ML case.

$$d\alpha_{ij} = d\mu [(\sigma_{ij})_L - (\sigma_{ij})_y] \quad (2-32)$$

where

$$d\mu = \frac{(\partial f_y / \partial \sigma_{ij}) d\sigma_{ij} - 2q dq}{[(\sigma_{kl})_L - (\sigma_{kl})_y] (\partial f_y / \partial \sigma_{kl})} \quad (2-33)$$

Now, the description for any loading path in stress space can be done by using the yield, the memory and the limit memory surface.

### 2.2.3 Two examples to compare the proposed motion rule with Ziegler's rule

Two examples of loading paths in tension and shear stress space are designed for a comparison between the proposed motion rule and Ziegler's rule.

#### Example 1:

The loading path consists of three steps. In step 1, the material is subjected to a tension stress from  $\sigma_x=0$  MPa, at point 0, to  $\sigma_x=300$  MPa, at point B, which exceeds the yield stress of the material,  $\sigma_0=200$  MPa, at point A. The second step is the unloading from  $\sigma_x=300$  MPa, at point B, to  $\sigma_x=-150$  MPa, at point C. During the first two steps the shear stress is maintained at zero. Subsequently, in the third step the tension stress  $\sigma_x$  is maintained at -150 MPa, while the shear stress  $\tau_{xy}$  increases from  $\tau_{xy}=0$  MPa, at point C, to  $\tau_{xy}=218$  MPa, at point E. Loading to point E which is on the



limit memory surface, means that the material will fail at this point. The loading path in fig.(2-3) is denoted by  $0 \rightarrow A \rightarrow B \rightarrow C \rightarrow D \rightarrow E$ . This figure shows the motion of the yield surface centre according to Ziegler's rule, whereas that obtained by the proposed rule is shown in Fig.(2-4). The locus of the yield surface centre during the loading process is represented by a series of filled circles. For the proportional loading portion ( $0 \rightarrow A \rightarrow B \rightarrow C$ ) both rules show that the direction of the motion of the yield surface centre is along the loading direction. For the nonproportional loading portion ( $C \rightarrow D \rightarrow E$ ), the direction of the motion of the centre by Ziegler's rule deviates considerably from the loading direction, whereas in the case of the proposed rule the deviation from the loading direction is much less and is parallel to the loading direction after the loading point exceeds the memory surface obtained in the tension loading. It is apparent that both rules describe the motion of the yield surface successfully, but the proposed rule is in better agreement with the experimental results of Phillips [2-7]. It should be pointed out that when the loading point passes by the memory surface obtained in tension loading, the locus of the yield surface centre indicates a fluctuation, this is because the memory surface should be thought more of the nature of a thin boundary layer in stress space than as a sharp delimiting line [2-7].

#### Example 2:

The loading path in this example consists of shear loading and unloading followed by tensile loading. It is denoted by  $0 \rightarrow A \rightarrow B \rightarrow C \rightarrow D \rightarrow E$  in Fig.(2-5), where the trajectory of the motion of the centre given by Ziegler's rule is also depicted. The trajectory predicted by the proposed rule is shown in Fig.(2-6). The direction of the motion of the yield

surface indicated by the proposed rule is closer to the loading direction than that by Ziegler's rule.

## 2.3 Change in size of the yield surface during monotonic and cyclic loadings

### 2.3.1. Review

If different yield criteria are employed, the yield surface will be different in form and size. When von Mises yield criterion is considered, the yield surface is a circular cylinder perpendicular to the deviatoric plane in the principal stress space. In two dimensional subspaces the yield surface, or more correctly, the yield locus is elliptical in form, and will retain its form during the plastic deformation. Thus, the change of the yield surface in size can be attributed to the change in the major axis of the ellipses, or in general, the 'radius' of the yield surface.

A hardening modulus curve was proposed in refs.[1-3] and [2-9] based on the experimental observations, which described the material hardening process. The isotropic and kinematic hardening models were but two particular cases of this curve. The hardening modulus curve relates the tangent modulus of the stress-strain curve with an area ratio of the memory or the subsequent yield surface to the initial yield surface:

$$E_t ( \omega , k ) = E_0 e^{-\frac{(\omega - 1)^2}{2k^2}} \quad (2-34)$$

where  $\omega = A/A_0$  represents the area ratio;  $k$  is a material parameter indicating the extent of hardening, and  $E_0$  is the tangent modulus at a point on the initial yield surface. For

a von Mises material, when Eq.(2-28) is used to express the subsequent yield surface, the area ratio  $\omega$  is equal to  $q^2/\sigma_0^2$ , here  $\sigma_0$  is yield stress. Then, the radius of the subsequent yield surface  $q$  can be written from Eq.(2-34) as

$$q^2 = \sigma_0^2 [ 1 - k \sqrt{2 \ln(E_0/E_t)} ] \quad (2-35)$$

If the uniaxial stress-strain relation of the material is known, then the tangent modulus  $E_t$  at a loading point exceeding the yield stress of the material,  $\sigma_0$ , can be easily obtained. This loading point corresponds to the memory surface and a subsequent yield surface, both surfaces are tangent to each other at this point. The radius of the subsequent yield surface can thus be found from Eq.(2-35).

For monotonic loading, the hardening modulus curve can describe the variation of the radius of the yield surface successfully. However, for the cyclic loading the hardening modulus curve is not appropriate due to its limitation during the reloading after an unloading. Ellyin and Xia [1-5] used the accumulated plastic length,  $l_p$ , as an internal variable to measure the change in the radius  $q$  of the yield surface and the change of the tangent modulus,  $E_t$ , thereby fulfilling the description of the transient hardening in cyclic loading. It was assumed that

$$\frac{\partial q}{\partial l_p} = \beta (q_{st} - q) \quad (2-36)$$

$$\frac{\partial E_t}{\partial l_p} = \beta (E_{t,st} - E_t) \quad (2-37)$$

where  $l_p = \int (2/3 d\epsilon_{ij}^p d\epsilon_{ij}^p)^{1/2}$ , while  $q_{st}$  and  $E_{t,st}$  are stable values of  $q$  and  $E_t$  respectively,

$\beta$  is a material constant. Comparing the calculated results with the experimental curves of a transient hardening process, good agreement was obtained.

### 2.3.2. Treatment of the radius of the yield surface

Generally, the response of materials to cyclic loading may include cyclic hardening, cyclic softening and cyclic stability. The behaviour of materials in the transient process is an important property of materials. However, in analyses of some practical problems, such as a finite element analysis of fatigue crack growth, the transient process may be neglected in order to simplify the problem. In fact, most materials reach a stable response during the cyclic loading only after several tens or hundreds of cycles. Compared with the total fatigue life or the crack growth rate, several hundreds of cycles may not be significant. It is therefore, reasonable in the analysis to consider that the crack growth takes place under a stable state after the initial transient process. Furthermore, if the transient process is involved in the analysis, then the initiation of the crack should also be considered. This may lead to a loss of the expected main purpose due to the fairly complex situation.

Usually, in a finite element analysis of the fatigue crack growth the material is considered to be in a stable state, the monotonic stress-strain curve is replaced by the cyclic stress-strain curve and the cyclic yield stress  $\sigma_{0c}$  is used instead of the monotonic yield stress of the material,  $\sigma_0$ . In addition, it is assumed that the material follows the kinematic hardening rule, i.e. the radius of the yield surface for any material point does not change during the whole loading process and will be equal to the cyclic yield stress

$\sigma_{uc}$ . In this manner, the constitutive model used is simplified, and the essential features of the material are approximately matched.

However, unlike the monotonic stress-strain curve, the cyclic stress-strain curve is not a curve which the material points trace in the cyclic loading. This curve is obtained by connecting the tips of the stable hysteresis loops of several companion specimens tested at different fully reversed strain ranges. Only the stress-strain hysteresis loops are the curves that material points trace at different strain ranges in the stable state. In practical problems, such as in an analysis of crack tip stress-strain field, the material points have different strain level. Therefore, it is important to study the hysteresis loop shapes during cyclic deformation in order to relate the cyclic stress to the strain during the loading history of material points.

As early as 1926, Masing [2-10] assumed that the loading and unloading branches of the stress-strain hysteresis loop were geometrically similar to the monotonic stress-strain curve with a scale factor of two. Some experimental observations by Morrow [2-11], Halford [2-12] and Abdel-Raouf et al. [2-13] showed that the cyclic stress-strain curve, defined as the locus of the tips of the various sized stabilized hysteresis loops under fully reversed cyclic conditions, when magnified by a factor of two, accurately described the hysteresis loop shape. This type of behaviour of materials is called Masing behaviour and materials which exhibit Masing behaviour are called Masing materials. In contrast to Masing behaviour, steady hysteresis loop shapes for a wide range of structural metals reveal variations during the cyclic loading. This is regarded as Non-Masing behaviour.

The steady state stress-strain hysteresis loops for a typical Masing material, AISI 304

stainless steel [2-13], and a typical Non-Masing material, A-516 Gr 70 carbon steel [2-14], are shown in Fig.(2-7) (a) and (b) respectively. The lower tips of these loops are translated to the origin of the coordinate axes. It can be seen that for the Masing material the upper branches of the hysteresis loops coincide and form a unique curve which is the cyclic stress-strain curve magnified by a factor of two. For the Non-Masing material the hysteresis loops are somewhat different, depending on the imposed cyclic strain amplitude. The yield stress for each stable loop (at 0.2% offset or any other yield definition) increases and the nonlinear portion of the upper branches of each loop comes down with the increased imposed strain. This implies that for each hysteresis loop there exists a specific radius of yield surface which is very different from the cyclic yield stress  $\sigma_{0c}$ . In addition, the shape of the hysteresis loops are totally different from that of the cyclic stress-strain curve.

That, as mentioned earlier, a cyclic stress-strain curve with the kinematic hardening rule is used in a finite element analysis, is valid only for Masing materials. For Non-Masing materials a different approach is needed.

Generally, a simple formula is employed to describe the stress-strain curve or cyclic stress-strain curve in a finite element analysis. A popular formula is Ramberg-Osgood relation [2-15]

$$\frac{\epsilon}{\epsilon_0} = \frac{\sigma}{\sigma_0} + \alpha \left( \frac{\sigma}{\sigma_0} \right)^n \quad (2-38)$$

where  $\sigma_0$  is yield stress,  $\epsilon_0 = \sigma_0/E$ ,  $\alpha$  and  $n$  are material constants. The slope of the curve at the elastic portion is given by Young's modulus  $E$ . Since the Ramberg-Osgood relation

has three parameters, it allows for a better fit to the experimental stress-strain curves.

When the material constants  $\sigma_0$ ,  $\alpha$  and  $n$  vary, the shape of the curve described by Ramberg-Osgood relation will change. The effect of each constant by itself on the shape of the curve is illustrated in Fig.(2-8) for  $\sigma_0$ , Fig.(2-9) for  $\alpha$  and Fig.(2-10) for  $n$ , comparing to an original Ramberg-Osgood curve with:  $E=204 \times 10^3$  MPa,  $\sigma_0=178.4$  MPa,  $\alpha=0.09$  and  $n=5.31$ . It is apparent from these figures that the increase of  $\sigma_0$  causes the increase in both elastic and plastic portions of the curve, while an increase in  $\alpha$  and  $n$  results in the decrease of the plastic portion of the curve. The effect of  $\alpha$  and  $n$  on the elastic portion of the curve is negligible.

It can be expected that the hysteresis loops can be expressed by Ramberg-Osgood relation with a scale factor of  $1/2$ , but that the material constants  $\sigma_0$ ,  $\alpha$  and  $n$  might be different. Thus, the challenge is how to obtain a hysteresis loop from a known cyclic stress-strain curve. Alternatively, if the material constants  $\sigma_{0c}$ ,  $\alpha_c$  and  $n_c$  for a cyclic stress-strain curve are given, how to find out  $\sigma_{0l}$ ,  $\alpha_l$  and  $n_l$  for each hysteresis loop. A simple exponential function may be used to obtain the yield stress of each hysteresis loop for different strain ranges:

$$\sigma_{0l} = \sigma_{0c} e^{A \left( \frac{\epsilon_{eff,max}}{\epsilon_{0c}} - 1 \right)} \quad (2-39)$$

where  $\sigma_{0c}$  is the cyclic yield stress,  $\epsilon_{0c} = \sigma_{0c}/E$ ,  $\epsilon_{eff,max}$  is the maximum effective strain reached by the material point, and  $A$  is material constant determined from appropriate tests. The material constants  $\alpha_l$  and  $n_l$  can be obtained from the relations similar to Eq.(2-39), respectively. For the purpose of simplification, however, it can assume that  $\alpha_l$

remains equal to that of the cyclic stress-strain curve. Then, the constant  $n_1$  can be determined by solving Ramberg-Osgood relation after knowing the yield stress  $\sigma_{01}$  from Eq.(2-39) and the point on the cyclic stress-strain curve corresponding to the maximum effective strain. This point is also on the hysteresis loop to be found.

Figure (2-11) shows the cyclic stress-strain curve and six steady hysteresis loops at different strain ranges for A-516 Gr 70 carbon steel (solid lines) from [2-14]. Through fitting the cyclic stress-strain curve by Ramberg-Osgood relation one obtains  $\sigma_{0c}$  of 178.4 MPa,  $\alpha_c$  of 0.09 and  $n_c$  of 5.31. The yield stress  $\sigma_{01}$  for each hysteresis loop is calculated from Eq.(2-39) with the constant A equal to 0.03. Finally, substituting the yield stress  $\sigma_{01}$  thus obtained, and the stress and strain values corresponding to each maximum effective strain into Ramberg-Osgood relation and keeping  $\alpha_1=0.09$ , we get the  $n_1$  for each hysteresis loop. The dashed lines in Fig.(2-11) represent the hysteresis loops by using the above method. The agreement between the experimental and predicted curves is seen to be good.

Thus, by using Eq.(2-39) the change of the radius of the yield surface can be described for both Masing and Non-Masing materials. For Masing materials the constant A in Eq.(2-39) is equal to zero.

## 2.4 Formulation in the matrix form

For the convenience of computer-based manipulations Eq.(2-8) with von Mises' type of yield function, Eq.(2-27) and (2-28), can be written in matrix forms for different conditions.



#### 2.4.1. Plane stress condition

For an initially isotropic material, the plane stress condition is prescribed by

$$d\tau_{xx} = d\tau_{yy} = d\sigma_{zz} = d\epsilon_{xx} = d\epsilon_{yy} = 0 \quad (2-40)$$

The plane stress equations can be reduced from Eq.(2-8) by putting the conditions Eq.(2-40) into Eq.(2-8). Their matrix form is

$$\begin{Bmatrix} d\sigma_{xx} \\ d\sigma_{yy} \\ d\tau_{xy} \end{Bmatrix} = \begin{bmatrix} L_{11} & L_{12} & L_{13} \\ L_{21} & L_{22} & L_{23} \\ L_{31} & L_{32} & L_{33} \end{bmatrix} \begin{Bmatrix} d\epsilon_{xx} \\ d\epsilon_{yy} \\ d\gamma_{xy} \end{Bmatrix} \quad (2-41)$$

where

$$L_{11} = \frac{E(1-\nu)}{(1+\nu)(1-2\nu)} - h(2\bar{\sigma}_x - \bar{\sigma}_y)^2$$

$$L_{12} = \frac{E\nu}{(1+\nu)(1-2\nu)} - h(2\bar{\sigma}_x - \bar{\sigma}_y)(2\bar{\sigma}_y - \bar{\sigma}_x)$$

$$L_{13} = -h(2\bar{\sigma}_x - \bar{\sigma}_y)(3\bar{\tau}_{xy})$$

$$L_{21} = L_{12}$$

$$L_{22} = \frac{E(1-\nu)}{(1+\nu)(1-2\nu)} - h(2\bar{\sigma}_y - \bar{\sigma}_x)^2$$

$$L_{23} = -h(2\bar{\sigma}_y - \bar{\sigma}_x)(3\bar{\tau}_{xy})$$

$$L_{31} = L_{13} \quad , \quad L_{32} = L_{23}$$

$$L_{33} = \frac{E}{2(1+\nu)} - h(3\bar{\tau}_{xy})^2$$

and

$$h = \frac{E}{1+\nu} \frac{g}{\frac{1-\nu}{g} + 6q^2 g}$$

$$g = \frac{1}{4q^2} \left( \frac{1}{E_t} - \frac{1}{E} \right)$$

$$\bar{\sigma}_x = \sigma_{xx} - \alpha_{xx}, \quad \bar{\sigma}_{yy} = \sigma_{yy} - \alpha_{yy}$$

$$\bar{\tau}_{xy} = \tau_{xy} - \alpha_{xy}$$

#### 2.4.2. Plane strain condition

Plane strain is characterized by

$$d\varepsilon_{zz} = d\varepsilon_{zx} = d\varepsilon_{zy} = d\tau_{zx} = d\tau_{zy} = 0. \quad (2-42)$$

In this case, Eq.(2-8) can be reduced, and the matrix form of the constitutive relation is expressed as

$$\begin{Bmatrix} d\sigma_{xx} \\ d\sigma_{yy} \\ d\tau_{xy} \\ d\sigma_{zz} \end{Bmatrix} = \begin{bmatrix} Z_{11} & Z_{12} & Z_{13} \\ Z_{21} & Z_{22} & Z_{23} \\ Z_{31} & Z_{32} & Z_{33} \\ Z_{41} & Z_{42} & Z_{43} \end{bmatrix} \begin{Bmatrix} d\varepsilon_{xx} \\ d\varepsilon_{yy} \\ d\gamma_{xy} \end{Bmatrix} \quad (2-43)$$

where

$$Z_{11} = \frac{E(1-\nu)}{(1+\nu)(1-2\nu)} - h(2\bar{\sigma}_x - \bar{\sigma}_y - \bar{\sigma}_z)^2$$

$$Z_{12} = \frac{E \nu}{(1+\nu)(1-2\nu)} - h(2\bar{\sigma}_x - \bar{\sigma}_y - \bar{\sigma}_z)(2\bar{\sigma}_y - \bar{\sigma}_z - \bar{\sigma}_x)$$

$$Z_{13} = -\frac{1}{2} h(2\bar{\sigma}_x - \bar{\sigma}_y - \bar{\sigma}_z)(6\bar{\tau}_{xy})$$

$$Z_{21} = \frac{E \nu}{(1+\nu)(1-2\nu)} - h(2\bar{\sigma}_y - \bar{\sigma}_z - \bar{\sigma}_x)(2\bar{\sigma}_x - \bar{\sigma}_y - \bar{\sigma}_z)$$

$$Z_{22} = \frac{E(1-\nu)}{(1+\nu)(1-2\nu)} - h(2\bar{\sigma}_y - \bar{\sigma}_z - \bar{\sigma}_x)^2$$

$$Z_{23} = -\frac{1}{2} h(2\bar{\sigma}_y - \bar{\sigma}_z - \bar{\sigma}_x)(6\bar{\tau}_{xy})$$

$$Z_{31} = -h(6\bar{\tau}_{xy})(2\bar{\sigma}_x - \bar{\sigma}_y - \bar{\sigma}_z)$$

$$Z_{32} = -h(6\bar{\tau}_{xy})(2\bar{\sigma}_y - \bar{\sigma}_z - \bar{\sigma}_x)$$

$$Z_{33} = \frac{E}{2(1+\nu)} - \frac{1}{2} h(6\bar{\tau}_{xy})^2$$

$$Z_{41} = \frac{E \nu}{(1+\nu)(1-2\nu)} - h(2\bar{\sigma}_z - \bar{\sigma}_x - \bar{\sigma}_y)(2\bar{\sigma}_x - \bar{\sigma}_y - \bar{\sigma}_z)$$

$$Z_{42} = \frac{E \nu}{(1+\nu)(1-2\nu)} - h(2\bar{\sigma}_z - \bar{\sigma}_x - \bar{\sigma}_y)(2\bar{\sigma}_y - \bar{\sigma}_z - \bar{\sigma}_x)$$

$$Z_{43} = -\frac{1}{2} h(2\bar{\sigma}_z - \bar{\sigma}_x - \bar{\sigma}_y)(6\bar{\tau}_{xy})$$

$$h = \frac{E}{1+\nu} \frac{g}{\frac{1+\nu}{E} + 6q^2 g}$$

$$g = \frac{1}{4q^2} \left[ \frac{1}{E_1} - \frac{1}{E} \right],$$

and

$$\bar{\sigma}_{xx} = \sigma_{xx} - \alpha_{xx}, \quad \bar{\sigma}_{yy} = \sigma_{yy} - \alpha_{yy}, \quad \bar{\sigma}_{zz} = \sigma_{zz} - \alpha_{zz},$$

$$\bar{\tau}_{xy} = \tau_{xy} - \alpha_{xy}$$

### 2.4.3. Three dimension

In three dimension case, the matrix form of the constitutive relation can be written as:

$$\begin{Bmatrix} d\sigma_{xx} \\ d\sigma_{yy} \\ d\sigma_{zz} \\ d\tau_{xy} \\ d\tau_{yz} \\ d\tau_{zx} \end{Bmatrix} = \begin{bmatrix} D_{11} & D_{12} & D_{13} & D_{14} & D_{15} & D_{16} \\ D_{21} & D_{22} & D_{23} & D_{24} & D_{25} & D_{26} \\ D_{31} & D_{32} & D_{33} & D_{34} & D_{35} & D_{36} \\ D_{41} & D_{42} & D_{43} & D_{44} & D_{45} & D_{46} \\ D_{51} & D_{52} & D_{53} & D_{54} & D_{55} & D_{56} \\ D_{61} & D_{62} & D_{63} & D_{64} & D_{65} & D_{66} \end{bmatrix} \begin{Bmatrix} d\epsilon_{xx} \\ d\epsilon_{yy} \\ d\epsilon_{zz} \\ d\gamma_{xy} \\ d\gamma_{yz} \\ d\gamma_{zx} \end{Bmatrix} \quad (2-44)$$

where

$$\begin{aligned} D_{11} &= \frac{E(1-\nu)}{(1+\nu)(1-2\nu)} - h(2\bar{\sigma}_x - \bar{\sigma}_y - \bar{\sigma}_z)^2 \\ D_{12} &= \frac{E\nu}{(1+\nu)(1-2\nu)} - h(2\bar{\sigma}_x - \bar{\sigma}_y - \bar{\sigma}_z)(2\bar{\sigma}_y - \bar{\sigma}_x - \bar{\sigma}_z) \\ D_{13} &= \frac{E\nu}{(1+\nu)(1-2\nu)} - h(2\bar{\sigma}_x - \bar{\sigma}_y - \bar{\sigma}_z)(2\bar{\sigma}_z - \bar{\sigma}_x - \bar{\sigma}_y) \\ D_{14} &= -h(2\bar{\sigma}_x - \bar{\sigma}_y - \bar{\sigma}_z)(3\bar{\tau}_{xy}) \\ D_{15} &= -h(2\bar{\sigma}_x - \bar{\sigma}_y - \bar{\sigma}_z)(3\bar{\tau}_{yz}) \\ D_{16} &= -h(2\bar{\sigma}_x - \bar{\sigma}_y - \bar{\sigma}_z)(3\bar{\tau}_{zx}) \\ D_{21} &= D_{12} \\ D_{22} &= \frac{E(1-\nu)}{(1+\nu)(1-2\nu)} - h(2\bar{\sigma}_y - \bar{\sigma}_x - \bar{\sigma}_z)^2 \\ D_{23} &= \frac{E\nu}{(1+\nu)(1-2\nu)} - h(2\bar{\sigma}_y - \bar{\sigma}_x - \bar{\sigma}_z)(2\bar{\sigma}_z - \bar{\sigma}_x - \bar{\sigma}_y) \end{aligned}$$

$$D_{24} = -h (2\bar{\sigma}_y - \bar{\sigma}_x - \bar{\sigma}_z)(3\bar{\tau}_{xy})$$

$$D_{25} = -h (2\bar{\sigma}_y - \bar{\sigma}_x - \bar{\sigma}_z)(3\bar{\tau}_{yz})$$

$$D_{26} = -h (2\bar{\sigma}_y - \bar{\sigma}_x - \bar{\sigma}_z)(3\bar{\tau}_{zx})$$

$$D_{31} = D_{13} \quad , \quad D_{32} = D_{23}$$

$$D_{33} = \frac{E(1-\nu)}{(1+\nu)(1-2\nu)} - h (2\bar{\sigma}_z - \bar{\sigma}_x - \bar{\sigma}_y)^2$$

$$D_{34} = -h (2\bar{\sigma}_z - \bar{\sigma}_x - \bar{\sigma}_y)(3\bar{\tau}_{xy})$$

$$D_{35} = -h (2\bar{\sigma}_z - \bar{\sigma}_x - \bar{\sigma}_y)(3\bar{\tau}_{yz})$$

$$D_{36} = -h (2\bar{\sigma}_z - \bar{\sigma}_x - \bar{\sigma}_y)(3\bar{\tau}_{zx})$$

$$D_{41} = D_{14} \quad , \quad D_{42} = D_{24} \quad , \quad D_{43} = D_{34}$$

$$D_{44} = \frac{E}{2(1+\nu)} - h (3\bar{\tau}_{xy})^2$$

$$D_{45} = -h (3\bar{\tau}_{xy})(3\bar{\tau}_{yz})$$

$$D_{46} = -h (3\bar{\tau}_{xy})(3\bar{\tau}_{zx})$$

$$D_{51} = D_{15} \quad , \quad D_{52} = D_{25}$$

$$D_{53} = D_{35} \quad , \quad D_{54} = D_{45}$$

$$D_{55} = \frac{E}{2(1+\nu)} - h (3\bar{\tau}_{yz})^2$$

$$D_{56} = -h (3\bar{\tau}_{yz})(3\bar{\tau}_{zx})$$

$$D_{61} = D_{62} \quad , \quad D_{62} = D_{26} \quad , \quad D_{63} = D_{36}$$

$$D_{64} = D_{46} \quad , \quad D_{65} = D_{56}$$

$$D_{66} = \frac{E}{2(1+\nu)} - h (3\bar{\tau}_{xy})^2$$

$$h = \frac{E}{1+\nu} \frac{g}{\frac{(1+\nu)}{E} + 6q^2g}$$

$$g = \frac{1}{4q^2} \left[ \frac{1}{E_t} - \frac{1}{E} \right]$$

and

$$\bar{\sigma}_{xx} = \sigma_{xx} - \alpha_{xx} \quad , \quad \bar{\sigma}_{yy} = \sigma_{yy} - \alpha_{yy} \quad , \quad \bar{\sigma}_{zz} = \sigma_{zz} - \alpha_{zz}$$

$$\bar{\tau}_{xy} = \tau_{xy} - \alpha_{xy} \quad , \quad \bar{\tau}_{yz} = \tau_{yz} - \alpha_{yz} \quad , \quad \bar{\tau}_{zx} = \tau_{zx} - \alpha_{zx}$$

## 2.5 Brief summary

Several issues pertaining to the elastic-plastic deformation, including evolution of the yield surface and the change in size of the yield surface, have been discussed. A constitutive model developed by Ellyin, Xia and Wu is presented and further improved. This model is simple enough to be used effectively in computer programs and matches the essential features of the time-independent elastic-plastic behaviour of materials reasonably well for both monotonic and cyclic loading under complex loading paths.

It is worthwhile to mention that while this constitutive model is used for the finite element analyses in Chapters 3 and 4, its formulations are compiled into a subroutine which is inserted in ADINA code. Relations (2-41) and (2-43) are used for the plane

stress and plane strain conditions, respectively. The motion of the centre of the yield surface,  $\alpha_{ij}$  is defined by Eqs.(2-29) and (2-32). The instantaneous tangent modulus  $E_t$  is calculated from Eqs.(26) and (31) in ref.[1-5]. Meanwhile, some models in ADINA, such as von Mises isotropic hardening model for small deformation and finite deformation, are employed in a comparative sense.

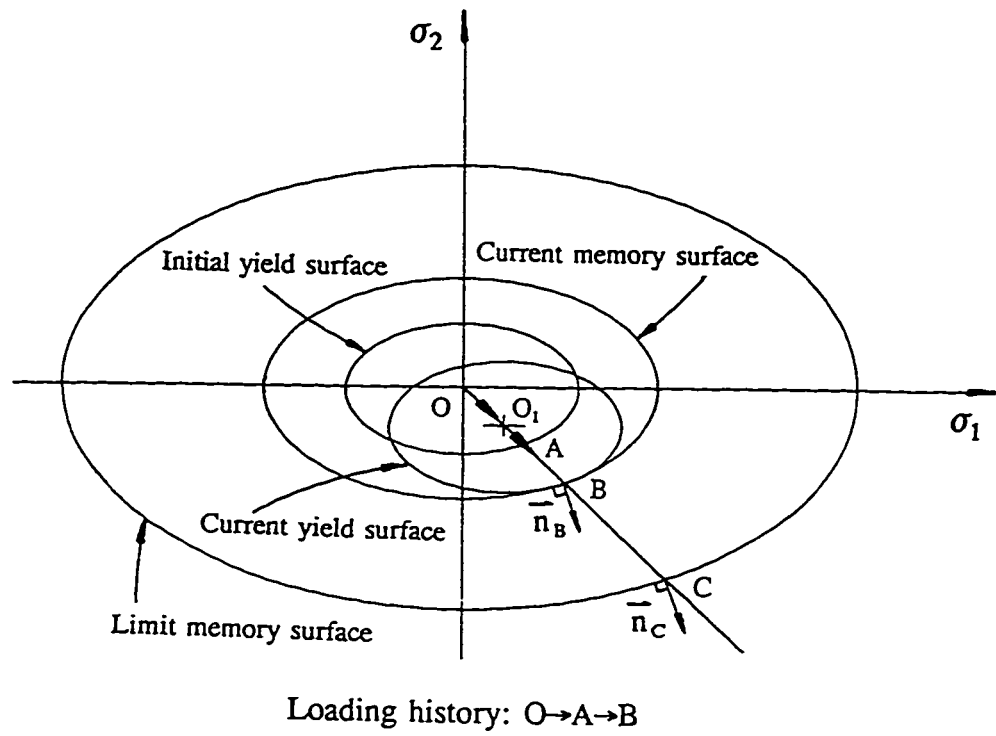


Fig.(2-1) A schematic representation of the motion of yield surface for monotonically proportional loading.



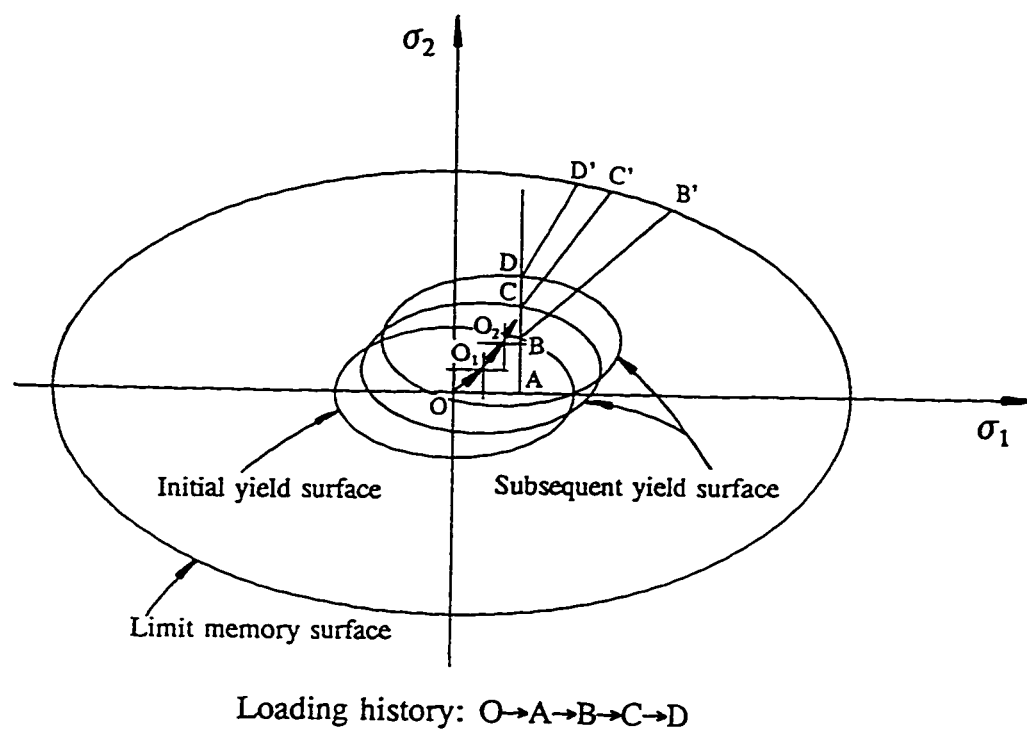


Fig.(2-2) A schematic representation of the motion of yield surface for monotonically nonproportional loading.

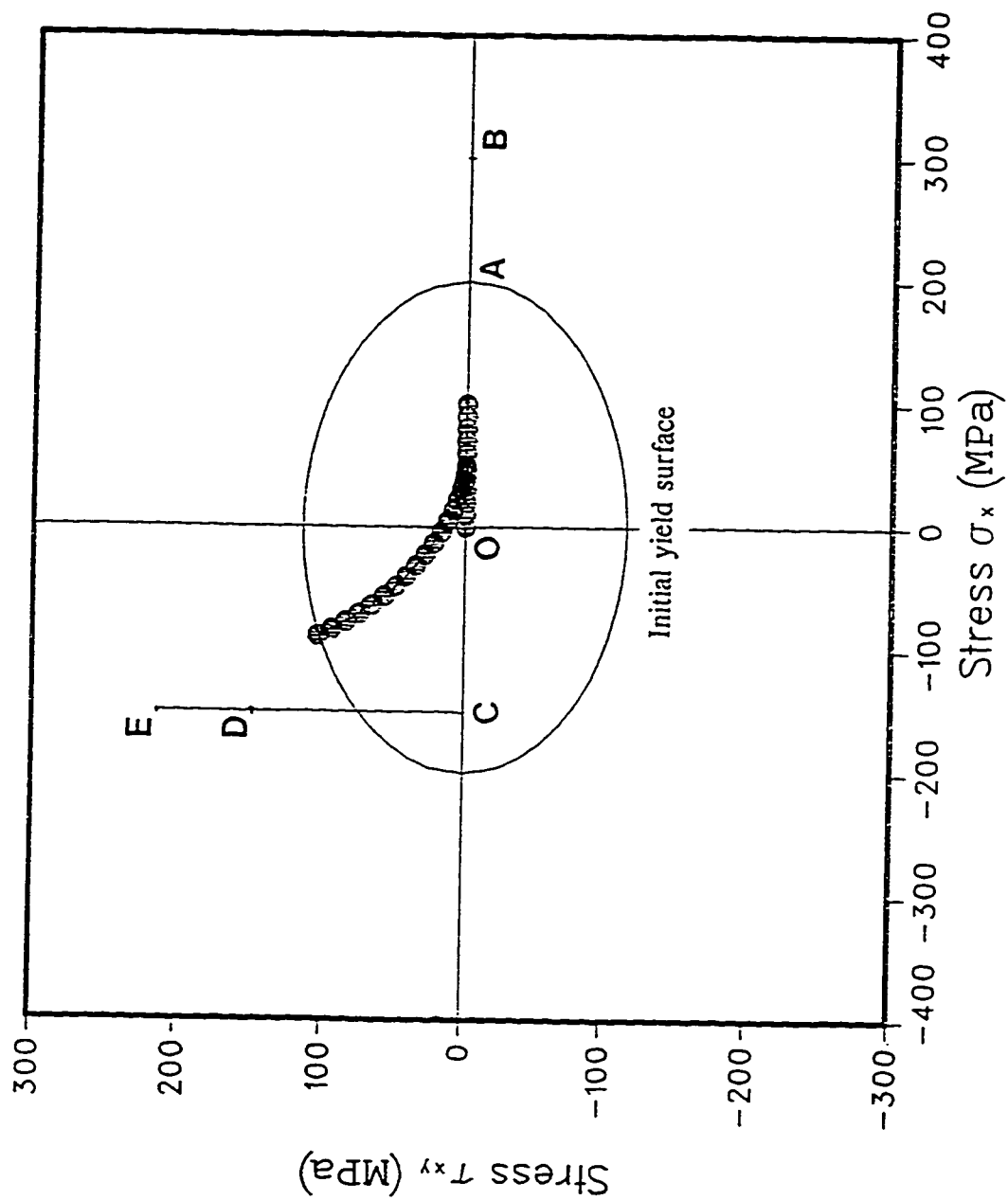


Fig.(2-3) The motion of the centre of yield surface by Ziegler's rule under loading path  $O \rightarrow A \rightarrow B \rightarrow C \rightarrow D \rightarrow E$  in tension-torsion space.

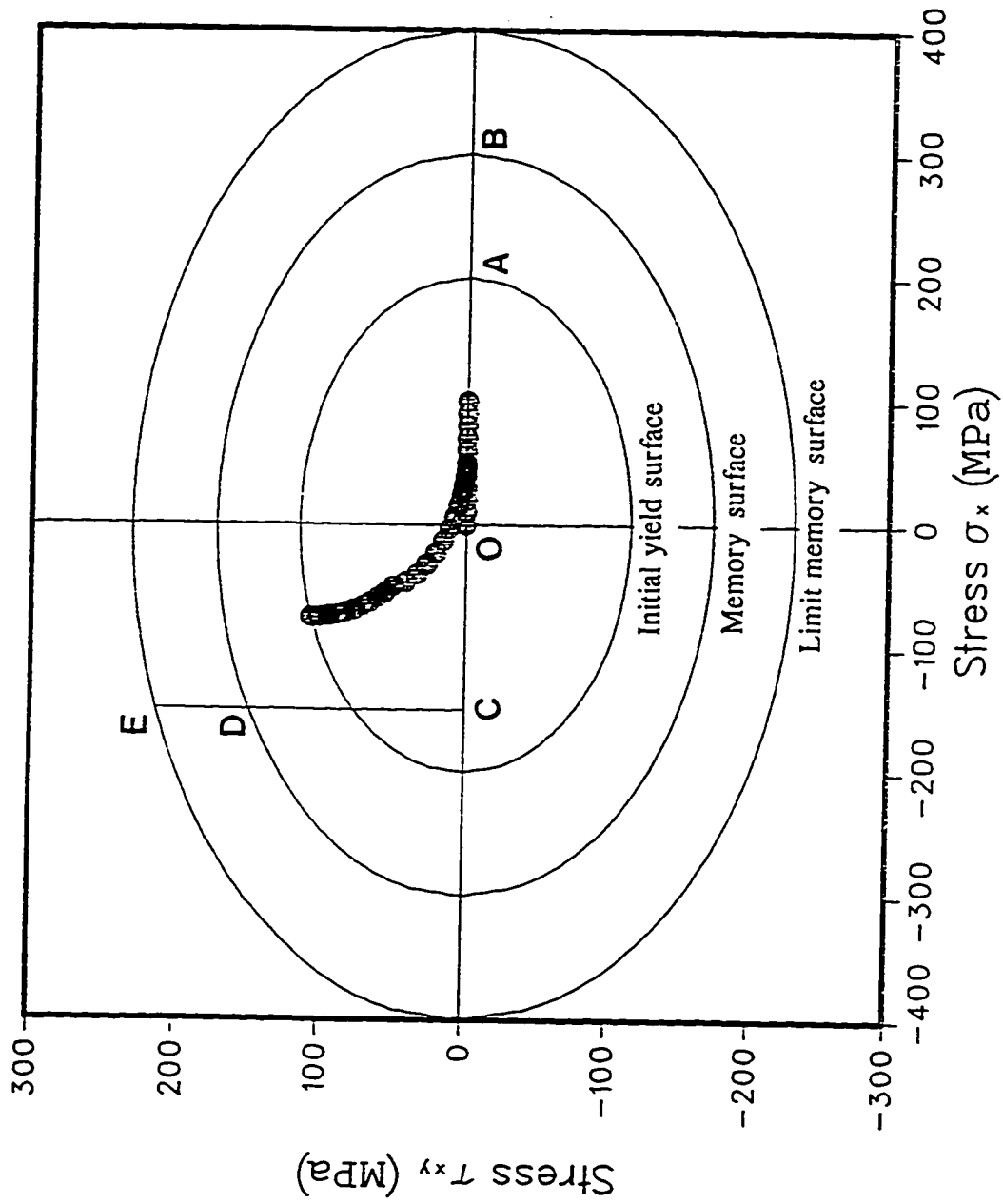


Fig.(2-4) The motion of the centre of yield surface by the proposed rule under loading path  $O \rightarrow A \rightarrow B \rightarrow C \rightarrow D \rightarrow E$  in tension-torsion space.

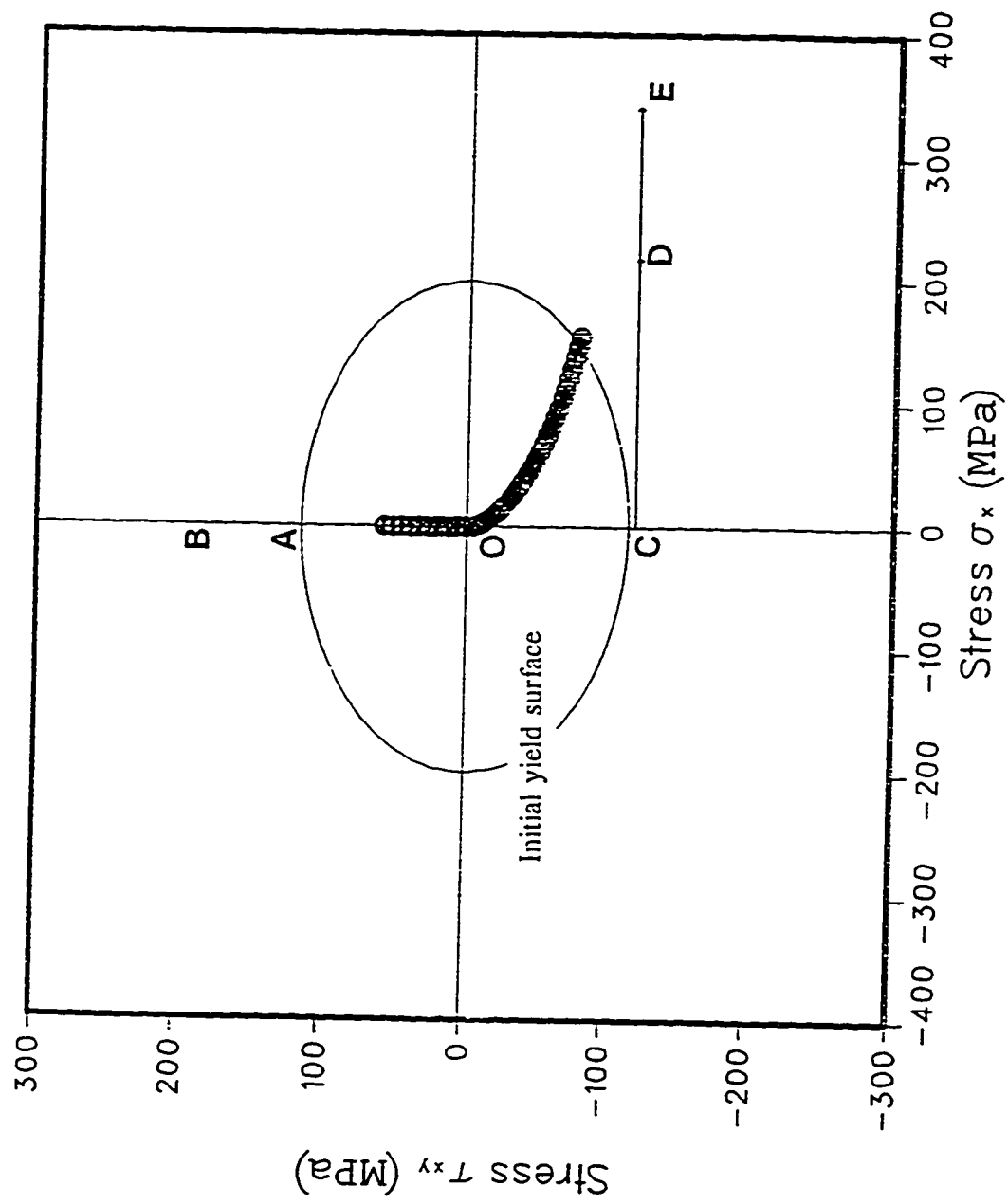


Fig.(2-5) The motion of the centre of yield surface by Ziegler's rule under loading path  $O \rightarrow A \rightarrow B \rightarrow C \rightarrow D \rightarrow E$  in tension-torsion space.

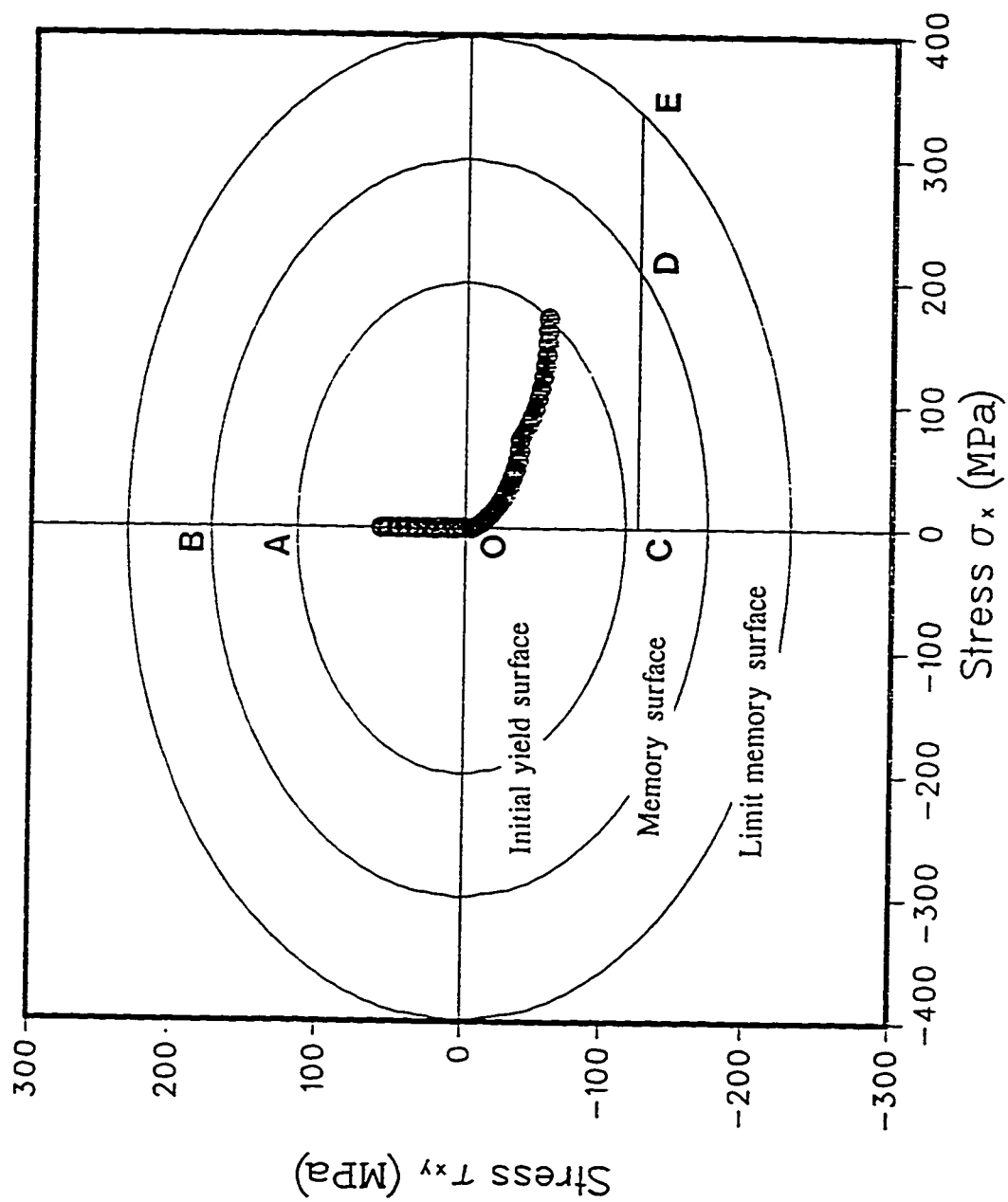


Fig.(2-6) The motion of the centre of yield surface by the proposed rule under loading path  $O \rightarrow A \rightarrow B \rightarrow C \rightarrow D \rightarrow E$  in tension-torsion space.

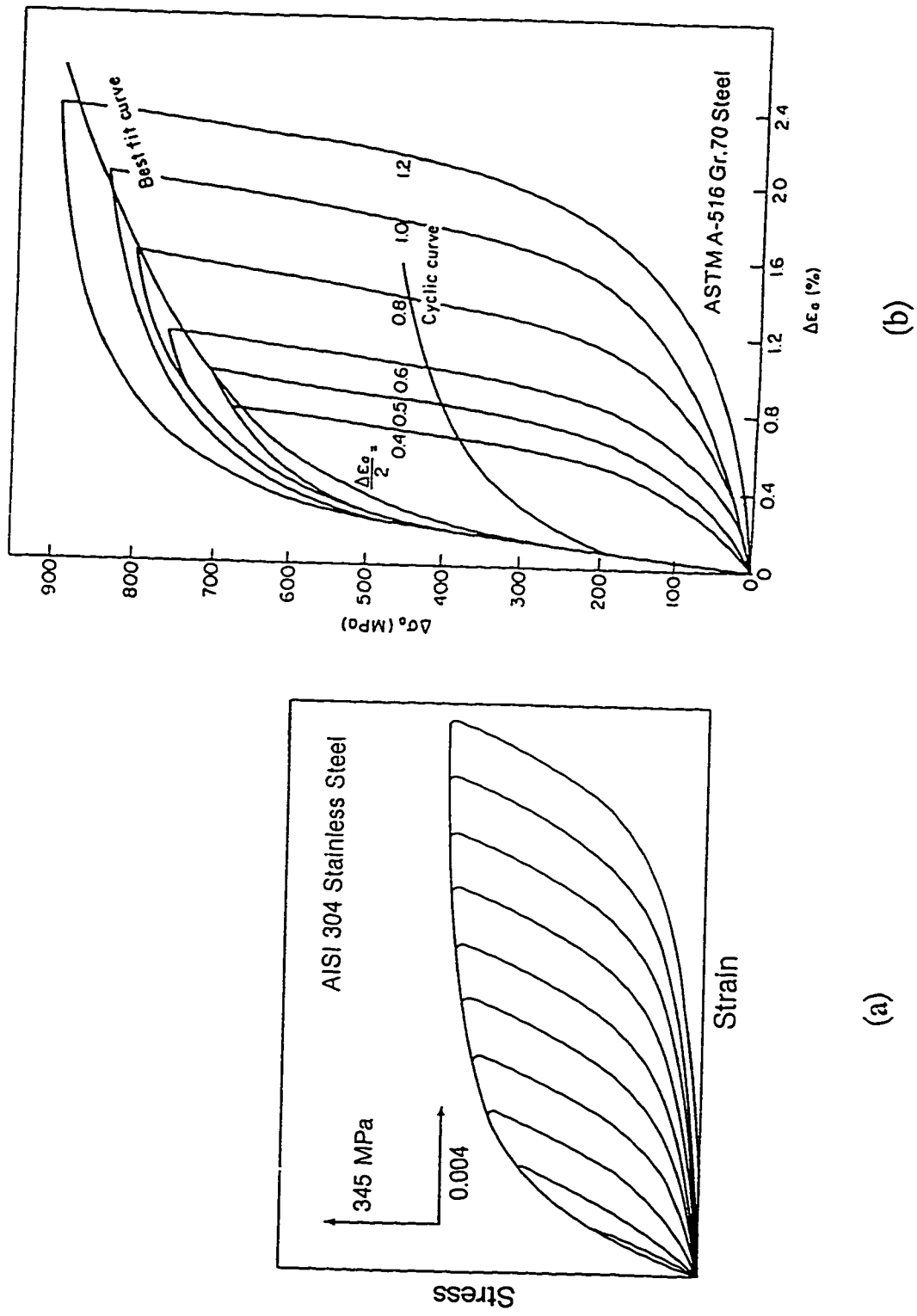


Fig. (2-7) (a) Stress-strain hysteresis loops showing Masing behaviour[2-13].  
 (b) Stress-strain hysteresis loops showing Non Masing behaviour[2-14].

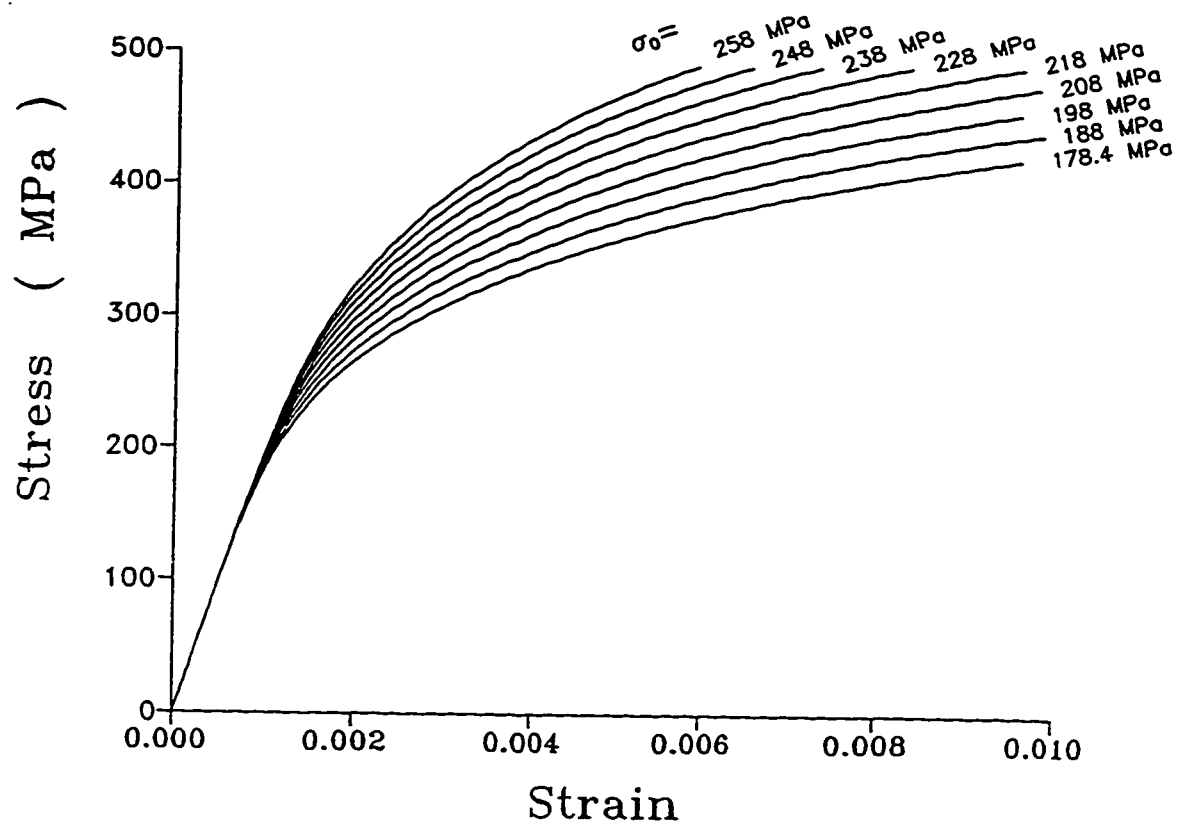


Fig.(2-8) Effect of the yield stress  $\sigma_0$  on the stress-strain curve described by Ramberg-Osgood relation.

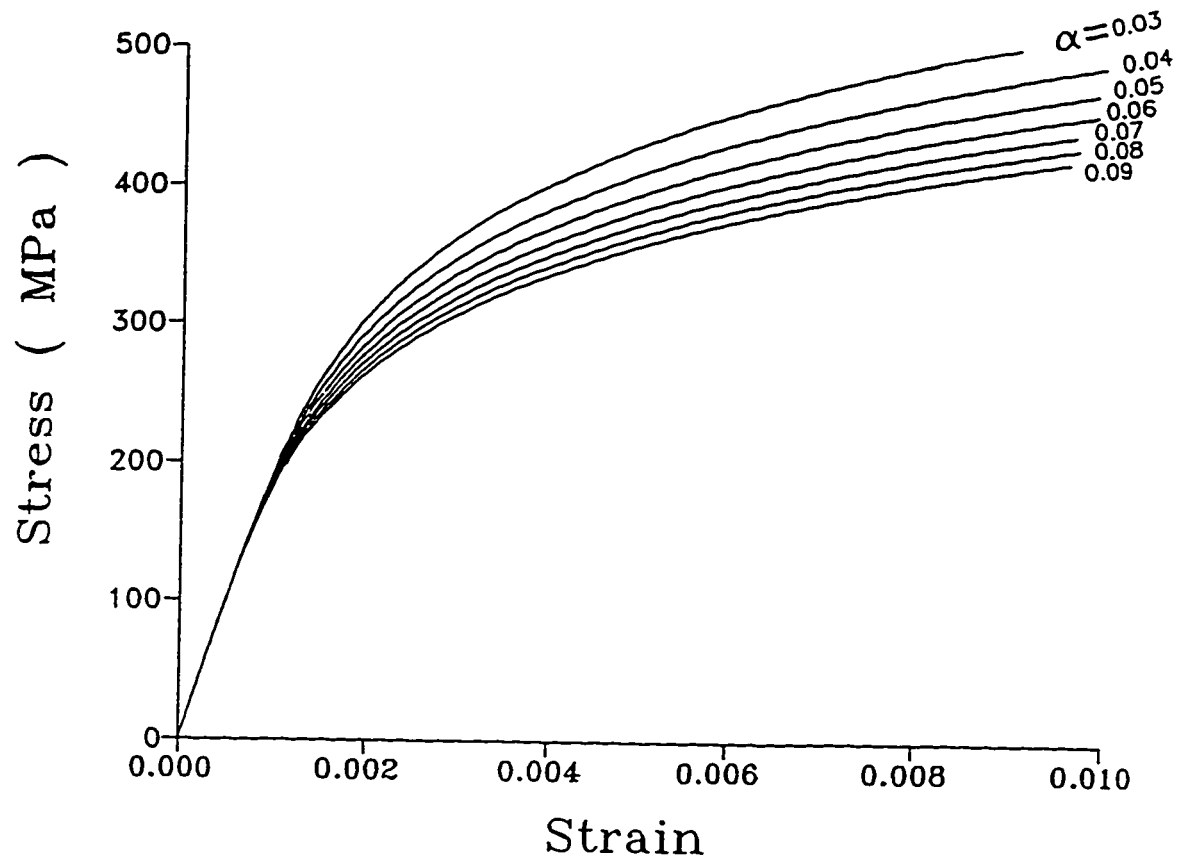


Fig.(2-9) Effect of the material constant  $\alpha$  on the stress-strain curve described by Ramberg-Osgood relation.



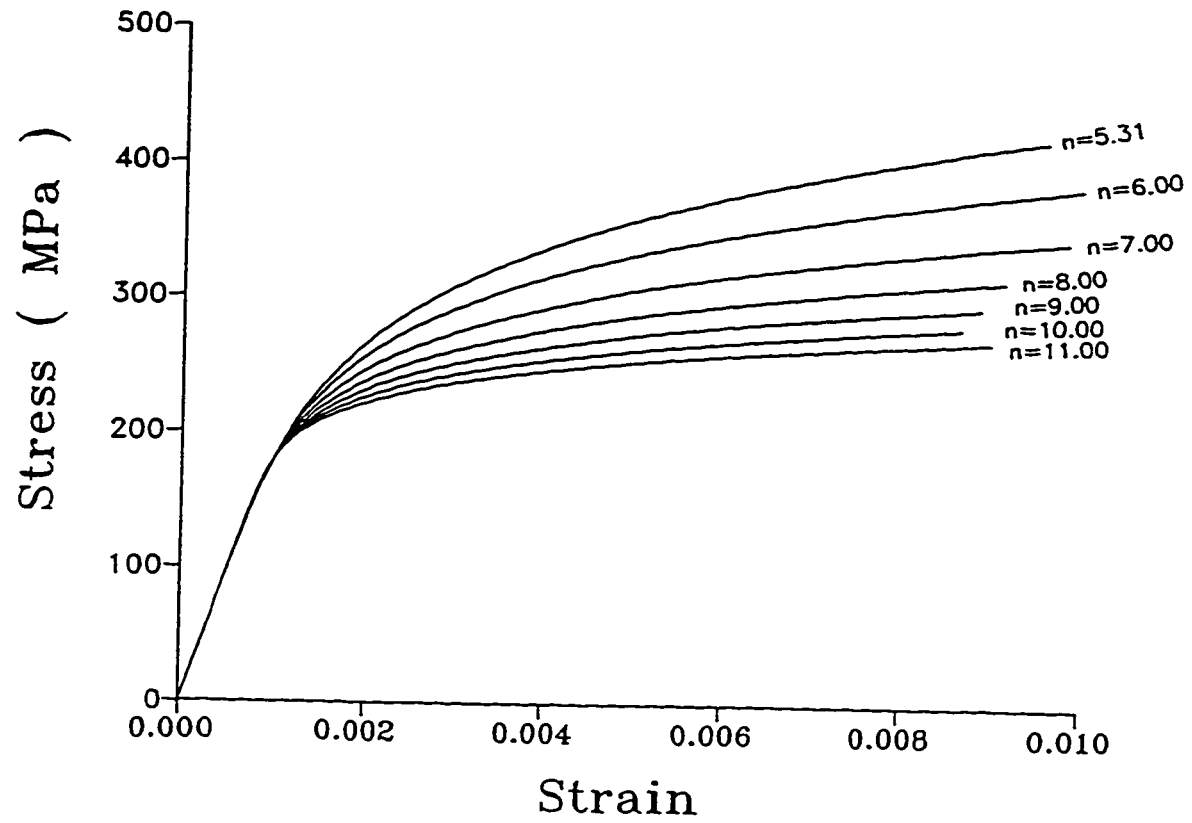


Fig.(2-10) Effect of the material constant  $n$  on the stress-strain curve described by Ramberg-Osgood relation.

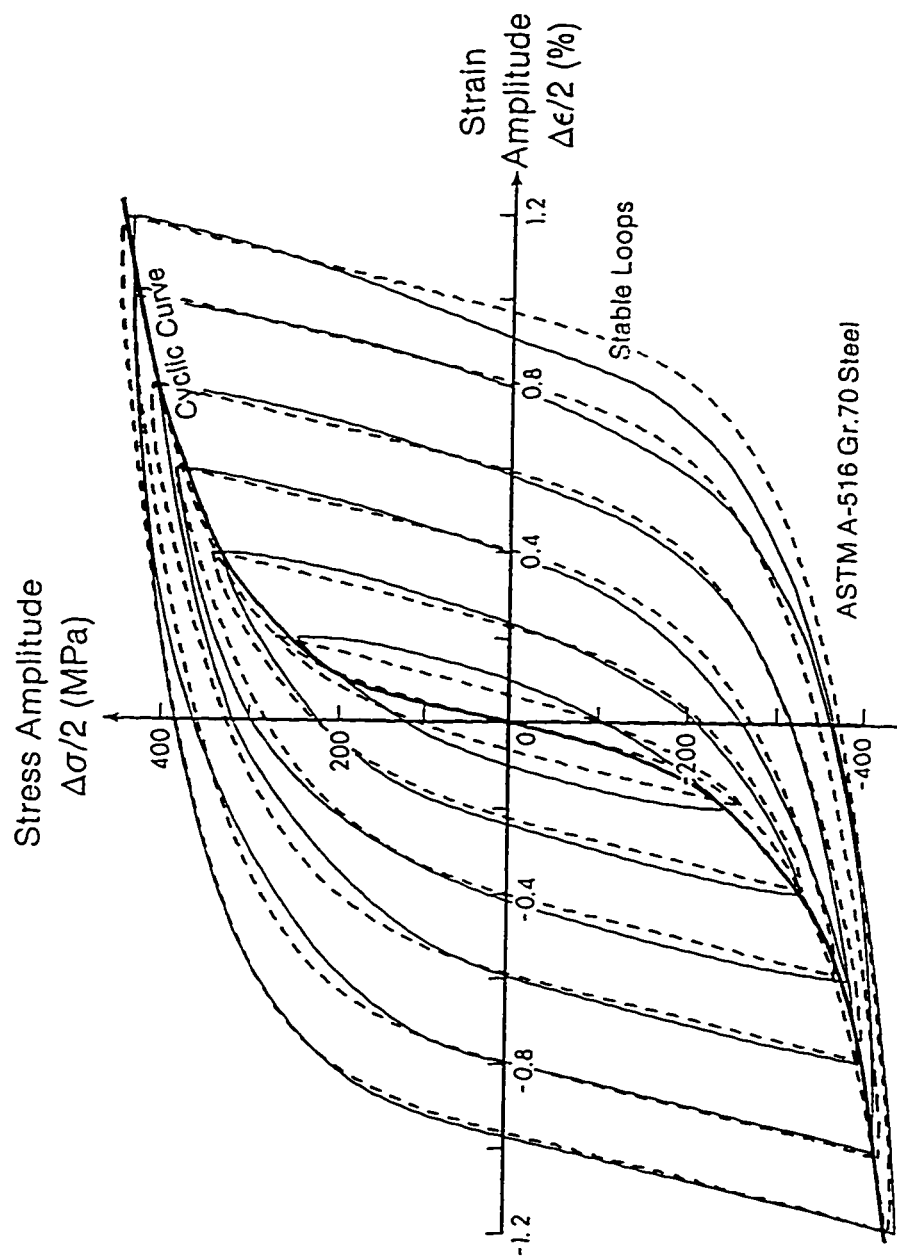


Fig (2-11) The stress-strain curves (Dashed lines), which are described by the Ramberg-Osgood relation and followed by the material points in different strain ranges, are in good agreement with the experimental curves (Solid lines) [2-14] during a cyclic loading in steady state.

## CHAPTER 3

# EFFECT OF HYDRIDE PRECIPITATION ON THE ELASTIC-PLASTIC STRESS FIELD NEAR A CRACK TIP

### 3.1 Introduction

The occurrence of delayed failure in zirconium alloys due to hydrogen embrittlement. was reported in the early 1960's [3-1]. The effect of hydrostatic stress gradient on the concentration of mobile hydrogen was clearly established by Li, Oriani and Darken [3-2]. Experimental investigation in the next decade indicated that the mechanism of delayed hydride cracking (DHC) was diffusion of hydrogen up the stress gradient and formation of hydride platelets at regions of high stress, e.g. crack like defects or notch tips. The brittle hydride, subjected to high stress, cracks and then the process repeats itself in an intermittent fashion [3-3] [3-4].

Several models have been proposed to calculate the flux of hydrogen and the rate of hydride growth, e.g. see [3-3] ~ [3-7]. The nature of the stress field in front of a crack-like defect in the presence of hydrides, is important because not only does it influence the hydrogen flux but also the fracture of the hydride may be stress magnitude dependent. This aspect was emphasized by Simpson and Puls [3-6] who stated that "details on the alterations of the crack tip stress field by the precipitation event are required." Many experiments have been performed using a variety of techniques to

determine the effect of various factors, such as hydride size, matrix strength and crack tip stress state on the delayed hydride cracking [3-8] ~ [3-10]. However, obtaining an accurate estimate of crack tip stress field alteration due to hydride precipitation has proven to be a difficult task. One of the difficulties is that the hydrogen migrates to the plastic zone of a loaded crack, and a major part of the precipitation takes place in the plastically deformed zone. Thus, elastic analysis cannot be used to predict the stress field re-distribution. In a recent investigation, Eadie and Ellyin [3-11] applied Rice's superposition method to a rigid-plastic strip (Dugdale-Barenblatt model) to obtain stresses in front of a crack due to hydride precipitation. The solution indicated a compressive region just ahead of the crack tip, and an extended plastic zone. Because of the assumptions involved in the foregoing analytical method, the results obtained may be regarded as an extreme case as far as the compressive stress zone is concerned.

It is the objective of this chapter to investigate the change in the crack tip stress and strain fields due to hydride growth by using an elastic-plastic finite element analysis. The first pre-requisite for an elastic-plastic analysis, is to incorporate an appropriate constitutive model in a finite element code. The proposed constitutive model in Chapter 2 as a small deformation model is employed by compiling it as a subroutine which is inserted in ADINA. How to simulate the process of the hydride precipitation in the finite element analysis should be the next requisite. A loading procedure which provides a basis for the analysis is designed to match this process. Then, the analyses under plane stress and plane strain conditions are discussed respectively. The analysis under plane strain

condition receives more attention. Finally, in order to ascertain the effect of the crack tip blunting on the initial location of the hydride precipitation a finite deformation constitutive model which is introduced by ADINA is employed in the finite element analysis.

### **3.2 Modelling and loading procedure**

Delayed hydride cracking (DHC) has been observed in pressure tubes in CANDU reactors. These are moderately thick (4 mm) Zirconium-2.5 Niobium extruded tubes which contain natural uranium fuel bundles that are cooled by pressurized deuterium-oxide (heavy water). Because the transverse stress is twice the longitudinal stress, the most severe flaw is a longitudinal crack. At reactor operating temperatures (523 to 585 K), the minimum critical crack length of cold-worked Zr-2.5 wt% Nb pressure tubes is 73 mm, which is 18 times the tube wall thickness [3-12]. When the stable propagation of the crack along the longitudinal direction is considered, the plane-stress condition is assumed to be suitable. When the propagation of the crack along radial direction is investigated, the stress state should be under a plane-strain condition. Because Zr-2.5 wt% Nb pressure tubes are stronger in the transverse direction than in the longitudinal direction [3-12], the investigation under plane-strain condition is more important. The finite element analyses under plane-stress and plane-strain conditions are performed in §3.3 and §3.4 respectively.

A centre cracked panel subjected to a uniformly distributed tensile load perpendicular to the crack plane, is chosen to study the effect of hydride formation (precipitation and

expansion). The load at the panel boundary (remote stress) is increased from the initial value of zero to a pre-determined level in small increments. This loading corresponds to the pressurization of the tube. During formation of the hydride (precipitation and expansion) the remote stress (hoop stress) is kept constant.

To simulate the effect of hydride formation, the material in front of the crack is subjected to an appropriate displacement. The distance along the crack plane which is subjected to a displacement, denotes the length of the hydride, and the value of prescribed displacement indicates precipitation and expansion of hydride, Fig. (3-1).

The rationale for the above described loading procedure is as follows. The concentration of mobile hydrogen in front of the crack and formation of hydride platelet, results in the matrix material being displaced. We assume that the hydride platelet formed at the crack tip has a normal parallel to the applied load and that its major precipitation and expansion are in the direction of the normal [3-3] ~ [3-8]. The precipitation and expansion of hydride then cause stress re-distribution at the front of the crack.

It is to be noted that the growth of hydrides is a time dependent process, e.g. see Fig. 4 in ref. [3-13]. In the modelling, the final hydride length is achieved through the imposition of stepwise displacements on nodes in the front of the crack, as will be explained in §3.3.2 and §3.4.2. Experimental observations have indicated that the length of the hydride varies from 10 to 100  $\mu\text{m}$  and its thickness from 1 to 2  $\mu\text{m}$  [3-8].

It was mentioned earlier that the precipitation and expansion of hydride are simulated in the finite element analysis by imposing a displacement perpendicular to the crack

plane. Imposing a displacement on a node on the crack plane (plane of symmetry) does not imply that the node is free. The node still bears a certain force that can be calculated from the element stresses to which the node belongs. This is different from crack propagation. After crack propagation, the nodes symmetrically on the two sides of the crack are free and they no longer carry a force perpendicular to the crack plane. There is a gap between the nodes on the two sides of the crack. While the displaced nodes have symmetric points at the opposite side of the crack plane respectively. Between a displaced node and its symmetric point there exists an interaction, which can be envisaged as a force in a spring connecting the node and its symmetric point with a certain stiffness. This weaker stiffness as compared to the matrix material, represents the hydride material stiffness.

Both the precipitation and the expansion of hydride lead to the increase of the hydride platelet volume, so they are assumed as a united process in the finite element analysis. Starting from a stress-free crack (initial crack in the finite element model), there should not be any hydride platelet at the region of the crack tip. Following the precipitation and the expansion of hydride, the volume of the hydride platelet increases in its thickness and length. Thus, the adopted procedure is a realistic one. Note that both the length of the hydride and its thickness are increased in steps to simulate nucleation, precipitation and growth, see Fig.(3-1), §3.3.2 and §3.4.2.

It should be noted that a node can be "fixed" by prescribing a zero displacement component for all its degrees of freedom. This is, however, different from imposing a fixity boundary condition at the node. Because the prescribed degrees of freedom are

retained in the system matrices (i.e. equation numbers are assigned), whereas the degrees of freedom at which fixity conditions are imposed, are deleted from the system matrices.

### 3.3 The analysis under plane stress condition

#### 3.3.1 Finite element mesh and material properties

The mesh for a centre-cracked panel to be used in the finite element analysis is shown in Fig.(3-2). Because of symmetry, only one quarter of the panel is considered. A total of 189 isoparametric rectangular elements are used together with 517 nodes. The elements in a region near the crack tip have eight nodes and the rest are four node elements. Between the two types of elements the use of the variable-number-nodes elements can be effective, and constraint equations are frequently useful to preserve compatibility between elements in the transition region. To provide the information required in the solution, the near-tip elements must be small to compare with the length of the hydride platelet. The smallest element length is 0.156 mm, or 0.00372 w, where w is the width of the half-panel, 42 mm. The half crack length a is 10 mm.

For cold worked Zr-2.5% Nb there is very little strain hardening at room temperature. The strain hardening exponent is in the range 0.02 to 0.05 [3-12]. A middle value is chosen to fit Ramberg-Osgood relation:

$$\frac{\epsilon}{\epsilon_0} = \frac{\sigma}{\sigma_0} + \alpha \left( \frac{\sigma}{\sigma_0} \right)^n \quad (3-1)$$



where the material's yield stress  $\sigma_0$  is 247.4 MPa, and  $\epsilon_0 = \sigma_0/E$ , while the elastic modulus  $E$  is 200000 MPa. The material constants  $n$  and  $\alpha$  are 37.9 and 0.438 respectively. The stress-strain curve described by Ramberg-Osgood relation is indicated in Fig.(3-3).

### 3.3.2 Loading steps

The uniformly distributed tensile load perpendicular to the crack plane on the panel increases from zero to 56 MPa during the first 27 steps. For the half crack length of 10 mm, the load of 56 MPa corresponds to the stress intensity factor  $K_I = 10 \text{ MPa}\sqrt{\text{m}}$ . After step 27, the far-field stress is kept at 56 MPa. Then, the first three nodes in front of the crack tip are displaced  $2.5 \mu\text{m}$  perpendicular to the crack plane during the following 9 steps. This procedure is further explained in the case of plane strain condition, §3.4. The distance among the three nodes is considered to be the length of the hydride platelet. The nodal displacement represents the thickness of the hydride platelet. Thus, the hydride platelet grows from an absence to  $2.5 \mu\text{m}$  thick and  $234 \mu\text{m}$  long during the whole loading procedure.

### 3.3.3 Results and discussion

The stress and strain distributions for the several chosen steps are plotted in Figs.(3-4) and (3-5), along the  $x_1$  axis ( $\theta=0$ ). The crack tip is situated at the origin of the coordinate axes which have been made dimensionless by dividing by  $\sigma_0$  and parameter  $(K_I/\sigma_0)^2$  respectively, where  $K_I$  is the stress intensity factor for the Mode I deformation. The parameter  $(K_I/\sigma_0)^2$  has the unit of length and it contains a measure of the far-field

loading through definition of  $K_I$ . From step 1 (15 MPa), step 14 (41 MPa) and step 27 (56 MPa), it can be seen that with an increasing load, the stresses in front of the crack tip increase and reach the yield stress of the material and the size of the plastic zone grows gradually. After step 27, the stresses in the region corresponding to the length of the hydride platelet appear to be unloading due to the displacing nodes.

At step 30 (displacement of 1.5  $\mu\text{m}$ ) the stresses on the length corresponding to the hydride platelet decrease, so that an elastic region is formed in the presented plastic zone. When the elastic region extends gradually with growth of the displacements, the plastic zone also extends outward. This is because the dilatation of the hydride platelet acts as an additional opening force on the material beyond the hydride platelet.

From Fig.(3-5), the change of strains is similar to the change of stresses during the whole loading process. But the decrease of strains in the region corresponding to the length of the hydride platelet is very small. It seems that the hydride growth has an insignificant influence on the strains.

The plastic zone surrounding the crack tip is shown in Fig.(3-6) for step 27 of loading. Each point in Fig.(3-6) identified by a + symbol represents a Gauss integration point which has yielded. Hence, the total of the yielded Gauss integration points depicts the plastic zone size and shape. The maximum distance from the crack tip,  $r_p$ , is found along the line ( $\theta=0$ ) and is about

$$r_p = 0.323 \left( \frac{K_I}{\sigma_0} \right)^2 \quad (3-2)$$

which is very close to the value predicted by Irwin's plane stress condition.

$r_p = 0.318 (k_I/\sigma_0)^2$  [3-14]. Each point in Fig.(3-6) identified by a  $\oplus$  symbol form an elastic region corresponding to step 36. The appearance of the elastic region in the plastic zone at the crack tip should mitigate the crack growth.

Figure (3-7) shows the accumulated strain energy density at the point in front of the crack tip with the loading process. It is quite clear that the accumulated strain energy density increases from step 1 to step 27 and decreases from step 28 to step 36. Using the strain energy density as a damage parameter [3-15], it can be seen that the damage is diminished due to the dilation of the hydride platelet ahead of the crack tip.

#### 3.3.4 Conclusions

A qualitative picture of stress changes which result from the hydride precipitation and expansion is given by using finite element analysis. The volume dilation of the hydride platelet ahead of the crack tip decreases the stresses caused by the far-field tensile stress. An elastic region appears in the plastic zone in front of the crack tip. In the case of a growing crack this would imply a retardation or crack arrest.

### 3.4 The analysis under plane strain condition

#### 3.4.1 Finite element mesh and material properties

The mesh for a quarter of a centre-cracked panel to be used in the finite element analysis is shown in Fig.(3-8) for section I, and Fig.(3-9) for section II and section III.

For the sake of clarity, the crack tip region in Fig.(3-8) (indented area) is enlarged and displayed as section II of Fig.(3-9). Otherwise section II fits into the opening of section I, and likewise, section III in Fig.(3-9) fits into the opening of section II with proper scale. Note that the crack is located at the left bottom corner of Fig.(3-8).

A plane-strain centre cracked panel is a closer representation of a pressure tube with a tensile stress along the transverse direction of the tube, than a single edge cracked panel. Because of symmetry, only one quarter of the panel is considered. In order to capture crack tip stress as accurately as possible, and to observe the stress distribution near the crack tip within a distance of  $2\delta_i$  (CTOD), the size of the smallest element near the crack tip is  $0.625 \mu\text{m}$  which is of the order of the grain width of the material. The mesh contains 574 nodes and 466 plane-strain isoparametric quadrilateral elements. The width of one quarter of the panel is 40 mm and the half length of the crack is 4 mm.

It is worth noting that variable-number-node elements were used for the transition from the small to large elements. A uniformly distributed larger size element ( $2.5 \mu\text{m}$ ) along the crack plane for a distance greater than  $20 \mu\text{m}$  showed similar stress distribution ahead of the hydride.

The stress-strain curve for Zr-2.5 wt% Nb at  $250^\circ\text{C}$  fitted into Ramberg-Osgood relation (3-1) is given by [3-16]

$$\frac{\epsilon_e}{\epsilon_o} = \frac{\sigma_e}{\sigma_o} + 0.33 \left[ \frac{\sigma_e}{\sigma_o} \right]^{22.7} \quad (3-3)$$

where  $\sigma_e$  is the von Mises effective stress,  $\epsilon_e$  is the corresponding effective strain defined as

$$\sigma_e^2 = 3 s_{ij} s_{ij} / 2, \quad s_{ij} = \sigma_{ij} - \delta_{ij} \sigma_{kk} / 3. \quad (3-4)$$

$$\varepsilon_e^2 = 2 e_{ij} e_{ij} / 3, \quad e_{ij} = \varepsilon_{ij} - \delta_{ij} \varepsilon_{kk} / 3 \quad (3-5)$$

The value of the yield strength,  $\sigma_0$ , was taken as 555 MPa, and Young's modulus  $E$  and Poisson's ratio  $\nu$  were set at 82.7 GPa and 0.34, respectively [3-17]. This curve is shown in Fig.(3-10).

It is necessary to point out that the constitutive model used can not deal with changes of temperature, that is, the constitutive model describes isothermal stress-strain relations. The effect of temperature is manifested by the stress-strain curve obtained through the experiment under the given temperature.

#### 3.4.2 Loading steps

The applied far-field stress was increased from zero to 80 MPa ( $K_I = 9 \text{ MPa}\sqrt{\text{m}}$ ) in 23 step increments. After loading step 23, the far field stress was kept constant, and displacements were imposed on eleven nodes ahead of the crack tip in six steps as shown in Fig.(3-1). The applied loading sequence is displayed in Fig.(3-11). The abscissa indicates the loading steps whereas the ordinate shows the applied far-field stress magnitude on the left scale and the applied displacement value on the right scale. In this figure the maximum applied displacement is  $0.25 \mu\text{m}$ , and the distance along which this displacement is imposed (11 nodes) is  $10 \mu\text{m}$  which denotes the length of the hydride platelet.

### 3.4.3. Results and discussion

The results of the finite-element analysis for a stationary crack subject to monotonically increasing far field stress are presented first. Fig.(3-12) shows the distribution of the stress component normal to the crack plane ( $\sigma_{22}$ ) for four values of the stress intensity factor  $K_I = 6, 7, 8$  and  $9 \text{ MPa}\sqrt{\text{m}}$ . Unless stated otherwise, in this and following figures, the stress is normalized with respect to the yield stress,  $\sigma_0$ , and the distance along the crack,  $X_I$ , is divided by a length parameter  $(K_I/\sigma_0)^2$ . Note that the plastic zone size is proportional to  $(K_I/\sigma_0)^2$ . The distribution depicted in Fig.(3-12) is very similar to that reported by Rice and Johnson [3-18].

The plastic zone around the crack tip is defined as the locus of all points where the effective stress,  $\sigma_e$ , in Eq.(3-4) is equal or exceeds the yield strength,  $\sigma_0$ . The extent of the plastic zone for various  $K_I$  values is depicted in Fig.(3-13). This figure shows the actual size of the plastic zone, with the length scale indicated in the upper left hand corner. Contours of the hydrostatic pressure  $(\sigma_{11} + \sigma_{22} + \sigma_{33})/3$  are shown in Fig.(3-14) for  $K_I = 9 \text{ MPa}\sqrt{\text{m}}$  in the absence of hydride. It is seen that the hydrostatic pressure gradient is very steep near the crack tip, as expected. Thus, the hydrogen will diffuse toward the crack tip and a hydride platelet will form in front of the crack.

The distribution of the normal stress component along the crack plane following hydride expansion, is shown in Fig.(3-15). In this figure the imposed expansion varies from  $0.1$  to  $0.25 \text{ }\mu\text{m}$ . It is seen that the magnitude of stress ahead of the crack tip decreases with increased hydride expansion, and the steep stress gradient at the crack tip either vanishes or changes sign. A compressive stress develops near the front end of the

hydride (farthest from the crack tip) and for the higher values of hydride expansion. plastic deformation with compressive stresses takes place at about  $X_1/(K_I/\sigma_o)^2 \approx 0.03$ . The maximum tensile stress shifts to the front end of the hydride platelet. The stress redistribution due to the hydride formation is quite dramatic. The hydride will experience this stress value, and cracking may occur, only if the tensile stress exceeds the hydride's fracture stress.

A conclusion to be drawn from Fig.(3-15) is that the shift of the peak stress to the front end of the hydride platelet, will cause diffusion of hydrogen to this location. This will then produce the growth of the hydride along the crack plane away from the crack tip. Another observation is that since hydride precipitation causes a drop in the stress magnitude along the hydride length, the rate of hydride accumulation will gradually decrease. As a result the thickness of the hydride platelet will tend to be limited.

Here, it should be pointed out that the presence of compressive stress near the front end of the hydride platelet results from the uniform expansion of hydride. However, as soon as the hydrostatic pressure becomes negative, the hydride growth will cease at that location. In this case the hydride growth will be non-uniform, and a different modelling procedure has to be used.

The distribution of the strain component normal to the crack plane ( $\epsilon_{22}$ ) is shown in Fig. (3-16). There is a reduction in the strain magnitude with increased hydride expansion, however, near the crack tip, it is not as pronounced as the corresponding stress component,  $\sigma_{22}$ , c.f. Figs.(3-15) and (3-16). A small distance away from the crack tip, the trends are very similar. Note that the maximum magnitude of  $\epsilon_{22}$  strain at the

crack tip is  $\epsilon_{zz} = 7\epsilon_o \approx 0.047$  (or 4.7%) in the absence of hydride.

Figure (3-17) shows contours of hydrostatic pressure for  $K_I = 9 \text{ MPa}\sqrt{\text{m}}$  with a hydride platelet of length  $L = 10 \mu\text{m}$ , and thickness  $D = 0.25 \mu\text{m}$ . Note that the high gradient region is shifted from the crack tip to the front end of the hydride platelet, c.f. Figs.(3-14) and (3-17). Along the hydride the hydrostatic stress gradient is not steep, and the rate of the hydride growth will slow down appreciably in this region.

The crack opening profile due to the applied load and superimposed hydride expansion is shown in Fig.(3-18). Also depicted in this figure, is the extent and the amount of the crack front imposed displacement. It is to be noted that following the convention in the fracture mechanics literature, the coordinates in Fig.(3-18) are non-dimensionalized through division by different values; thus the ordinate  $\delta/(K_I^2/E\sigma_o)$  is magnified about 150 times that of the abscissa. Therefore, the crack displacement profile is highly exaggerated. Nevertheless, it is seen that hydride expansion causes an increase in the crack tip opening (blunting), and consequently the stress decreases in front of the crack, see Fig.(3-15). The elastic unloading in front of the crack tip is associated with the blunting of the crack tip profile which results in the decrease of the stress peak in the crack tip.

At this stage, it may be useful to compare the crack opening displacement predicted by our analysis with that of the McMeeking for finite deformation [3-19]. Following the usual practice in finite element analyses, the crack opening displacement at the first node behind the crack tip will be taken as  $\delta_i/2$ . In our case for  $K_I = 9 \text{ MPa}\sqrt{\text{m}}$ ,  $\delta_i = 0.48 K_I^2/E\sigma_o$ . Extrapolation of the results reported in Table 1 of



McMeeking [3-19] gives a value of  $\delta_t = 0.505 K_I^2/E\sigma_0$ . The good agreement between the two results is not fortuitous. Sorensen [3-20] reports similar results between his small strain finite element analysis of stationary and steady state of an advancing crack and the work of McMeeking.

It is to be noted that while the crack opening displacements of both the small and finite deformation analyses are similar, the stress and strain distributions may differ very close to the crack tip. In the absence of hydride, the difference in stress and strain distributions between small and finite strain analysis becomes negligible at a distance of about  $2\delta_t$  beyond the crack tip. In our case for  $K_I = 9 \text{ MPa}\sqrt{\text{m}}$ ,  $\delta_t = 0.48 K_I^2/E\sigma_0 = 0.85 \text{ }\mu\text{m}$ , and  $2\delta_t = 1.7 \text{ }\mu\text{m}$ .

To investigate the effect of hydride length, three different lengths of hydride platelet were considered. Starting with a small hydride length of  $L_1 = 5 \text{ }\mu\text{m}$ , it was doubled in the next two cases, i.e.  $L_2 = 10 \text{ }\mu\text{m}$  and  $L_3 = 20 \text{ }\mu\text{m}$ , keeping hydride expansion the same,  $D = 0.1 \text{ }\mu\text{m}$ . Figure (3-19) shows the distribution of stress normal to the crack plane,  $\sigma_{22}$ , for the three cases. It is seen that the general trend is the same, except that the growth of the hydride platelet causes a slight increase in stress in front of the crack, a shift in the location of the maximum stress, and a noticeable decrease in the peak stress at the front end of the platelet. Fig.(3-19) indicates that for the same amount of expansion, a crack initiation near the crack tip is more likely to occur in a longer hydride.

The level of the peak stress at the front end of the hydride platelet depends on the end geometry. In Figs.(3-15) ~ (3-19), the change in platelet thickness (expansion) is

abrupt as depicted in insets in Figs.(3-15).(3-16) and (3-19). Fig.(3-20) shows the effect of the front end hydride geometry. It is noted that a gradual change in hydride expansion causes a drop in the peak stress magnitude, however, the crack tip stresses are unaffected. The change in the front end geometry of the hydride platelet also influences the plastic zone size. This is shown in Fig.(3-21), in which three plastic zones are depicted. The solid line shows that caused by loading only. The broken lines show that due to the hydride expansion. There is an elastic enclave in the front of the crack and the plastic zone is shifted away from the crack front. The plastic zone is the smallest for the hydride with the gradual front end geometry.

For a blunted crack, the peak stress is slightly removed from the crack front, and hydride formation may start at this location and grow away from the crack. To investigate this possibility, the start of the hydride platelet was removed from the crack tip a distance three times the crack tip opening displacement ( $3\delta_t$ ) which gives  $X_1/(K_I/\sigma_o)^2 \approx 0.01$ . The stress distribution for the above case is compared to that when hydride starts at the crack tip (all previous cases) in Fig.(3-22). It is noted that the stresses at the hydride platelet extremities decrease while the stresses in the matrix material between hydride platelet and crack tip, also at the front end of the hydride platelet, increase. This points out that the subsequent hydride growth would be in two directions along the two ends of the hydride platelet with an almost equal growth rate, and it will quickly reach the crack tip.

Thus, irrespective of the location of the initial hydride formation, at the crack tip or  $2-3 \delta_t$  removed from it, after a certain time (or growth) the hydride geometry will be

similar to those shown in Figs.(3-15) ~ (3-19).

#### 3.4.4 Conclusions

The effect of hydride precipitation and expansion on the stress, strain and displacement fields near the crack tip, were investigated. The results of an elastic-plastic finite element analysis with an appropriate material constitutive model lead to the following conclusions:

- (1) The proposed loading procedure consists of loading a centre cracked panel in plane-strain condition. Once the imposed far field stress (or stress intensity factor) reaches a predetermined value, it is then kept constant. The hydride formation in front of the crack is subsequently simulated by imposing stepwise displacements along the hydride length, see Figs.(3-1) and (3-11).
- (2) Hydride formation (expansion) causes an elastic unloading in front of the crack (removal of the peak stress) and a shift of the peak stress to the front end of the hydride. The hydride will subsequently grow away from the crack tip, and the rate of the hydride precipitation will decrease along the crack front, see Figs.(3-15) ~ (3-17).
- (3) Depending on the hydride expansion, a compressive normal stress may develop near the front end of hydride, see Fig.(3-15).
- (4) An increase in the hydride length leads to a shifting of the maximum from the hydride front end to the crack tip. This may initiate cracking of the

hydride at this region, see Fig.(3-19).

- (5) The initial location of the hydride formation with respect to the crack tip may have negligible influence on the above conclusions, since the subsequent hydride growth will be towards the crack tip, see Fig.(3-22).

This will be further discussed in the following section.

### 3.5 The analysis using a finite deformation model

According to the concept of the chemical potential of a mobile species in an elastically stressed solid established by Li, Oriani and Darken [3-2], the hydrostatic stress gradient is the driving force to concentrate the mobile hydrogen to the region of high tensile stress. The place which has the peak hydrostatic stress should be the point of initiation for hydride precipitation.

Rice and Johnson [3-18] studied crack tip blunting in mode I by using slip line solutions. Their solution enforced smooth blunting of the crack tip and as a result a region of high strain develops ahead of the crack in contrast to the sharp crack case. The stress adjacent to the free surface is limited by yielding but builds up away from the tip due to triaxiality. As in the sharp crack case, the largest stress is  $3\sigma_0$ , where  $\sigma_0$  is the yield stress in tension and is located a distance approximately  $2\delta_t$  ahead of the tip, where  $\delta_t$  is the crack tip opening displacement.

McMeeking [3-19] used large deformation finite element analysis to model the blunting of a sharp crack under small scale yielding in plane strain conditions. The constitutive model was that of von Mises with isotropic hardening and accounted for rotation of the

principal deformation directions. The finite element results were compared with the slip line results of Rice and Johnson. The agreement between both results is quite close as far as the position and magnitude of stress maximum are concerned.

It is generally believed that crack tip blunting always occurs in practice. A blunted crack tip acts as a free surface and locally reduces the triaxiality of the stress state. Thus increased blunting decreases the maximum stress and moves its location away from crack tip. More essentially, the plastic deformation at the crack tip is always accompanied with finite deformation.

In view of the above-mentioned facts, an argument has been put forward: if hydride starts to precipitate at hydrostatic stress peak, the initial location of hydride should be at the place about  $2\delta_t$  from the crack tip instead of at the crack tip. Although the initial location of the hydride formation was discussed in §3.4, it is necessary to prove conclusion (5) arrived in §3.4 under the finite deformation condition.

In this section, a constitutive model of von Mises isotropic hardening with updated Lagrangian formulation is employed. Thus, material and geometric nonlinearities of the material are considered at the same time and large strain conditions can be modeled. It should point out that due to the limitation of ADINA program, the selection of the isotropic hardening model is not suitable for reversed loading (unloading). It is only because the unloading is restricted within a rather small range, that the results can be accepted.

### 3.5.1 A comparison of results between a small deformation model and a finite deformation model

In order to clarify the effect of finite deformation, a comparison of stress and strain distributions, crack profiles and plastic zones between a small deformation model and a finite deformation model is made for monotonic loading. In addition, to discard the influence by other factors, both models used belong to that of von Mises isotropic hardening, one with only the material nonlinearity for the small deformation and another with the material nonlinearity and with an updated Lagrangian formulation for the finite deformation. The finite element mesh, crack geometry and material properties are the same as that in §3.4. Also, the finite element analysis is under plane strain conditions.

The distributions of stress component normal to the crack plane ( $\sigma_{22}$ ) at the different stress intensity factors: 6, 7, 8 and 9 MPa $\sqrt{m}$  are shown in Fig.(3-23) for the small deformation model and in Fig.(3-24) for the finite deformation model. Like the results obtained earlier in Fig.(3-12) by the constitutive model proposed in Chapter 2, in Fig.(3-23) following the increase of the stress intensity factor the ratio of  $\sigma_{22}$  to the yield stress  $\sigma_0$  ahead the crack tip increases and maintains the maximum values at the crack tip. While in Fig.(3-24), the stresses just ahead the crack tip have a marked decrease after the ratio of  $\sigma_{22}$  to  $\sigma_0$  goes beyond 3, though the decrease is limited in a small region. When the stress intensity factor is small, such as  $K_I=6$  MPa $\sqrt{m}$ , the maximum stress is still at the crack tip, then it moves away from the crack tip with the increase of the stress intensity factor. At  $K_I=9$  MPa $\sqrt{m}$  the location of the peak stress is about  $0.0059x_1/(k_I^2/\sigma_0^2)$ , i.e.  $x_1=0.00156$  mm which is less than  $2\delta_t=0.00253$  mm obtained by

Rice and Johnson's analysis ( $\delta_t = 0.717K_I^2 / (E\sigma_0)$ ) [3-18]. In the further calculation, at  $K_I = 12 \text{ MPa}\sqrt{\text{m}}$ , the location of peak stress is 0.00281 mm from the crack tip, while  $2\delta_t = 2 \times 0.717K_I^2 / (E\sigma_0) = 0.00450 \text{ mm}$ . The results show that during increased loading the location of the peak stress is away from the crack tip only at the larger stress intensity factor for a stationary crack, and the distance between the crack tip and the location of the peak stress is less than the  $2\delta_t$  derived by Rice and Johnson. The results also imply that the effect of the crack tip blunting appears only when the stress intensity factor reaches a certain value: the higher the stress intensity factor, the stronger the effect of the crack tip blunting.

The distributions of the effective plastic strain are displayed in Fig.(3-25) for the small deformation model and in Fig.(3-26) for the finite deformation model. At  $K_I = 6 \text{ MPa}\sqrt{\text{m}}$  the effective plastic strains at the crack tip for the two models are almost the same. But when the stress intensity factor increases the effective plastic strains ahead the crack tip for the finite deformation model increases more quickly. At  $K_I = 9 \text{ MPa}\sqrt{\text{m}}$  the effective plastic strain at the crack tip for the small deformation model is 4.7%, 7 times  $\epsilon_0$ , and for the finite deformation model is 6.1%, 9 times  $\epsilon_0$ . It is noted that the maximum effective plastic strain is not located at the crack tip, but immediately behind the crack tip (not plotted), where the shear strain component plays a dominant role. The shear strain values are 27.4% and 30.45%, respectively.

Here, it should be noted that the increase of strains at the crack tip with the increase of the stress intensity factor is strengthened by the crack tip blunting: while the increase of stresses at the crack tip in the same process is weakened by the crack tip blunting.

There is a turning point in the change of the stresses from increasing to decreasing at the crack tip.

Experimental observations also indicate the maximum strain is at the crack tip. see a critical review of crack growth mechanisms by Davidson and Lankford [3-21] and deformation of grains around a blunted crack tip using a metallographic method by Luo et al. [3-22]. The maximum deformation of the material does not move away from the crack tip.

The fact that Li, Oriani and Darken chose the hydrostatic stress gradient as a driving force to concentrate the mobile species [3-2] is based on an elastically stressed solid. In the elastic range, the maximum stress corresponds to the maximum strain. When the strain at the crack tip exceeds the yield strain of the material several times or by an order of magnitude, the choice of the stress gradient as the driving force might need to be reconsidered.

Figure (3-27) shows the crack profiles at  $K_I=9 \text{ MPa}\sqrt{\text{m}}$  for both models. the solid line for the finite deformation model and the dashed line for the small deformation model. The coordinate axes have been made dimensionless by the parameter  $(K_I/\sigma_0)^2$  for the distance from the crack tip which is numbered zero and the parameter  $K_I^2/E\sigma_0$  for the displacement of the nodes on the crack bank. The difference between the two crack profiles is not large. The maximum difference of the displacements at the second node behind the crack tip is about 4.2%. In order to show the effect of the crack tip blunting following the increase of the stress intensity factor, Fig.(3-28) illustrates the crack profiles at  $K_I=6, 9$  and  $12 \text{ MPa}\sqrt{\text{m}}$  in millimetre unit for the displacement of the nodes



on the crack flank. When  $K_I = 6 \text{ MPa}\sqrt{\text{m}}$  the crack profiles of both models are almost the same, while for  $K_I = 12 \text{ MPa}\sqrt{\text{m}}$  the maximum difference at the second node behind the crack tip is only 6.8%. This again emphasizes that the effect of crack tip blunting becomes stronger with the increase of the stress intensity factor. At the same time, it seems that the crack profile is not sensitive to the crack tip blunting in comparison with stress and strain.

The plastic zones at  $K_I = 9 \text{ MPa}\sqrt{\text{m}}$  are shown in Fig.(3-29) for the small deformation model and in Fig.(3-30) for the finite deformation model. The cross symbols represent Gauss integration points which have yielded. The total of the yielded Gauss integration points depicts the plastic zone size and shape. The two plastic zones are almost identical. The effect of the finite deformation is restricted within a very small region at the crack tip, which is surrounded by the plastic zone.

### 3.5.2 The effect of the crack length

The stress intensity factor is a parameter for crack propagation, it is linearly related to stress and directly related to the square root of a crack length. In an operating condition, the applied stress, such as the pressure in a tube, is fixed. The effect of the crack length on the stress distribution is investigated by using the finite deformation model.

Three different meshes are used to obtain three crack lengths:  $a = 0.8 \text{ mm}$ ,  $a = 2.08 \text{ mm}$  and  $a = 4.0 \text{ mm}$ , where  $a$  is the half-length of the crack. Four load levels applied here are 53 MPa, 62 MPa, 71 MPa and 80 MPa, which correspond to the stress intensity factors

of 6, 7, 8 and 9 MPa  $\sqrt{\text{m}}$  for  $a=4.0$  mm. The distributions of stress  $\sigma_{22}$  for three crack lengths at the four load levels are shown in Figs.(3-31), (3-32) and (3-33) respectively. For the small crack length,  $a=0.8$  mm, the peak stress is still located at the crack tip and the value of the peak stress grows with the increase of load. The ratio of  $\sigma_{22}$  to  $\sigma_0$  at the crack tip reaches and exceeds 3. It seems that the effect of the crack tip blunting on a shorter crack is not significant. When the crack length increases to  $a=2.08$  mm or  $a=4.0$  mm, the high level loads cause the peak stress to move away from the crack tip, and the ratio of  $\sigma_{22}$  to  $\sigma_0$  at the peak stress is kept at about 3.

It can be seen from the results above that under a fixed applied load the crack tip blunting has no distinct effect on a shorter crack, the maximum stress still is located at the crack tip, only when the crack length reaches a certain value will the position of the maximum stress move away from the crack tip.

### 3.5.3 The effect of the start location of the hydride precipitation

It is clear from §3.5.1 and §3.5.2 that the location of hydrostatic stress peak depends on the applied load for a stationary crack or on the crack length under a fixed load. When the hydrostatic stress peak is at the crack tip, the start location of the hydride precipitation is placed at the crack tip as done in §3.3 and §3.4.

In order to find the change of the stress distribution when the hydride starts to precipitate at the stress peak which is not at the crack tip, firstly, the far-field stress is applied to a certain value which creates a stress field, then, the node on the crack plane corresponding to the peak stress is prescribed to a very small displacement which imitates

the start of hydride precipitation. The redistribution of stress will show the new stress peaks which indicate the subsequent hydride growth.

The stress distribution for  $K_I=9 \text{ MPa}\sqrt{\text{m}}$  and  $a=4.0 \text{ mm}$  is plotted by the solid line in Fig.

(3-34) as shown in Fig.(3-33). The peak stress is at  $0.0059x_1/(K_I^2/\sigma_0^2)$ . The displacement of  $0.02 \mu\text{m}$  is given to the node at the same place. The stress redistribution is plotted by the dashed line. It can be seen that the stresses at the two extremities of the precipitated hydride rise up. This causes the hydride to grow from the start location along the positive and the negative direction of the  $x$  axis with almost the same speed, and it will quickly reach the crack tip. The result obtained is consistent with conclusion (5) in §3.4.

It is noted that displacing a node will cause unloading in the region near the node. The use of an isotropic hardening model is not appropriate for unloading. The results here only are an acceptable approximation due to the small unloading.

#### 3.5.4 Conclusions

For an elastic-plastic stress field near the crack tip described by a finite deformation constitutive model the position of the hydrostatic stress peak as the start location of the hydride precipitation is investigated. The following conclusions are obtained:

- (1) For a stationary crack, the stress component normal to the crack plane at the crack tip increases with the increase of the applied load. after achieving the maximum value (about  $3\sigma_0$ ) it decreases. the peak stress moves forward from the crack tip in the meantime, see Fig.(3-24).

- (2) For a stationary crack, the effective strain at the crack tip increases with the increase of the applied load, and the rate of increasing accelerates. The maximum deformation of the material remains at the crack tip from the beginning to the end process, see Fig.(3-26).
- (3) The crack profile does not seem to be sensitive to the crack tip blunting as compared with stress or strain, see Fig.(3-28).
- (4) When a crack is shorter, the effect of the crack tip blunting is negligible. the location of maximum stress remains at the crack tip until the crack grows to a certain length, see Figs.(3-31) ~ (3-33).
- (5) When the initiating location of the hydride precipitation is placed at the hydrostatic stress peak which is ahead the crack tip, the same conclusion as the small deformation model is obtained, see Fig.(3-34).

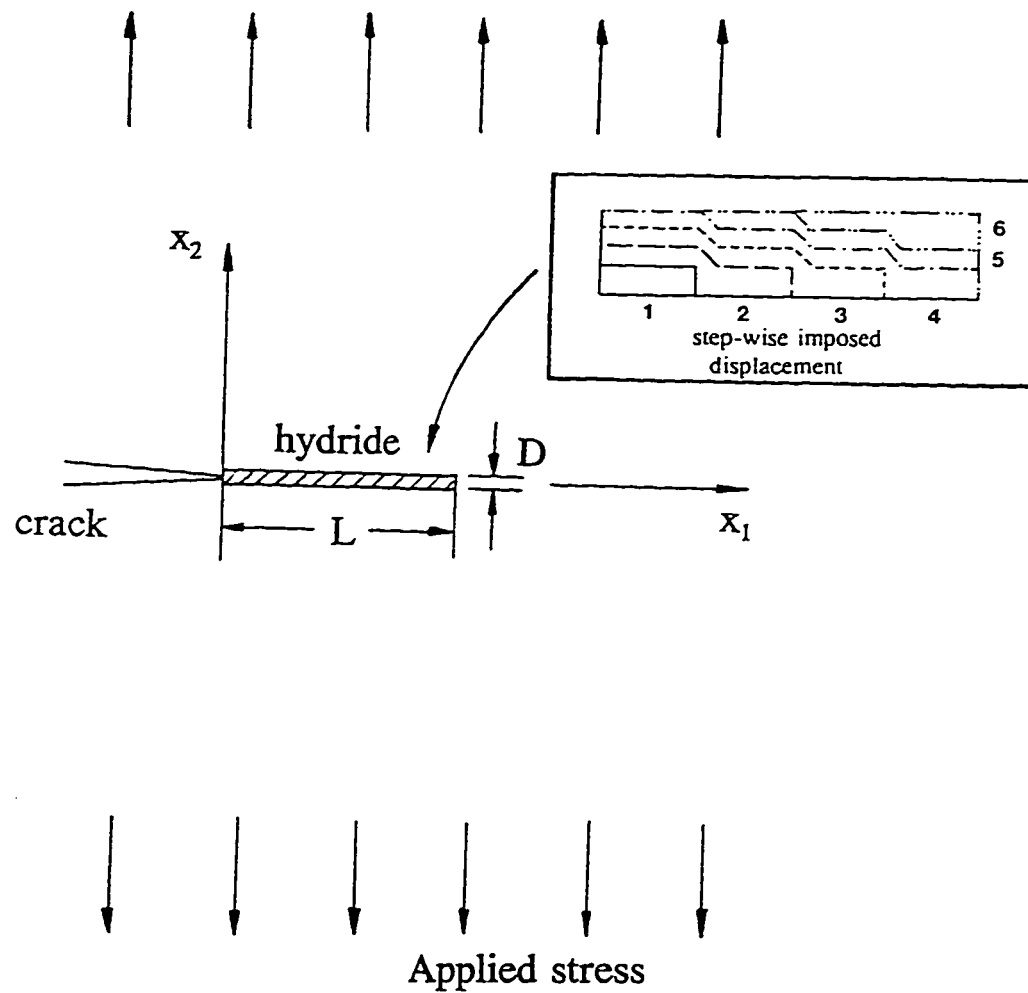


Fig.(3-1) A schematic of a crack with its coordinate system, far field applied stress, and precipitated hydride. Details of stepwise modelling of hydride formation and expansion are given in the inset.

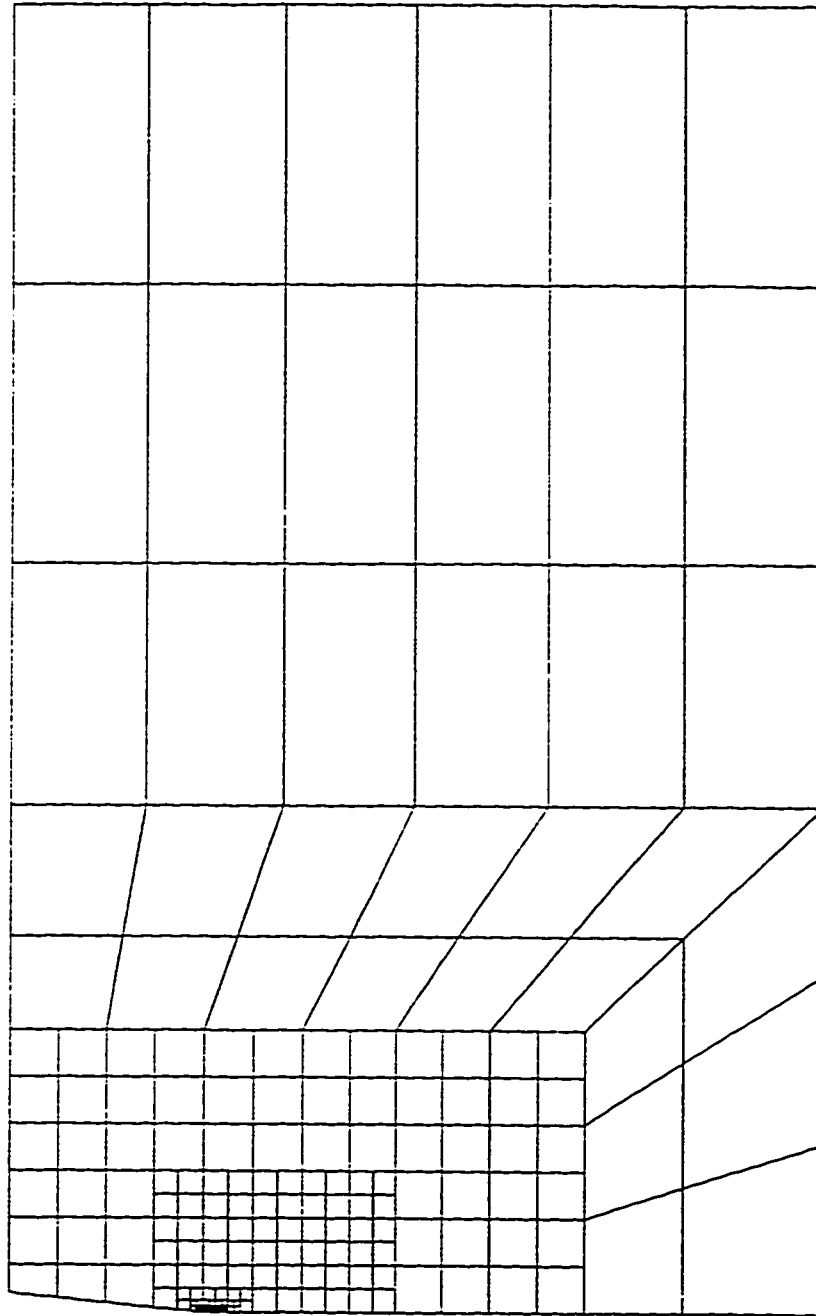


Fig.(3-2) Finite element mesh of a quarter cracked panel with 189 element and 517 nodes. The width of the half-panel is 42 mm, the half-crack length is 10 mm.

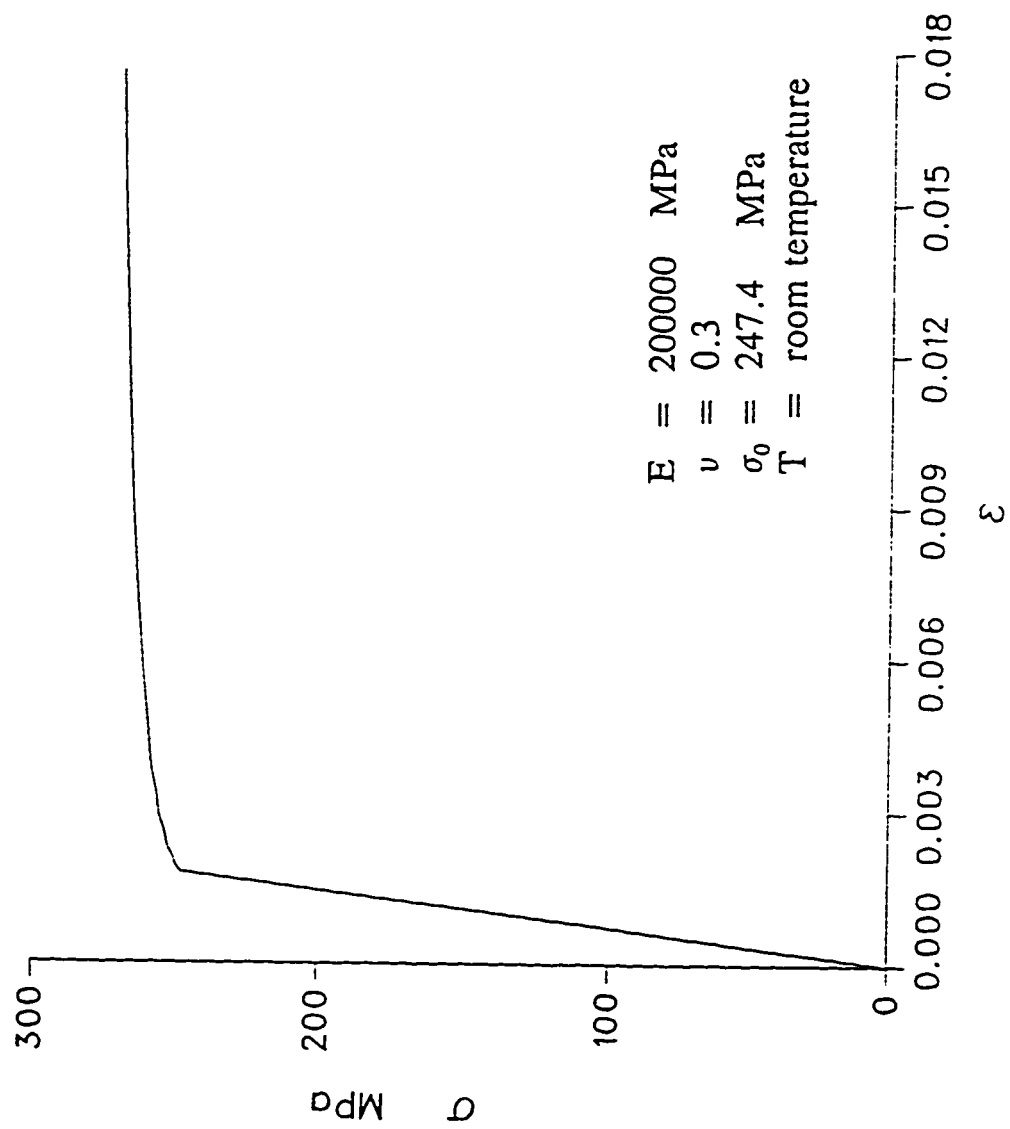


Fig.(3-3) A stress-strain curve of Zr-2.5% Nb at room temperature.

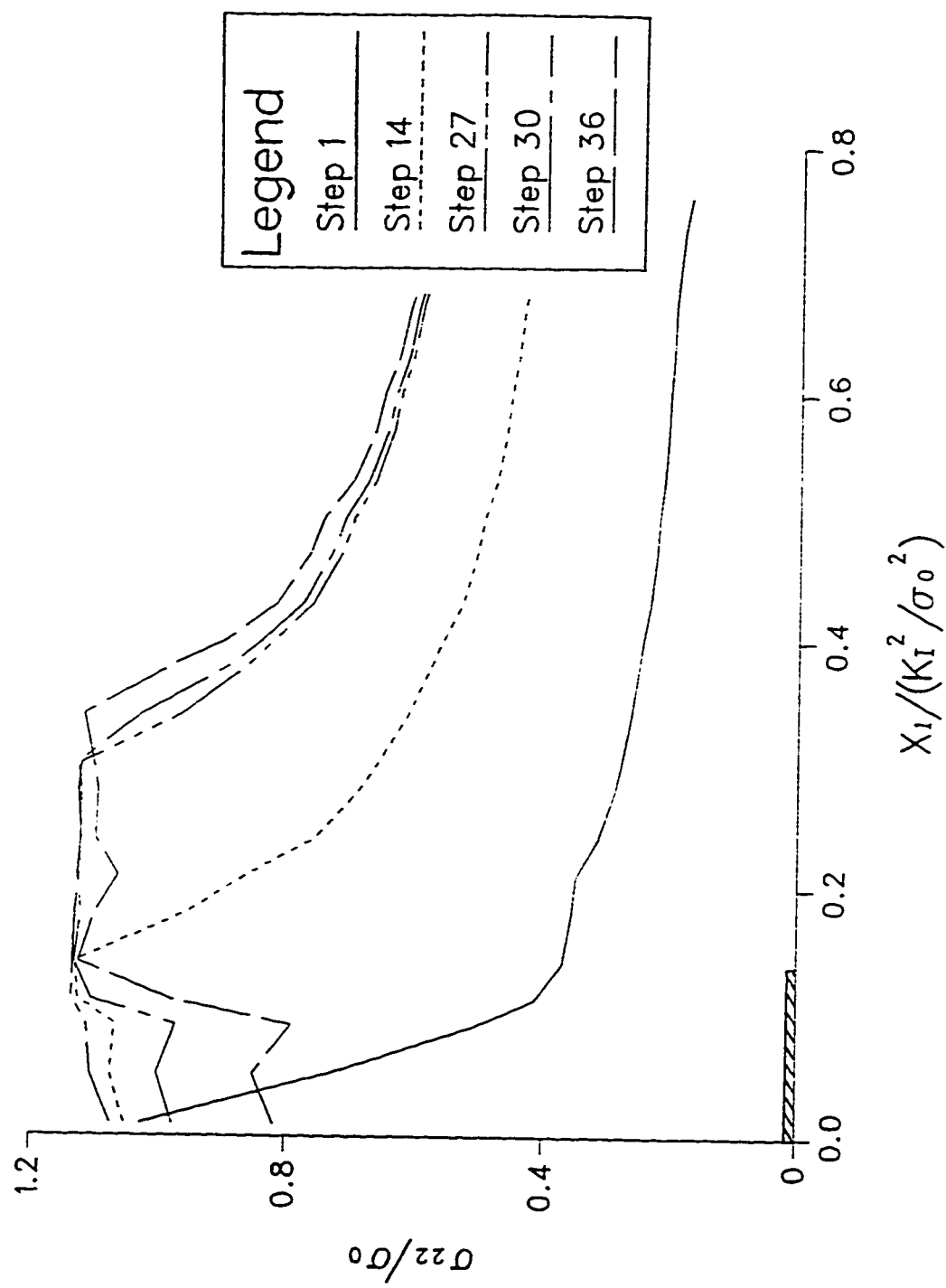


Fig.(3-4) Distributions of stress component normal to the crack plane for several specific loading steps.



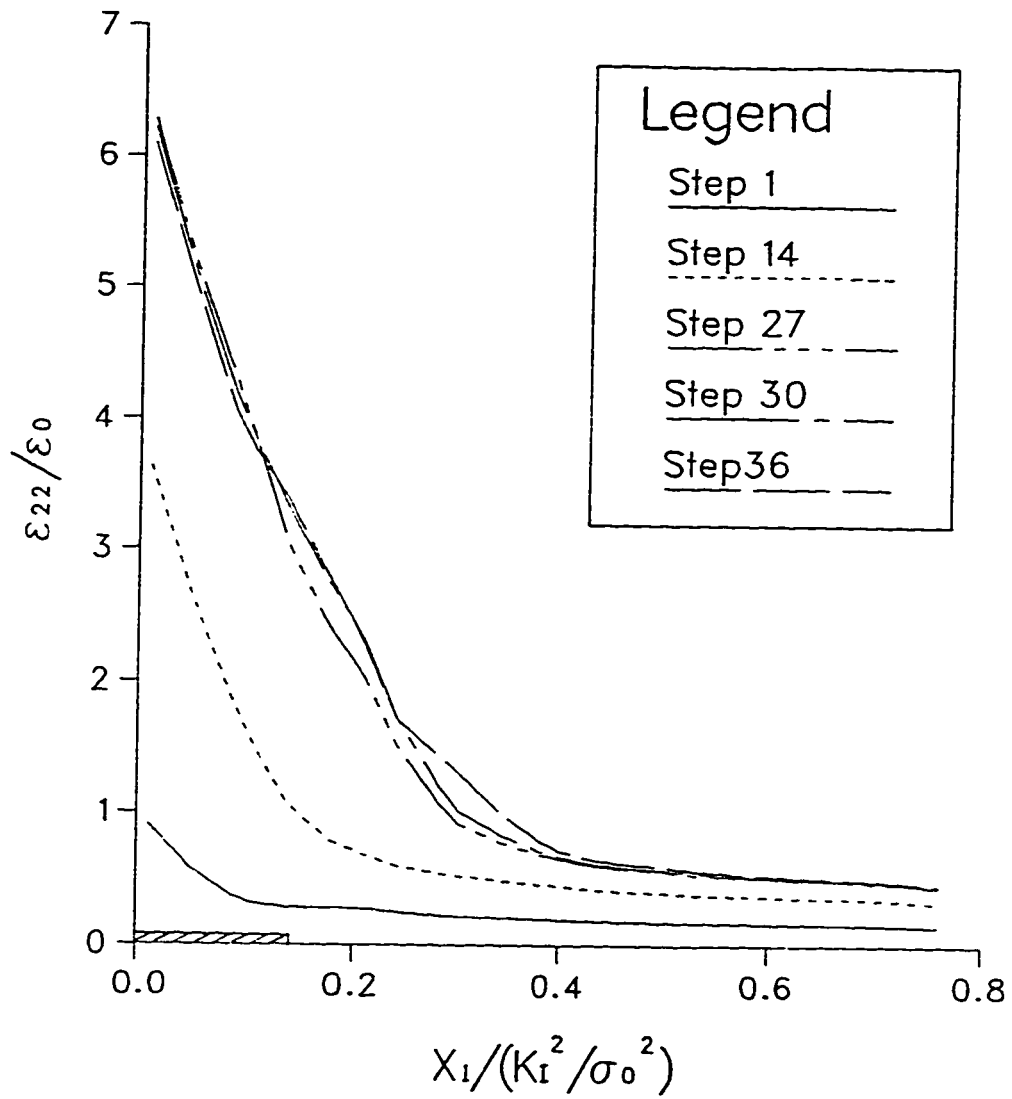


Fig.(3-5) Distributions of strain component normal to the crack plane for several specific loading steps.

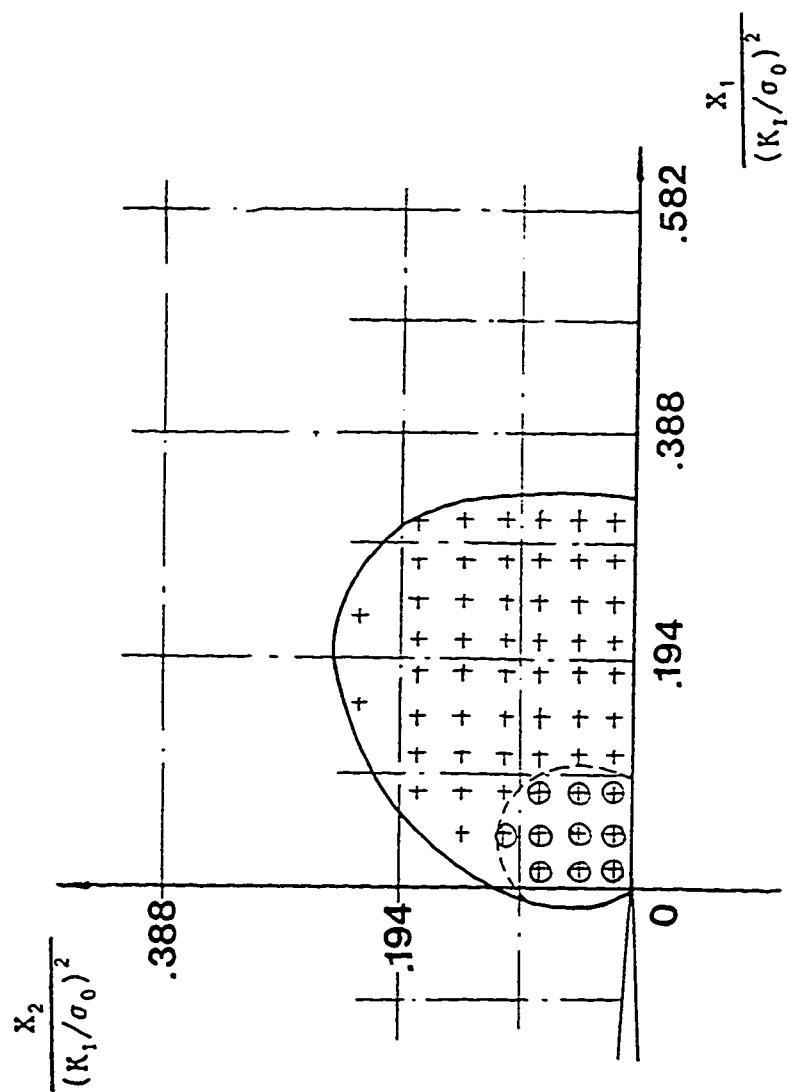


Fig.(3-6) The plastic zone in front of the crack tip at loading step 27 (load =80 MPa) and the elastic zone caused by displacing nodes ahead the crack tip at loading step 36 (load =80 MPa, displacement =2.5 $\mu$ m).

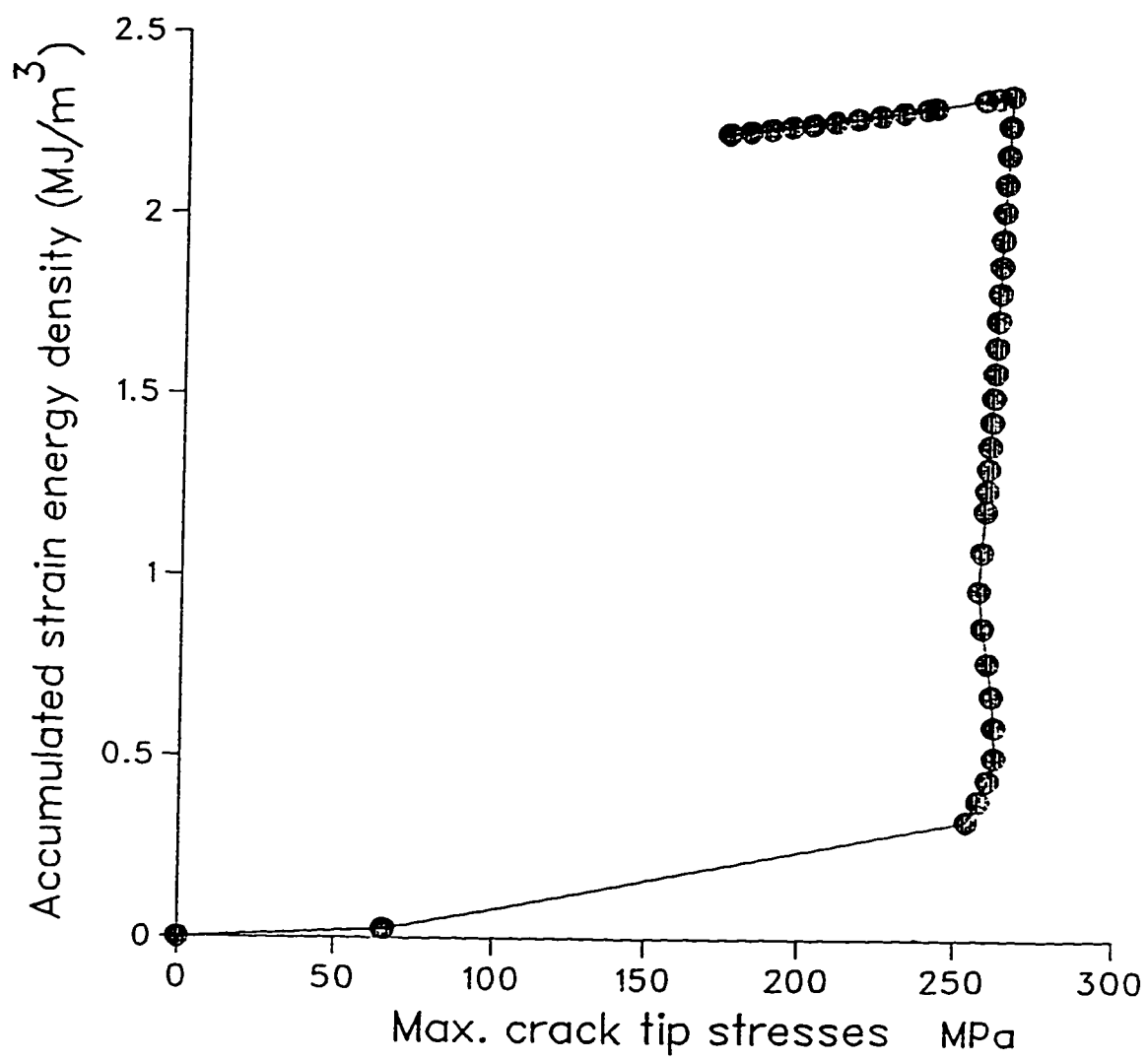
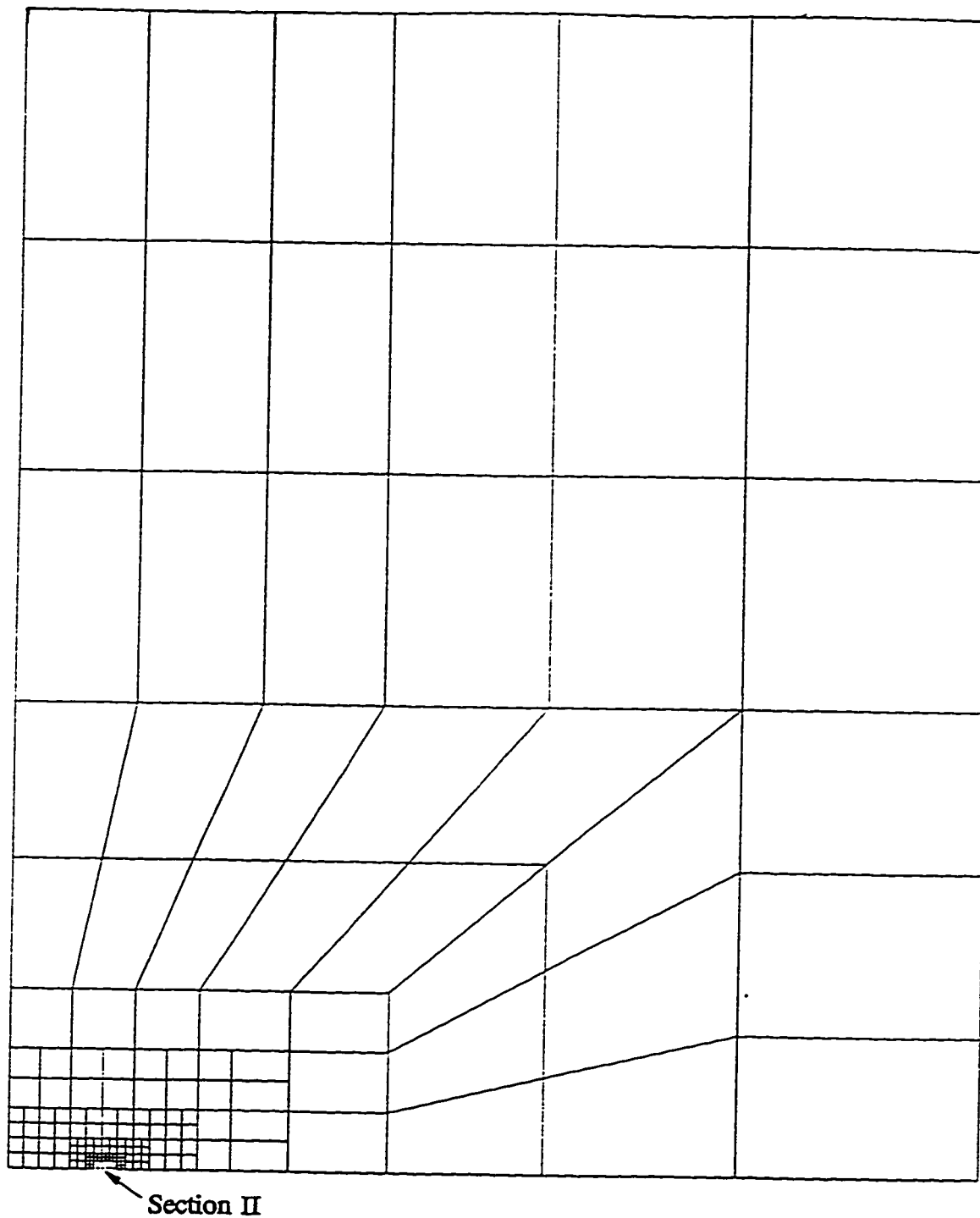


Fig.(3-7) Accumulated strain energy density for the applied load history.



Elements = 466

Nodes = 574

Half width of panel = 40 mm

Half crack length = 4 mm

Minimum size of element = 0.625  $\mu\text{m}$

Fig.(3-8) Finite element mesh of a quarter cracked panel, denoted as section I.  
The crack is located in the bottom left corner and the indentation  
represents crack tip region which is enlarged in Fig.(3-9).

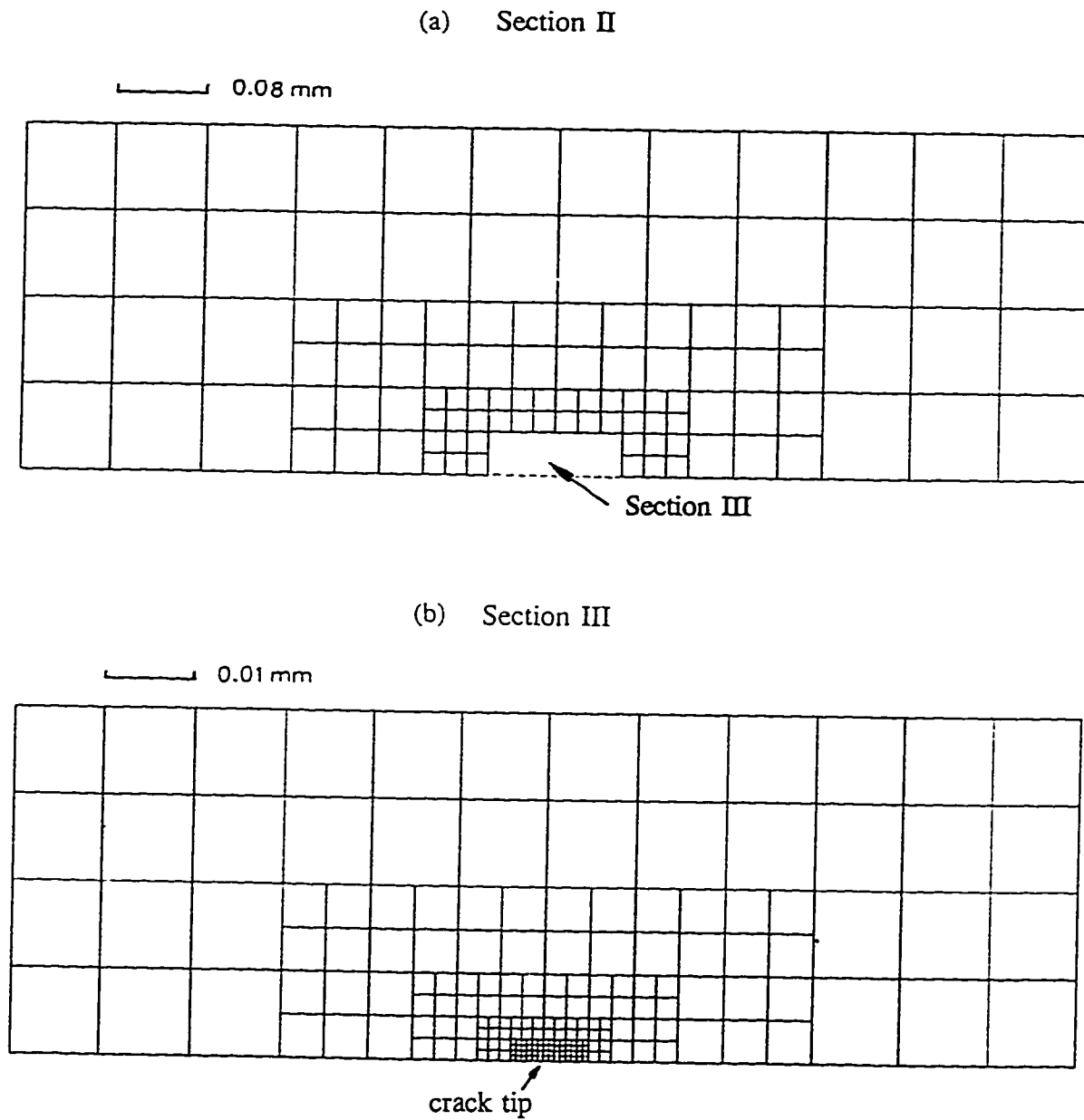


Fig.(3-9) Finite element mesh of crack tip region (b) which fits into the indentation of section II(a) which in turn fits into the indentation of Fig.(3-8).

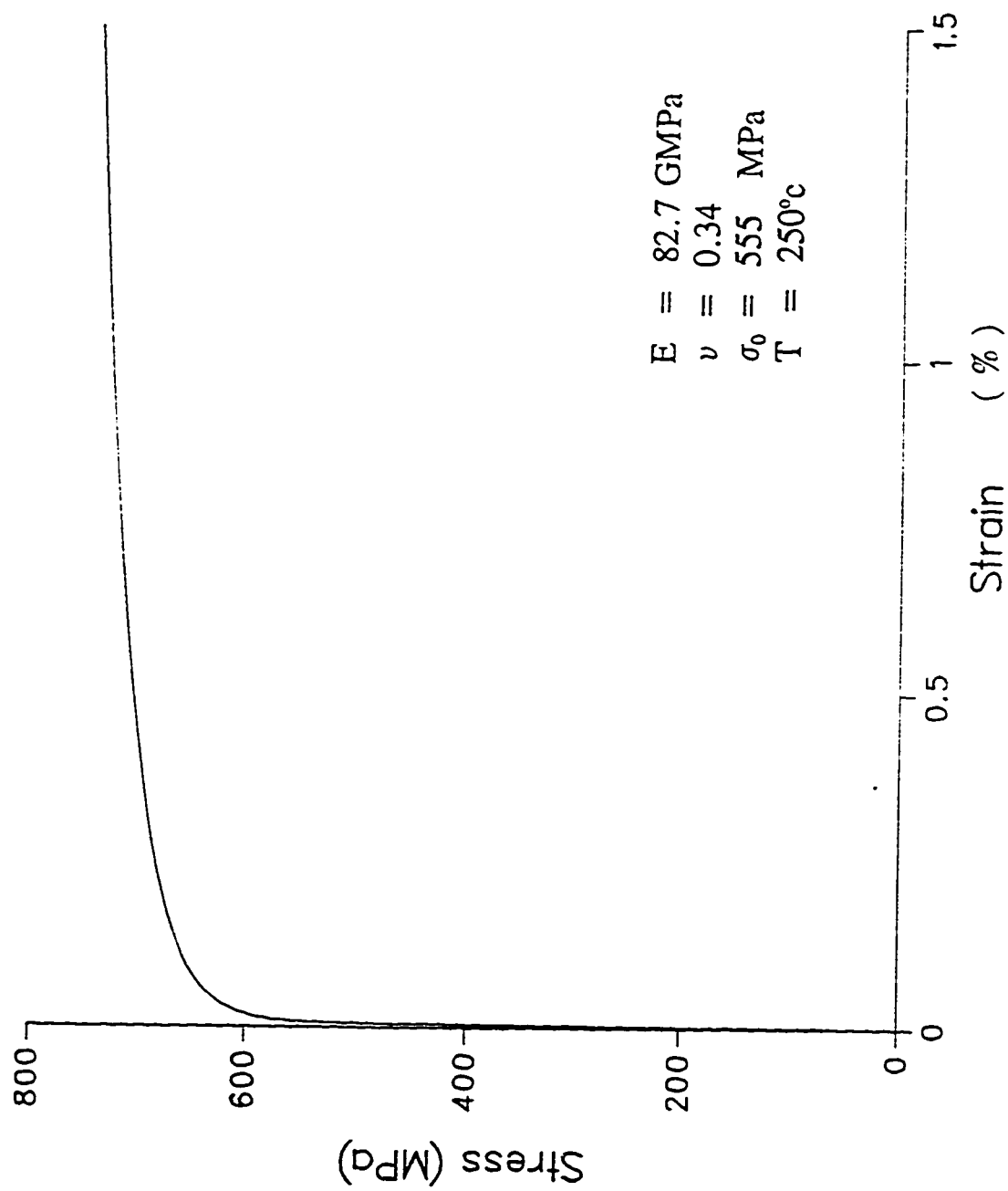


Fig.(3-10) The stress-strain curve for Zr-2.5% Nb at 250°C.

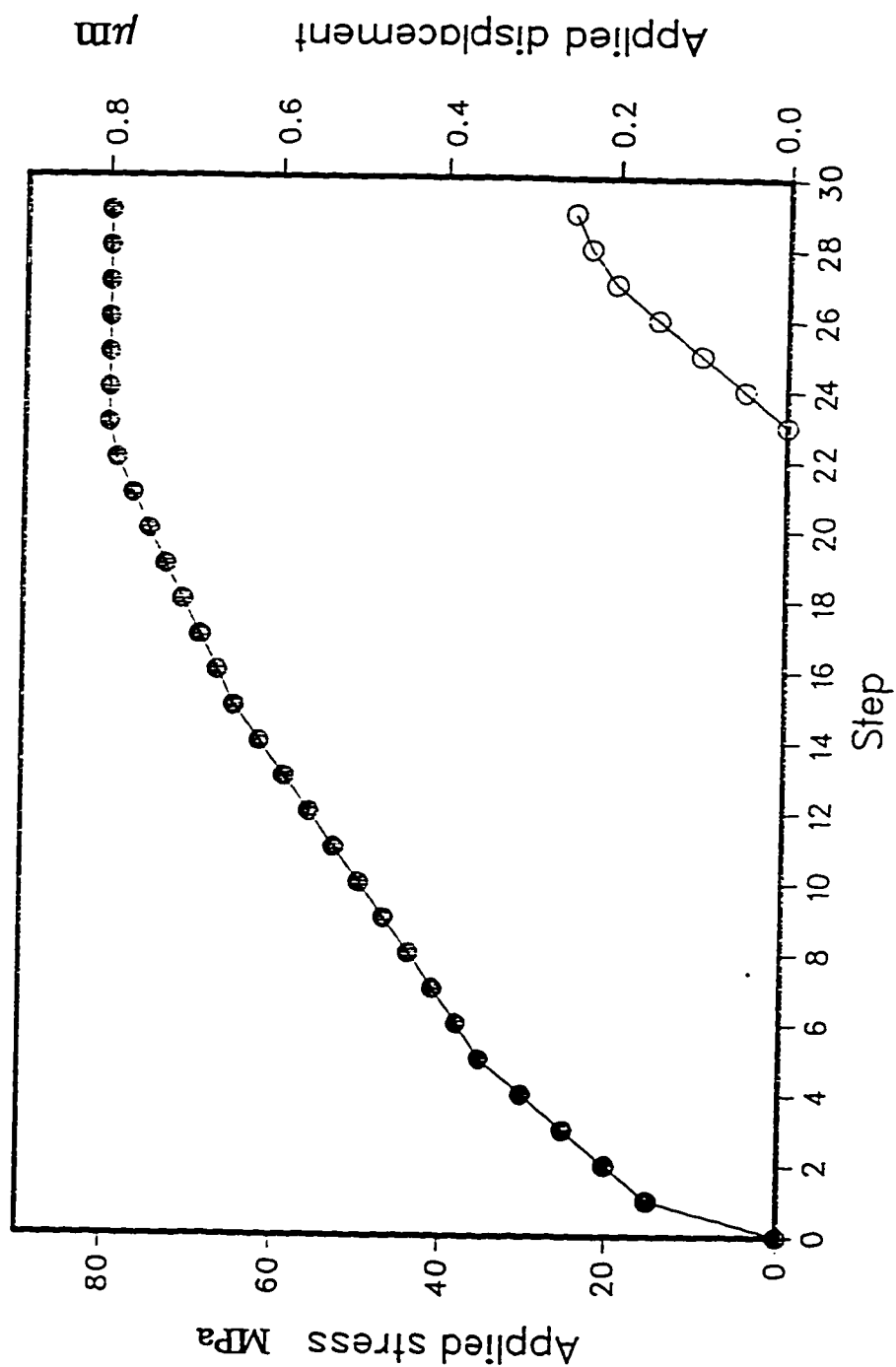


Fig.(3-11) Increments of applied far field stress (filled circles) with the left scale, and stepwise increase of hydride expansion (empty circles) with the right scale. Numbers in abscissa correspond to the progression of the loading process.

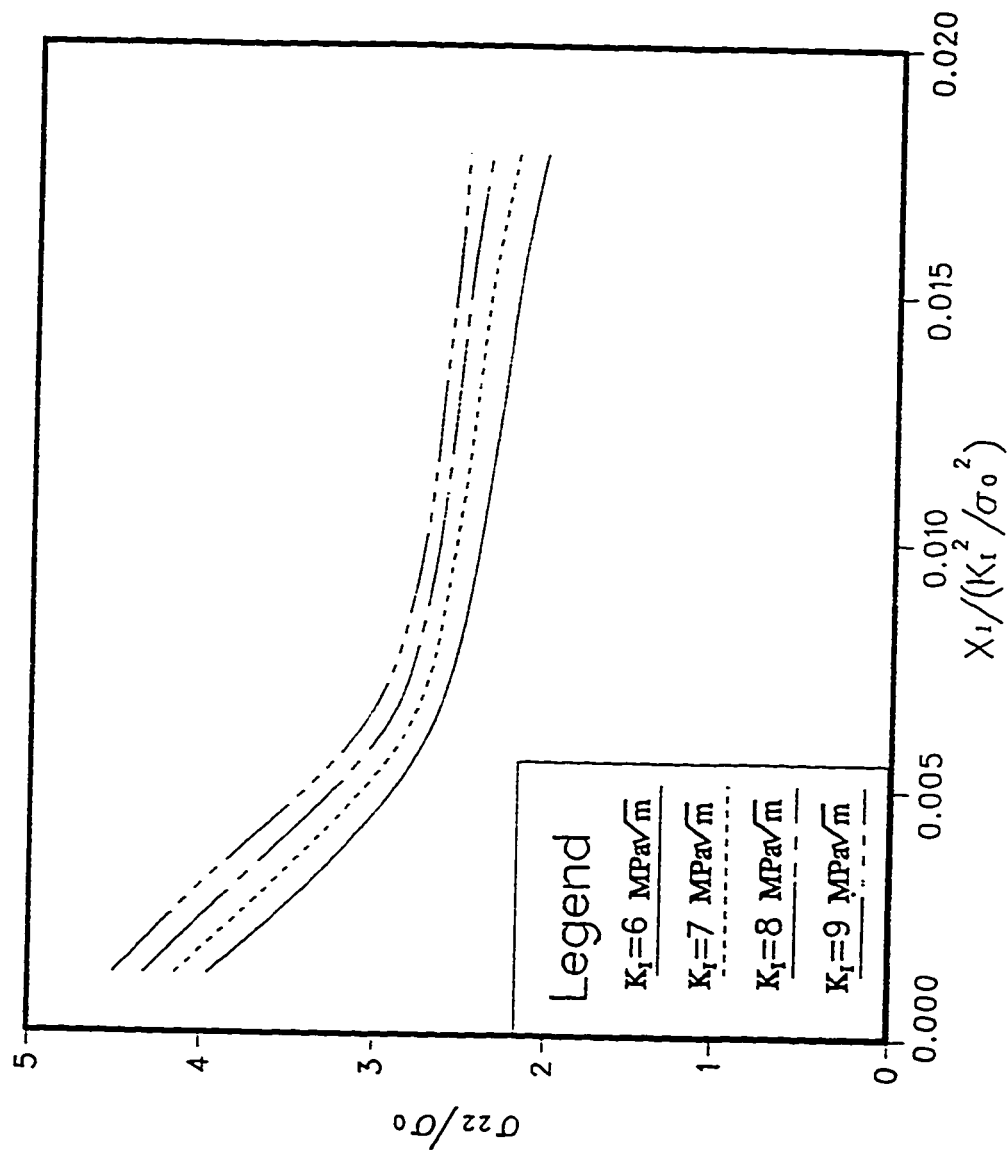


Fig. (3-12) Distribution of stress component normal to the crack plane for various stress intensity factors,  $X_1 = 0$  indicates the crack tip.



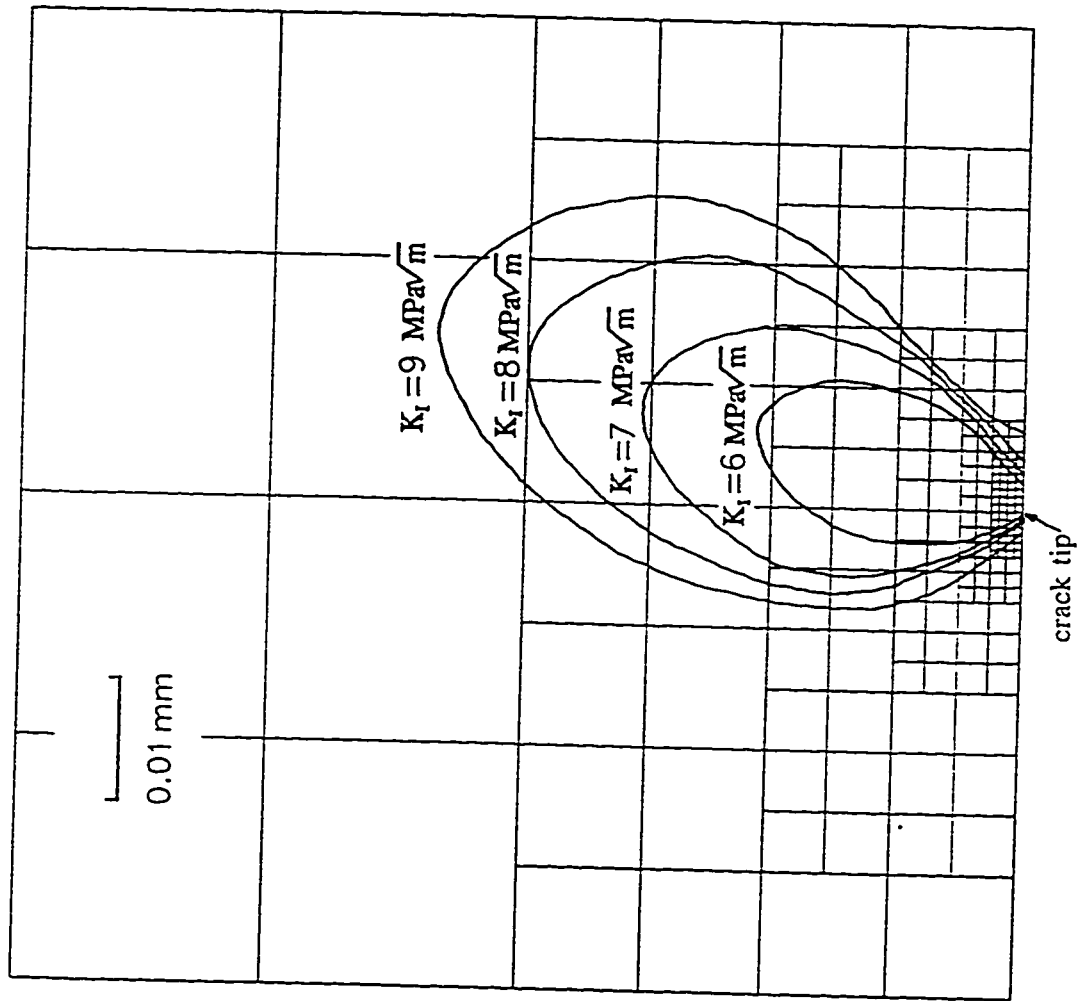


Fig.(3-13) Plastic zone size in front of the crack as a function of stress intensity factor.

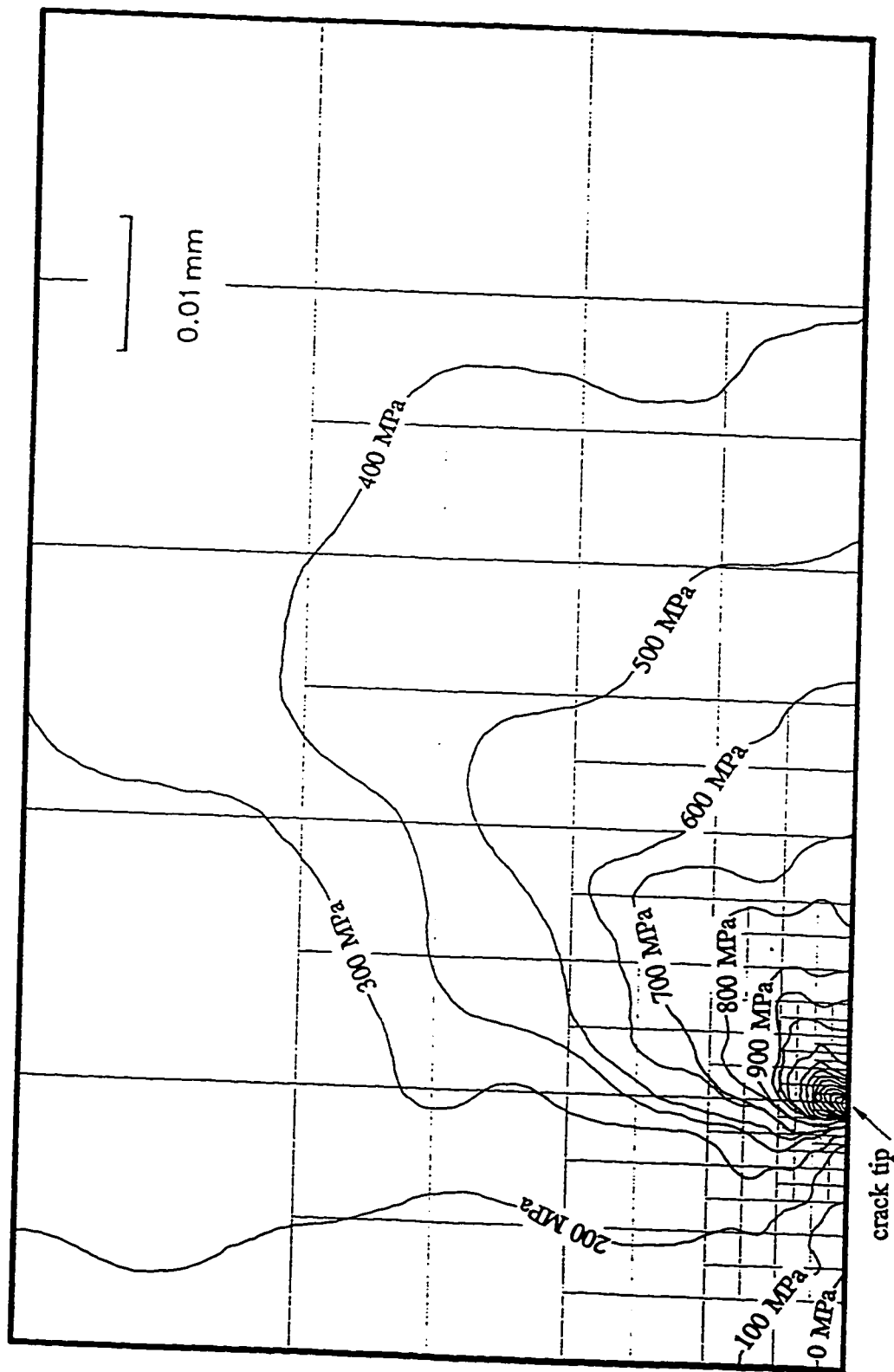


Fig.(3-14) Hydrostatic stress contours for the cracked panel, in the absence of hydride.

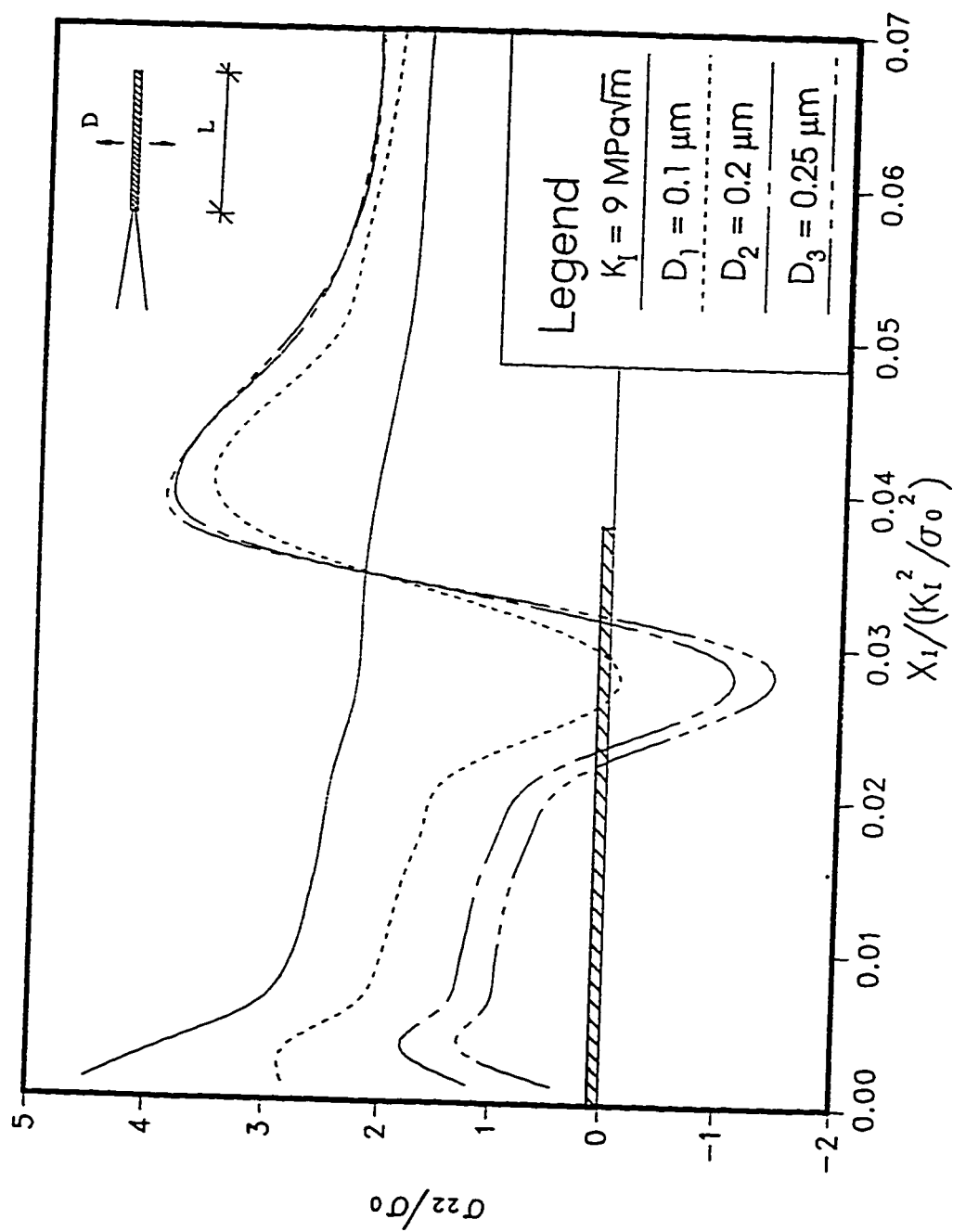


Fig.(3-15) Distribution of stress component normal to the crack plane due to hydride expansion. (Length of hydride platelet  $L = 10 \mu\text{m}$ ,  $X_1 = 0$  denotes the crack tip.)

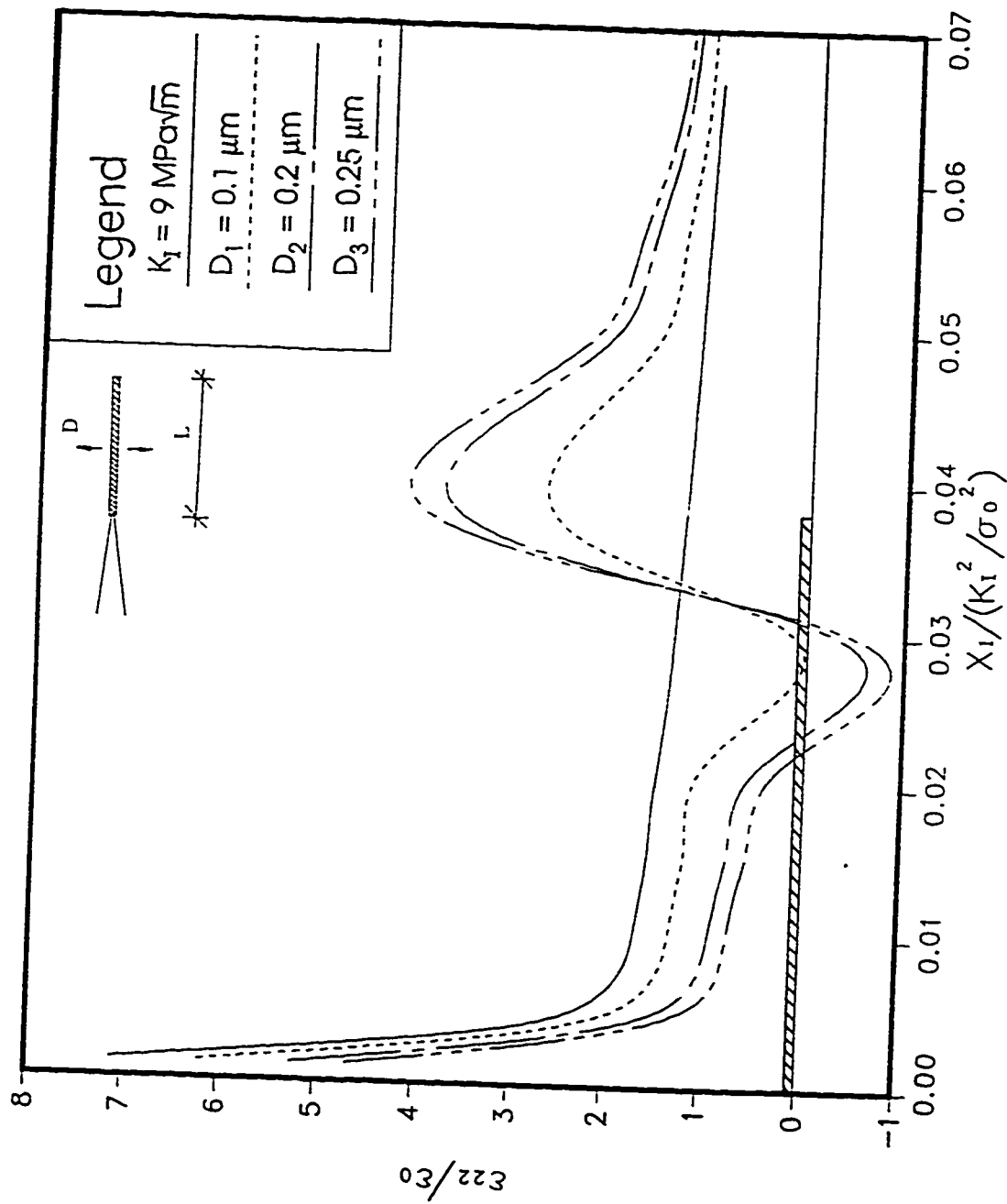


Fig.(3-16) Distribution of strain component normal to the crack plane due to hydride expansion. (Length of hydride platelet  $L = 10 \mu\text{m}$ ,  $X_1 = 0$  denotes the crack tip.)

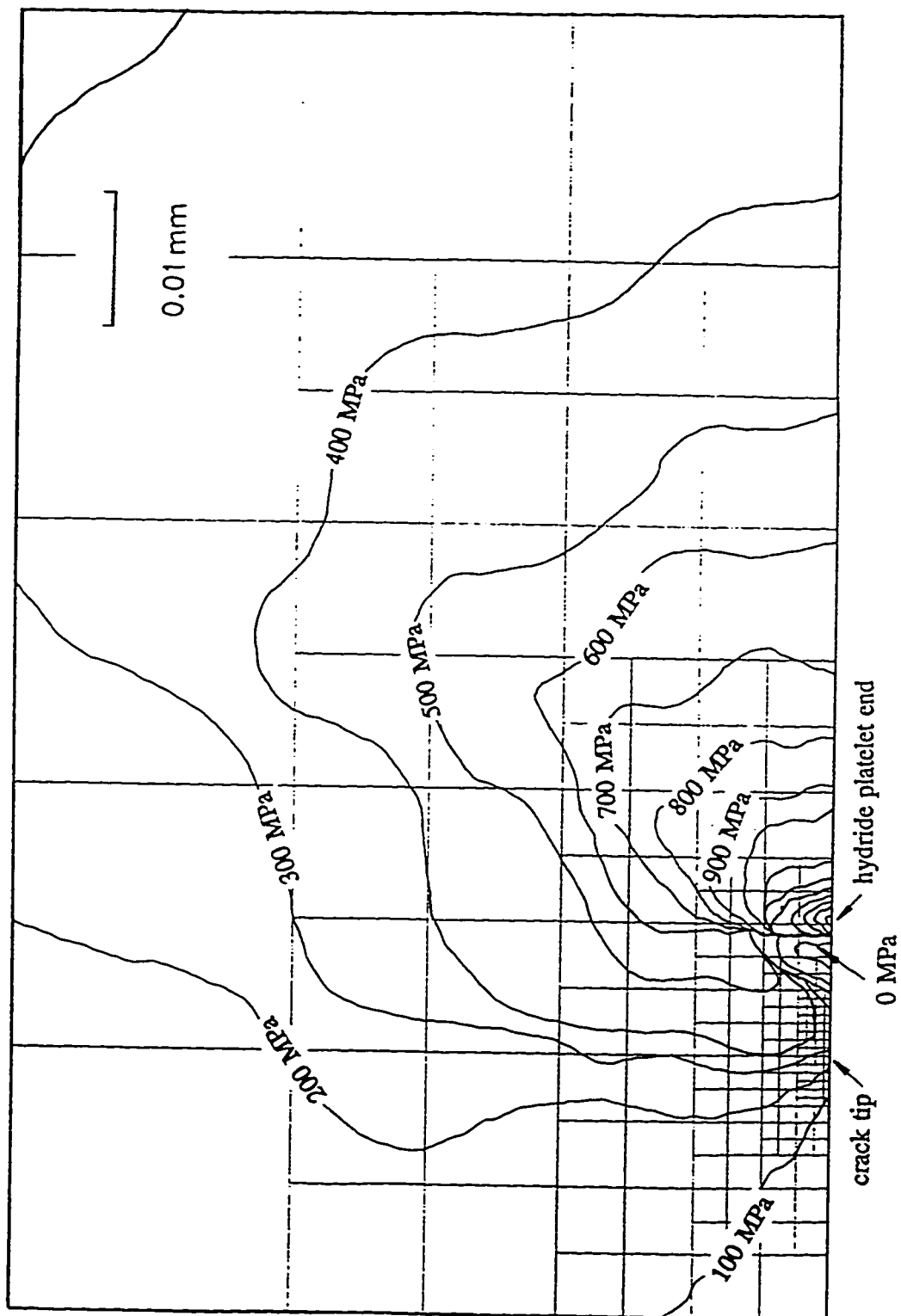


Fig.(3-17) Hydrostatic stress contours after expansion of a hydride platelet of length  $L = 10 \mu\text{m}$  by  $D = 0.25 \mu\text{m}$ .

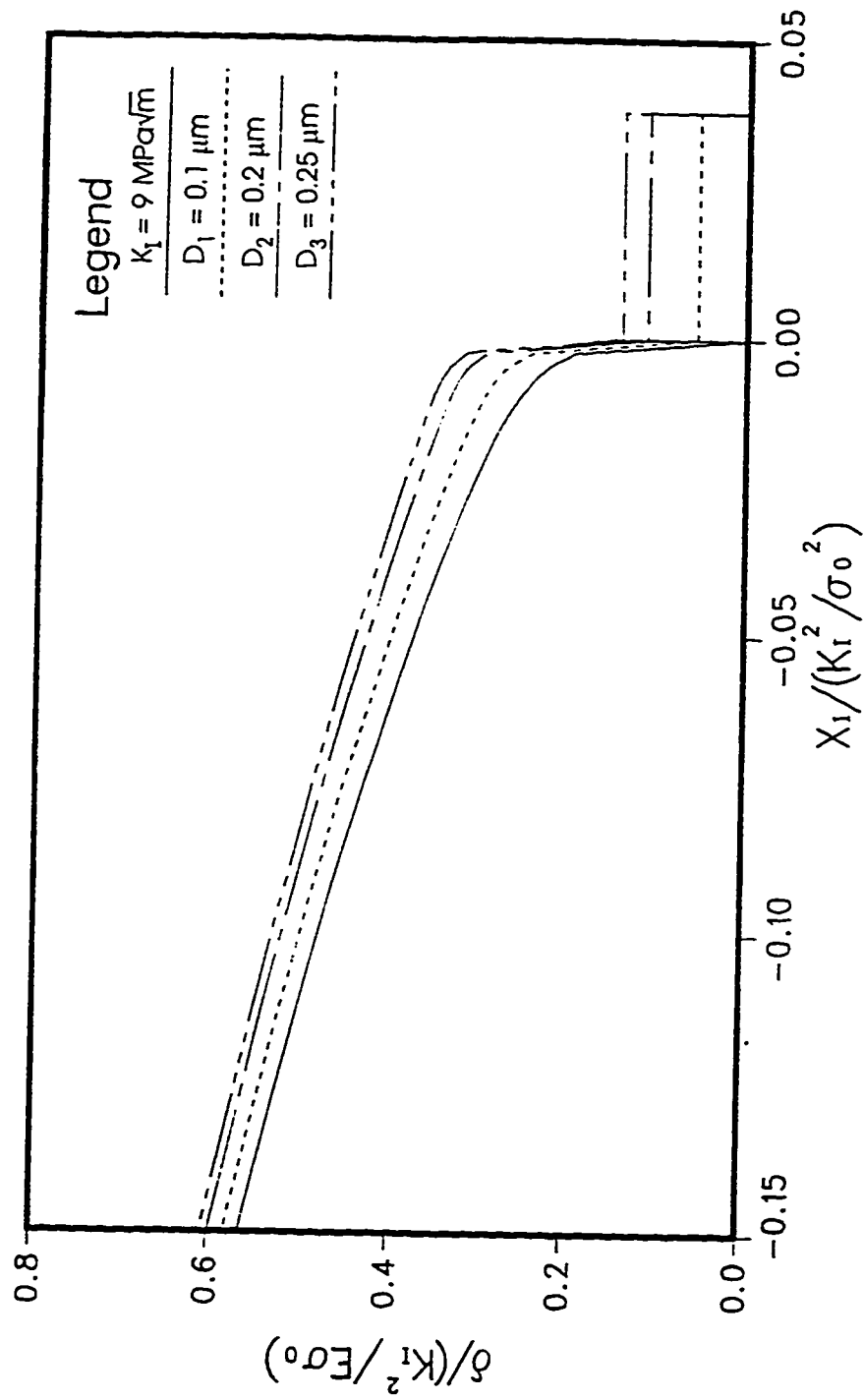


Fig.(3-18) Crack opening profile before and after hydride expansion. (Length of hydride platelet  $L = 10 \mu m$ , and note that the coordinates are non-dimensionalized by different quantities, see text.)

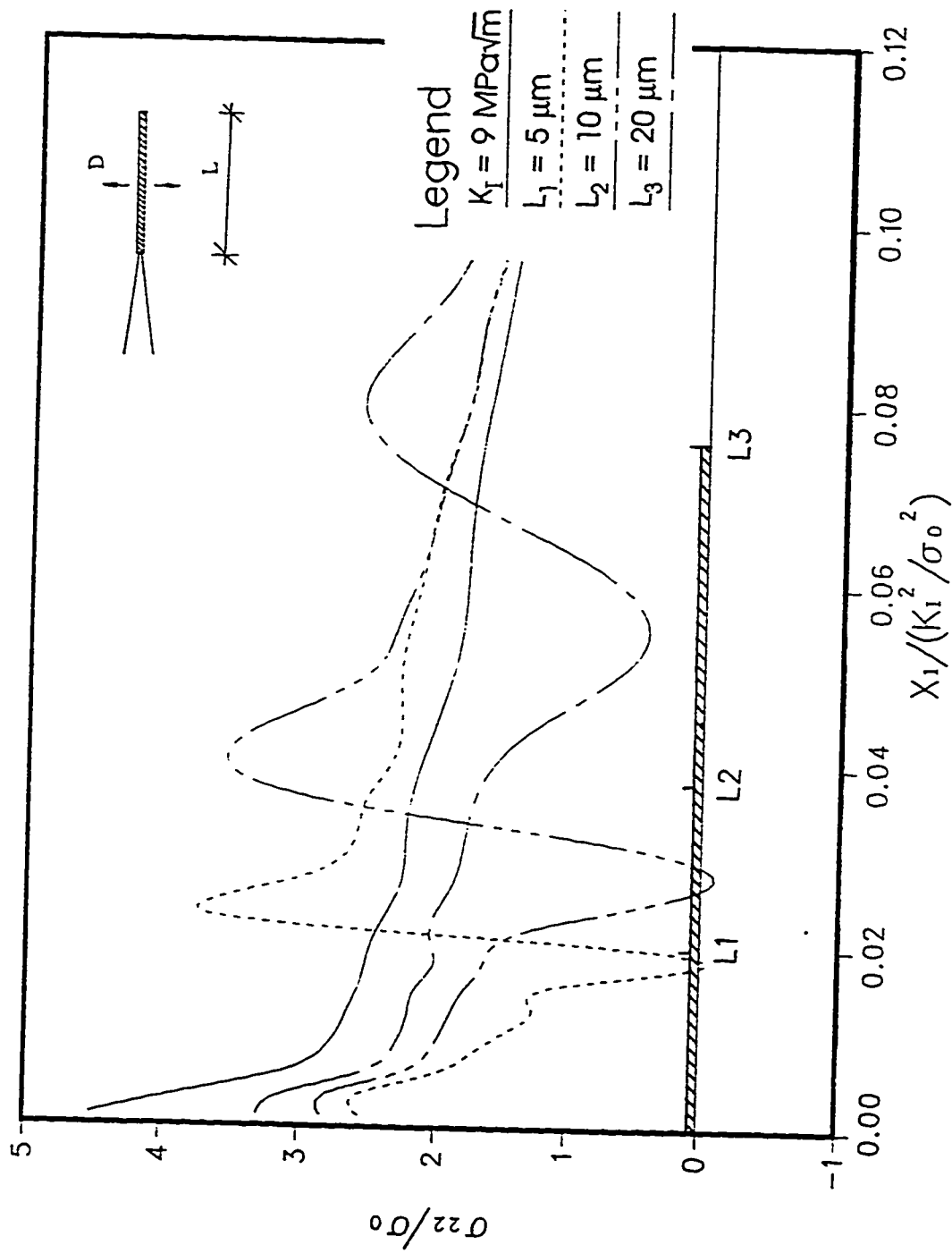


Fig.(3-19) Effect of different hydride length on the normal stress distribution.  
(Expansion of hydride platelet  $D = 0.1 \mu\text{m}$  for all three cases.)

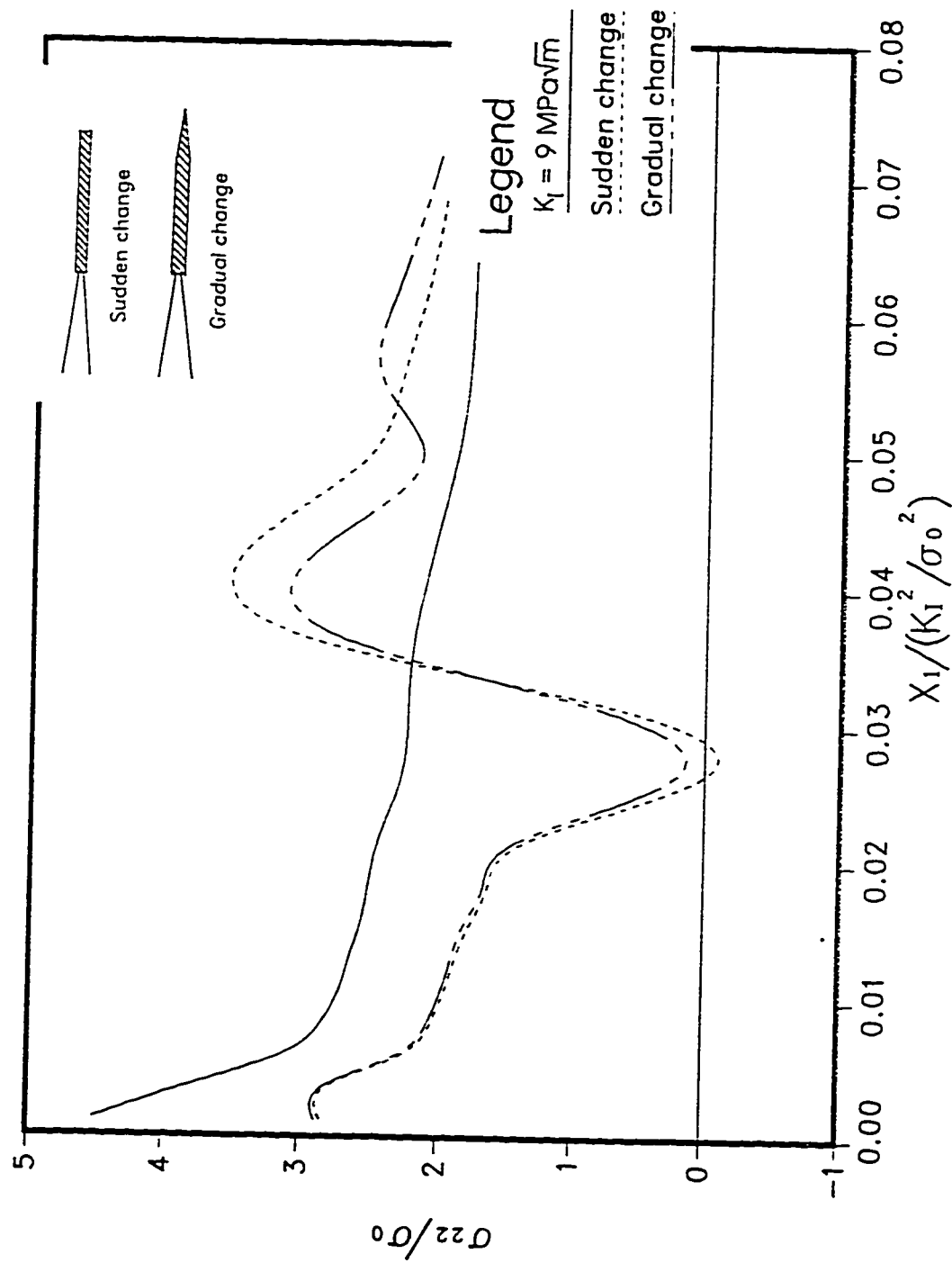


Fig.(3-20) Effect of hydride front end geometry on the normal stress distribution for a hydride platelet of length  $L = 10 \text{ }\mu\text{m}$  expanding by  $D = 0.1 \text{ }\mu\text{m}$ .



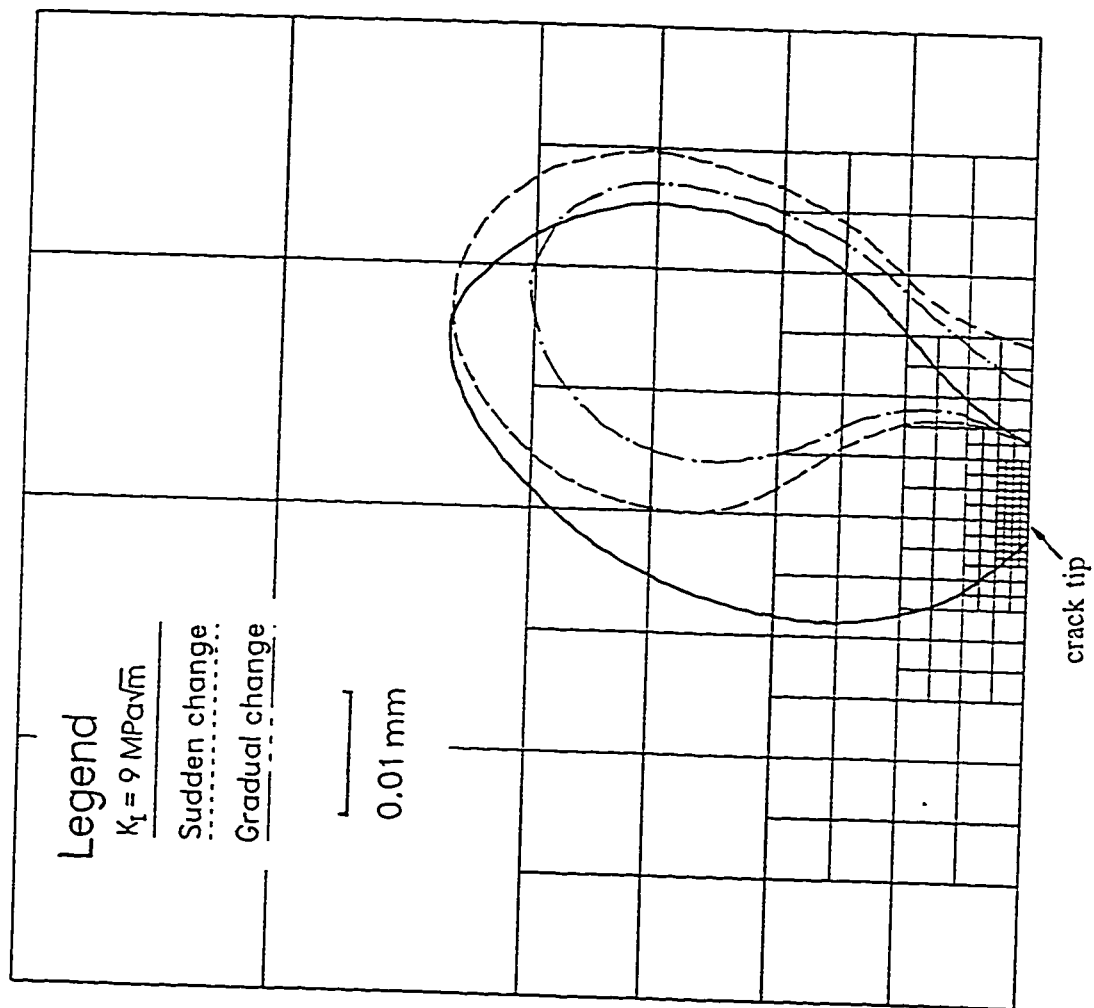


Fig. (3-21) Effect of hydride front end geometry on the plastic zone size for a hydride platelet of length  $L = 10 \text{ } \mu\text{m}$  and expansion of  $D = 0.1 \text{ } \mu\text{m}$ .

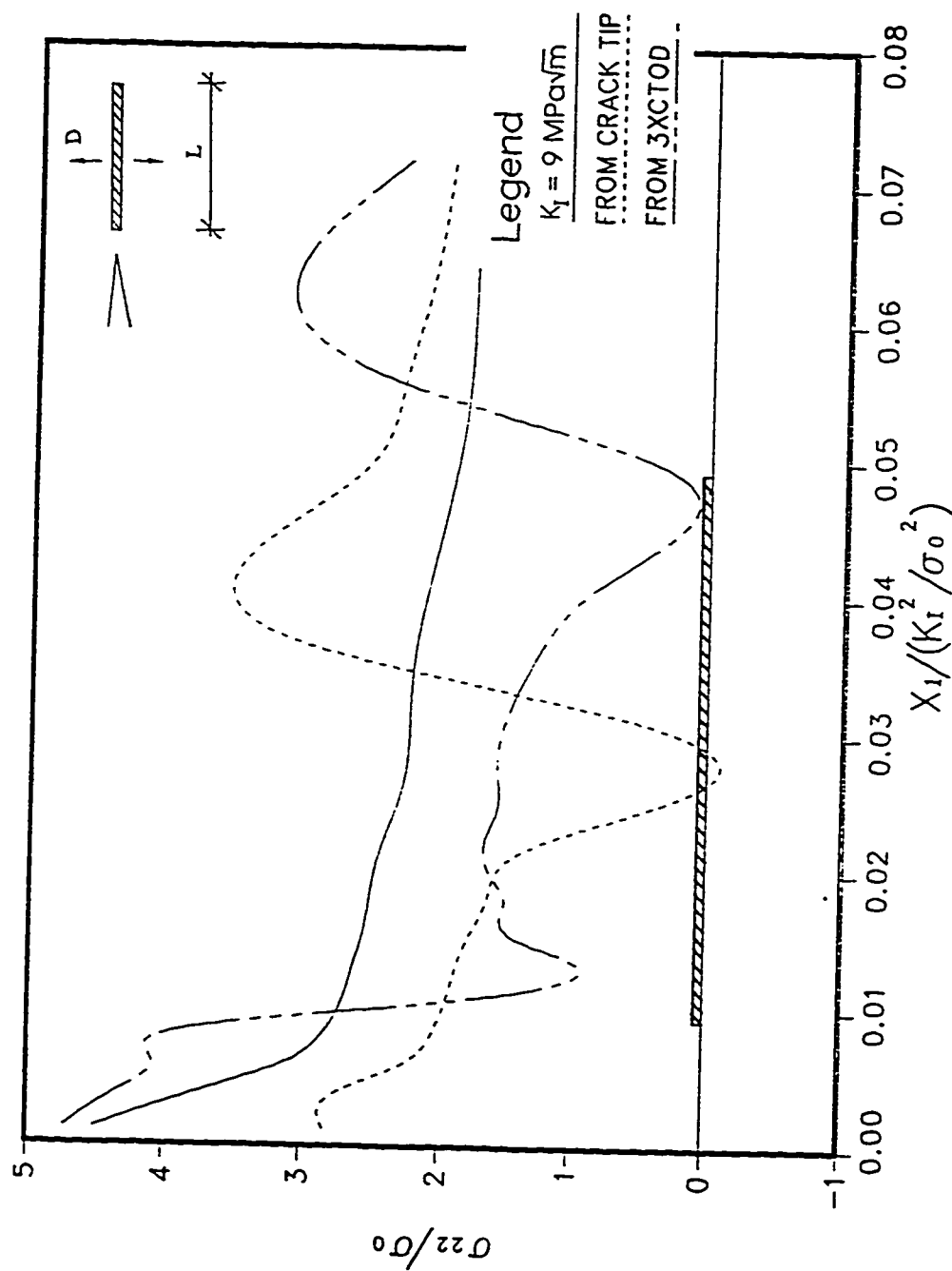


Fig.(3-22) Effect of location of the hydride from the crack tip on the normal stress distribution. (Hydride length  $L = 10 \mu\text{m}$  and its expansion  $D = 0.1 \mu\text{m}$ .)

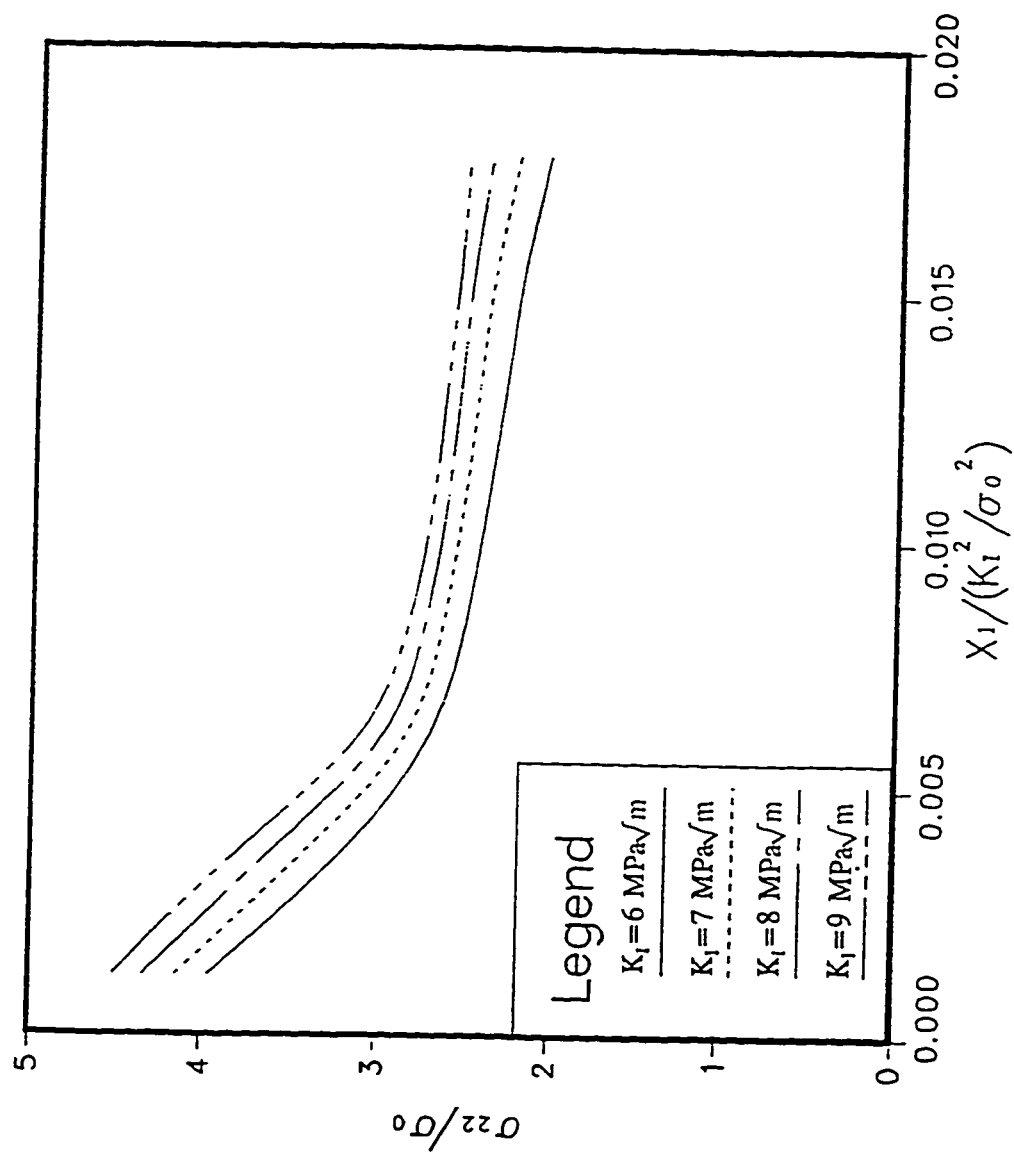


Fig.(3-23) Distributions of stress component normal to the crack plane for various stress intensity factors by von Mises isotropic hardening small deformation model.

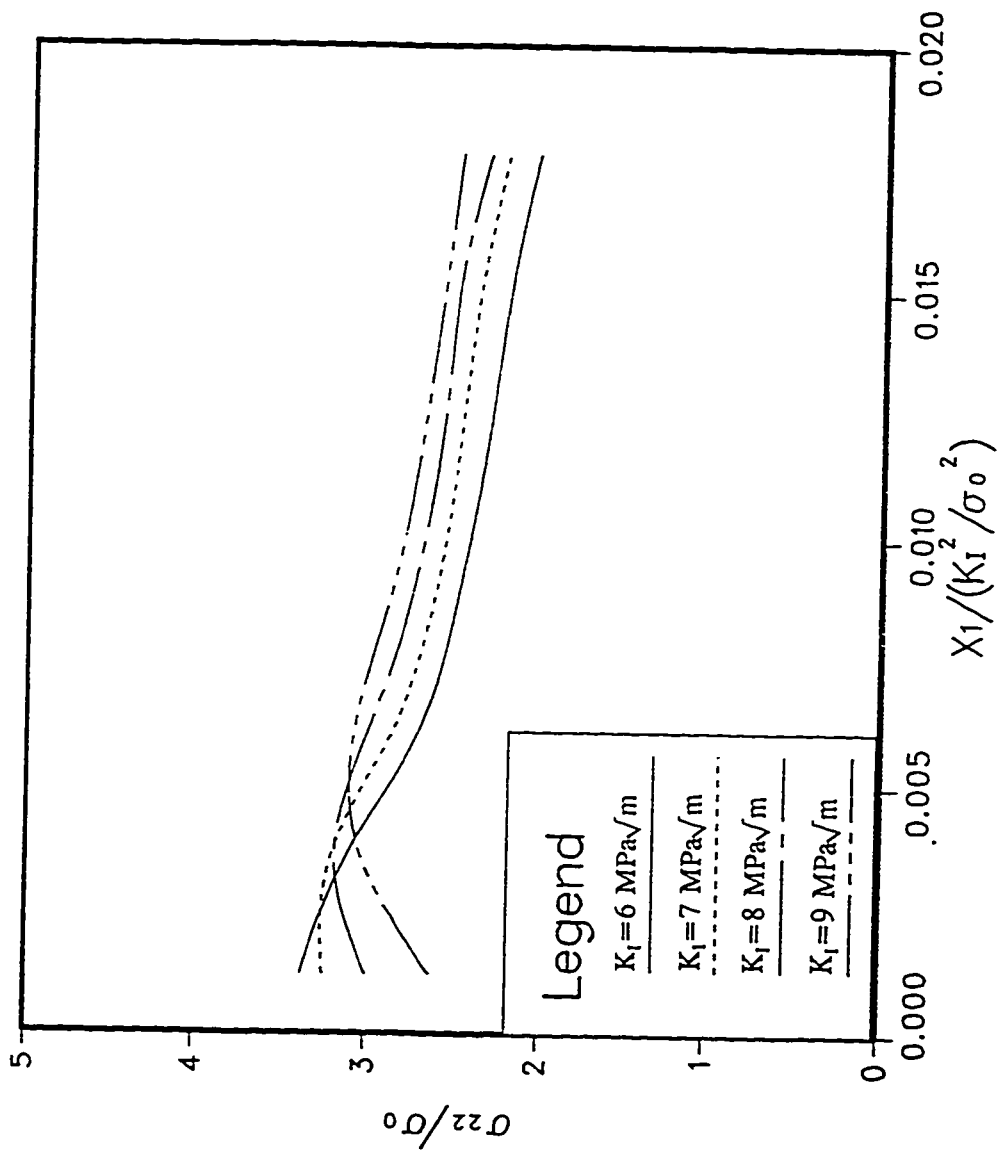


Fig.(3-24) Distributions of stress component normal to the crack plane for various stress intensity factor by von Mises isotropic hardening finite deformation model.

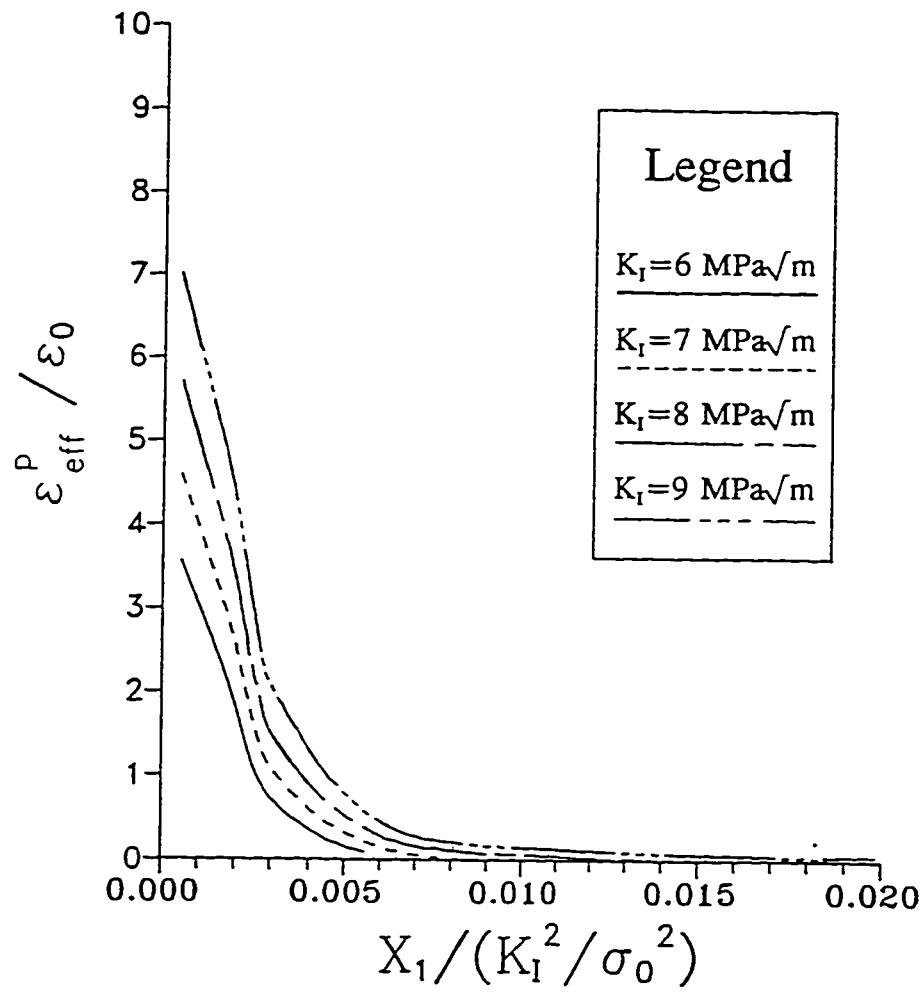


Fig.(3-25) Distributions of strain component normal to the crack plane for various stress intensity factor by von Mises isotropic hardening small deformation model.

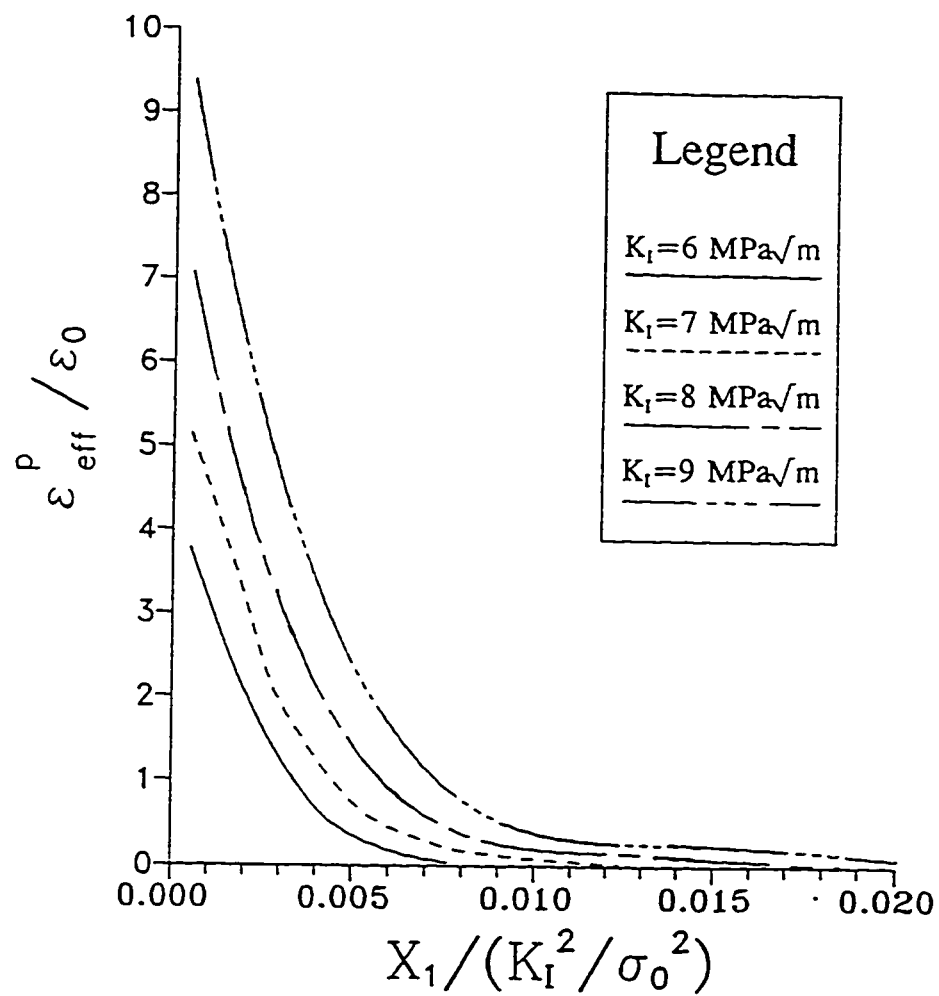


Fig.(3-26) Distributions of strain component normal to the crack plane for various stress intensity factors by von Mises isotropic hardening finite deformation model.

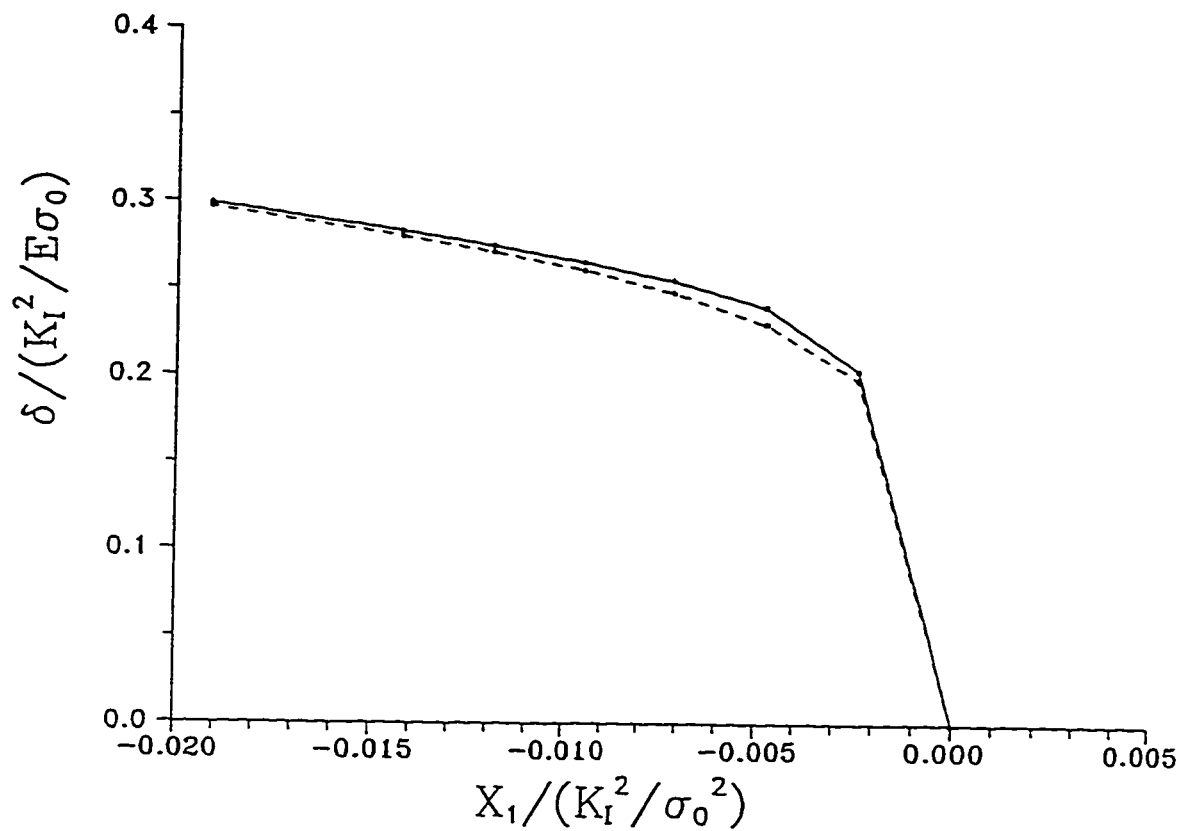


Fig.(3-27) Crack opening profiles at  $K_I=9 \text{ MPa}\sqrt{\text{m}}$  in the dimensionless coordinates by von Mises isotropic hardening small deformation model (dashed line) and finite deformation model (solid line).

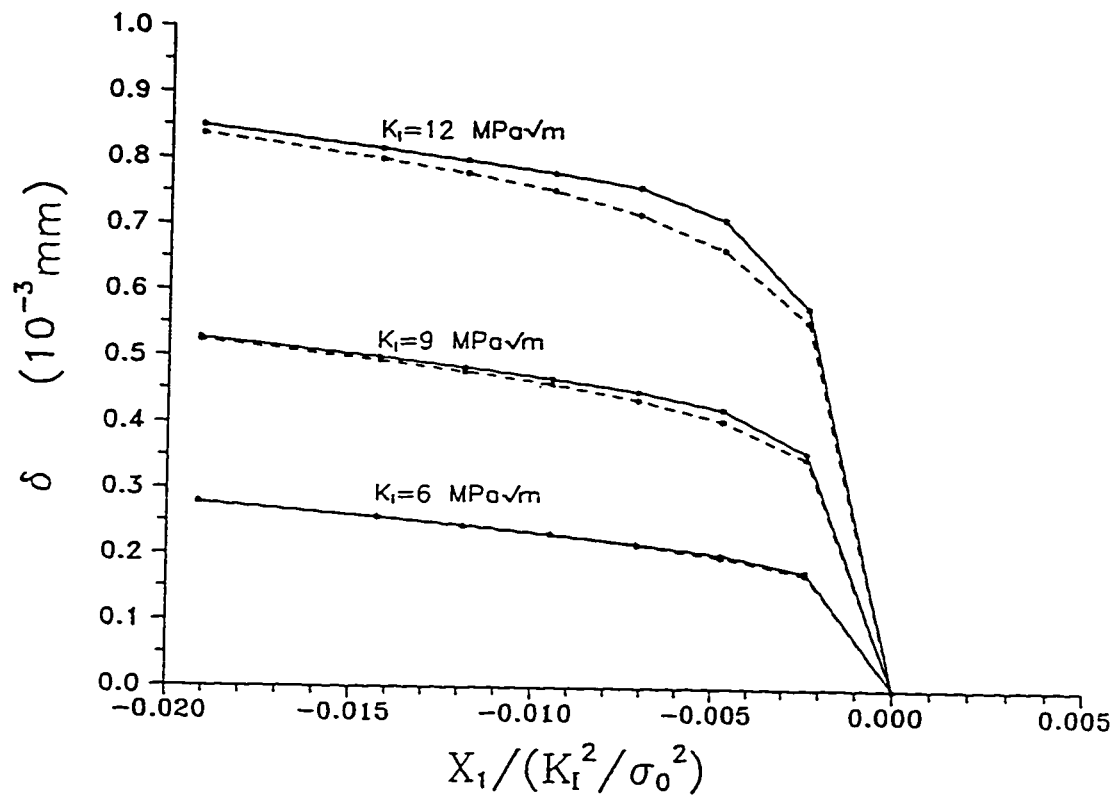


Fig.(3-28) Crack opening profiles at  $K_I=6, 9, 12$  MPa√m in millimetre unit by von Mises isotropic hardening small deformation model (dashed lines) and finite deformation model (solid lines).



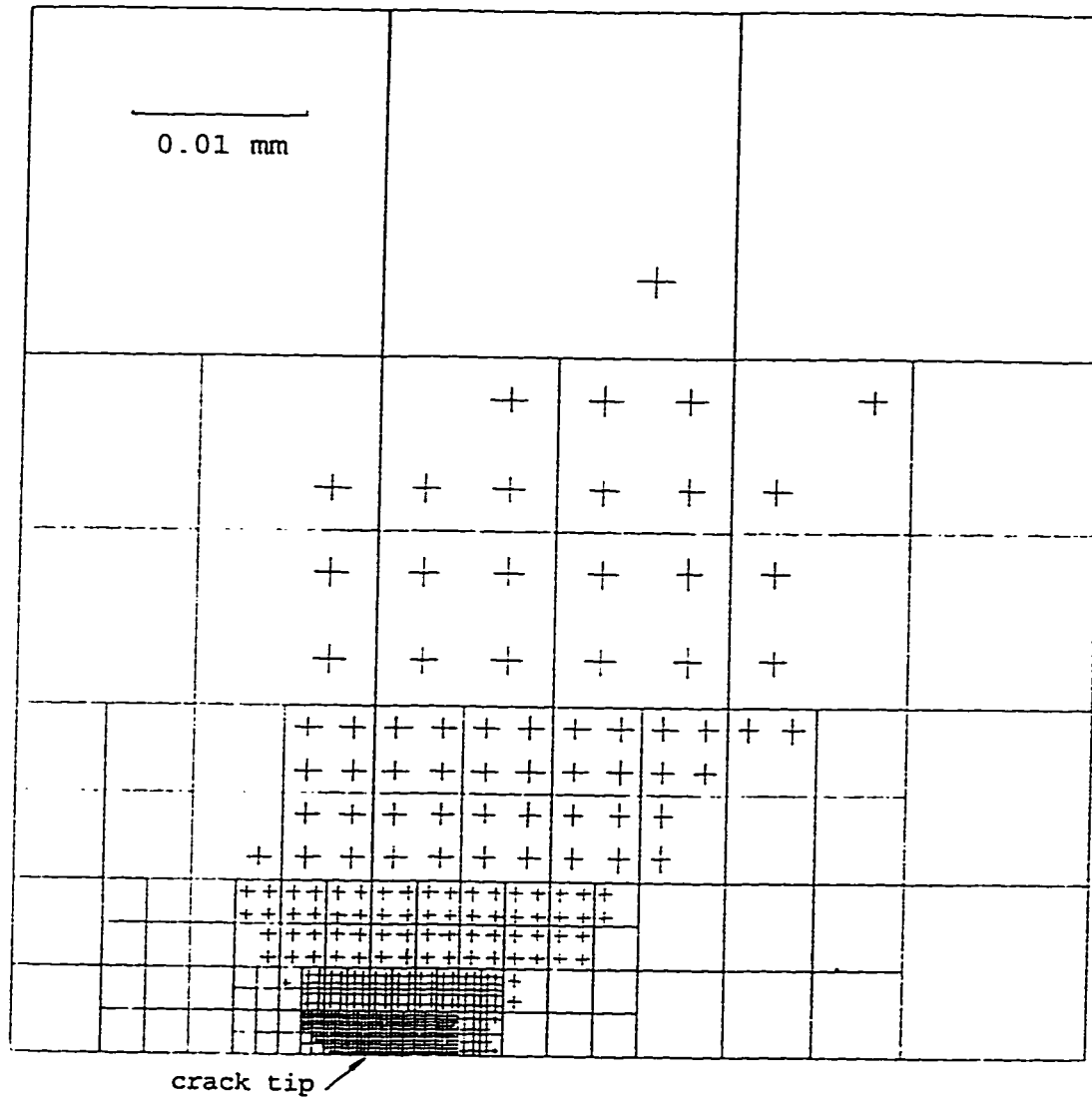


Fig.(3-29) The plastic zone at the stress intensity factor of  $9 \text{ MPa}\sqrt{\text{m}}$  by von Mises isotropic hardening small deformation model.

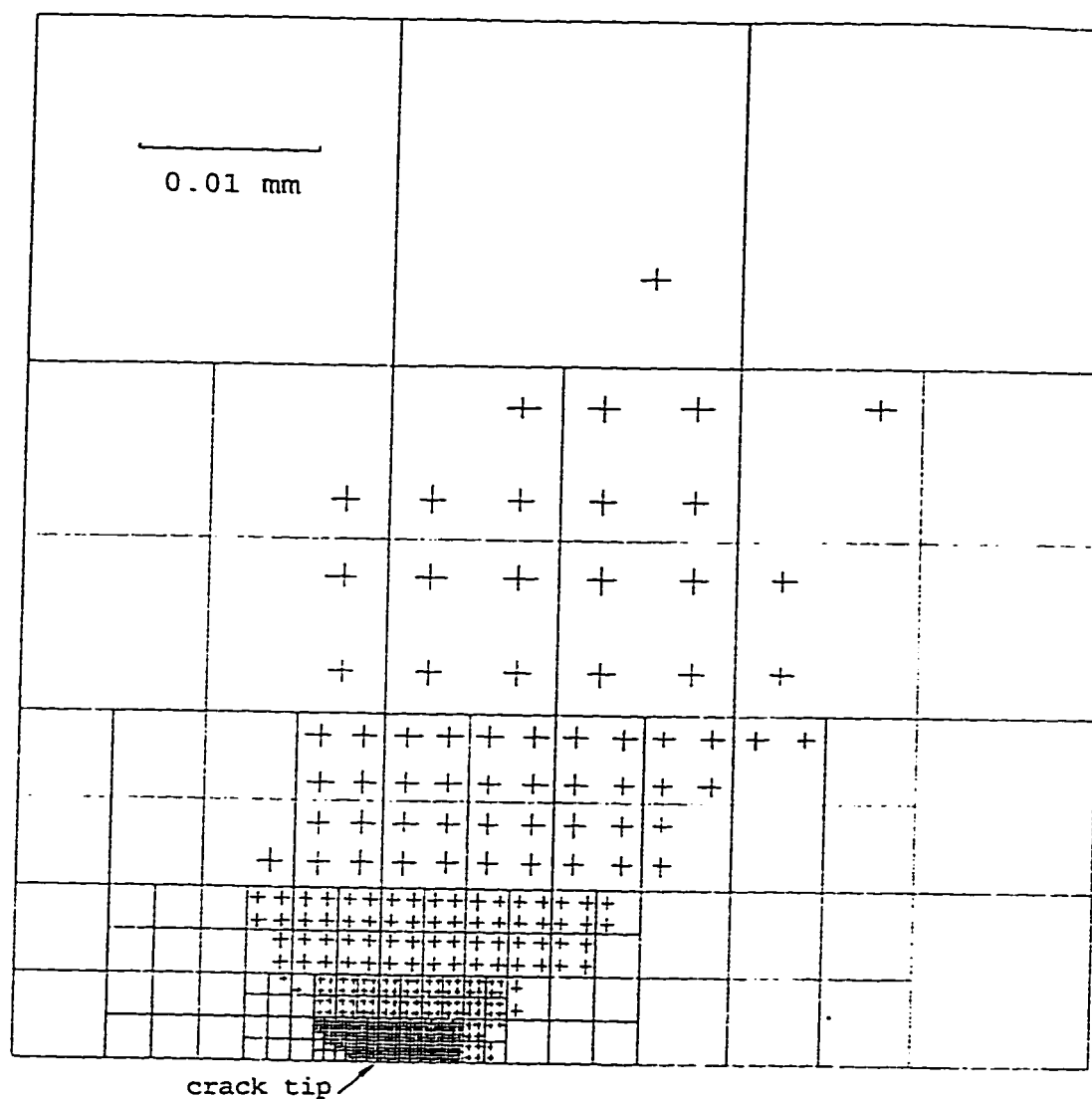


Fig.(3-30) The plastic zone at the stress intensity factor of  $9 \text{ MPa}\sqrt{\text{m}}$  by von Mises isotropic hardening finite deformation model.

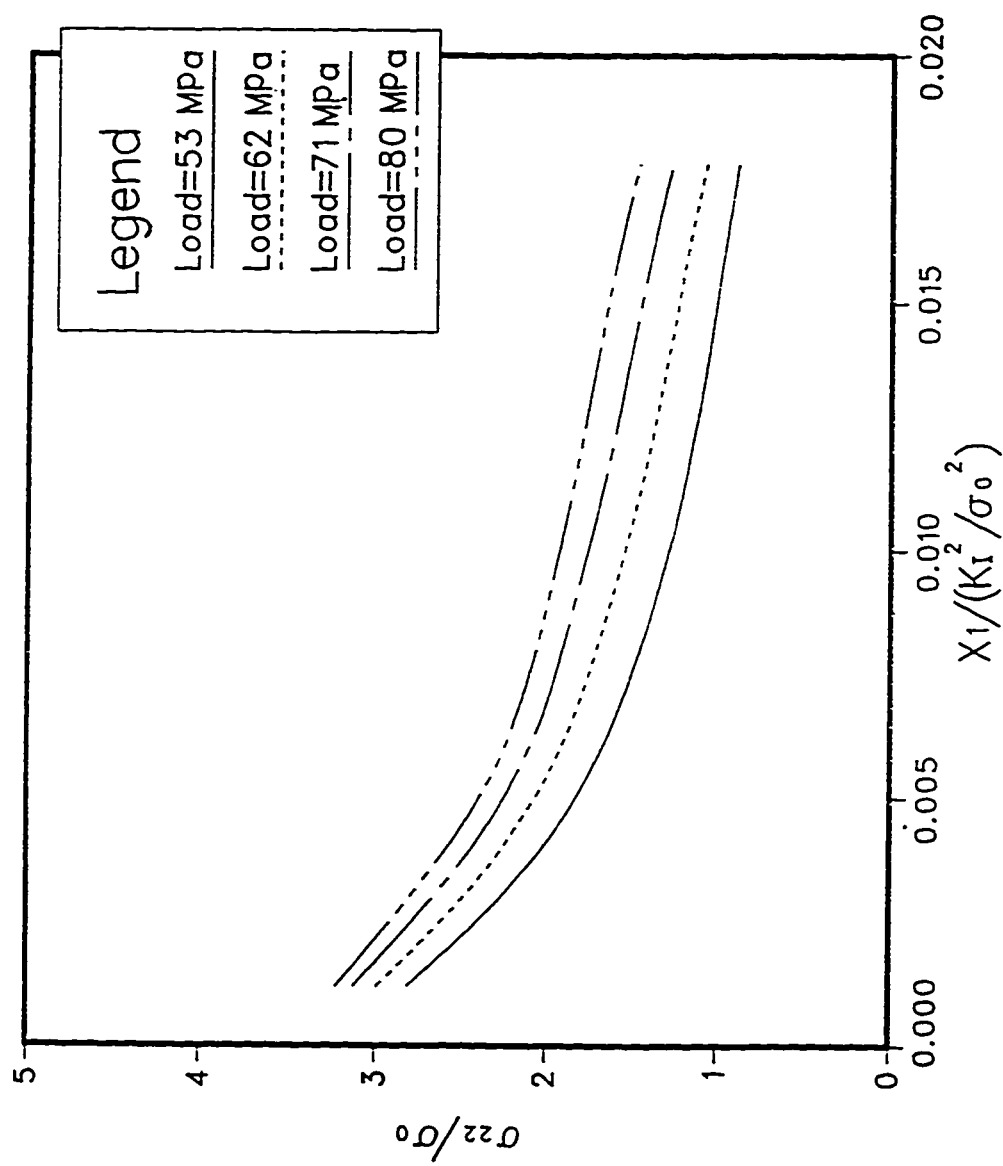


Fig.(3-31) Distributions of stress component normal to the crack plane for a crack length  $a=0.8$  mm under various applied stress by von Mises isotropic hardening finite deformation model.

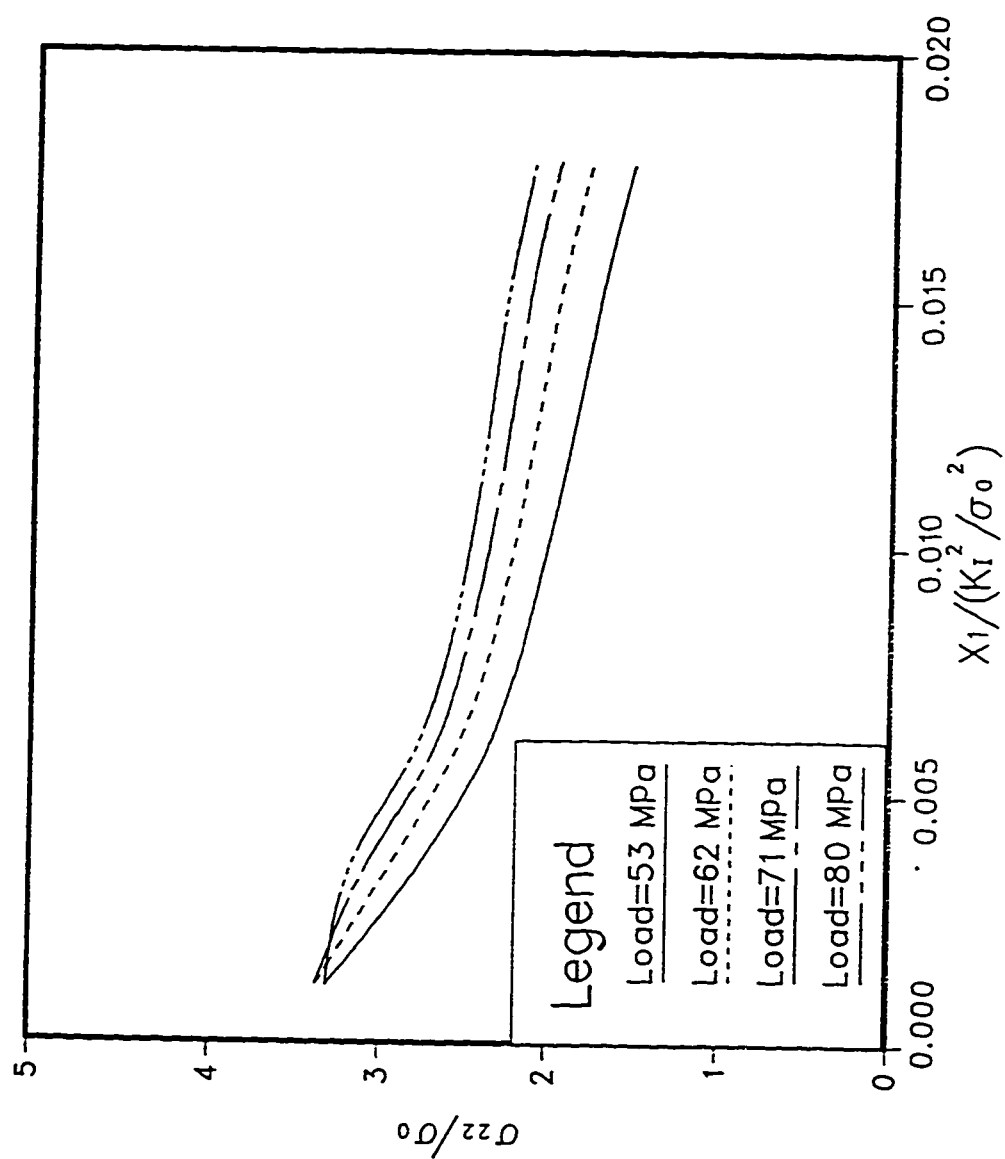


Fig.(3-32) Distributions of stress component normal to the crack plane for a crack length  $a=2.08$  mm under various applied stress by von Mises isotropic hardening finite deformation model.

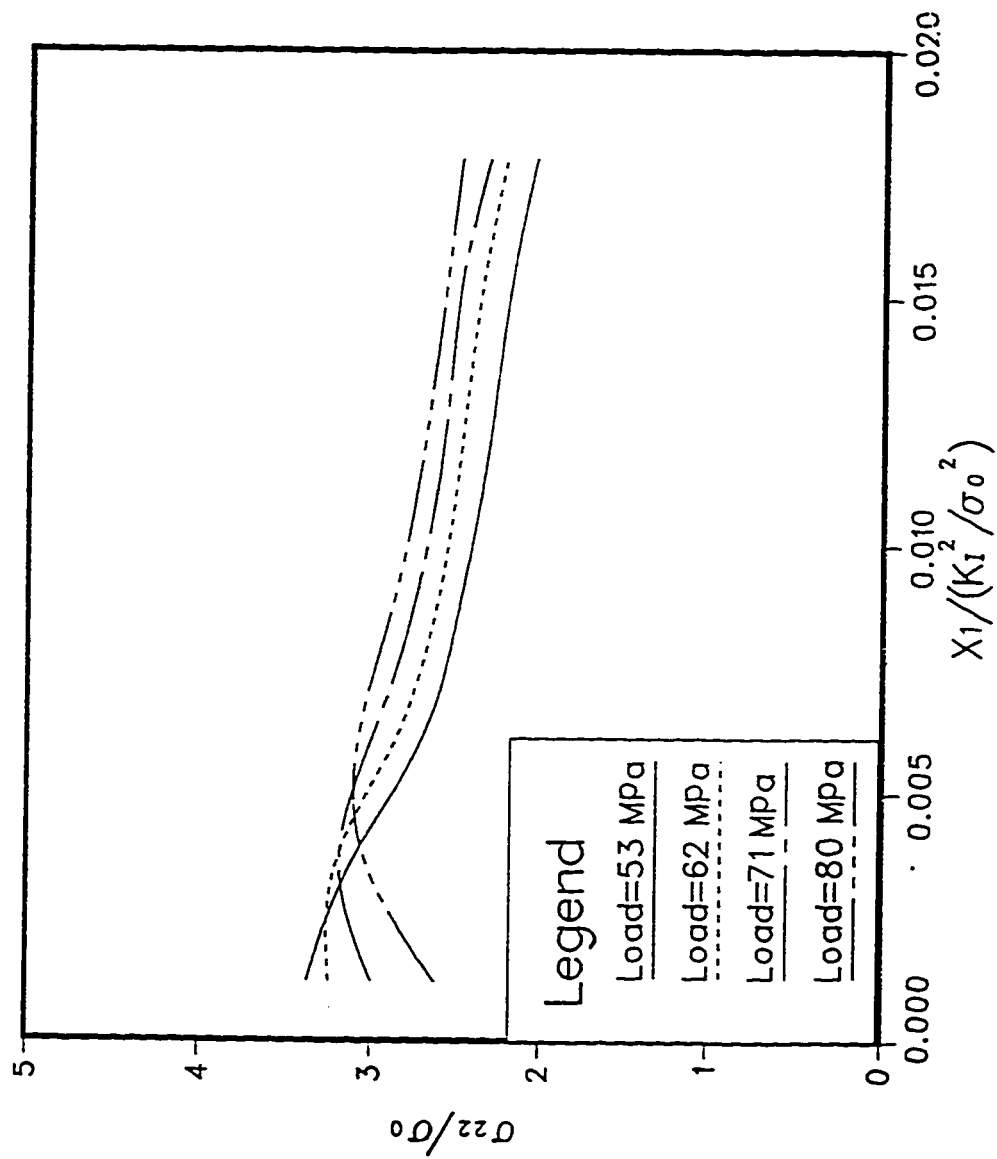


Fig.(3-33) Distributions of stress component normal to the crack plane for a crack length  $a=4.0$  mm under various applied stress by von Mises isotropic hardening finite deformation model.

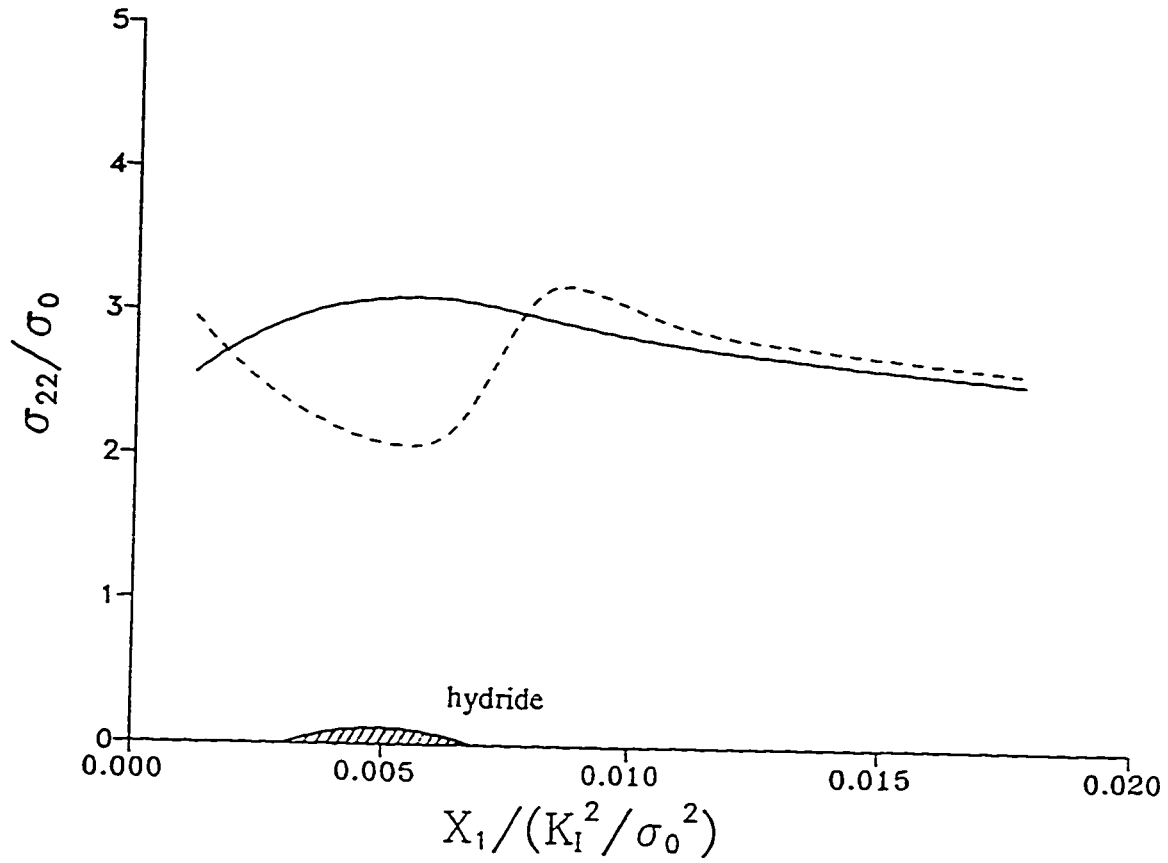


Fig.(3-34) . The stress distributions before (solid line) and after (dashed line) precipitating the hydride at the peak stress.

## CHAPTER 4

# STUDY OF THE CRACK CLOSURE UNDER CYCLIC LOADING BY ELASTIC-PLASTIC FINITE ELEMENT ANALYSIS

### 4.1 Introduction

In 1968, Elber at the University of New South Wales, Australia, observed that fatigue-crack surfaces contact with each other even during tension-tension cyclic loading. He concluded that the crack closure phenomenon is a direct consequence of the permanent tensile plastic deformations left in the wake of the propagating crack [4-1]. This simple observation and the explanation of the crack closure phenomenon provided explanation for many other crack growth characteristics observed experimentally. The most significant practical applications are the correlation of crack-growth rate data and predicting crack growth under variable-amplitude loading. Elber suggested [4-2] that crack propagation can occur only during that portion of the loading cycle in which the crack is fully open at the crack tip. Based on this suggestion, an effective stress range is defined:

$$\Delta \sigma_{eff} = \sigma_{max} - \sigma_{op} \quad (4-1)$$

The ratio of  $\Delta \sigma_{eff}$  to total applied stress range ( $\Delta \sigma$ ) is defined as the stress intensity range ratio,  $U$ , and is given by

$$U = \frac{\Delta \sigma_{eff}}{\Delta \sigma} = \frac{\sigma_{max} - \sigma_{op}}{\sigma_{max} - \sigma_{min}} \quad (4-2)$$

Elber further suggested that the well known crack growth relationship by Paris [4-3] should be written in terms of effective stress intensity factor range,  $\Delta K_{eff}$ , instead of  $\Delta K$  :

$$\frac{da}{dN} = c(\Delta K_{eff})^m = c(U\Delta K)^m \quad (4-3)$$

Since then, a great deal of effort has been expended in an attempt to measure, characterize and predict crack closure behaviour and its effect on crack growth rates. Predictably, the experimental approach has played a major role in this area. Various methods have been used for establishing the crack opening and crack closing levels. A common method used is the compliance of the specimen. A displacement gauge is usually placed along the crack flank at some point, and the load-displacement curve is recorded. The change in the slope of the load-displacement curve gives an indication of crack opening and closing. Measuring some factors related to the crack closure by direct observation with high resolution microscopy techniques is another method. A review of different methods used to measure crack closure is shown in [4-4].

The analytical approach for fatigue crack closure is relatively difficult, and only few models have been proposed. Budiansky and Hutchinson [4-5] formulated an analytical



model for crack closure based on the ideally-plastic Dugdale-Barenblatt model. Plastic wake residual stretches and crack opening loads as functions of the applied load range were derived. An analytical crack closure model was developed by Newman [4-6] for a central crack in a finite-width specimen subject to a uniformly applied stress. This was also based on the Dugdale model, but was modified to leave plastically deformed material in the wake of the crack. The plastic zone size and crack surface displacements can be obtained by superposition of two simple elastic problems.

The numerical approach was also used from the beginning. The elastic-plastic finite element analyses of growing fatigue cracks have been studied. In this regard the works of Newman and McClung are noteworthy. Although Newman is not the first to study the crack-growth and crack-closure behaviour using finite element analysis, a general trend of numerical approach in this area during the past twenty years can be seen from his works [4-7] to [4-11]. He originally suggested a crack-tip node release scheme [4-8] in which the boundary condition change, characterizing crack growth, was achieved by changing the stiffness of the spring elements connected to boundary nodes of a finite element mesh. In his analysis [4-9], he attempted to employ a critical strain crack-growth criterion. This led to a research direction despite some questions, such as the critical strain should change following the increase of crack length. In the analysis of crack closure under plane strain conditions [4-10] Newman and his co-investigators concluded that plasticity induced closure only occurred during a transient period when a crack evolved from a stationary state (initial crack) to a steady-state condition of a growing fatigue crack. Further investigation involved a three-dimensional, elastic-plastic, finite-

element analysis of crack growth and closure under cyclic loading to study the behaviour of a crack in a finite-thickness middle-crack tension specimen [4-11].

McClung and collaborators have published several papers about the finite element analysis of fatigue crack closure [4-12] to [4-16]. In their major papers, [4-12] and [4-13], a model for the elastic-plastic finite element simulation of fatigue crack growth and crack closure was presented and evaluated from the following aspects: mesh refinement, effect of notches, effect of initial crack length and crack-tip node release scheme. Also, the opening and closing behaviour of fatigue cracks was studied with special attention to the effects of maximum stress, material properties and constitutive model. It is worth mentioning that in the earlier studies they followed the crack-tip node release scheme by Newman et al. However, McClung et al. [4-16] later stated that because the large stiffness values imposed when constraining a crack line node were a source of possible numerical difficulties in the finite element scheme, the truss (spring) elements were entirely removed and boundary conditions on crack line nodes were directly imposed in the usual way. At the same time, they concluded that node release at maximum load or minimum load gave exactly the same crack opening levels in nearly all cases examined. (They did not mention the closing levels, which were very different in two cases.) Thus, node release at minimum load was chosen by McClung et al. as a new standard scheme.

In this study, a new, and more comprehensive constitutive model is employed in the finite element analysis (see Chapter 2 for the description of the constitutive model). A simple and efficient crack-tip node release scheme is proposed allowing any commercial finite element analysis program such as ADINA and ANSYS etc. to be used. For

constant amplitude cyclic loading. special attention is given to some basic concepts of fatigue crack growth and crack closure behaviour. New definitions of crack opening stress and closing stress in the numerical analysis, are presented. After a comparison of crack-tip node release at maximum or minimum load, the deficiency of releasing crack-tip node at minimum load is described. The energy release principle for crack growth is explained through the release of nodes. For constant amplitude cyclic loading with a single overload or with a single underload (compressive overload) the results obtained adequately explain the delayed retardation and the acceleration of crack advance. Finally, crack growth from a notch tip, under compression-compression constant amplitude cyclic loading, is investigated.

## **4.2 Finite Element Modelling**

### **4.2.1 Elastic-plastic material model**

The elastic-plastic constitutive relation described in Chapter 2 is used under plane stress condition. A subroutine CUSER 2, using the matrix forms of this relation, is inserted into the ADINA system, hence, any advantage of ADINA computer code, such as numerous choices of equilibrium iteration methods and element birth and death options, can be used.

It should be noted that the transient process of materials during cyclic loading is not considered in this finite element analysis. The material is assumed to be in steady state: the yield radius of every material point will not change during cyclic loading. Thus, in

fact, the kinematic hardening rule is employed with the stress-strain cyclic curve of the material.

#### 4.2.2 Mesh and Material Properties

Due to the symmetry, only one-quarter of a centre-cracked panel needs to be considered in the finite element analysis. The mesh is composed of 442 isoparametric quadrilateral elements with 588 nodes and is shown in Fig.(4-1). For the sake of clarity, the crack-tip region is enlarged and displayed below the main mesh. The half-width of the panel is 40 mm, and the size of the smallest elements near the crack tip is 0.02 mm. So, element lengths near the crack tip are 0.0005 of the total mesh width. The initial half crack length is 4 mm.

The truss elements used for simulating the crack extension are not shown in this figure, their connection and location can be seen in Fig.(4-3). The total number of truss elements depends on the distance of crack extension which is predetermined in the analysis. And the truss elements always have linear elastic materials.

The panel material is assumed to be a typical structural steel and shows Masing behaviour with a yield stress (limit of linear response),  $\sigma_0$ , of 200 MPa and a modulus of elasticity of  $200 \times 10^3$  MPa. The monotonic stress-strain curve and cyclic stress-strain curve for this material are shown in Fig.(4-2). The latter has a yield stress (cyclic yield stress),  $\sigma_{0c}$ , of 230 MPa and is taken in finite element analysis with a form of Ramberg-Osgood relation:

$$\frac{\epsilon_e}{\epsilon_0} = \frac{\sigma_e}{\sigma_{0c}} + 0.02 \left( \frac{\sigma_e}{\sigma_{0c}} \right)^{6.0} \quad (4-4)$$

where  $\sigma_e$  is the von Mises effective stress,  $\epsilon_e$  is the corresponding effective strain.

#### 4.2.3 A new crack-tip node release scheme

After incorporating an appropriate constitutive model, the most important task is to decide how to simulate the crack growth in a finite element analysis. The reliability of results will be directly influenced by the simulation scheme of crack growth.

There are two types of techniques to simulate crack growth. The first one is to use special crack-tip elements. Atluri and co-investigators [4-17] [4-18] constructed circular-sector-shaped singularity elements surrounding the crack-tip, then translated the whole set of crack-tip core elements by an arbitrary distance,  $\Delta a$ , in the direction of intended crack extension, to simulate the crack growth. Zhang, Hsu and Wang [4-19] proposed a sort of breakable elements which were placed along the crack line, then used the so-called breakable element algorithm to move the crack-tip within a single element.

The second type is the nodal release technique. Before Newman's work, researchers changed boundary conditions of the crack-tip node directly to get the node free or fixed. When the crack-tip is free, the crack advances the length of an element. The approach Newman selected to change boundary conditions was to connect two springs to each boundary node [4-8]. For free nodes, the spring stiffness was set equal to zero. For fixed nodes, the spring stiffness was assigned an extremely large value. Newman stated that, "The use of springs to satisfy boundary conditions was selected because an efficient

technique to modify coefficients of the elastic stiffness matrix was incorporated into the nonlinear analysis program."

As mentioned earlier, McClung followed Newman's approach in his earlier study. Then because the large stiffness values imposed when a crack line node was constrained were a source of possible numerical difficulties in the finite element scheme, McClung removed the truss (spring) elements entirely, and changed the boundary conditions on crack line nodes directly in the usual way. He could do this without worrying about convergence of the iterative solutions because he found that node release at maximum load or minimum load during the cyclic loading gave exactly the same crack opening levels, and consequently the crack-tip nodes were released at the minimum load. More will be said about this problem later.

A new node release scheme proposed herein is an extension of Newman's technique, see Fig.(4-3). A bundle of truss elements, each element has a unit cross-sectional area, is used to connect to each boundary node ahead of the initial crack tip. The truss elements in each bundle share two nodes at their ends, and behave in a linear elastic fashion. The stiffness of each truss element in the bundle has a different value from extremely large (Young's modulus  $E=0.1 \times 10^{12}$  MPa) to a value near zero. When the truss elements of the bundle are cut one by one, the bundle can behave with different stiffness values. The stresses or strains in the bundle of truss elements can exactly show the tensile or compressive force borne by the connected node. The truss element with the largest stiffness can keep the node on the crack line to be fixed, ensuring that the symmetry condition is satisfied. While releasing a node at the maximum load of cyclic

loading, this bundle of truss elements is cut one at a time through an element death option provided by the ADINA code. Theoretically, there is no convergence difficulty for this node release technique as long as a proper number of truss elements is provided. For a free node on the crack surface to be fixed during unloading, a pair of contact surfaces is set up on the crack line. One contact surface of the pair is the contactor surface belonging to the material studied; the other surface, the target surface, can be rigid hence preventing the displacement of a free node on the crack surface from being a negative value.

This node release scheme has several advantages compared to other schemes. It is simple. It does not need a special computer program; any commercial computer system, such as ADINA and ANSYS, can be used directly. It is efficient. Node release can be accomplished at any time during the cyclic loading process irrespective of the magnitude of the deformation caused due to the release of the node. Also, several nodes can be released simultaneously, for example during a single overload cycle. Finally, it is accurate. The exact values for crack opening stress and closing stress can be obtained.

It should be pointed out that the finite element analyses which use the node release scheme are intended to display behavioral mechanisms and not to predict the conditions under which a crack growth will progress. A steady state crack growth of one element per loading cycle implies that the rate of crack extension is therefore fixed independently of the level of the applied stress. For plasticity induced closure, however, such analyses will be sufficient to get significant results.

### 4.3 Analysis of crack extension under a constant-amplitude loading and releasing crack-tip nodes at the top of each loading cycle

This section presents results obtained for a constant-amplitude cyclic loading (CA-loading), and releasing crack-tip nodes at the top (maximum load) of each loading cycle (T-release).

#### 4.3.1 Crack opening and closing stress levels

Figure (4-4) shows the first twenty cycles of a CA-loading applied to a centre-cracked panel. The maximum remote stress is  $0.3\sigma_{0c}$ , and the ratio of minimum to maximum applied stress,  $R$ , is zero. The ring symbols represent the points at which the crack fully opens, and the solid symbols indicate the points at which the crack starts closing. Because of the assumption of no prior plastic deformation, the crack initially opens at the first loading step which can have a infinitesimal stress. At the maximum applied stress, the crack-tip node is released and the crack grows to the length of an element (0.02 mm). During unloading, the crack starts closing at about  $0.12\sigma_{0c}$ . The opening stress level reaches a relative stability at about  $0.11\sigma_{0c}$  of the fifth loading cycle, though the opening stress level has reached the relative stability at the first loading cycle. The so-called relative stability means that the whole system, which includes the centre-cracked panel subjected to a constant-amplitude cyclic loading and the crack growth, growing one element for one loading cycle, reaches a relatively balanced state from the beginning. Or, it can be said that the residual stresses in the region near the crack tip, caused by plastic



deformation, reach a certain level from zero. After five loading cycles the crack opening stress and closing stress increase slowly and steadily and do not stabilize to constant values, respectively. Table (4-1) shows the change of the crack opening stress for each cycle in a numerical sense. It can be seen clearly that before reaching relative stability the crack opening stress has a quick increase, after which the rate stabilizes at about 1 MPa for each 5 or 6 cycles. The maximum stress, maximum strain and CTOD for each loading cycle are also listed in Table (4-1). Before achieving relative stability they decrease gradually at a slow rate, then change in a similar manner to that of the crack opening stress after the relative stability.

The crack opening stress and closing stress will not be a stable value because the crack length grows for each loading cycle. The increase of the crack length under CA-loading is similar to that of an increased-amplitude cyclic loading applied to a centre-cracked panel with a stationary crack. In other words, the centre-cracked panel is subjected to loads with increased stress-intensity factor at each cycle, although the increase of the factor is small because the growth of the crack is small each time.

The experimental results of Ho et al. [4-20], Ashbaugh [4-21] and Ray et al. [4-22] demonstrated that as crack length increased, the crack opening loads or the crack closing stress intensity factor increased under constant amplitude load conditions.

#### 4.3.2 A new definition of crack opening stress and closing stress

For most researchers, the crack opening stress is identified as the applied stress at which the crack first becomes fully open (the last node is released) and the crack closing

stress is defined as the applied stress at which any part of the crack first closes (the first node makes contact). Meanwhile, the opening stress and closing stress are governed usually by the node immediately behind the current crack tip along the crack line [4-8.4-16].

The implication of "opening" should be that the crack has a potential capability to propagate, while "closing" implies the crack can not propagate. So, two questions have to be raised. First, when the displacement of the node immediately behind the current crack tip becomes positive, is the crack then fully open? While this is a necessary condition, it is not sufficient one, because a positive displacement of this node only implies that the crack is open at this node, without guaranteeing that it is open between this node and the current crack-tip node. Second, when a part of the crack has closed first, but the crack-tip node still carries a tensile force (similar to that following a single overload), can it be said that the crack is closed? Conversely, when all of the finite element nodes on the crack surface have a positive displacement, but the crack-tip node bears a compressive stress during unloading, can it be said that the crack is still opened? The answer is evidently no!

In this work, the crack tip, instead of the node immediately behind it, will be directly employed to determine the crack opening and closing stresses. The definitions used in this study are as follows.

When the compressive stress borne by the crack-tip node from the connected truss elements changes to a tensile one, the crack is deemed fully open. The corresponding far field applied stress is taken to be the crack opening stress. When the tensile stress borne

by the crack-tip node from the connected truss elements is changed to a compressive one. this then indicates the initiation of crack closure. The corresponding applied far field stress is taken to be the crack closing stress.

The definitions proposed here fit the new node release scheme. That is, the stress or the strain in the truss elements which connect the crack-tip node is provided as a judgment of the crack opening or closing.

The results of both old and new definitions are shown in Fig.(4-5). The ring symbols and solid symbols represent the points corresponding to the opening stress and closing stress, respectively, for the new definition, as shown in Fig.(4-4). The cross symbols indicate the points at which the crack opens during loading and closes during unloading using the earlier definition. It can be seen that after achieving relative stability, the two definitions give very similar opening stresses. This is because the size of elements on the crack line in this finite element analysis is very small. As the crack opens a node at a time from the initial crack tip to the current crack tip, it is evident that the smaller the distance is between two nodes, the smaller is the difference of opening stresses for the two nodes.

The crack closing stresses given by the two definitions are different because the crack tip first closes (or the crack-tip node first 'senses' a compressive stress), then the node immediately behind it closes after further unloading.

#### 4.3.3 Applied load vs displacement

In order to compare the above results with experimental observations, a loading

procedure that removes the effect of artificial releasing of nodes at the final loading cycle is proposed. The node will be released at the top of the first 7 cycles only, while the displacement of the initial crack-tip node will be recorded for the whole eighth cycle. The displacements of the initial crack-tip node are believed to approximate the displacements measured by a gauge located at the crack mouth in a typical crack closure experiment. The relationship between the applied load and the displacement at the initial crack-tip node is shown in Fig.(4-6). It is well known that the initial crack is always in an open state under the tension-tension cyclic loading. The crack starts to open at the initial crack-tip node with an infinitesimal stress, see Point A in Fig.(4-6). Then, the crack opens progressively from Point A towards the current crack tip, Point B, with increasing tensile load. After Point B the crack is fully open. The process of opening from Point A to Point B, is nonproportional. The cross symbols mark the points at which each node opens, starting from the initial crack tip to the current crack tip. Opening of the last two nodes (i.e. within the last 0.04 mm of the current crack tip) requires a larger load increment. Except for the first and the last two, the rest of the nodes open in a proportional increment of the load applied, since these nodes have the same residual stress and strain due to the crack advance (to be explained later). During the unloading process the crack starts to close at Point C; and at Point D, the node immediately behind the crack tip closes; the crack is fully closed at Point A. These results indicate exactly the same trend observed experimentally by Davidson [4-23]. Thus, using the current crack-tip node to determine the crack opening and closing stress will better simulate the experimental results.

#### 4.3.4 Plastic zone

The plastic zone is composed of the locus of all Gauss integration points with the effective stresses equal to, or exceeding the cyclic yield stress,  $\sigma_{0c}$ . Fig.(4-7) shows the plastic zones at the maximum load before releasing the crack-tip node for the first, the second and the tenth loading cycle on the background of the mesh used. The plastic zone size,  $r_p$ , is about nine element lengths (0.18 mm) for the first loading cycle. Surprisingly, this value is exactly identical with that given by Irwin's expression assuming plane stress condition, which is three times larger than the corresponding plane-strain.

$$r_p = \frac{1}{2\pi} \left( \frac{K_I}{\sigma_0} \right)^2 \quad (4-5)$$

The plastic zone shape displayed is a typical one for the von Mises yield criterion. The plastic zone for the second loading cycle does not change just like the first plastic zone, but moves forward by one element. But for the tenth loading cycle, the plastic zone size increases about a half-element.

The reversed plastic zones at minimum load for each loading cycle are very small, occupying only about one element. The reversed plastic zone for the first loading cycle is marked in Fig.(4-7) by the cross symbols, which represent the Gauss integration points with compressive stress  $\sigma_{22}$  and the effective stresses equal to, or exceeding the cyclic yield stress of the material.

It should be pointed out that the crack opening stress reaches a relatively stable value before the advancing crack tip reaches the end of the plastic zone caused by the first

loading cycle. The change in crack opening stresses does not have a direct relation with the plastic zone size, because the strain distribution due to plastic deformation is not uniform in the plastic zone.

#### 4.3.5 Crack profile and CTOD

Crack profiles of twenty loading cycles at the maximum load, before node release are shown in Fig.(4-8) by plotting displacements of the nodes on the crack surface versus their distances,  $r$ , from the initial crack tip. It is to be noted that the unit used for both ordinate and abscissa is the same, but the scale of the former is about 225 times larger than that of the latter. The first crack profile which starts from the initial crack tip is obtained without the residual plastic deformations. For each subsequent profile there is a sudden change at the point corresponding to the initial crack tip. If the first crack profile is moved forward, so that its starting point coincides with that of each subsequent profile, then a quick comparison between the two profiles will indicate a difference at the front of the initial crack tip. This difference is not the residual plastic deformation, but is caused by it.

The shape of the profiles manifests a relationship between the displacement of each node and its distance behind the current crack tip. Davidson [4-24] proposed that fatigue crack opening displacements in Mode I (CODI) almost always have been found to be proportional to the square root of the distance ( $d$ ) behind the crack tip, so that

$$CODI = c_0 \sqrt{d} \quad (4-6)$$

If  $c_0$  is chosen to be 0.05, the profiles in Fig.(4-8) are in good agreement with Eq.(4-6).

As a characterizing parameter for welds and welded components of structural steels, the CTOD was introduced by Wells [4-25] as far back as 1961. Wells argued that the stress at a crack tip always reached a critical value (in a purely elastic case  $\sigma \rightarrow \infty$ ). If this is true, then it is the plastic strain in the crack tip region that controls fracture. A measure of the amount of crack tip plastic strain is the displacement of the crack flanks, especially at or very close to the tip. An expression for the CTOD was derived by Burdekin and Stone using the Dugdale strip yield model for an elastic-perfectly plastic material in 1966 [4-26]:

$$\delta_t = \frac{8\sigma_0 a}{\pi E} \ln \sec\left(\frac{\pi \sigma}{2\sigma_0}\right) \quad (4-7)$$

For small scale yielding it reduces to:

$$\delta_t = \frac{K_I^2}{E\sigma_0} \quad (4-8)$$

An operational definition of the crack-tip opening displacement  $\delta_t$  suggested by Rice (private communication with D. M. Tracey, 1975, see [4-27]) defines  $\delta_t$  as the opening distance between the intercept of two 45°-lines, drawn back from the tip with the deformed profile. Then, Rice and Sorensen [4-28] used this definition and Hutchinson's (1968) and Rice and Rosengren's (1968) (herein after denoted by HRR) theoretical result

that  $\delta \sim r^{1/(n+1)}$  very near the crack tip to determine  $\delta_t$ . By setting  $r = \frac{1}{2}\delta_t$  in the crack opening displacement equation

$$\delta = \delta_1 \left( \frac{r}{r_1} \right)^{\frac{1}{n+1}} \quad (4-9)$$

where  $\delta_1$  can be the opening displacement at the first node behind the crack tip.  $r_1$  is the position of that node and  $n$  is the hardening parameter in the Ramberg-Osgood's stress-strain relation.

A relation suggested by Tracey [4-27], based on Rice's definition and his finite element calculations for small-scale yielding, is

$$\delta_t = 0.49 \frac{K^2}{E\sigma_0} \left( \frac{n+1}{n} \right) \left[ (n+1) \frac{\sigma_0}{\sqrt{3}} \right]^{\frac{1}{n}} \quad (4-10)$$

Experimentally, CTOD has been defined as the crack opening displacement at a distance of 1  $\mu\text{m}$  behind the crack tip by Davidson [4-23]. Newman proposed [4-29] a simple definition of CTOD in an elastic-plastic finite element analysis with a critical crack-tip-opening displacement as the crack growth criterion. The crack opening displacement of the first node behind the crack tip was defined as CTOD. In his elastic-plastic finite element analysis the minimum element size in the crack-tip region was 0.4 mm and was 0.00157 of the total mesh (specimen) width.

Using Newman's definition, the CTOD for each loading cycle in this study is given by



Table (4-1). The CTOD for the first cycle is  $0.686 \mu\text{m}$  which is the CTOD of a corresponding stationary crack. After 9 loading cycles (in other words, after crack propagation through the initial plastic zone) the CTOD reaches a relatively stable value. After that, the CTOD increases slowly, but steadily following the increase of the crack length.

Using Equation (4-6) and Davidson's definition corresponding to the results on Table (4-1), the CTOD for the first cycle is  $0.1535 \mu\text{m}$ . While using the Equation (4-9) and Rice's definition, the CTOD is  $0.3486 \mu\text{m}$ . Equations (4-8) and (4-10) predict a CTOD for the first cycle of  $1.3 \mu\text{m}$  and  $2.32 \mu\text{m}$ , respectively.

It is difficult to comment on these different definitions based on the obtained CTOD values, however, it should be noted that if the crack opening displacement of the first node behind the crack tip is used to determine the CTOD, either directly or indirectly (extrapolation using Equation (4-6) or (4-9)), the choice of the element-size becomes important. This is because it not only fixes the position of the first node, but also it influences the accuracy of the finite element analysis.

#### 4.3.6 Stress distribution

In order to explain the crack opening and closing behaviour, the distributions of stresses corresponding to the different loading points of a typical loading cycle (Cycle 8) are given in Fig.(4-9a) and Fig.(4-9b). The abscissa represents the distance from the initial crack tip; its one scale unit ( $0.02 \text{ mm}$ ) corresponds to the length of an element. The vertical dashed lines display the positions of elements (6), (7), (8) and (9) counting from

the initial crack tip. The loading points on the cycle for each curve are indicated in the upper right-hand inset. The current crack tip is located at point A. It should be noted that the stress values for each curve do not belong to the points exactly on the crack line, but to the Gauss integration points located 0.00226 mm from the crack line. Three Gauss integration points nearest the crack line are used for each element.

The curve 1 for loading point 1 shows the residual stress distribution at the end of loading cycle 7. At this instant, the current crack tip is at point A between elements (7) and (8). The minimum value of the residual stresses is located behind the crack tip in element (7) near the node between elements (6) and (7). In element (8) the minimum value of the residual stresses is about -230 MPa, higher than the minimum value in element (7) by about 120 MPa. During loading, curve 2 corresponds to loading point 2 at which the node immediately behind the current crack tip has opened (Newman's definition). This demonstrates that although the node immediately behind the current crack tip opens, the current crack-tip node still bears a compressive stress. Increasing loading to point 3, the prior compressive stress borne by the current crack-tip node changes to positive; in other words, the stress on the current crack-tip node is zero, as shown by the curve 3. When loading to the maximum of the loading cycle (point 4), curve 4 becomes discontinuous at the crack tip. Although there is no singularity at the crack tip in finite element analysis as in a real material, the change of the stresses or strains is extreme in this area. A line linking stresses of two Gauss integration points at the front and back of the crack tip will not represent the real stress distribution. The peak stress in the front of the crack tip in element (8) does not rise sharply because the

increase in stress with loading is superposed on the corresponding residual stresses which is about -230 MPa as mentioned earlier. It is worth noting that element (8) is subjected to a maximum tensile stress for a second time since releasing the node in last cycle. Following loading to point 4, the crack-tip node (point A) is released. During the release process, stress reversal takes place in element (8) and element (9) starts to stretch (the first maximum tension); the current crack tip is transferred from point A to point B. The peak stress in front of the current crack tip in element (9) is greater than that in element (8) by about 80 MPa before the release node (c.f. Fig.(4-9a&b)). There are two factors contributing to this result from opposite directions. The first one is the higher residual stress in element (9), which leads to a higher peak stress. The second factor which reduces the peak stress is the irreversibility of plastic deformation. Drucker and Rice [4-30] gave an interesting example explaining the effect of such an irreversible phenomenon.

Consider two materials having identical stress-strain curves for the monotonic simple tension. One is non-linear elastic and the other is elastic-plastic. Cracked specimens of the two materials are loaded by clamping portions of the boundary and imposing displacements. The deformation patterns around the crack tip will be similar in both cases. Now suppose the crack is cut ahead by a saw under fixed boundary displacements. The non-linear elastic material will readjust its strain pattern to that resulting had the displacements been imposed on a body with the now longer crack, so that a severe strain concentration remains at the tip. Cutting ahead in the elastic-plastic material will produce little additional straining at the new crack tip.

In this study, the node release while keeping the applied load can be viewed as similar to cutting ahead under fixed boundary displacement in the above example. The irreversibility of plastic deformation in the elastic-plastic material used will not increase the peak stress, and it may reduce it.

Curves 6 and 7 in Fig.(4-9b) display the stress distributions for loading points 6 and 7, respectively. At loading point 6 the current crack tip, point B, bears zero stress and at loading point 7 the node just behind the current crack tip closes. The distribution of the residual stresses after loading cycle 8, (curve 8) is similar to curve 1 in Fig.(4-9a) moved forward one element.

#### 4.3.7 Strain distribution

Figures (4-10a) and (4-10b) show the strain distributions at the same loading points as that of the stress distribution for a typical loading cycle (cycle 8). The ordinate represents the strain perpendicular to the crack line,  $\epsilon_{22}$ , which is the dominant component of strain in the plane stress condition. Note that the yield strain of the material used is 0.00115.

Curves 1 and 8 show the distributions of the residual strains after loading cycle 7 or loading cycle 8, respectively. It can be seen that in the wake of the moving crack tip, the residual strain keeps a constant value of about 0.5 percent which is about 5 times yield strain. If Fig.(4-10a) is superimposed on Fig.(4-10b), the area between curve 1 and curve 8 represents the change of residual strain for one loading cycle. This area only involves six elements with the current crack tip at its centre. Curves 2 and 3 which correspond to the opening of the node behind the current crack tip and the current crack-

tip node, respectively, are almost the same. At the top of the loading cycle, the peak strain of curve 4 is about 7 times of the yield strain of the material. After releasing the node, the crack tip is transferred from point A to point B. The peak strain for curve 5 is less than that of curve 4 because of the irreversibility of plastic deformation. Curve 6 shows the strain distribution when the tensile force borne by the current crack tip node, point B, reverses to a compressive one, while curve 7 shows the strain distribution when the node behind the current crack tip has zero displacement during unloading.

#### 4.3.8 Stress-strain history

Another way to observe the changes of stresses and strains during cyclic loading is to study the stress-strain history of a particular material point as the crack tip advances towards it and passes it. see Fig.(4-11). This point is chosen to lie slightly above the crack line, and outside of the initial plastic zone. It is very close to 11<sup>th</sup> node counting from the initial crack tip, i.e. the first Gauss integration point of the 11<sup>th</sup> element. The initial plastic zone size along the crack line encompasses nine elements. The loading cycles, shown below Fig.(4-11), are denoted by the numbers on the cycles, which also represent the corresponding points on the stress-strain relation curve. For example, nine is the loading point at the top of the ninth cycle before releasing the node; nine prime is the loading point at the top of ninth cycle after the node has been released; while nine double prime is the loading point at the end of the ninth cycle. The corresponding positions of these three points can be seen from the stress-strain relation curve of the particular material point.

During the first two or three cycles, the relationship between stresses and strains is linear. Then, the plastic deformation (non-linear relationship) for each cycle increases gradually as the crack tip approaches the particular point. After releasing the node at the 10<sup>th</sup> loading cycle (point 10'), the current crack tip reaches the 11<sup>th</sup> node, or approximately the chosen material point. The crack length does not change during unloading from point 10' to point 10'' and reloading from 10'' to point 11. Considerably more plastic deformation takes place during this process. From loading point 11, the 11<sup>th</sup> node starts to be released while keeping the applied maximum remote stress constant. Consequently, the 11<sup>th</sup> element including the material point will be unloaded from maximum stress level and the next element (element 12) will be stressed at a higher level.

It has been pointed out that the unloading of the 11<sup>th</sup> element and loading of 12<sup>th</sup> element are due to the node release instead of the remote stress change. Displacement of the 11<sup>th</sup> node increases from zero following the decrease of its normal stress, and at the end of the releasing process (point 11'), the node is free with a certain value of displacement and a zero normal stress. Meanwhile the current crack tip is transferred from the 11<sup>th</sup> node to the next node (12<sup>th</sup> node). For the chosen material point near the 11<sup>th</sup> node there is a slight compressive normal stress at the loading point 11' as shown in Fig.(4-11). Following loading point 11', the remote stress decreases to point 11''. The stress-strain relation curve appears as an almost vertical segment at first, which implies that during closing of the opened crack the chosen material point (or node 11) moves down freely. Its strain is not to be changed following the increase of compressive stress.

When the 11<sup>th</sup> node contacts the crack line, the stress-strain relationship appears almost linear until loading point 11''. The curve from point 11'' to point 12 represents the stress-strain relationship of the node just behind the current crack tip during the loading part of cycle. When the 12<sup>th</sup> node is released, the stress-strain curve goes from point 12 to 12' then to 12'' during the unloading part of the cycle. For the next loading cycle (13<sup>th</sup> loading cycle) the change of the stress-strain curve is similar to the last loading cycle, only the range of the change is smaller due to the increased distance from the current crack tip.

It is seen from Fig.(4-11) that the residual stress of the chosen material point at each cycle end increases during first several cycles, then decreases to a minimum value when the crack tip just passes this point. Finally it stabilizes at a certain compressive value following passage of the crack tip. The residual strain of this point increases with cycles until the crack tip reaches it. When the crack tip passes this point, the residual strain also stabilizes to a certain value (about 0.5 percent).

#### 4.3.9 Energy release

Griffith, as early as 1921, proposed the concept of crack energy release after his landmark work on glass rods. The basic idea behind his theory is that if the strain energy released by the strain field after a small advance of a crack is greater than the energy required to create the new fractured surfaces, then the crack will begin to propagate. Irwin and Orowan generalized Griffith's ideas to apply to metals and other engineering materials independently.

Consider an infinite plate of unit thickness that contains a through-thickness crack of length  $2a$  and that is subjected to a uniform tensile stress,  $\sigma$ , applied at infinity. Irwin-Orowan's energy balance equation may be written as

$$\frac{dW}{dt} = \frac{dU}{dt} + \frac{dT}{dt} + \frac{dU_\gamma}{dt} \quad (4-11)$$

where  $W$  = work performed by external forces

$U$  = strain energy of the loaded cracked plate

$T$  = kinetic energy of the whole system

$U_\gamma$  = irreversible consumed energy (surface energy caused by the formation of the crack surfaces)

$t$  = time

Supposing the whole system is under quasi-static (the crack either does not grow or grows stably), then the kinetic energy of the whole system does not change. i.e.  $dT/dt=0$ . By using

$$\frac{d}{dt} = \frac{d}{da} \frac{da}{dt}, \quad (4-12)$$

equation 4-11 can be written as

$$\frac{d(W-U)}{da} = \frac{dU_\gamma}{da} \quad (4-13)$$



In the left hand part of Equation (4-13)  $dW/da$  represents the energy provided by the external work  $W$  per unit crack extension and  $dU/da$  is the increase of strain energy owing to the external work  $dW/da$ . Thus  $dW/da - dU/da$  is the amount of energy that remains available for crack extension. The right hand part,  $dU_\gamma/da$ , represents the surface energy of the crack surfaces. This is the energy needed for the crack to grow.

It should be pointed out that  $dW/da - dU/da$  is the energy release rate,  $G$ , as defined by Griffith. Finally, the relation between the energy release rate  $G$ , and the stress intensity factor  $K_I$ , can be obtained through

$$G = \frac{K_I^2}{E'} \quad (4-14)$$

where  $E' = E$  for plane stress and  $E' = E/(1-\nu^2)$  for plane strain.

In this study the process of releasing a node while keeping the maximum applied stress constant characterizes a course of energy release. As the node at the crack tip is being released, the work is done by the truss elements connecting this node. Following cutting of the truss elements one by one, the tensile force in the remaining truss elements decreases and the displacement of this node increases. The work done is given by

$$W_\gamma = \int_0^{\delta_0} F \cdot d\delta \quad (4-15)$$

where  $\delta$  is the displacement of the node being released and  $\delta_0$  is the value of displacement corresponding to the end of release;  $F$  is the tensile force in truss elements. Note that the

tensile force and the increase of displacement point in opposite directions, so the work done will have a negative sign. Approximately, equation 4-15 can be replaced by

$$W_Y = \sum_i^N F_i \cdot \Delta \delta_i \quad (4-16)$$

where N is the number of the truss elements connecting the node which is being released. The work done by the truss elements permits the crack advance by one element length. thus the energy release rate is

$$G = 2 \frac{W_Y}{L_0} \quad (4-17)$$

where  $L_0$  is the length of one element: the factor of 2 reflects the symmetry of the cracked panel.

As an example, while releasing the node at the top of the first loading cycle the energy release rate by Eq.(4-17) is 161.31 N/m. For the sake of comparison, the energy release rate determined by Eq.(4-14) is 299.14 N/m. The difference between the two values results from the fact that Eq.(4-14) is derived under linear elastic condition while in this finite element analysis the area surrounding the crack tip undergoes appreciable plastic deformation.

#### **4.4 Analysis of crack extension under a constant-amplitude loading and releasing crack-tip nodes at the bottom of each loading cycle**

When a node release technique is used to simulate crack growth, the loading level at which the node will be released should be investigated first.

For monotonic loading various fracture criteria have been established employing special parameters, such as opening angle  $\alpha$  [4-31], stress intensity factor  $K$  [3-24] and the rate of the crack opening displacement  $\dot{\delta}$  [4-32]. These different fracture criteria imply that before releasing a node, the applied stress has reached a relative maximum value.

For cyclic loading, although some criteria such as critical strain crack-growth criterion [4-9], extension stress criterion [4-18] and a critical crack-tip opening displacement  $\delta_c$  [4-29], have been proposed, most researchers choose an arbitrary node-release stress level. Newman [4-8] released nodes at the maximum applied stress in each cycle. Ogura and Ohji [4-33] extended the crack at the applied stress level at which the reaction force at the crack-tip node approached zero. After examining four different node release methods--(i) release at a specified stress, (ii) at about 90% load during unloading, (iii) maintaining the maximum load during release and (iv) at 98% load during loading--Palazotto and Mercer [4-34] suggested that the node should be released with every cycle of loading at 98% of the maximum load. Sehitoglu and his co-workers, including Lalor, Sun and McClung [4-12,13,35 ~ 37], followed the concept advocated by Newman in their studies at first, then they released the crack-tip nodes immediately after attainment of the maximum load. McClung, Thacker and Roy [4-16] highlighted several significant

modifications in their finite element code. The modifications included that the truss elements attached to the crack line nodes were entirely removed because the large stiffness value of truss elements were a source of possible numerical difficulties. At the same time, they found that node release at the maximum load or minimum load gave exactly the same crack opening level in nearly all cases examined, so node release at the maximum load was dropped in favour of releasing the node at minimum load.

It is well known that the crack closure phenomenon is caused by plasticity. (Here, other factors influencing closure, e.g., roughness-induced closure, crack-filling closure and transitional closure will not be discussed.) The position of the loading point at which the crack-tip node is released has a major influence on the strain distribution near the crack tip. When the crack-tip node is released at different loading levels, why should the crack opening stress levels be the same? The purpose of this section is to compare the results obtained by releasing a node at the top of loading cycle (T-release) and at the bottom of loading cycle (B-release).

#### 4.4.1 Crack opening and closing stress levels

All conditions are the same as in Section 4.3 except crack-tip nodes are released at the bottom of the loading cycle instead of at the top of the loading cycle. Crack opening and closing stresses are shown in Fig.(4-12) by using two definitions. The ring symbols and solid symbols represent the opening stresses and the closing stresses for each cycle, using the newly proposed definition in §4.3.2, which judges the crack-tip node directly. The cross symbols indicate the opening stresses in the loading portion and the closing stresses

in the unloading portion by using the old definition which judges the node immediately behind the crack tip. The new definition gives the same level of closing stress and lower opening stress level, comparing with T-release, see Fig.(4-4). That means the new definition is sensitive to the release load point chosen for the crack opening stress level.

As stated by McClung [4-16], when the old definition is used, the B-release gives exactly the same crack opening stress level as that of T-release, only the crack closing level is much lower, see Fig.(4-5). It may be said that the old definition is not sensitive to the release point chosen for the crack opening stress level. However, the above conclusion is premature. What really happened for the B-release will be explained in Section 4.4.3.

#### 4.4.2 Crack profile

A comparison of the crack profiles between T-release and B-release is displayed in Fig.(4-13). The solid lines show the crack profiles after each cycle for T-release, the same as in Fig.(4-8), while the dashed lines indicate the corresponding crack profiles for the B-release scheme. A distinct difference between the crack profiles can be seen: in the advanced portion of the crack the profiles of B-release are larger than that of T-release, and in the original portion of the crack the profiles of T-release are larger. If the displacement of the first node behind the crack tip is defined as CTOD, then CTOD for T-release would be smaller than that for B-release.

#### 4.4.3 Stress distribution

Similar to Figs.(4-9a) and (4-9b) the stress distributions for different loading points of a typical loading cycle (loading cycle 8) are shown in Figs.(4-14a) and (4-14b). The positions of the loading points on the cycle are shown in the upper-right inset of each figure. Loading point 1 is at the end of the seventh loading cycle, with the corresponding residual stress distribution denoted by Curve 1. By comparing this with Curve 1 in Fig.(4-9a), it can be seen that both curves show a similar trend, but the stresses in Element (7) are higher than those in Fig.(4-9a), so that the maximum compressive stress is in Element (6) instead of Element (7). Now, the current crack tip is Point A between Elements (7) and (8), see Fig.(4-14a). Note that during the node release, transferring of the current crack tip from the node between Element (6) and Element (7) to Point A does not cause any stress change. But the residual compressive stresses in front of the current crack tip now have become much smaller, which is very different from those in Fig.(4-9a). It should be pointed out that the residual stresses in Element (6) near the node between Element (6) and Element (7) (or say, the residual stresses at the last two Gauss integration points of Element (6)) are exactly the same in both Figs.(4-9a) and (4-14a). This is why the node immediately behind the crack tip opens at the same stress level for both T-release and B-release, as pointed out by McClung et al. [4-16].

Loading point 2 corresponds to when the compressive stress borne by the current crack-tip node (Point A) becomes tensile (or simply, the current crack-tip node opens). It can be seen from Curve 2 that the current crack-tip node starts to be stretched, while the node immediately behind the crack tip still sustains a compressive stress, and its displacement should be zero.

As the load is continuously increased to Point 3, the node immediately behind the crack tip opens; this corresponds to Curve 3 which indicates that at this instant the current crack-tip node carries a tensile stress of about 130 MPa which is far more than the applied maximum stress. Transferring the current crack tip forward at the minimum stress causes smaller residual compressive stresses in front of the crack tip, and therefore the current crack-tip node opens before the node immediately behind the crack tip; this suggests that using the B-release scheme to determine the crack opening stress is not a proper procedure.

When loading to Point 4, the top of loading cycle 8, Element (8) as the first element in front of the crack tip is tensioned to the maximum load for the first time. This is not like Element (8) in Fig.(4-9a), where Element (8) as the first element in front of the crack tip has already been tensioned for second time when loading to the top of loading cycle 8. Curve 4 displays a rising peak stress in Element (8) because the corresponding residual compressive stress in Element (8) is small.

Unloading begins after loading point 4. Note that the current crack tip is still at Point A during the unloading portion of loading cycle 8. At Point 5 the tensile stress sustained by the current crack tip (Point A) changes to a compressive one. Curve 5 in Fig.(4-14b) shows that the Gauss integration points near Point A have sustained compressive stresses. Point 5 in Fig.(4-14b) and Point 6 in Fig.(4-9b) have the same stress level, because the stress distributions in front of the current crack tip at the top of the loading cycle before unloading are the same.

At Point 6, the node immediately behind the current crack tip contacts the crack line.

Point 6 in Fig.(4-14b) is lower than corresponding Point 7 in Fig.(4-9b) because the displacement of the node immediately behind the current crack tip in Fig.(4-14b) is higher than that of the corresponding node in Fig.(4-9b). It can be seen from Curve 6 in Fig.(4-14b) that by the time the node immediately behind the current crack tip closes, the current crack-tip node bears quite a large compressive stress.

At the end of loading cycle 8, Curve 7 shows the same residual stress distribution as Curve 1, only moved forward by one element.

#### 4.4.4 Strain distribution

The strain distributions for seven special loading points of a typical loading cycle (Cycle 8) are drawn in Figs.(4-15a) and (4-15b). Comparing these with Figs.(4-10a) and (4-10b) where strain distributions are illustrated for the T-release scheme, it is noted that the trends are the same for loading and unloading. However, the residual strains displayed by Curve 1 and Curve 7 are much less than those in Figs.(4-10a) and (4-10b). This is because the first element in front of the current crack tip during propagating of the crack will be twice stretched to the maximum extent for the T-release scheme, while only once for the B-release scheme. It is apparent that due to the large difference in residual strains a band of residual tensile deformation left in the wake of an advancing crack tip will cause different crack-opening stress levels.

#### 4.4.5 Crack opening stress vs closing stress

Elber chose the crack opening stress to define the effective stress range which directly



influences crack growth rates. This was based on the assumption that the crack closure stress would always be higher than the crack opening stress [4-1]. Numerous researchers have assumed that the crack opening stress and the crack closing stress are almost the same, so they have measured the closure load only. Flek [4-38] pointed out that in practice the difference between the closure load and opening load is often less than the scatter associated with closure measurements. Schijve in his keynote review [4-39] stated that the crack opening and closure stresses can be different, but the difference is small and perhaps negligible.

In the present finite element calculation, different definitions of the crack opening and closure result in different stress values. Using the newly proposed definition, monitoring the crack-tip node directly, the crack closure stress is slightly higher than the crack opening stress. The difference between the crack opening and closure stresses is less than 1 per cent of the amplitude of the loading cycle. This is because after releasing the node at the top of loading cycle, the peak stress in front of the current crack tip is slightly higher than before, see Figs.(4-9a) and (4-9b). Thus, unloading starts from a higher stress level than that reached during loading. When the previous definition based on the node immediately behind the crack tip is used, the crack closing stress is lower than the crack opening stress by about 7 per cent of the loading cycle amplitude. Fatigue cracks, generally, open progressively towards the crack tip and close progressively from the crack tip. When the previous definition is used in conjunction with the nodes released at the bottom of a loading cycle, the crack closing stress is much lower than the crack opening stress. The difference is about 19 per cent of the loading cycle amplitude.

#### 4.5 Analysis of a stationary crack

For a stationary crack, Rice [4-40] had excluded the occurrence of crack closure under cyclic tension loading in the stress analysis of the crack tip. He claimed that since a residual displacement remains at the crack tip after the load is removed, the crack surfaces remain propped apart by the plastic flow. In an earlier finite element analysis [4-41] no crack closure was indicated for a stationary crack under cyclic tension loading, even after a single overload. In it, the displacements of nodes on the crack surface were employed to judge the closure of the crack. The problem posed here is: can a stationary crack always have a potential capability to propagate during a cyclic loading? The newly proposed definition about crack closure can answer this question.

##### 4.5.1 Crack opening and closing stresses

The newly proposed definition is used to determine the crack opening and closing stresses, while keeping the initial length of the crack in Section 4.3 unchanged during the same cyclic loading. The results are shown in Fig.(4-16). The ring symbols indicate the stresses at which the compressive stress sustained by the crack-tip node is changing to a tensile one, in other words, stresses at which the crack tip begins to open during loading. The solid symbols indicate the stresses at which the tensile stress sustained by the crack-tip node becomes compressive, or the stress levels at which the crack tip begins to close during unloading. The crack closing stress at the first loading cycle is the same

as that in Fig.(4-4). Then the crack closing stress increases until it stabilizes at the seventh cycle. The crack opening stress is found to stabilize after six cycles. The stable value of crack opening stress is identical to the value at which the growing crack reaches the relative stability in Fig.(4-4).

#### 4.5.2 Crack profile

Profiles of the stationary crack for the maximum load (solid lines) and the minimum load (dashed lines) during a cycle are shown in Fig.(4-17). During cyclic loading, the displacements of nodes on the crack surface increase for both the maximum and minimum loads of the cycle. It should be pointed out that the crack profiles do not tend to stabilize, though the rate of change becomes small. This characterizes cyclic blunting of the crack.

### 4.6 Analysis for a single overload

#### 4.6.1 Review of the experimental results

So far, the discussion has been limited to constant amplitude cyclic loading. Since the service-load experienced by structures may not be of a constant amplitude type, the predictions of fatigue crack propagation under variable amplitude loading should also be investigated.

In the early 1960's, experimental work on aircraft flight simulation loading had shown the importance of interaction effects. As first described by Schijve [4-42], the application

of a single tensile overload results primarily in a delayed retardation in crack growth rates. Von Euw et al. [4-43] reported that the minimum fatigue crack propagation rate did not occur immediately following the application of the overload. Instead, the lowest growth rate was reached after the crack had extended over approximately one eighth to one quarter of the total overload plastic zone. Thus, the crack growth retardation is delayed for a while following an overload application. The concept of crack closure was used by Elber [4-2] to explain the delayed retardation of the crack growth after a single overload. In Fig. 10 of ref. [4-2], however, the crack opening stress of the loading cycle immediately after the overload cycle was much lower than the stabilized crack opening stress reached before the overload cycle. This implies that before the delayed retardation there is an acceleration in the crack growth rate. It follows that Elber's explanation of clamping action applied on the region near crack-tip by surrounding material cannot describe the brief acceleration of crack growth. Systematic observations on crack closure after an overload were reported by Paris and Hermann [4-44] whose upper opening loads (crack opening stress) increased dramatically immediately after the overload cycle. The delay phenomenon of retardation was evident, but no acceleration of crack growth was observed. Ward-Close and Ritchie [4-45], Word-Close, Blom and Ritchie [4-46] described the specific transient response after the application of a single tensile overload. This response indicates several distinct stages: before the overload there is steady-state crack growth at baseline levels; during the overload cycle, the magnitude of crack growth increment is about several ten times larger than that expected for constant amplitude cycling; following the overload cycle, there invariably is an acceleration in growth rates

relative to baseline steady-state levels, followed by delayed retardation and an eventual return to steady-state pre-overload behaviour. They attributed the acceleration to the removal or reduction of crack closure along the crack length by the overload. The removal of closure behind the pre-overload crack tip may be offset by closure generated by the ductile crack-growth increment formed by the overload cycle, in which case the acceleration may be reduced or not present. Carlson, Kardomateas and Bates [4-47] explained that the brief crack growth acceleration period results from the crack tip stretching, which reduces closure contact pressures between previously formed obstructions, and effectively increases the stress intensity factor range. The experimental results by Kumar [4-48] show that after the application of a single overload cycle, the crack closure load suddenly increases in subsequent loading cycles. Yet in more recent experiments by Goel and Chand [4-49] no crack growth rate acceleration was observed. Thus, the experimental evidence regarding the crack growth rate immediately following an overload is not consistent.

#### 4.6.2 Simulation procedure

When a node is released at each cycle to simulate the crack growth during cyclic loading, a steady state of crack growth rate is implied. Therefore, using such a node release technique in the finite element analysis to examine the crack closure for a variable amplitude loading would be an approximation. In such an approach, the focus should be on the relationship between the crack opening stresses and the residual stresses or the plastic deformation following the crack growth.

A procedure will be outlined to simulate a situation when a single overload is applied on the centre cracked panel during the constant amplitude cyclic loading. The same conditions as described in Section 4.3 are retained except for the application of a single 100% overload at the eighth cycle, where the crack opening stress has initially stabilized. Two methods are used to determine the magnitude of the crack growth increment at the top of the overload cycle. The first is to compare the plastic zone sizes caused by loading at the top of the constant amplitude cycle with that at the top of the overload cycle. The second is to compare the CTOD defined by the displacement of the node immediately behind the crack tip. The plastic zone size for loading at the top of the overload cycle is 4.67 times as large as the one for loading at the top of the constant amplitude cycle, while the CTOD of the former is 4.69 times that of the latter. So, at the top of the overload cycle 5 nodes will be released successively to simulate the increment of crack growth due to the overload. After that, the scheme of releasing one node per cycle is recovered.

#### 4.6.3 Crack opening and closing stresses

The crack opening stresses are represented by ring symbols while those for the crack closure are shown by solid symbols in Fig.(4-18) for a constant amplitude cyclic loading with a single overload cycle at the eighth cycle. Here the newly proposed definition is employed for crack opening and closing stresses; that is, the current crack-tip node itself instead of the node immediately behind the current crack tip is monitored for the crack opening or closing. Before the overload cycle, the crack opening and closing stresses

have already reached relative stability. During the overload cycle, only the closing stress rises sharply. After the overload cycle both the opening stress and closing stress increase from the stabilized level with the opening stress higher than the closing stress. Then both stresses decrease gradually to the previous stabilized level at the thirteenth cycle, continue to decrease to a minimum value at the sixteenth cycle, then return to the stabilized level gradually with slightly higher closing stress than opening stress.

When Paris' crack growth law modified by Elber, see Eq.4-3, is used to determine the crack growth rate, Figure (4-18) will imply a retardation in crack growth rates after the application of a single overload. The delay of the retardation is not clearly shown, although the crack opening stresses at the first two cycles after the overload cycle are almost the same. Note that during the overload cycle there is an acceleration in crack growth rates relative to the stabilized level because 5 nodes were released at the top of the overload cycle instead of one node. Following the retardation in crack growth rates, numerical calculation also displays a small acceleration Fig.(4-18), about which no experimental results are reported.

After the application of a single overload the crack neither opens progressively to the crack tip nor closes progressively from the crack tip. The crack opening and closing stresses determined according to the definition used by Newman and McClung, see Section 4.3.2, are shown in Fig.(4-19) by the cross symbols in the loading portion and the unloading portion of cycles respectively. Both the crack opening and closing stresses increase instantaneously, then decrease slowly as the current crack tip moves away from the overload residual field. In fact, it is the last node released at the top of the overload

cycle that still controls the crack opening and closing stresses. Note that when loading to a larger stress value but less than the opening stress, only nodes released at the top of the overload cycle keep their displacements at zero because of greater plastic tensile deformation in that area; the rest of the nodes on the crack surface, in front or behind that area, have already opened. Especially, the current crack-tip node has sustained a rather large tensile stress. At this moment, it would not be reasonable that the crack is still considered being close.

When the node immediately behind the current crack tip is always used to determine the crack opening or closing, the crack opening stresses represented by open squares and the crack closing stresses represented by filled squares are also displayed in Fig.(4-19). The general trend of the crack opening and closing stresses is similar to that of Fig.(4-18), when judging the crack-tip node itself. However, the delay of the retardation in crack growth rates is now clearly manifested.

#### 4.6.4 Crack profiles

The crack profiles of several cycles including the overload cycle are drawn in Fig.(4-20). The displacements of the nodes on the crack surface in the Y-direction are plotted as functions of the coordinate location,  $R$ . Note that although both units are in millimetre, the difference of the scales is about 87 times. The original point is the initial crack tip. The loading points corresponding to each curve are shown in the inset at the upper-right hand corner. Curves 1 and 2 represent the crack opening displacements before and after releasing the node at the top of the cycle before the overload cycle. At



the bottom of this cycle the displacements of nodes on the propagated crack surface are zero, but on the initial crack surface have some value (not plotted). Corresponding to loading point 3 and 4 at the top of the overload cycle, Curves 3 and 4 show the displacements before and after releasing 5 nodes. It can be seen from Curve 3 that the crack is blunted by the overload, and the CTOD defined by the node immediately behind the crack tip is about 5 times the CTOD for Curve 1, which is in a stable state for constant amplitude cyclic loading. At the bottom of the overload cycle, loading point 5, the displacements of the nodes released at the top of the overload cycle are zero, but the displacements of the nodes released before the overload cycle are non-zero and have larger values, see Curve 5. The residual displacements of the nodes released before the overload cycle are caused by the crack-tip blunting during the overload. After the overload cycle at loading points 6-10, the tops of the following loading cycles before releasing the node, the crack profiles display certain characteristics: the CTOD will increase gradually from a very small value to the stabilized value expected for the constant amplitude cyclic loading; at the location of the first node released during the overload cycle the crack profiles have a sudden change; at the last node released during the overload cycle the crack profiles take a concave shape; at the bottoms of the following loading cycles the crack profiles are similar to Curve 5. These characteristics imply that for the following loading cycles, the node last released for the overload cycle will first close during the unloading portion of the cycles and last open during the loading portion of the cycles.

#### 4.6.5 Stress distribution

The stress distributions at the top and the bottom of three loading cycles (before, during and after the overload cycle) are shown in Fig.(4-21). Curves 1 and 2 which are the same as Curves 4 and 8 in Fig.(4-9a) and Fig.(4-9b), show the distributions of the stress component  $\sigma_{22}$  at the top and the bottom of a typical loading cycle for the constant amplitude cyclic loading. At the top of the overload cycle before releasing the nodes, the peak stress increases by about 270 MPa over the last cycle. (For simplicity, stress distribution curves are drawn as continuous curves in the region near the current crack tip.) After releasing 5 nodes, the peak stress of Curve 4 becomes slightly lower than the previous value because of the irreversibility of the larger plastic deformation caused by the overload. When unloading from Point 4, the crack closes at much higher stress level also due to the larger plastic deformation. At the bottom of the overload cycle, Curve 5 corresponding to loading point 5 shows the distribution of the residual stress. It can be seen that compressive residual stresses in the region of five released nodes are of fairly large magnitude. The compressive residual stress decreases in magnitude comparing to Curve 2 at the wake of the pre-overload crack tip. However, about 5 to 6 elements in front of the current crack tip, the compressive residual stress increases in magnitude. When loading again from Point 5, the clamping action of the elastic material surrounding the plastic zone requires a larger, externally applied stress to open the crack, but at the same time the larger compressive residual stress at the current crack tip leads to a small drop of the crack opening stress level. It is the larger compressive residual stress that causes the delay of the retardation in crack growth rates.

Curve 6 shows the stress distribution at loading point 6, the top of the cycle immediately after the overload cycle (before releasing the node). The difference between Curve 1 and Curve 6 is quite apparent. The peak stress at the current crack tip is much lower, even less than the yield stress of the material. Meanwhile, the effective stress range  $\Delta\sigma_{\text{eff}}$  for this cycle is small. This suggests that there will be a retardation in crack growth rates.

If the current crack-tip node was not released at the top of this cycle, the stress distribution at the top for next cycle would be the same as Curve 6; and the opening and closing stresses for the next cycle would also be the same as those of this cycle. This is because the plastic deformation and the residual stress at the current crack tip do not change.

At loading point 7, the stress distribution is indicated by Curve 7 which coincides with Curve 5. This also explains why when loading to the top of the cycle next to the overload cycle, the stress peak at the current crack tip does not reach the yield stress of the material. For the following several cycles, the stress peak of each cycle rises gradually, but the residual stress curve at the bottom of each cycle is almost the same as Curve 5. During this period the plastic deformation caused by the overload plays a main role in the effect on the crack opening stress level. Since the plastic deformation reduces along with the moving away of the current crack tip from the overload region, see Fig.(4-22a), the crack opening stress decreases until the stabilized crack opening stress level for the constant amplitude cyclic loading. The stage of the delayed retardation in crack growth rates after a single overload finishes.

But the decrease of the crack opening stress does not stop. In the following two or three cycles the crack opening stress reduces continuously by a small amount, then rises gradually to the stabilized crack opening stress level again. No experimental report about this stage has been seen, but in numerical analysis this stage must exist. During the overload the material points in front of the current crack tip within about 5 elements undergo larger tensile stresses than the stable peak stress for the constant amplitude cyclic loading, see Fig.(4-21a). When the current crack tip approaches, the stresses experienced by these points are less than the stresses reached by these points during the overload. So, no new plastic deformation is produced: the residual stresses are the same with that caused by the overload. But by this time the current crack tip has already advanced to the region where the residual plastic deformation is less than that caused by the constant amplitude cyclic loading, see the residual strain distribution in Fig.(4-22a). The decrease of the plastic deformation and the increase of the residual stress results in the continuous decrease of the crack opening stress in the following two or three cycles. When the peak stress at the current crack tip in each following cycle exceeds the value reached by the same point during the overload, plastic deformation will be produced and increase gradually. The crack opening stress rises slowly until the stabilized level.

The residual stress distributions for different loading points--at the end of the cycle before the overload cycle, at the end of the overload cycle and at the end of the cycle after 12 cycles from the overload cycle--are shown by Fig.(4-21b) as Curves 1, 2 and 3. Here, Curves 1 and 2 are the same as Curves 2 and 5 in Fig.(4-21a). It is apparent from Curve 3 that after the overload the residual stress rises; in other words the

compressive residual stress decreases in magnitude, which lasts about 7 or 8 elements. Then the residual stress returns gradually to the stable level for the constant amplitude cyclic loading.

#### 4.6.6 Strain distribution

Similar to the stress distributions, the strain distributions for the same points of three loading cycles are shown in Fig.(4-22a). Curves 1 and 2 corresponds to the top and the bottom of the loading cycle just before the overload cycle, respectively. The residual plastic strains behind the current crack tip in Curve 2 are about 0.5 per cent as shown in Fig.(4-10a) for a typical loading cycle under constant amplitude loading. At the top of the overload cycle before releasing the nodes. Curve 3 indicates a strain peak at the current crack tip which is about 4 times the strain peak in Curve 1. But the strains in front of the current crack tip decrease rapidly. After releasing 5 nodes, Curve 4 displays two strain peaks corresponding to the beginning and the end of releasing the node. The first strain peak is less than the strain peak in Curve 3 because of unloading of that element when the current crack tip passes by, and the second strain peak is less than that in Curve 3 due to the irreversibility of plastic deformation. Curve 5 shows the residual strain distribution after the overload cycle. A region of large plastic deformation corresponding to the nodes released at the top of the overload cycle is left over. It should be noted, however, that in front of the current crack tip the effect of the large plastic deformation only lasts three or four elements after comparing with Curve 2. Curve 6 corresponding to the top of the cycle just after the overload cycle is surrounded by Curve

4 without the strain peak at the current crack tip. That means that only elastic deformation is produced for the loading portion of this cycle. At the bottom of the cycle just after the overload cycle, Curve 7 exactly coincides with Curve 5, but the current crack tip has already advanced one element length.

In the following 5 loading cycles the strain peak at the current crack tip for each cycle is not beyond Curve 4 and the residual strain distributions basically coincide with Curve 5. By this time the residual strain at the current crack tip is already lower than the stabilized residual strain level for the constant amplitude cyclic loading. This forces the crack opening stress to continue decreasing instead of stopping at the stabilized crack opening stress level. When the current crack tip continues advancing during the cyclic loading, the strain peak at the current crack tip will exceed Curve 4 and the peak increases gradually for each cycle. The residual strain at the current crack tip also rises gradually after reaching a minimum value. Consequently, the crack opening stress goes up progressively after it decreases a small amount from the stabilized crack opening level, and finally returns to the stable level.

The residual strain distributions shown by Curves 1, 2 and 3 are given by Fig.(4-22b) for three loading points: at the end of the cycle just before the overload cycle, at the end of the overload cycle and at the end of the cycle after 12 cycles from the overload cycle. Curves 1 and 2 are the same as Curves 2 and 5 in Fig.(4-22a), respectively. The first half of Curve 3 coincides with Curve 2, and the second half of Curve 3 goes up from Curve 2 by several degrees to the position of the current crack tip. Note that the positions of the current crack tips for Curves 1, 2 and 3 are 0.12 mm, 0.24 mm and 0.46

mm from the initial crack tip. The farther the current crack tip moves away from the overload, the higher is the residual strain at the position of the current crack tip, until it returns to the stabilized level for the constant amplitude cyclic loading. It can be concluded from Curve 3 that after the overload which causes a region of large residual plastic deformation there will be a region in which residual plastic deformation reduces and becomes lower than the stabilized level for the constant amplitude cyclic loading. This leads to lower crack opening stress than the stabilized level.

#### **4.7 Analysis for a single underload**

##### **4.7.1 Introduction**

Another type of variable amplitude cyclic loading is the constant amplitude cyclic loading with a single underload (or a compressive overload), which is also a common occurrence in service, particularly for aerospace applications. Relative to tensile overloads, much less work has been done on the study of underload. Topper and Yu [4-50] concluded that large compressive overloads (the absolute ratio of the single compressive overload divided by the maximum load in cycles is 336%) decreased the crack opening stress to below zero and the local strain at the crack tip decreased with compressive loading. But some other researchers, such as Zwerneman and Frank [4-51], claimed that isolated underload has no effect on crack growth rate. In a study by Zaiken and Ritchie [4-52], application of 100 to 300% single compressive overload (corresponding to one to three times the peak tensile loads) were observed to have no

effect on crack closure or crack growth of arrested cracks at the threshold. Only the application of 500% compressive overload caused immediate propagation of the arrested cracks.

To study the effects of a single underload, the prior loading condition is kept the same as in Section 4.3. except for a 200% underload applied at the end of the seventh cycle.

#### 4.7.2 Crack opening and closing stresses

The results of applying a constant amplitude loading with a 200% single underload are shown in Fig.(4-23). The crack opening and closing stresses for the first seven cycles are identical to those previously depicted in Fig.(4-4). After the seventh cycle, a compressive overload is applied to the extent that the far field stress is equal  $-0.6\sigma_{0c}$ . At the minimum load the current crack tip does not move, i.e. no node is released. On the eighth cycle the crack tip opens at a stress which is about 2.2% of  $\sigma_{0c}$  lower than the previous opening stress in the seventh cycle. During unloading of the eighth cycle the closing stress is almost the same as that in the seventh cycle. In the following cycles the crack opening and closing stresses return to the levels as if no compressive overload had happened. Therefore, the effect of the 200% compressive overload ( $\sigma^{\infty}_{\text{underload}} = -0.6\sigma_{0c}$ ) on the crack opening and closing stresses is small.

When a larger compressive overload, 300% of the peak tensile loads ( $\sigma^{\infty}_{\text{underload}} = -0.9\sigma_{0c}$ ), is applied after the seventh cycle, the crack opening stress for the eighth cycle is about 3.9% of  $\sigma_{0c}$  lower than the previous opening stress in the seventh cycle. The cross symbols in Fig.(4-23) represent the different opening and closing stresses for the



loading and unloading portions, respectively. It is evident that the effect of a compressive overload is far less than that of a tensile overload on the crack opening and closing stresses.

#### 4.7.3 Crack profiles

A few crack profiles corresponding to the top of the loading cycles prior to and after the compressive overload are shown in Fig.(4-24). Different profiles are obtained before and after the node has been released for one top. The numbers used to distinguish the profiles are displayed on the inset at the upper-right hand corner of the figure. It can be seen that before and after the compressive overload, the two profiles corresponding to the adjacent two cycles (the first profile is for the first cycle after releasing node: the second one is for the second cycle before releasing node) almost coincide except for the node just behind the current crack tip. The compressive overload, however, results in a slight deviation between Profiles 6 from 5, i.e. the displacements of the nodes on the crack surface for loading point 6 are higher than those for loading point 5. That means the compressive overload reduces the residual tensile plastic deformation caused by the constant amplitude cyclic loading.

At the end of any cycle, including at the compressive overload, the crack fully closed. However, it should be pointed out that the node, as the crack tip during applying the compressive overload, will never contact the crack line after the single compressive overload, i.e. the displacement of this node will be always greater than zero for the following cyclic loading.

#### 4.7.4 Stress distribution

The stress distributions for five loading points near the compressive overload are shown in Fig.(4-25). Curves 1 and 2 correspond to the top of the seventh cycle before releasing the node (Loading point 1) and the end of the seventh cycle (Loading point 2). They are identical to those shown previously in Fig.(4-21a). Before Loading point 2 the crack has already fully closed. During the compressive loading there is no stress concentration at the crack tip, thus Curve 3 corresponding to the maximum compressive load (Loading point 3) looks like Curve 2 but with a superposed stress equal to the applied remote stress between Loading points 2 and 3. When comparing Curves 2 and 4, i.e. the residual stress distributions before and after the compressive overload, it is noted that the difference is small and it is located near the current crack tip. The higher residual stress magnitude at the current crack tip in Curve 4 and the reduced residual tensile plastic deformation, see Fig.(4-26), both contribute to the decrease of the crack opening stress. When loading to Point 5, Curve 5 is almost the same as Curve 1 advanced by one element.

#### 4.7.5 Strain distribution

For the same five loading points the strain distributions are shown in Fig.(4-26). Curves 1 and 2 display respectively the strain distributions at the maximum load before releasing the node and at the bottom of a typical cycle for the constant amplitude cyclic loading, as shown previously in Fig.(2-22a). It can be seen from Curve 2 that about 0.5 per cent of residual strain is left behind the current crack tip. During compressive loading

no stress concentration occurs. Curve 3 for the maximum compressive load is the same as Curve 2, except for a superimposed compressive strain. The reduction of the strain near the current crack tip is slightly larger than that at other places. When the applied remote stress returns to zero at Point 4, the small difference at the region near the current crack tip between Curve 4 and Curve 2 indicates that the change of plastic deformation caused by the compressive overload is insignificant. This confirms that a 200% compressive overload results in a small decrease in the crack opening stress level. At Loading point 5 the material points near the current crack tip have slightly greater strains than those at Loading point 1. This is because before returning to the maximum load (Loading point 5) the crack-tip region sustained a larger compressive stress.

#### **4.8 Analysis for compression-compression cyclic loading**

##### **4.8.1 Introduction**

Fatigue crack growth under tension-tension cyclic loading has been extensively studied and documented. Under tensile loading, there is a stress concentration at the crack tip. It is this concentration that leads to the plastic tensile deformation which influences the opening and closing of the crack. At a crack tip the stress concentration induced by compressive loading is small. For a mathematical crack, as used in the previous sections, a compressive loading hardly produces stress concentration at the crack tip. Such a crack keeps closing during compression-compression cyclic loading where it is assumed that no crack growth occurs. For a notch however, experimental evidence indicates that a far-

field cyclic compressive loading can influence not only the initiation of a crack from the root of the notch , but also its propagation rates [4-53,54,55]. A crack can initiate and propagate from the root of notches or from geometric defects in a material subjected to remotely applied cyclic compressive loads because the compressive loads can cause a stress concentration at the root of a notch. When loading to the maximum compressive load, a compressive plastic zone is generated due to the stress concentration. Upon unloading to the minimum compressive load, the elastic material surrounding this compressive plastic zone tends to stretch the zone from all directions, thus causing tensile residual stresses. Fatigue cracks may initiate and grow due to the presence of a tensile residual stress field.

The present study is directed towards finding the crack opening and closing stresses and the total distance of crack growth, numerically. Attention is focused on the change of stress and strain components during the compressive-compressive cyclic loading.

#### 4.8.2 Numerical simulation

The finite element mesh shown in Fig.(4-1) remains the same except that the crack is replaced by a notch with 0.12 mm width and  $54^\circ$  opening angle. Figure (4-27) shows the mesh for a centre region near the notch root. The same material whose monotonic and cyclic stress-strain curves are shown in Fig.(4-2) is employed. Fully compressive cyclic loads are imposed on the centre-notched panel. The maximum applied stress, or minimum applied compressive stress, is zero. In order to determine the minimum applied stress, or maximum applied compressive stress, the stresses for different ratios of the far-

field applied compressive stresses over the cyclic yield stress of the material are examined. For the minimum applied stresses  $S_{\min} = -0.4\sigma_{oc}$  and  $S_{\min} = -0.5\sigma_{oc}$ , the stress distributions and the plastic zones at the minimum and maximum applied stresses are depicted in Fig.(4-28) by the dashed and the solid lines, respectively. When loading to  $-0.4\sigma_{oc}$  the compressive stress at the root of the notch is about -2.9 times of the cyclic yield stress; the monotonic plastic-zone size is about 0.32 mm (only half of the plastic zone is shown in the figure). Loading to  $-0.5\sigma_{oc}$  the corresponding values are about -3.0 times and 0.52 mm. At this time, the deformation of the notch itself is small: the displacement of the node at the middle of the notch flank is -0.0046 mm, far away from the connection of two flanks of the notch. It is seen that the response of the material under a monotonic compressive loading is identical to that under a monotonic tensile loading, only the positive sign is changed to negative. When unloading to zero, the minimum compressive load, the root of the notch is subjected to the residual tensile stress of 346.38 MPa for  $S_{\min} = -0.4\sigma_{oc}$ , and 404.31 MPa for  $S_{\min} = -0.5\sigma_{oc}$ . The reversed plastic zone is about two third of an element (0.013 mm), or is about two elements (0.04 mm) for the different  $S_{\min}$ . Relative to the monotonic plastic zones, the reversed plastic zones are quite small. In Fig.8 of reference [4-55] by Aswath et al. the reversed plastic zones, or cyclic plastic zones were greater relative to the monotonic plastic zones for the different loading levels, because an isotropic strain hardening model was used in their finite element analysis. Note that the reversed plastic zone is generated based on the larger permanent compressive deformation of the material near the notch root. The tensile deformation of the material induced by the surrounding material is not

sufficient to counteract the permanent compressive deformation caused by the applied maximum compressive stress, see Fig.(4-31).

It is to be noted that no crack growth criterion is used in this study. however, the initiation of a crack at the root of a notch is assumed to take place under a large residual tensile stress and the reversed plastic zone should be greater than one element. This is required because the crack propagation through crack-tip node release at each cycle is to be kept in the reversed plastic zone. Therefore, the far field stress of  $-0.5\sigma_{\infty}$  is chosen as the minimum applied stress for the constant amplitude compressive cyclic loading. At the end of each cycle the node at the root of the notch or at an advancing crack tip will be released. When the reversed plastic zone size is less than one element during the loading, the release of the crack-tip node will cease and the crack is considered having arrested.

#### 4.8.3 Crack opening and closing stresses

For the constant amplitude compressive loading with  $S_{\min} = -0.5\sigma_{\infty}$ , the crack opening and closing stresses are plotted in Fig.(4-29) by the ring and solid symbols, respectively. The ring on the first cycle denotes that the node at the root of the notch starts to bear a tensile stress during unloading, though the far-field applied stress is compressive with a magnitude of -53 MPa. After the first cycle, the crack opening and closing stresses are obtained by observing the positive or negative stresses of the node at the current crack tip. The opening stress increases cycle by cycle starting from the second cycle. This implies that the effective stress range defined by Elber reduces gradually. The crack

closing stress decreases slightly for the first three cycles, and then increases gradually, remaining higher than the corresponding opening stress. During the 11<sup>th</sup> loading cycle, the crack closes at an applied compressive stress of -17 MPa and then opens at -18 MPa. By this time, the effective stress range has decreased to 34% of the original value. At the end of the 11<sup>th</sup> loading cycle the reversed plastic zone is less than one element. Therefore, the crack-tip node release is no longer carried out and the crack is assumed to have arrested. The total distance that crack has propagated is about 0.20 mm.

If the definition used by Newman and McClung is employed to determine the crack opening and closing stresses, the same trend is observed. The cross symbols in Fig.(4-30) represent the crack opening stresses in the unloading portion of each cycle and the closing stresses in the loading portion of each cycle when using Newman's definition. For the sake of comparison the values obtained by the proposed definition also are shown in Fig.(4-30) as shown in Fig.(4-29). Note that no crack opening and closing stresses in the first cycle can be determined using Newman's definition.

The crack opening stress increases until the crack arrests with the total propagating distance of 0.2 mm, while the compressive plastic-zone size caused by the first loading cycle is about 0.52 mm. This indicates that there is no apparent relationship between the crack opening stress and the monotonic plastic zone size.

#### 4.8.4 Stress distribution

In order to understand the change of stresses at the notch root region during the compression-compression cyclic loading, the normal stress,  $\sigma_{22}$ , distributions at the

minimum and maximum applied compressive stresses for different loading cycles are plotted in Fig.(4-31) with the root of the notch as the origin of the coordinate. Also, the stresses at the root of the notch and each advancing crack tip are shown by two groups of solid dots for the minimum and maximum applied stresses of each loading cycle. The dashed lines represent the stress distributions for the first cycle as was shown in Fig.(4-28) by solid lines. Note that these stress distributions indicate the effect of the notch under applied loads only; the release of the notch-root node, or in other words, the crack initiation has not been taken into account. When loading to the maximum applied compressive stress, a large compressive plastic zone is generated. While unloading to the minimum applied compressive stress (zero in this case) a tensile stress region at the root of the notch is formed by stretching the material surrounding the compressive plastic zone. Obviously a large tensile stress at the root of the notch will initiate a crack.

The solid lines represent the stress distributions at the 8<sup>th</sup> cycle at the maximum and minimum applied compressive stresses. The stress distribution at the maximum applied compressive stress is similar to that for the first cycle: it only decreases slightly in front of the current crack tip and increases slightly with a saw tooth shape in the wake of the tip. The minimum stress is still at the root of the notch instead of the current crack tip. The compressive plastic zone is still at the front of the notch root and it expands by only one element. This implies that advancing of the crack tip does not change the range of compressive plastic deformation which is caused by the stress concentration of the notch under the applied compressive stresses. The stress at each advancing crack tip is shown by individual solid dots and it initially increases, but the rate of the increase slows down



gradually as the crack tip grows away from the root of the notch. The stress distribution at the minimum applied compressive stress has a tensile peak value at the current crack tip which causes continuous crack growth. The tensile peak stress for each loading cycle is displayed by another group of individual solid dots. The tensile peak stress has a jump between the first and the second loading cycle, because the stress concentration is caused by the notch for the first cycle, and by the crack for the second cycle during tensioning. Then the tensile peak stress decreases gradually till the crack arrests. The stress values for the nodes behind the current crack tip are close to zero because these nodes remain inside the compressive plastic zone; however, they can displace during the unloading process.

#### 4.8.5 Strain distribution

The normal strain  $\epsilon_{22}$  distribution at the maximum and minimum applied compressive stresses for the first cycle (dashed lines) and the 8<sup>th</sup> cycle (solid lines) are displayed in Fig.(4-32). The strains at the root of the notch and each advancing crack tip are also shown by two groups of individual solid dots for the maximum and minimum applied compressive stresses during each loading cycle. Several characteristics of strain distribution can be seen in Fig.(4-32). At the maximum applied compressive stress during the first cycle, the strains vary significantly in one third of the plastic-zone size near the root of the notch, and then remain almost constant in the rest of the zone. At the minimum applied compressive stress of the first cycle, the strains ahead of the notch-root remain compressive although a tensile stress region is formed there by the stretch of the

surrounding material, see Fig.(4-31). Following cyclic loading the normal strain at each advancing crack tip increases gradually at the maximum applied compressive stress, while at minimum applied compressive stress it increases to a certain value after 5 cycles then decreases progressively. This leads to a reduction of the strain range at the advancing crack tip with the crack growth. It can be concluded that when the strain range reduces to a critical value, a crack arrest occurs. It should be pointed out that the strains ahead of the notch root decrease during the whole cyclic loading.

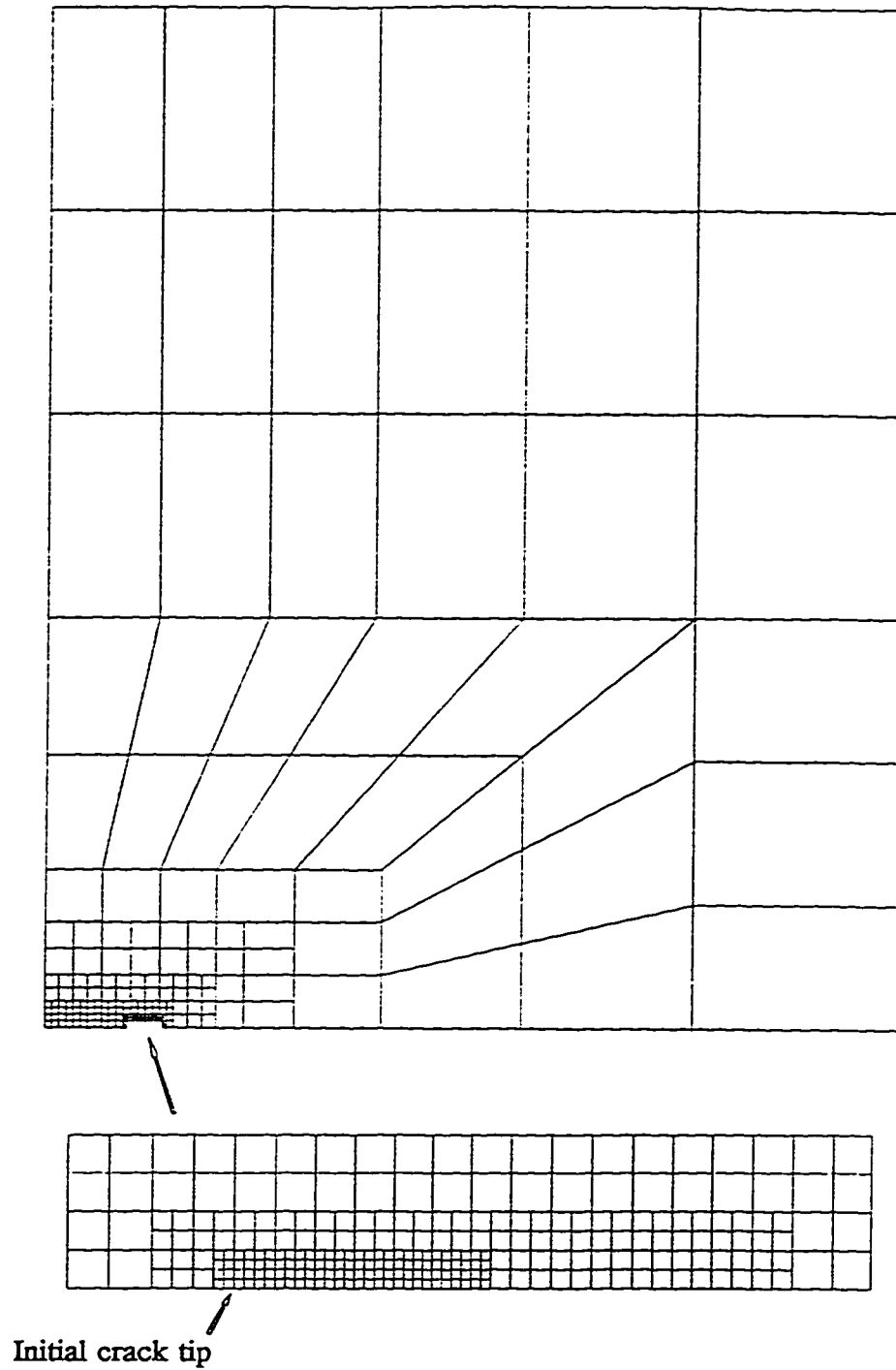
#### 4.9 Conclusions

- (1) The proposed crack-tip node release scheme is simple and effective in practice.
- (2) The proposed definitions of the crack opening and closing stresses describe the opening and closing of cracks more accurately, and can be generalized to stationary cracks and overload cases.
- (3) The crack opening or closing stress level does not stabilize: instead, it increases following crack propagation after a attainment of a relative stability.
- (4) The change of crack opening stresses is not directly related to the monotonic plastic zone size caused by the first loading cycle.
- (5) Fatigue cracks open progressively, and proportionally in the middle part of a loading cycle, towards the crack tip with an increasing load. However, opening of the last two nodes (0.04 mm from the crack tip)

requires a larger load increment.

- (6) Fatigue crack profiles for constant amplitude loading have been found to be proportional to the square root of the distance behind the crack tip.
- (7) Although various reasons have been put forward to explain the effects on crack closure, residual tensile deformation left in the wake of an advancing crack tip and in front of the crack tip, and residual compressive stresses at the crack tip are considered to be two major causes. A residual tensile deformation raises the crack opening stress, while a residual compressive stress lowers it.
- (8) The process of releasing the crack-tip node at the maximum applied load in the finite element analysis can be identified with the energy release process defined by Griffith.
- (9) Releasing the crack-tip node at the top or the bottom of the loading cycle results in different residual stresses and strains at the crack tip. Calculating the crack opening stress in finite element analysis by releasing the crack-tip node at the bottom of the loading cycle has major drawbacks.
- (10) The crack opening stress is slightly higher than the crack closing stress.
- (11) A single overload results in a large residual tensile deformation ahead of the crack tip, which causes an increase of the crack opening stress level (the retardation in crack growth rates), and large residual compressive stresses at the crack tip, which reduces the crack opening stress level (the delay of the retardation).

- (12) After a single overload, there is a stage following the delayed retardation in crack growth rate. In this stage the crack opening stress is lower than the stabilized crack opening level for the constant amplitude loading.
- (13) After a single underload, the change of the residual stresses and strains is not appreciable; the crack opening stress decreases slightly.
- (14) A compression-compression cyclic loading can initiate cracks at a notch root and cause them to grow due to the existence of a residual tensile stress field near the notch root. The maximum residual tensile stress decreases at each loading cycle leading to crack arrest.
- (15) During crack propagating from the root of a notch under compression-compression cyclic loading, the crack opening stress increases; in other words, the effective stress range decreases, till the crack arrests.



Elements=442    Nodes=588    Half width of panel=40 mm

Half crack length=4 mm    Minimum size of element=0.02 mm

Fig.4-1 Finite element mesh of one-quarter of a centre-cracked panel used in this study.

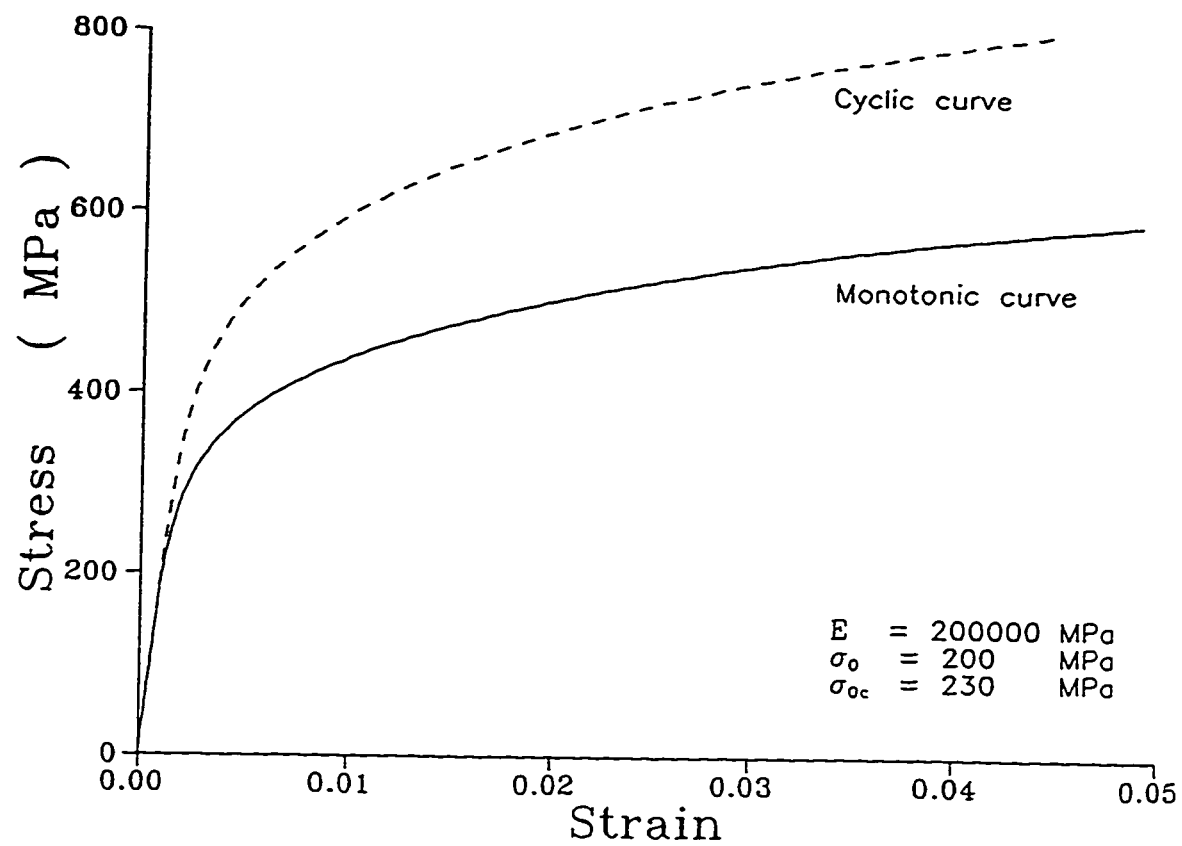


Fig.4-2 Monotonic and cyclic stress-strain curves for a typical structural steel.

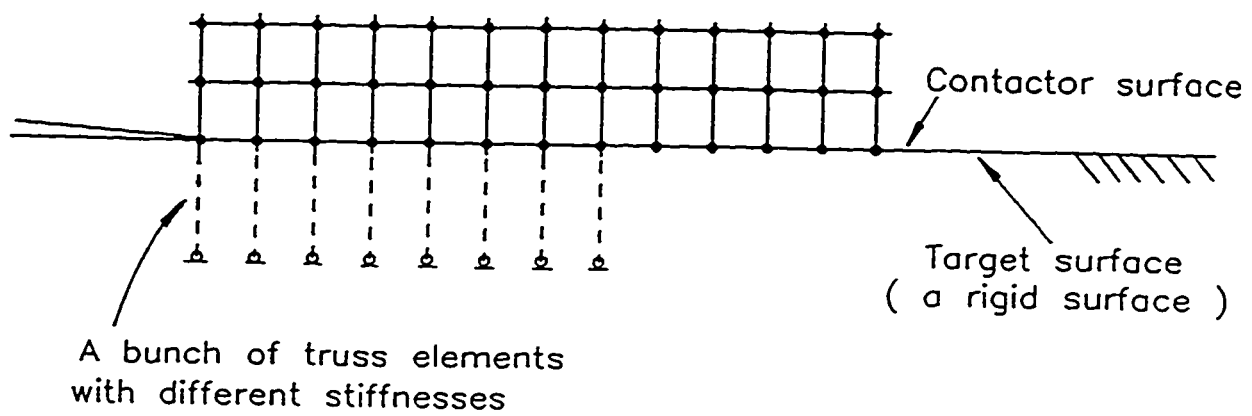


Fig.4-3 A schematic of truss elements connected to boundary nodes and a pair of contact surfaces set up on the crack line.

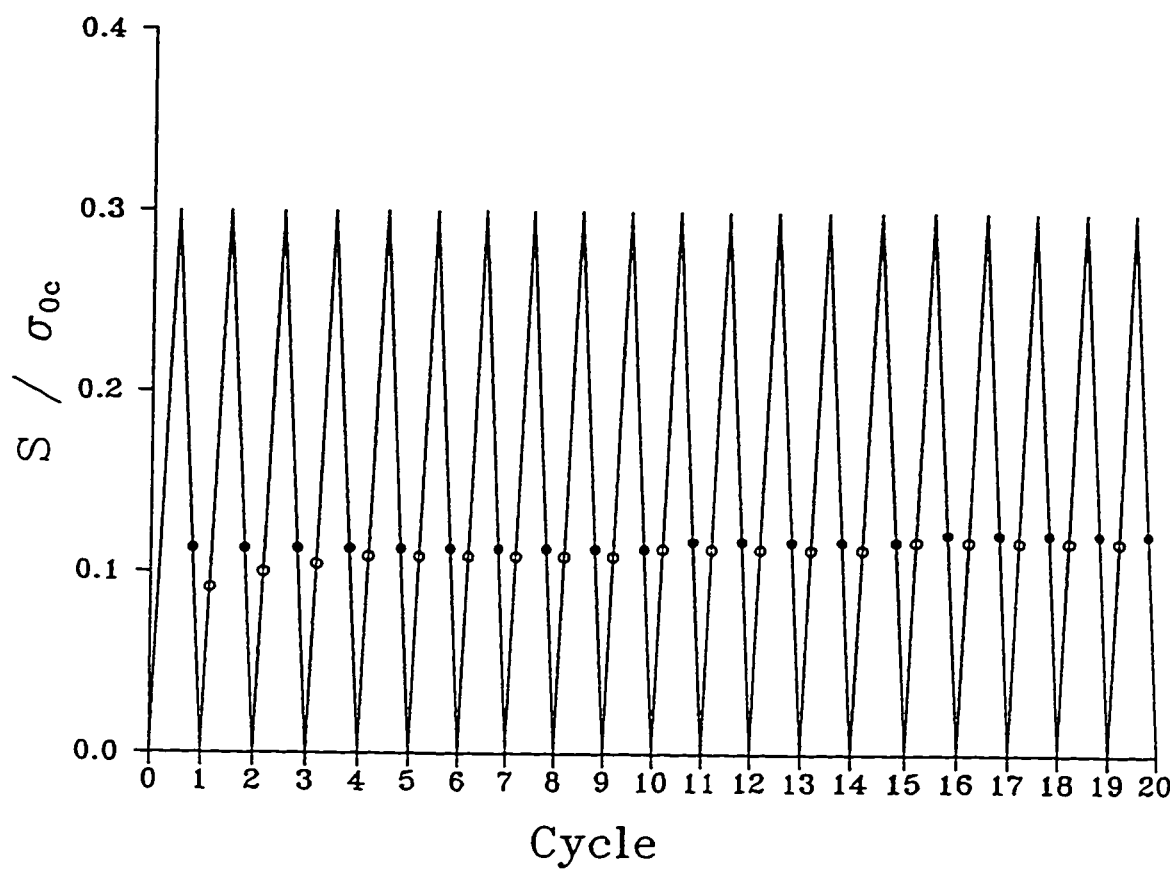


Fig.4-4 Crack opening stresses and closing stresses for constant-amplitude cyclic loading with  $S_{max}=0.3\sigma_{0c}$  and  $R=0$  under releasing node at the top of the cycles.



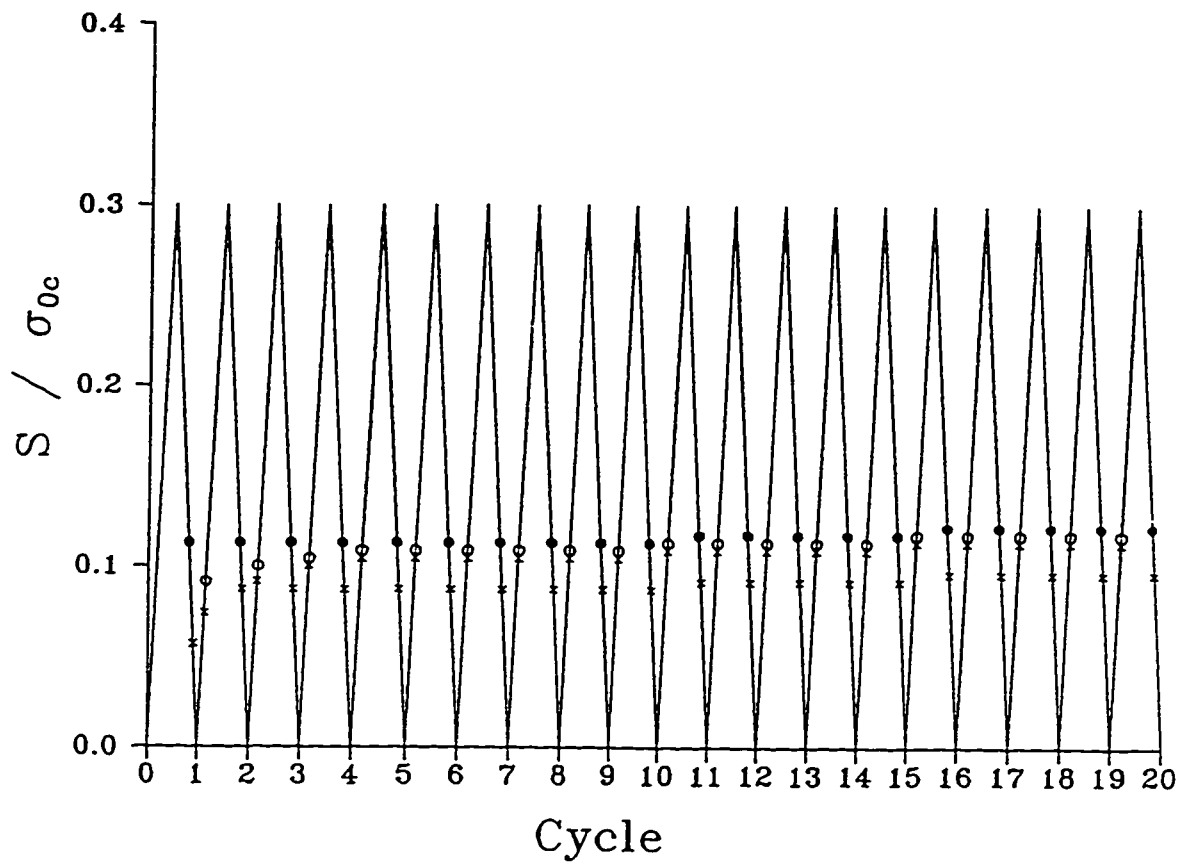


Fig.4-5 A comparison between the new and old definitions for crack opening stress and closing stress.

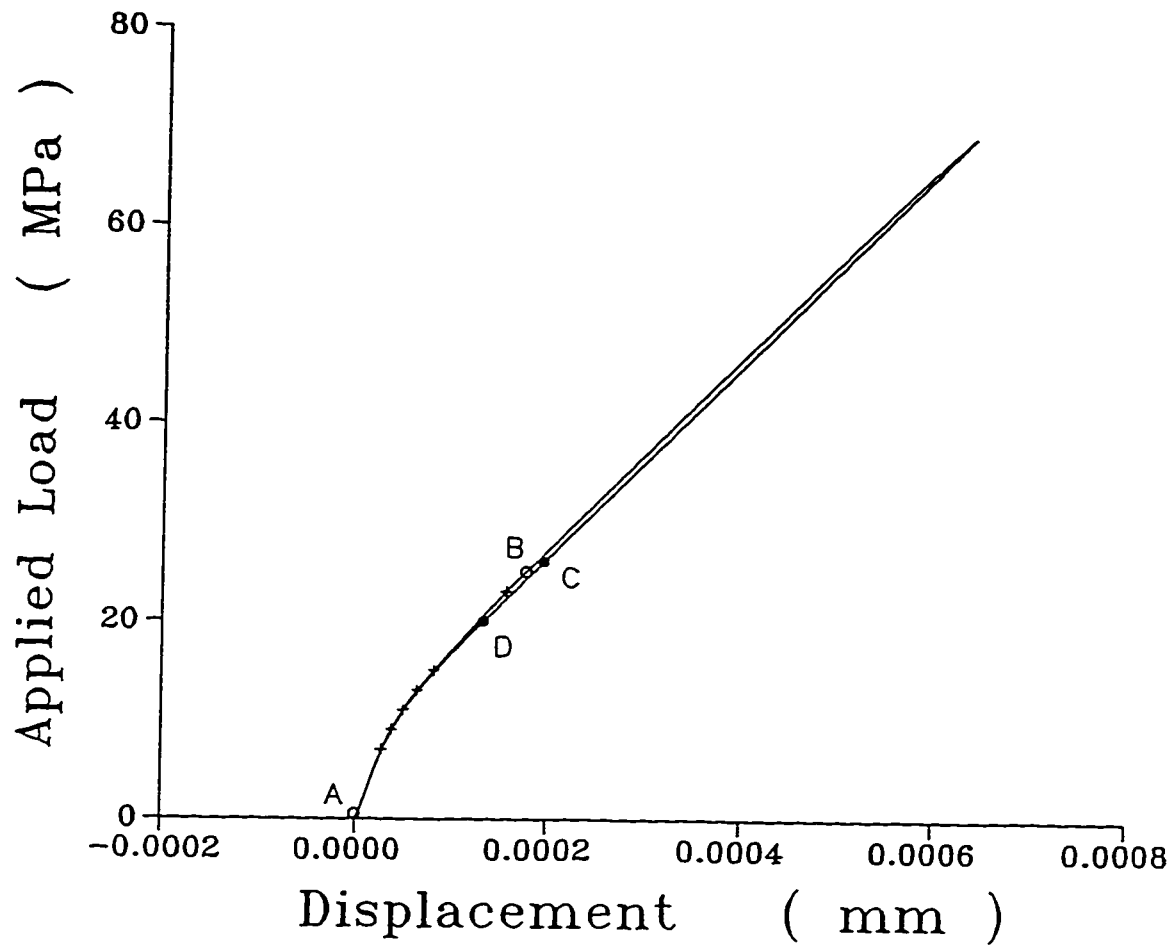


Fig.4-6 Applied load-displacement relationship without the effect of artificial releasing node.

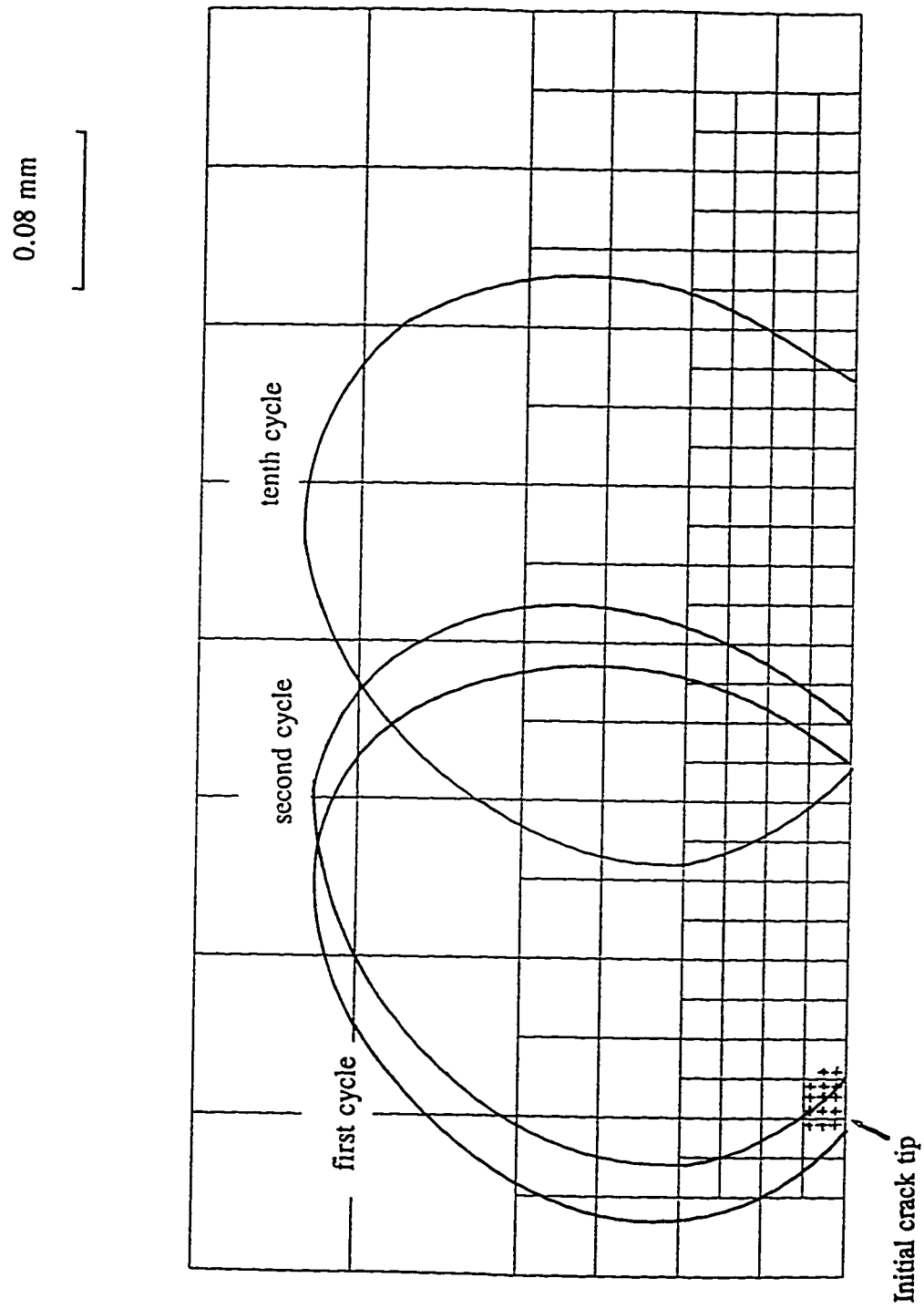


Fig.4-7 Plastic zones for the first, second and tenth cycle and reversed plastic zone for the first cycle identified by cross symbols.

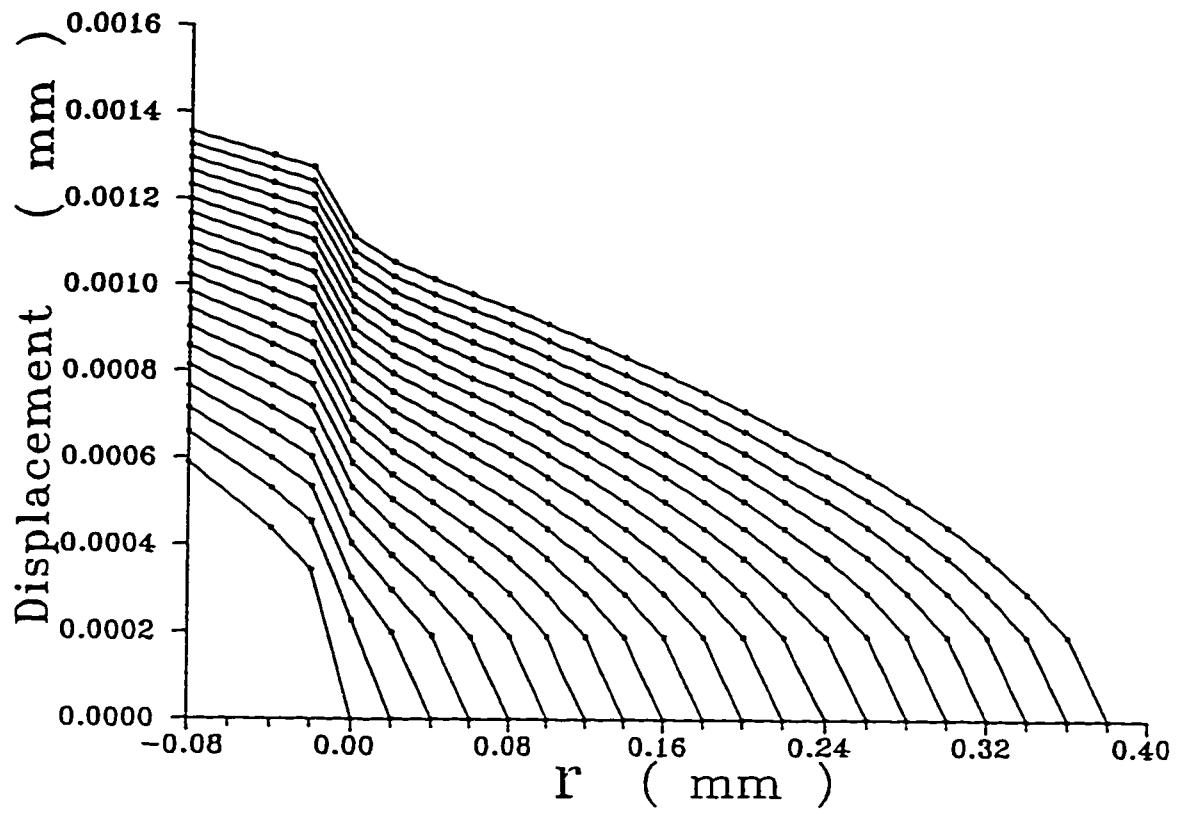


Fig.4-8 Crack profiles under constant-amplitude crack extension with  $S_{\max} = 0.3\sigma_{0c}$  and  $R=0$ .

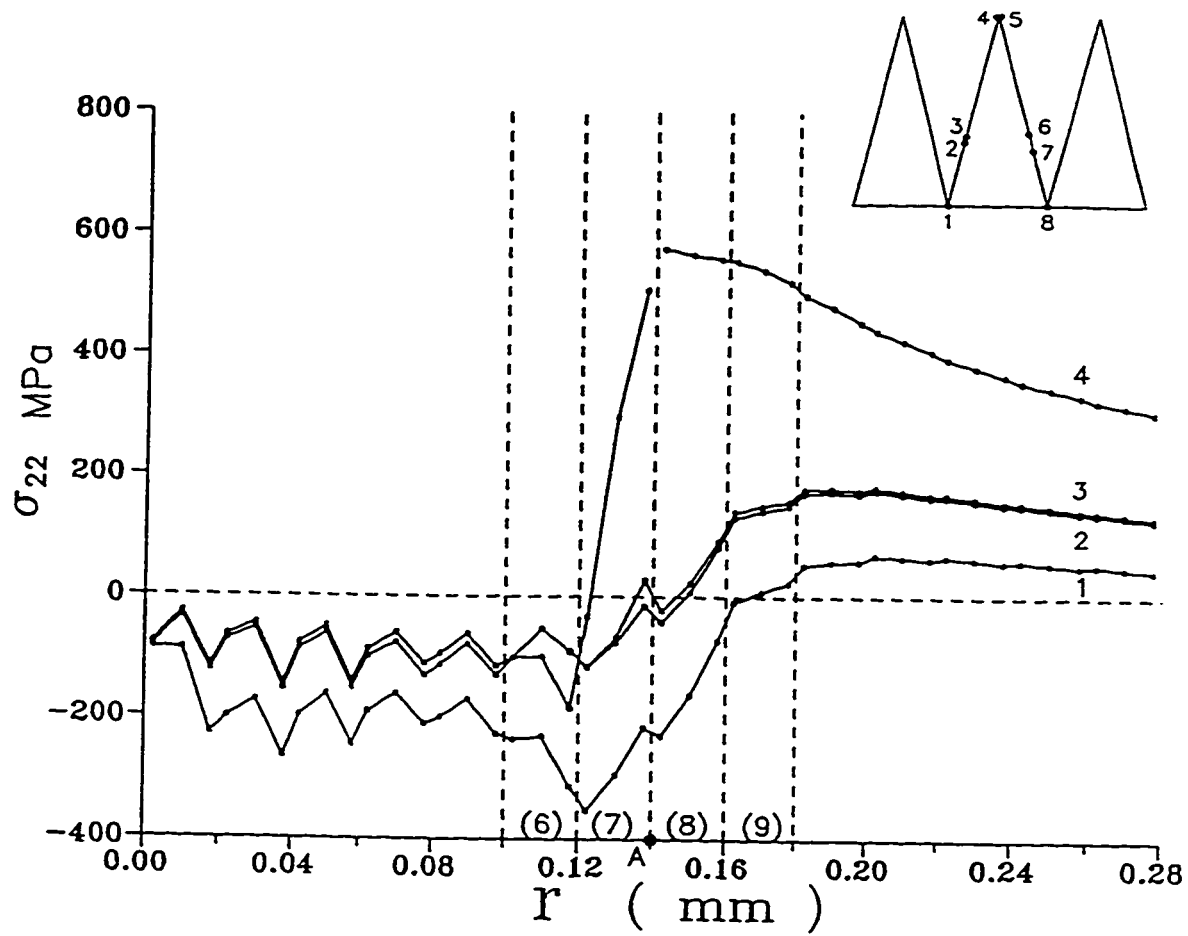


Fig.4-9a Stress distributions for special points on a typical loading cycle under releasing node at the top of loading cycles, Part 1.

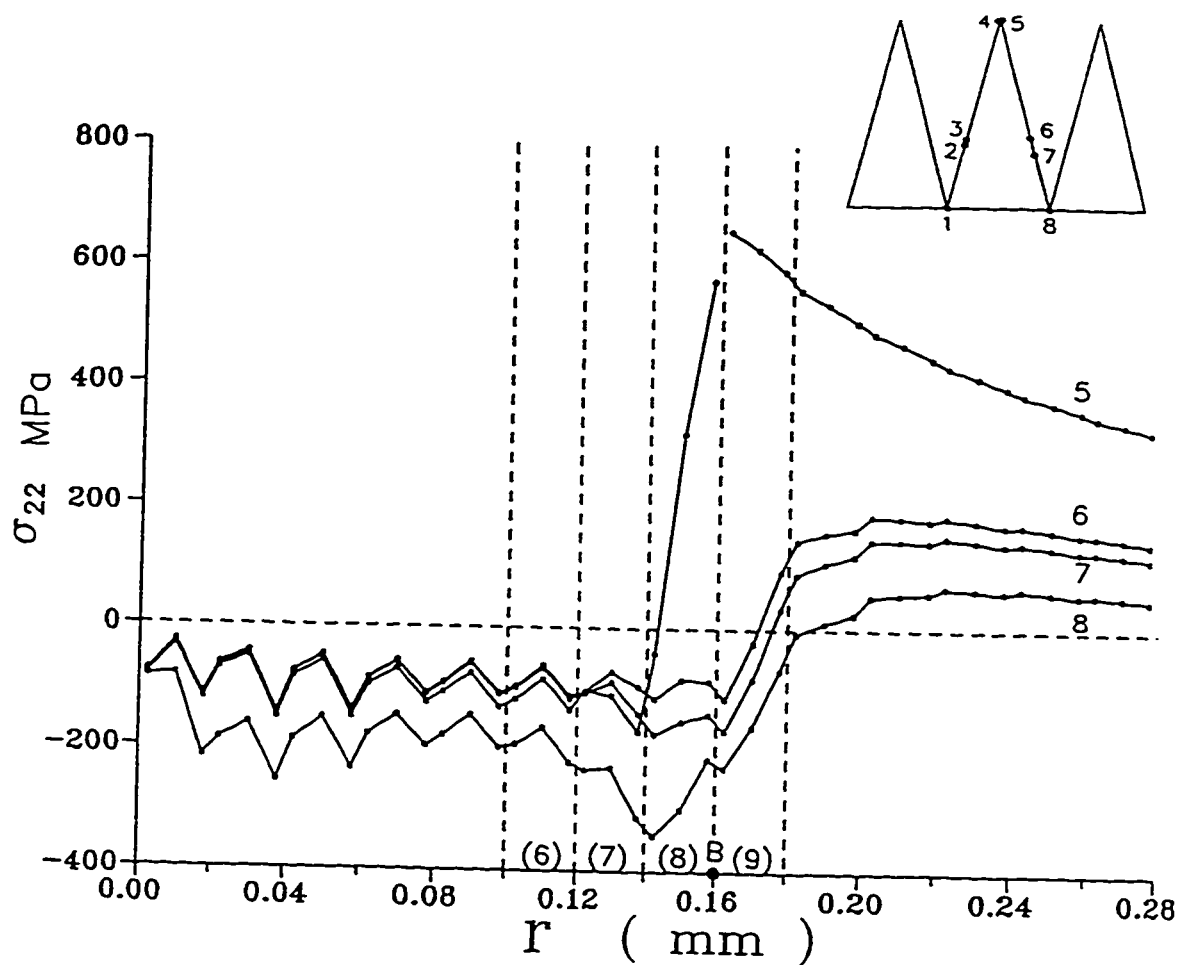


Fig.4-9b Stress distributions for special points on a typical loading cycle under releasing node at the top of loading cycles, Part 2.

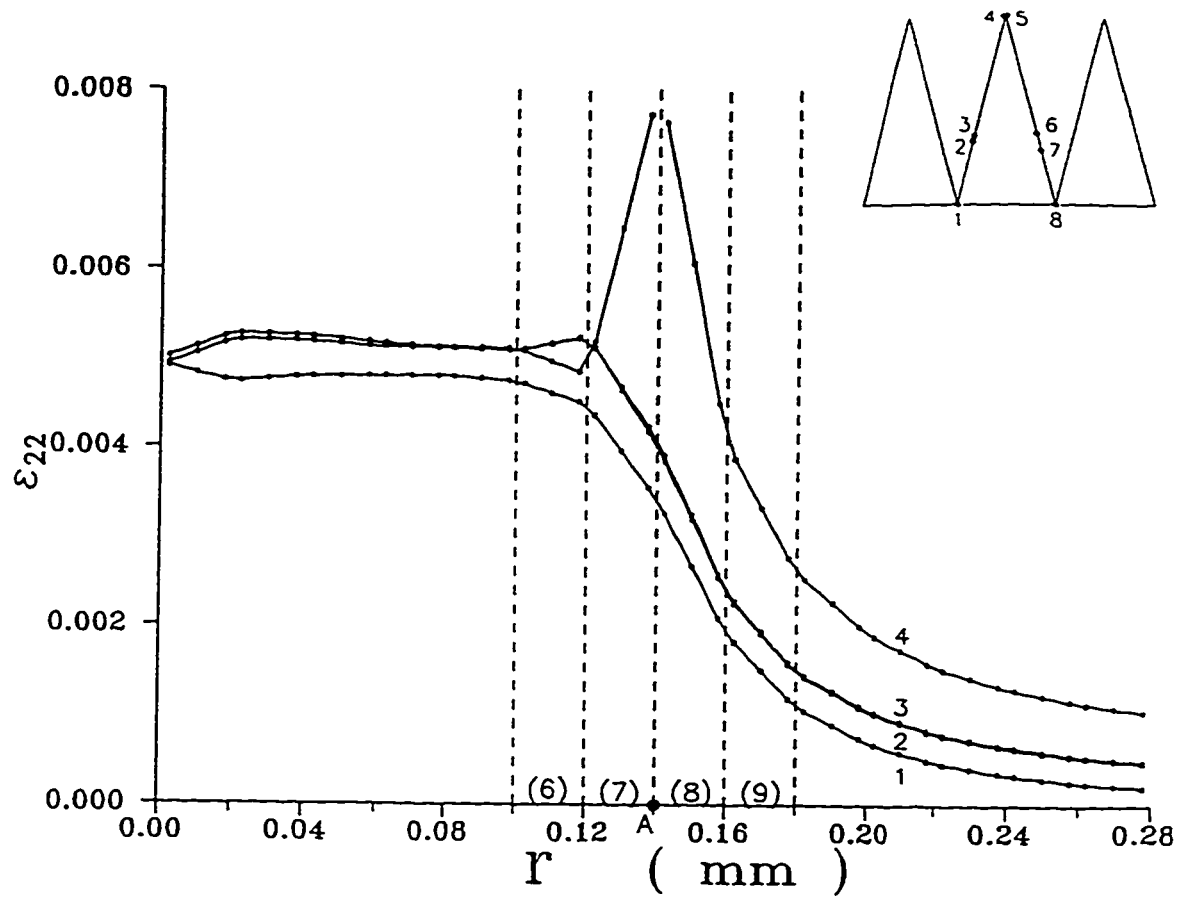


Fig.4-10a Strain distributions for special points on a typical loading cycle under releasing node at the top of loading cycles, Part 1.

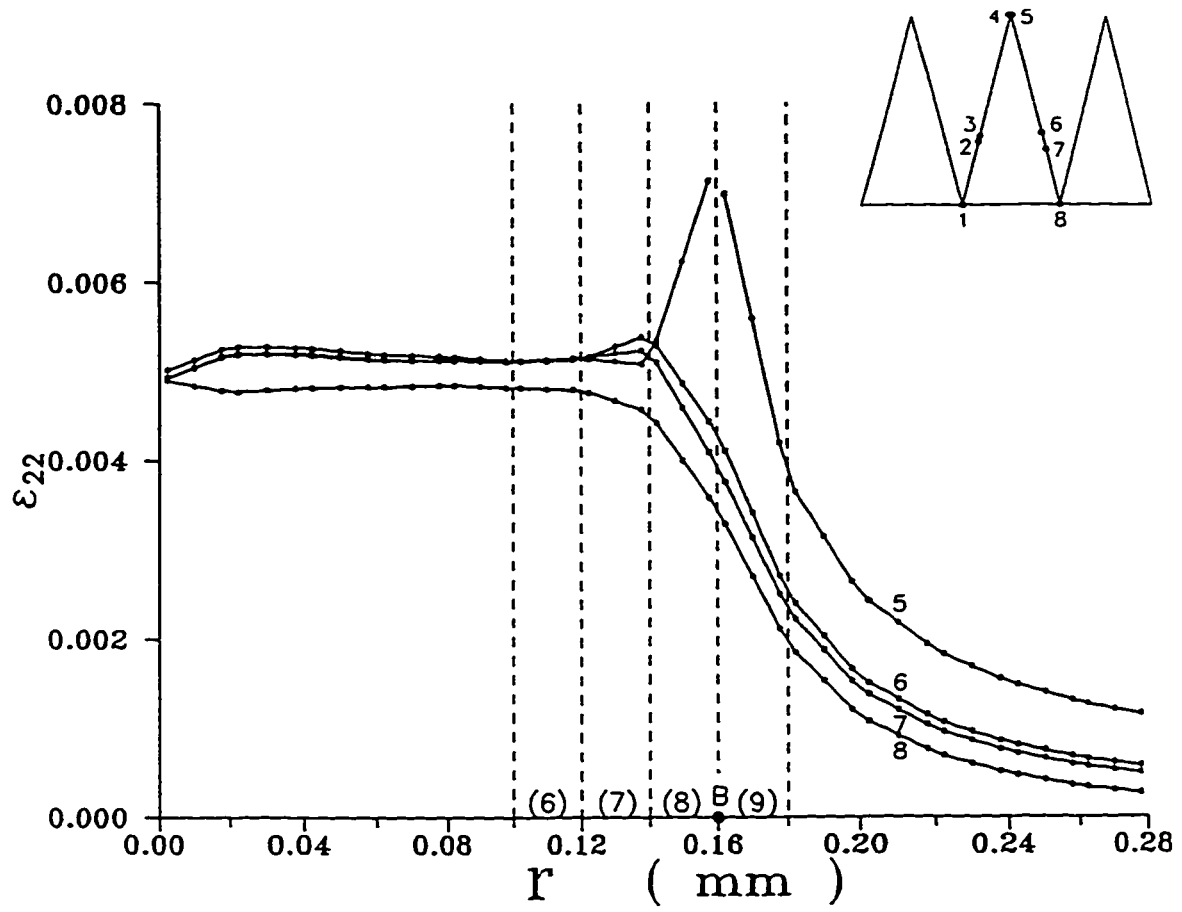


Fig.4-10b Strain distributions for special points on a typical loading cycle under releasing node at the top of loading cycles, Part 2.



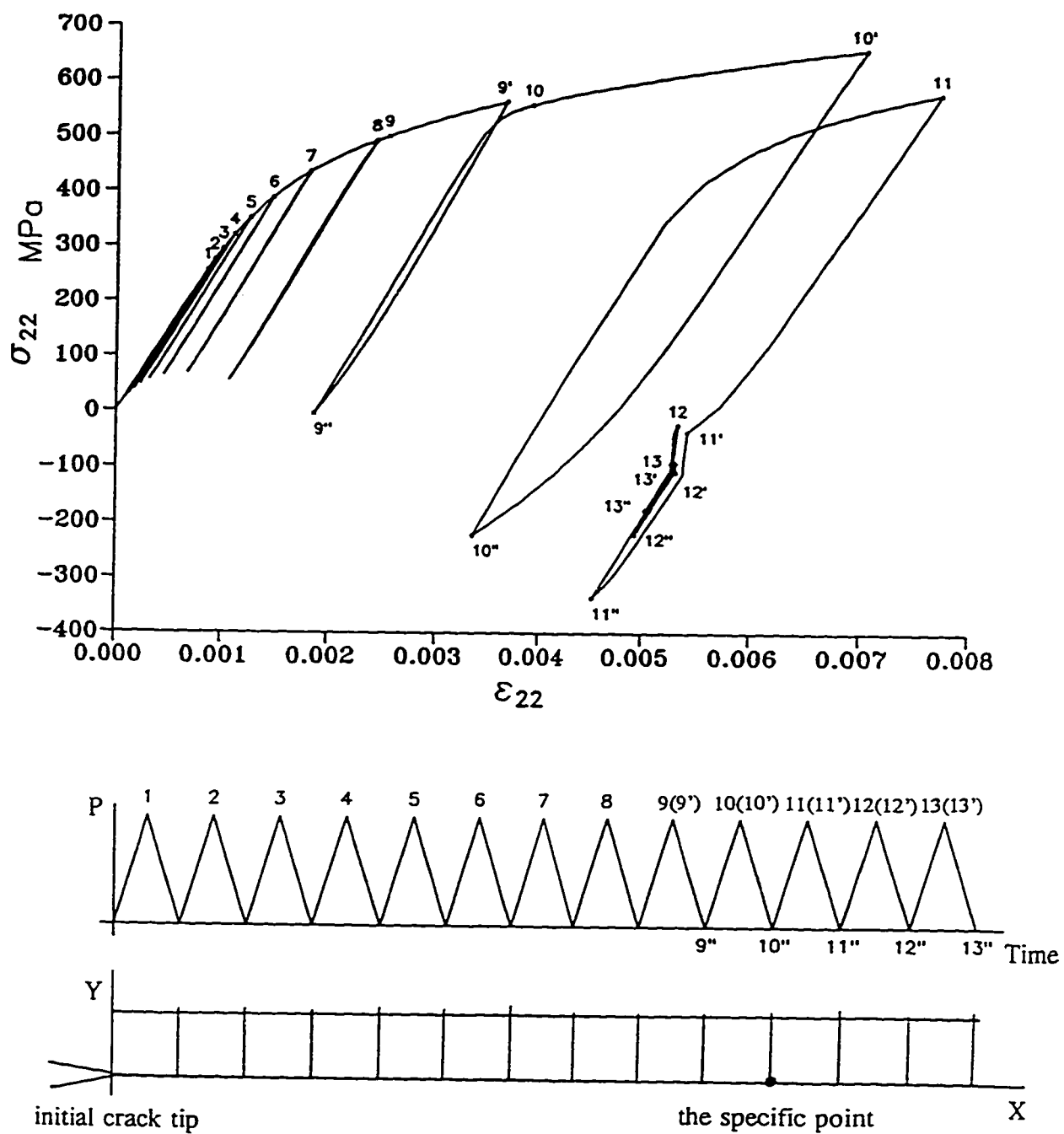


Fig.4-11 Cyclic stress-strain history at a point along the crack as the crack tip approaches and passes.

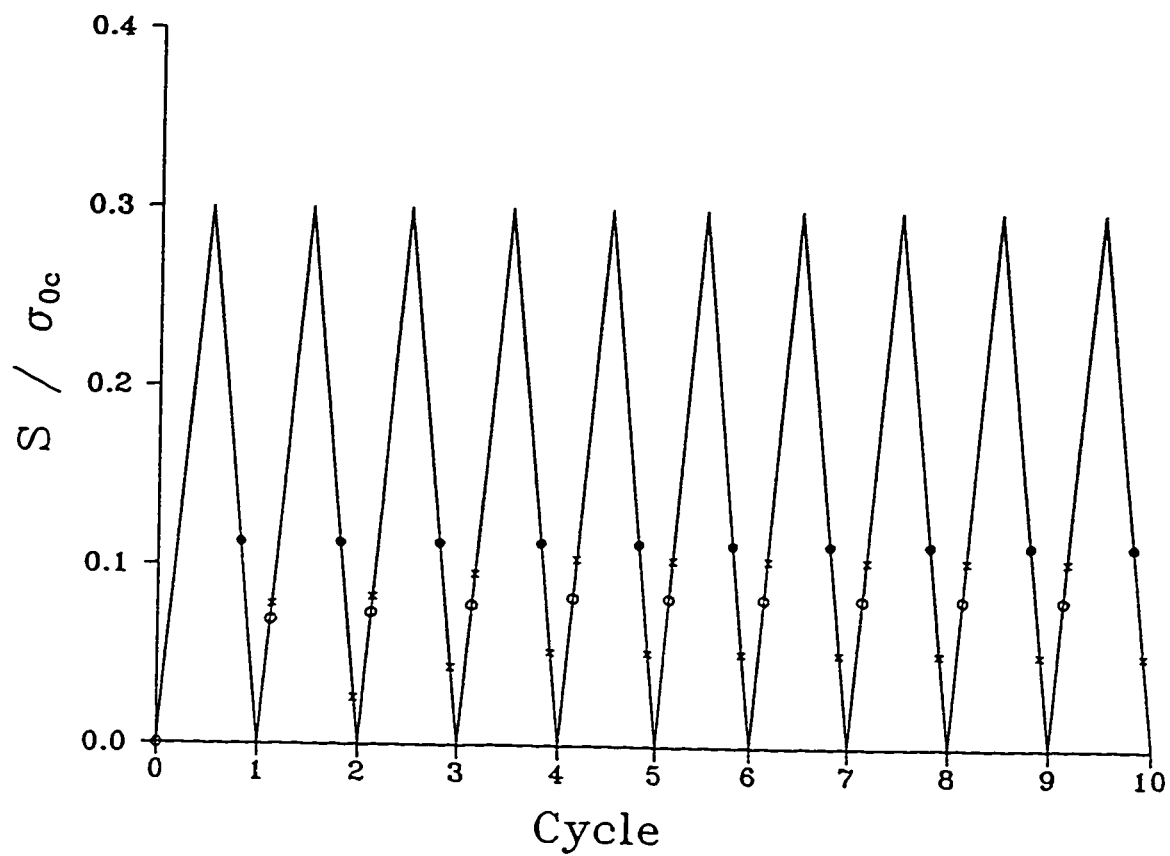


Fig.4-12 Crack opening stresses and closing stresses by the new and old definitions under releasing node at the bottom of the loading cycles.

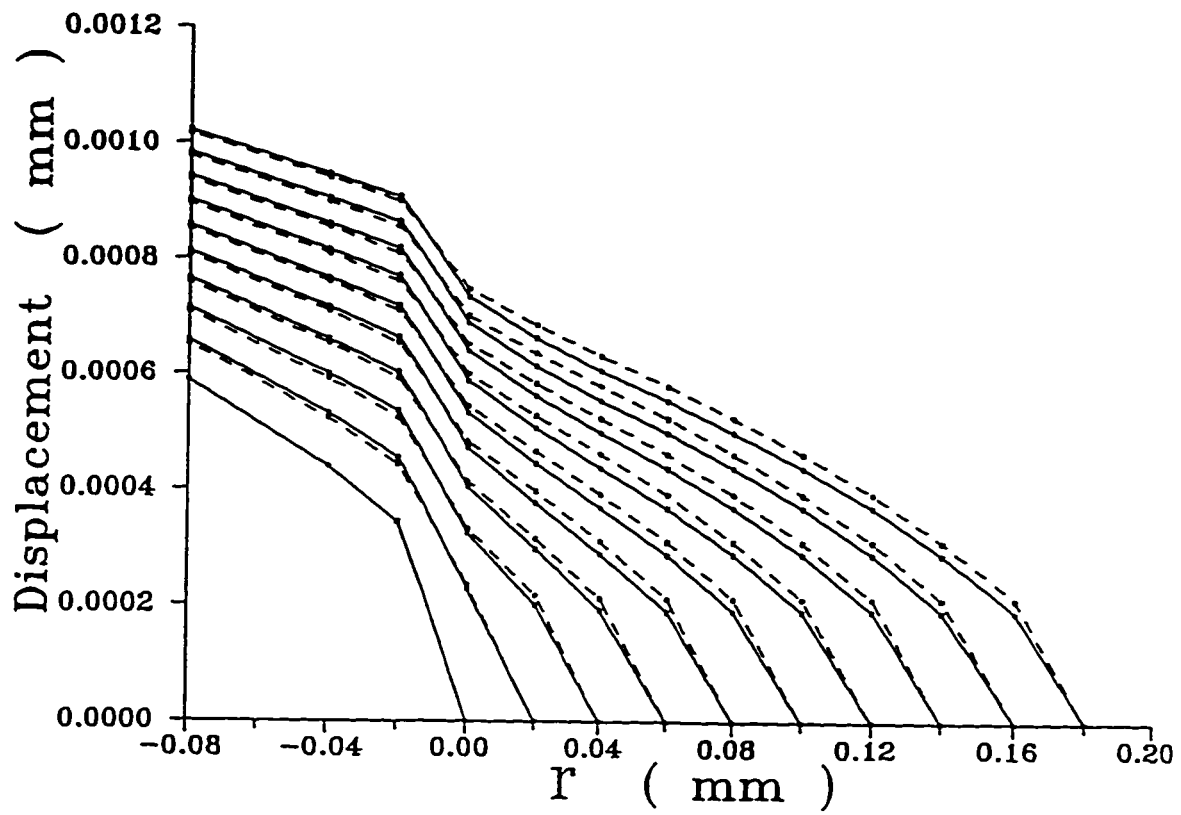


Fig.4-13 A comparison between crack profiles for releasing node at the top or the bottom of loading cycles.

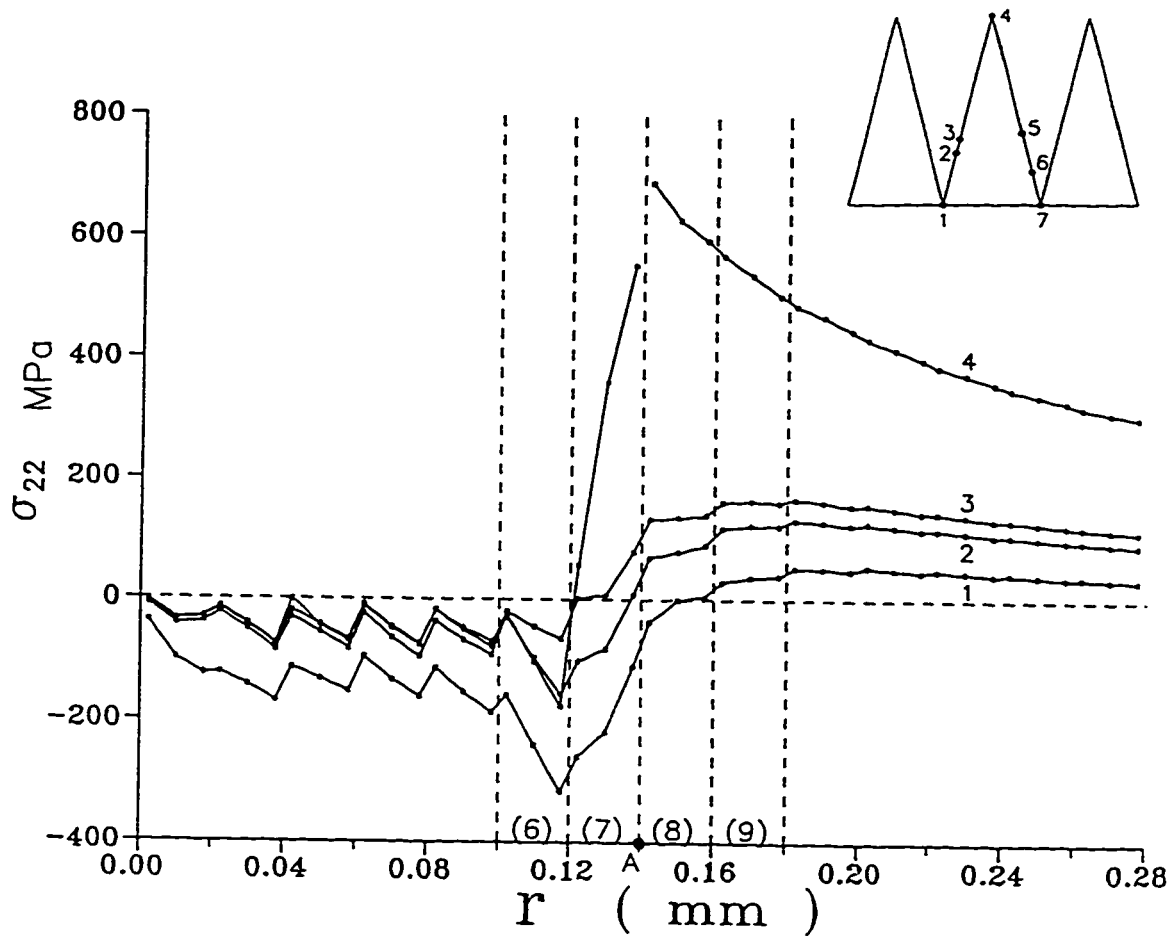


Fig.4-14a Stress distributions for special points on a typical loading cycle under releasing node at the bottom of loading cycles, Part 1.

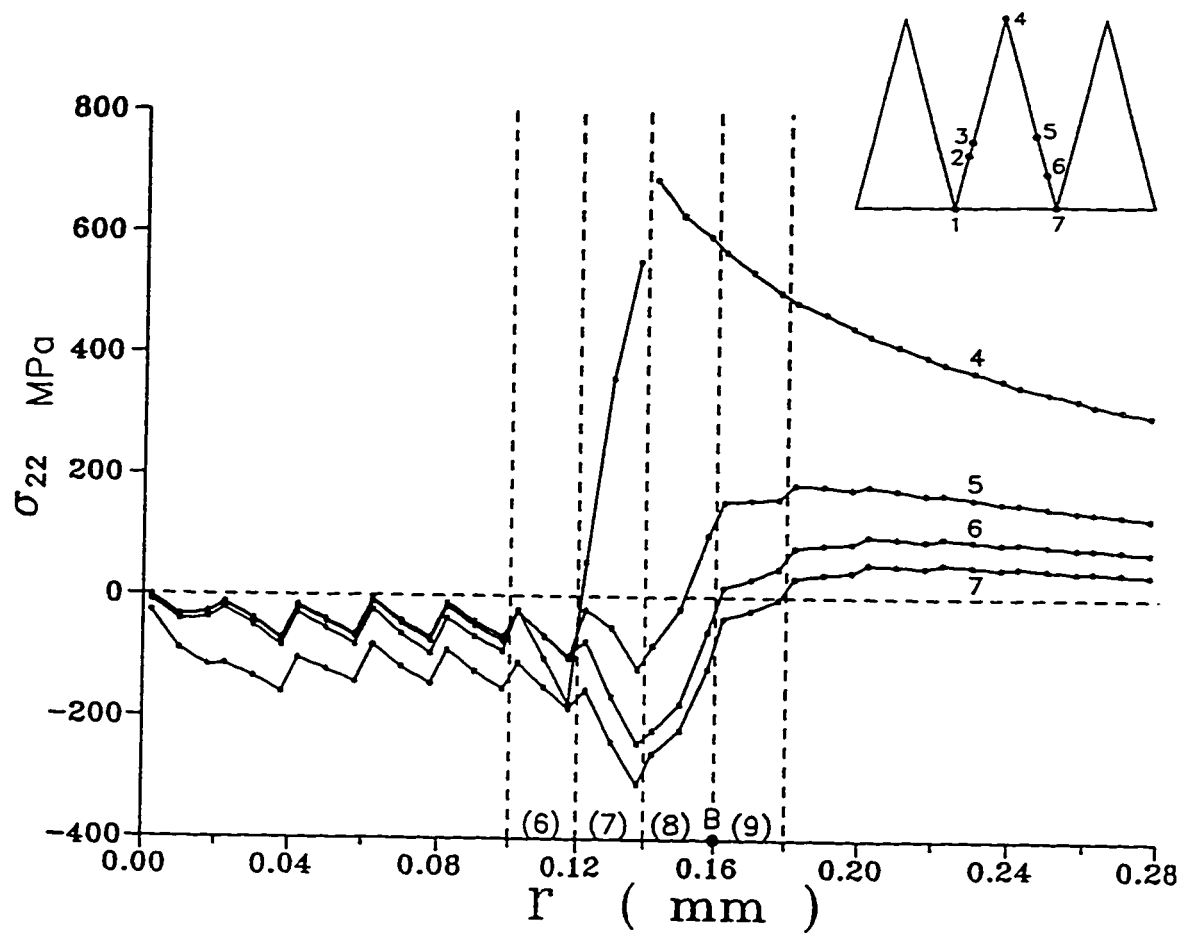


Fig.4-14b Stress distributions for special points on a typical loading cycle under releasing node at the bottom of loading cycles, Part 2.

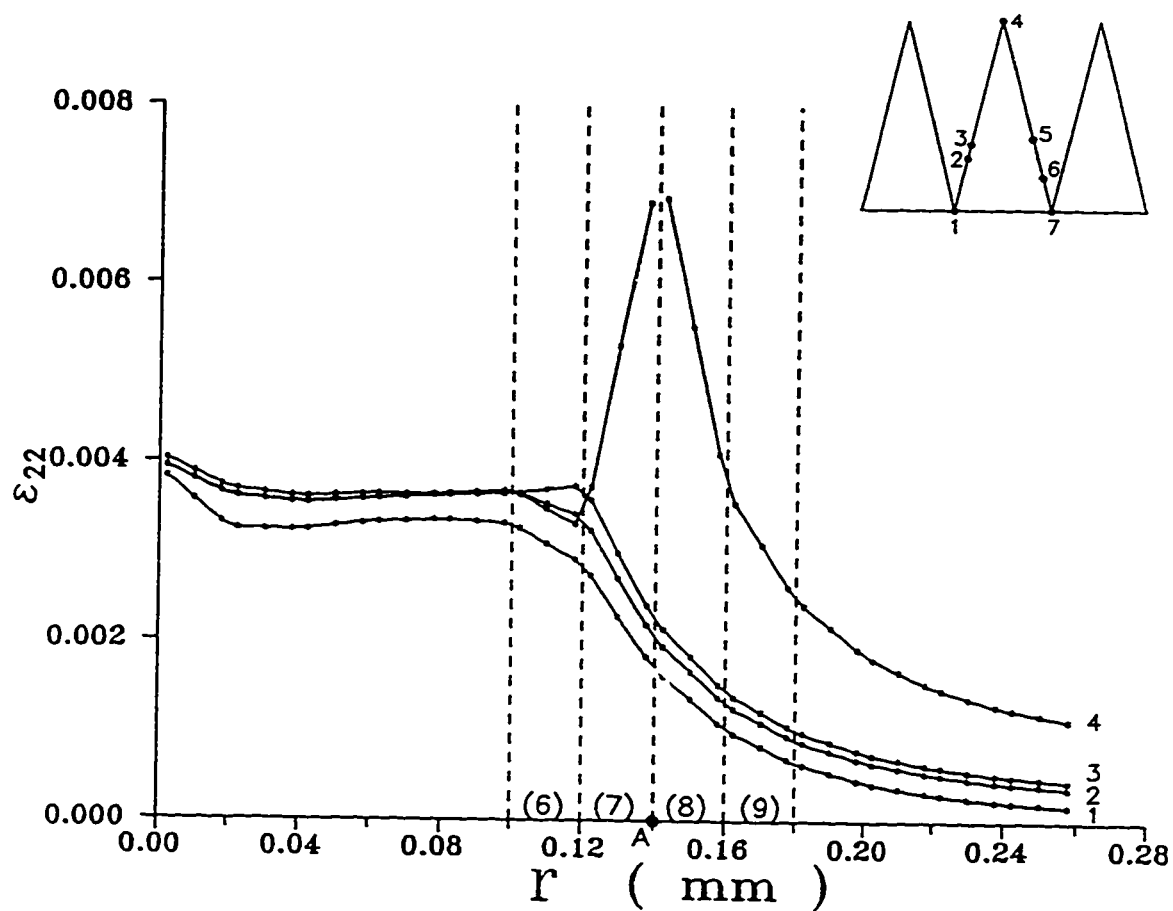


Fig.4-15a Strain distributions for special points on a typical loading cycle under releasing node at the bottom of loading cycles, Part 1.

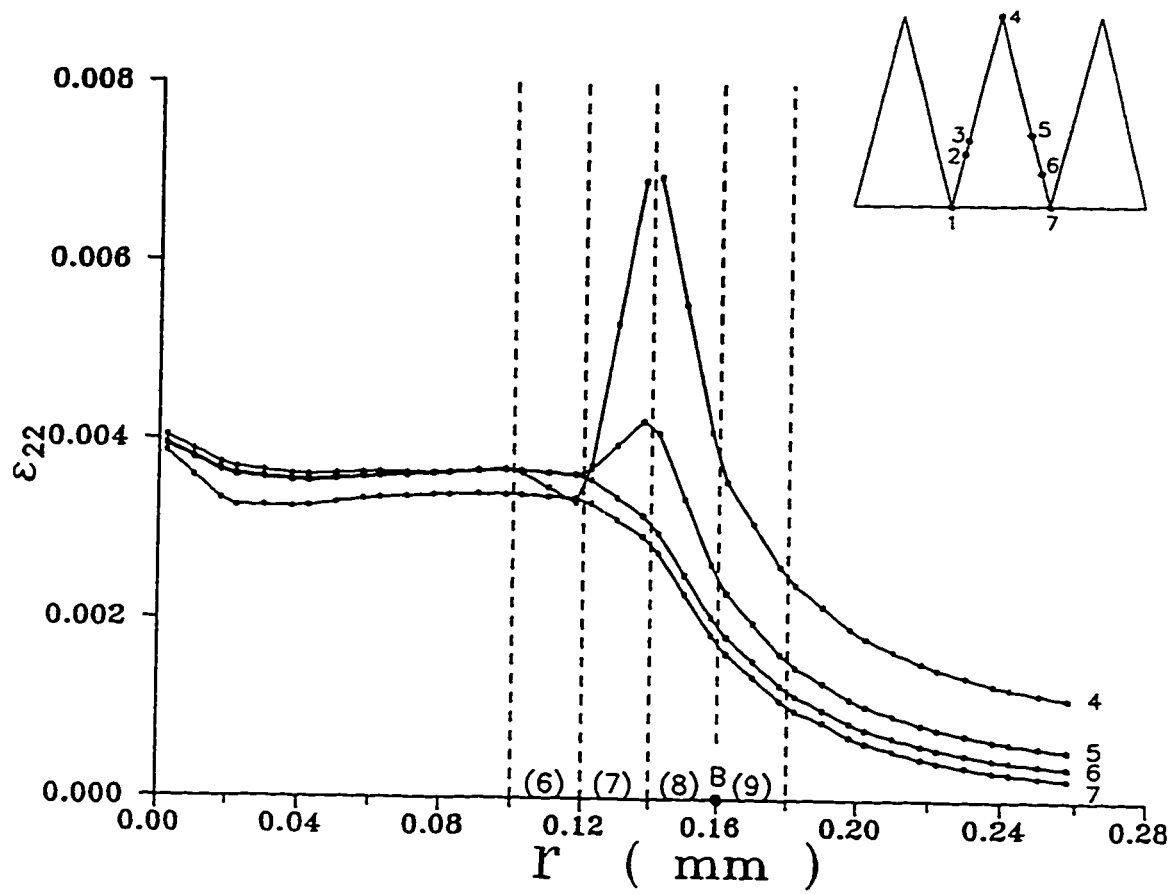


Fig.4-15b Strain distributions for special points on a typical loading cycle under releasing node at the bottom of loading cycles, Part 2.

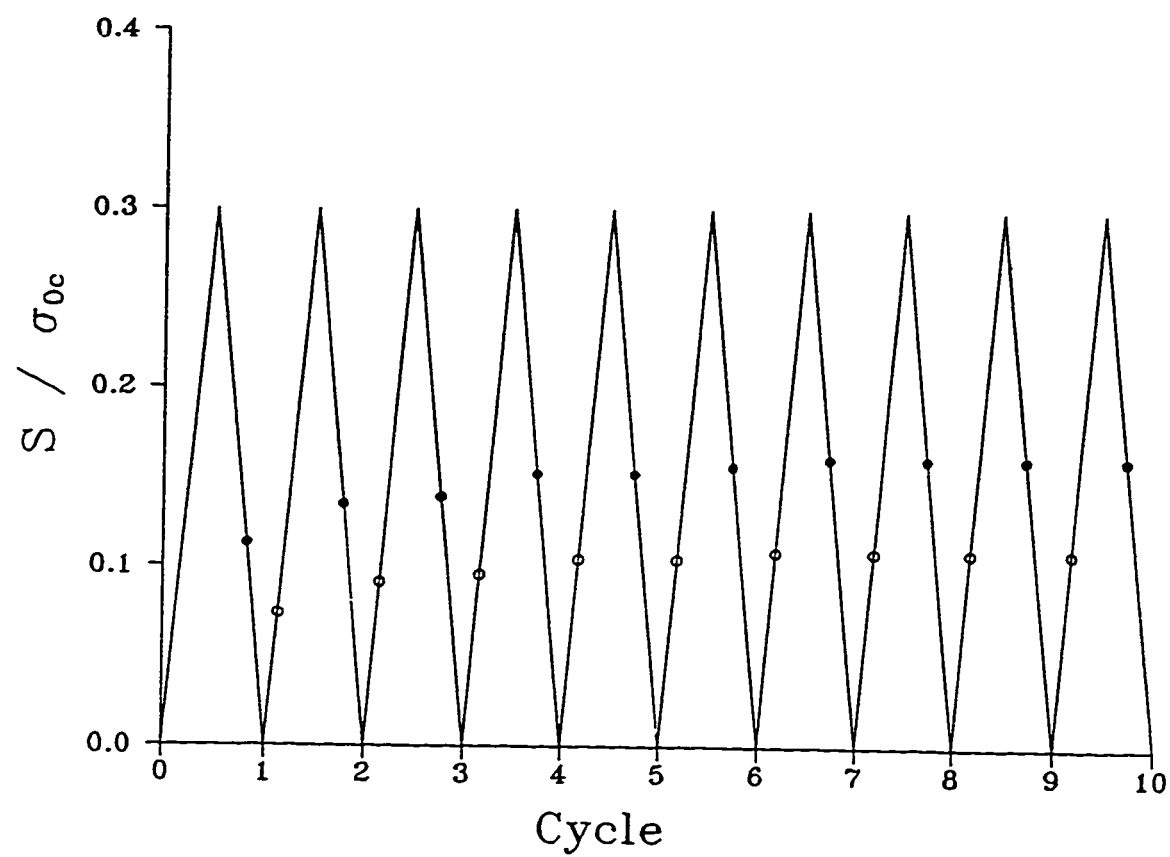


Fig.4-16 Stress opening stresses and closing stresses of a stationary crack by new definition.



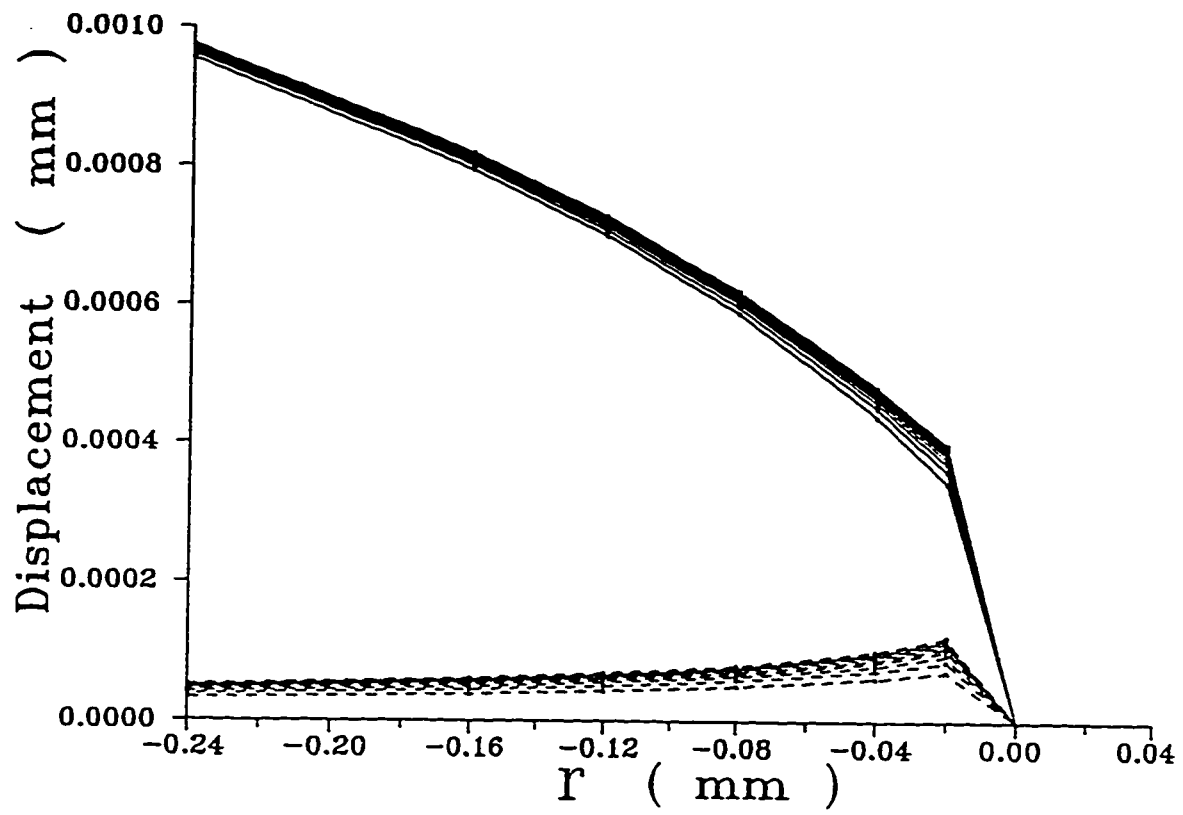


Fig.4-17 Crack profiles of a stationary crack for each constant-amplitude loading cycle.

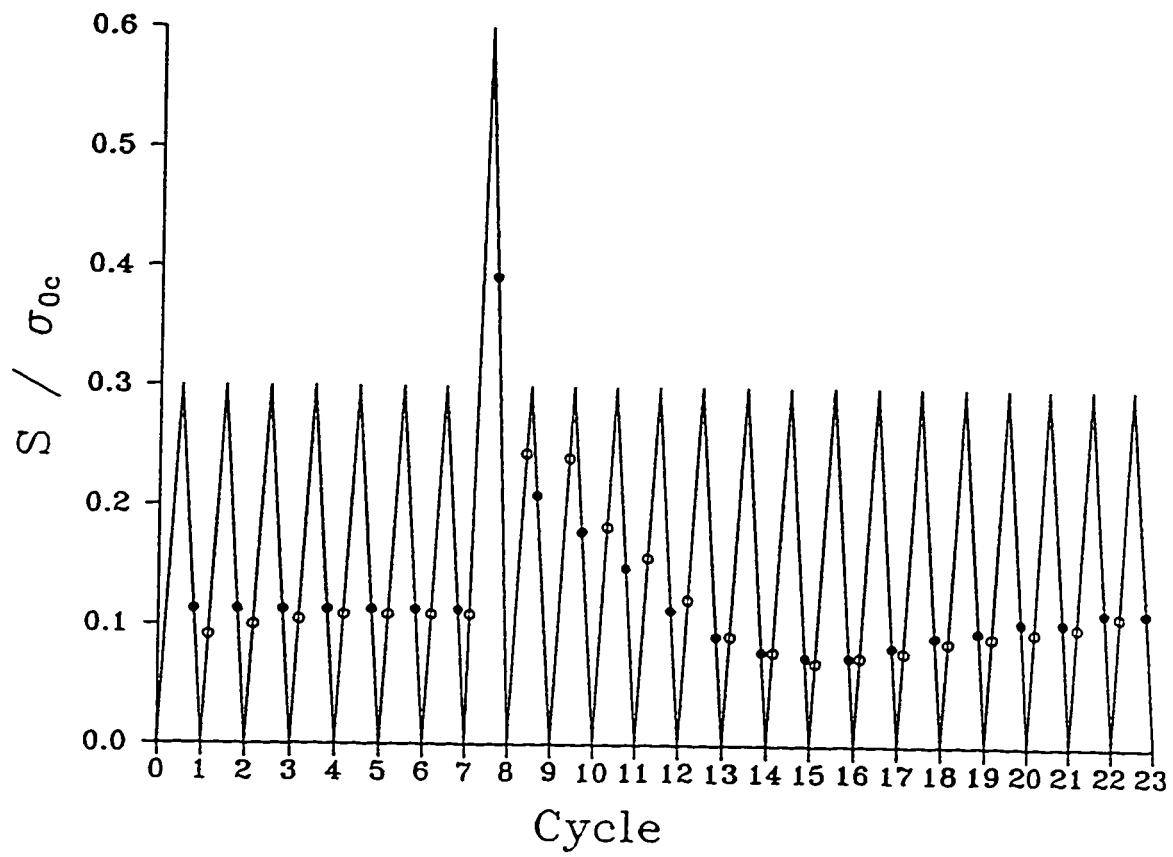


Fig.4-18 Crack opening stresses and closing stresses under constant-amplitude cyclic loading with a single 100% overload by new definition.

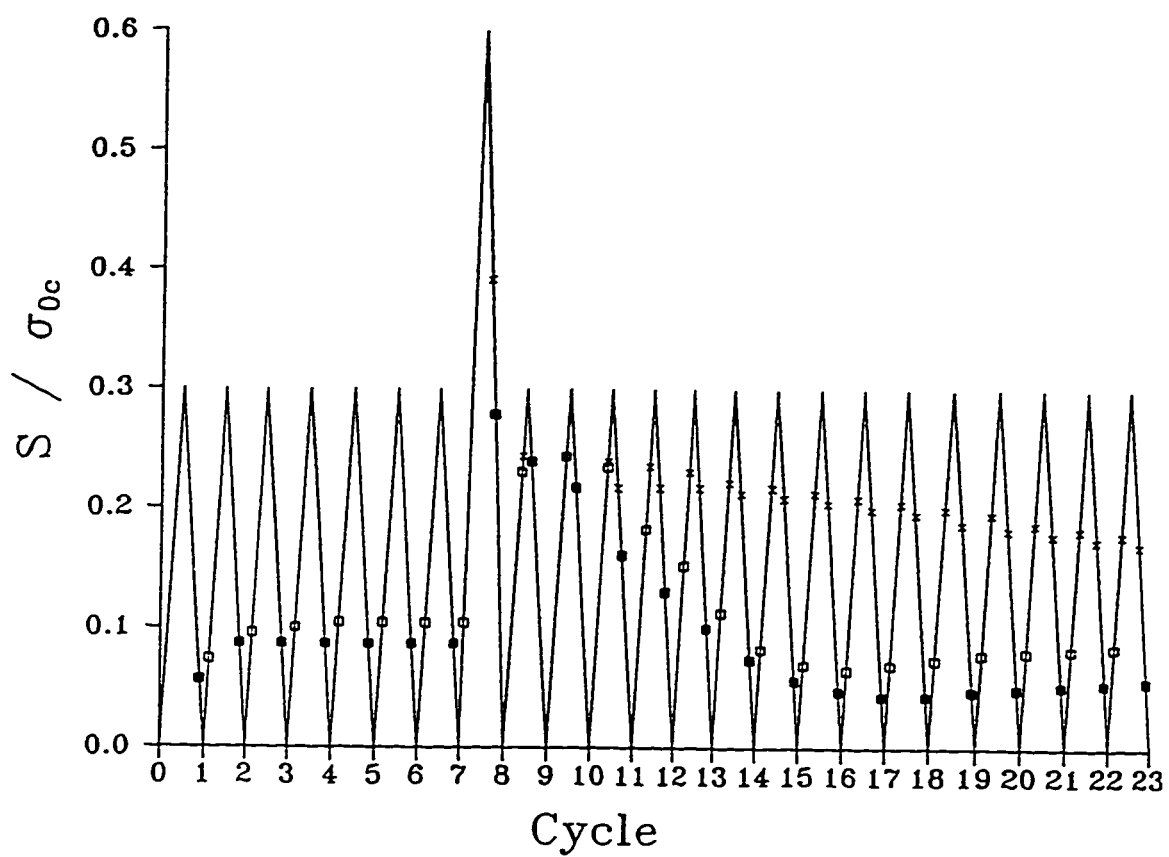


Fig.4-19 Crack opening stresses and closing stresses under constant -amplitude cyclic loading with a single 100% overload by old definition.

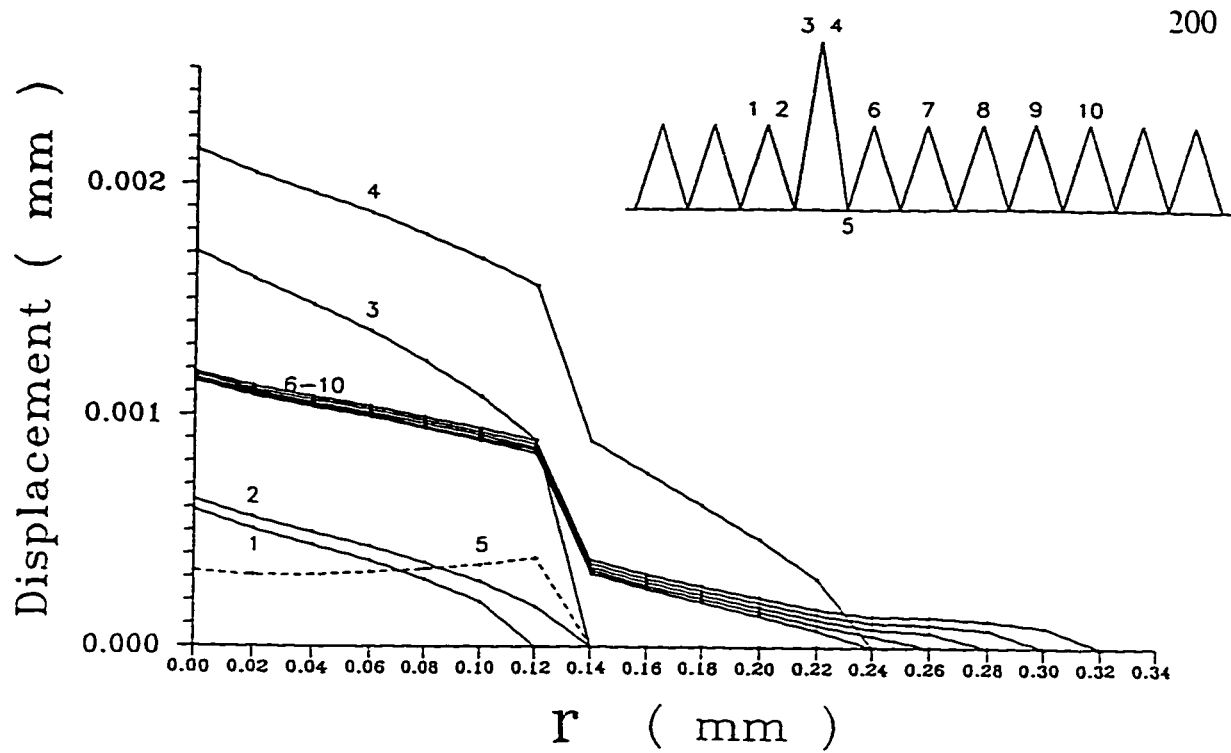


Fig.4-20 Crack profiles under constant-amplitude cyclic loading with a single 100% overload.

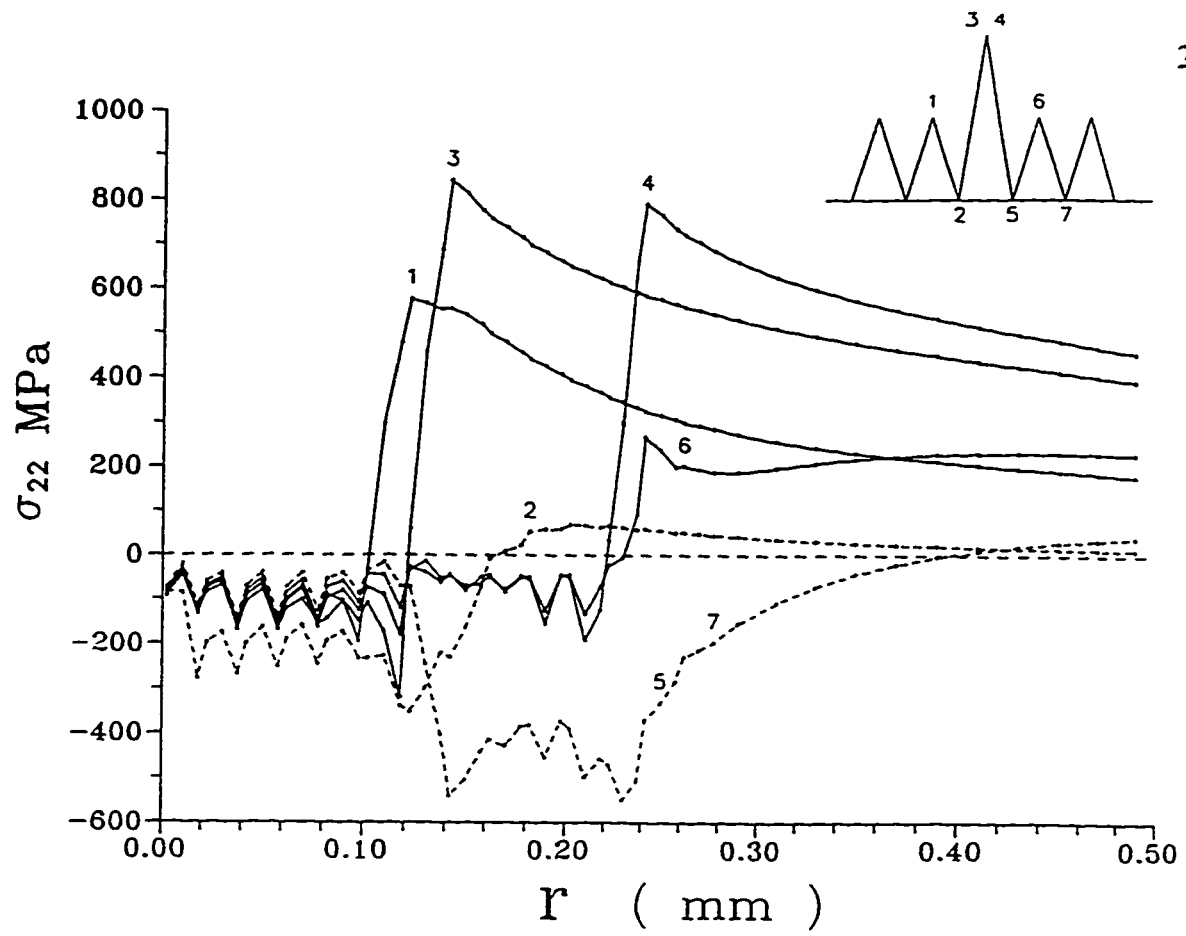


Fig.4-21a Stress distributions for special points near the overload cycle.

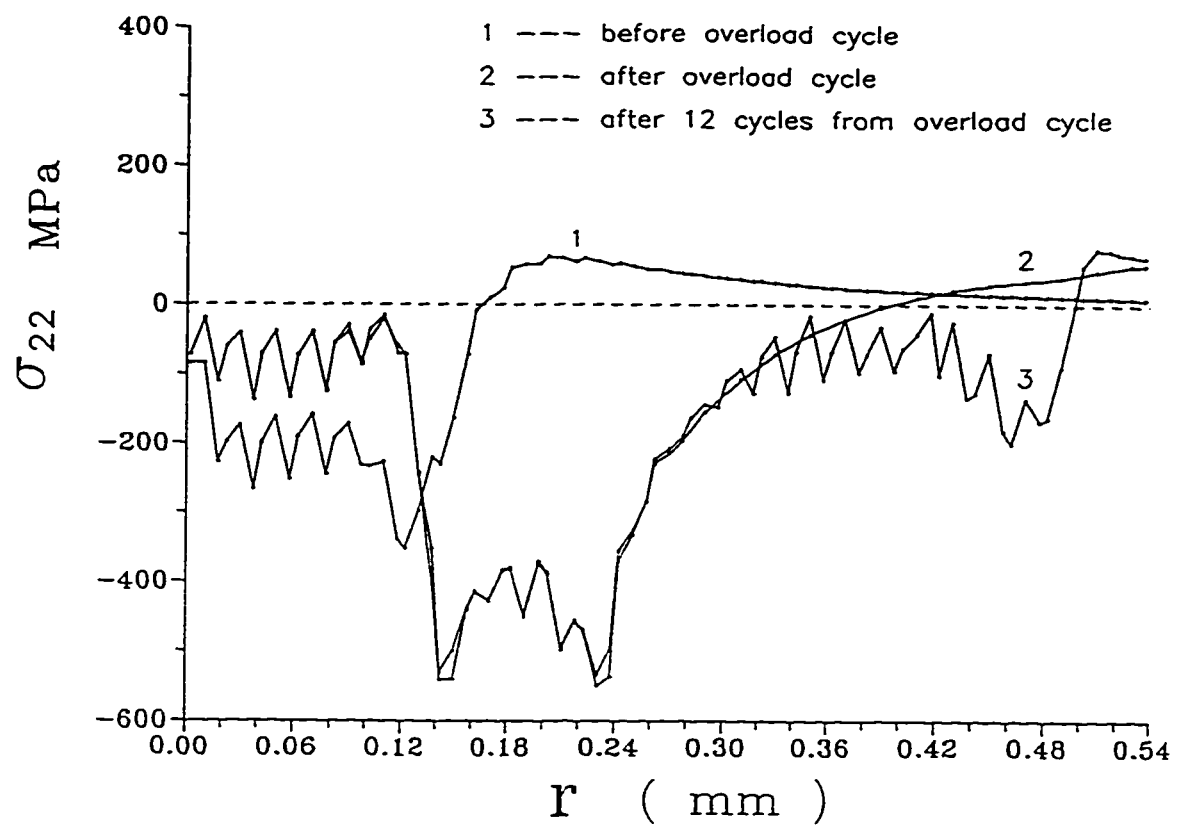


Fig.4-21b Residual stress diatributions for the cycle before overload cycle, overload cycle and the cycle after 12 cycles from overload cycle.

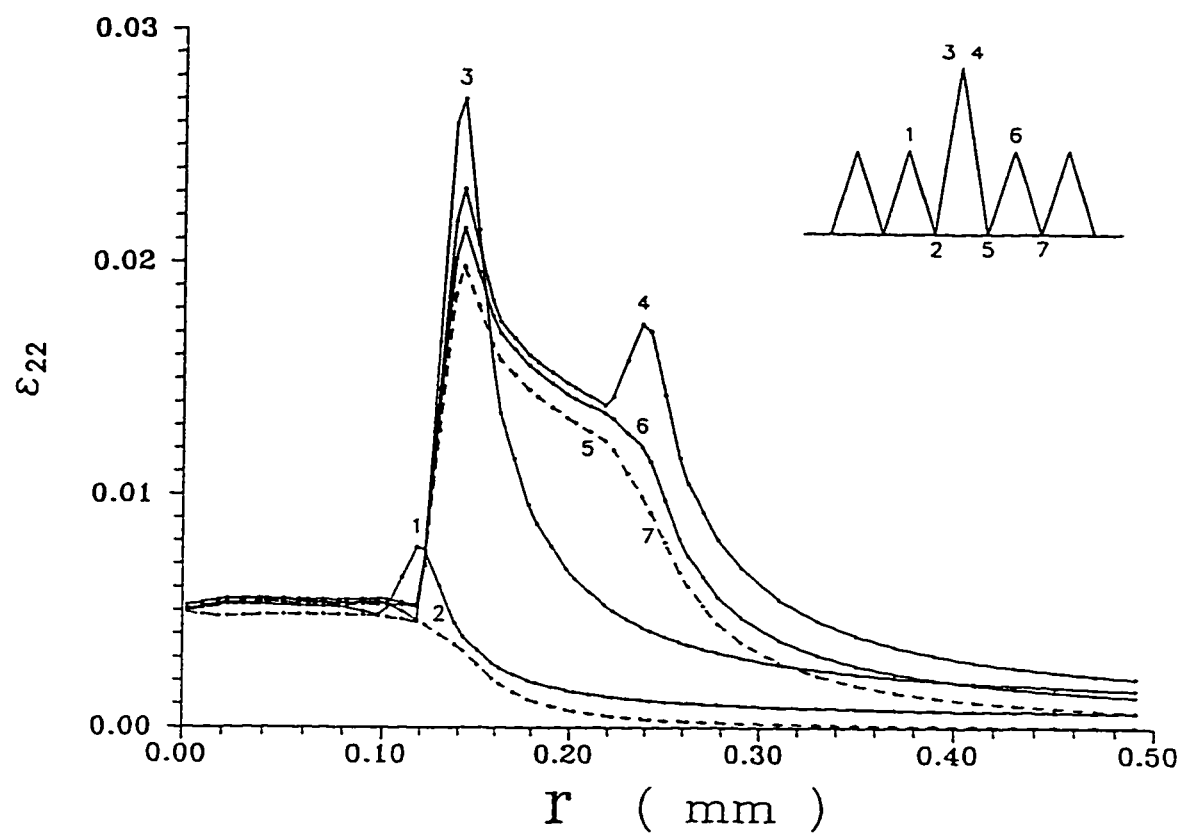


Fig.4-22a Strain distributions for special points near the overload cycle.

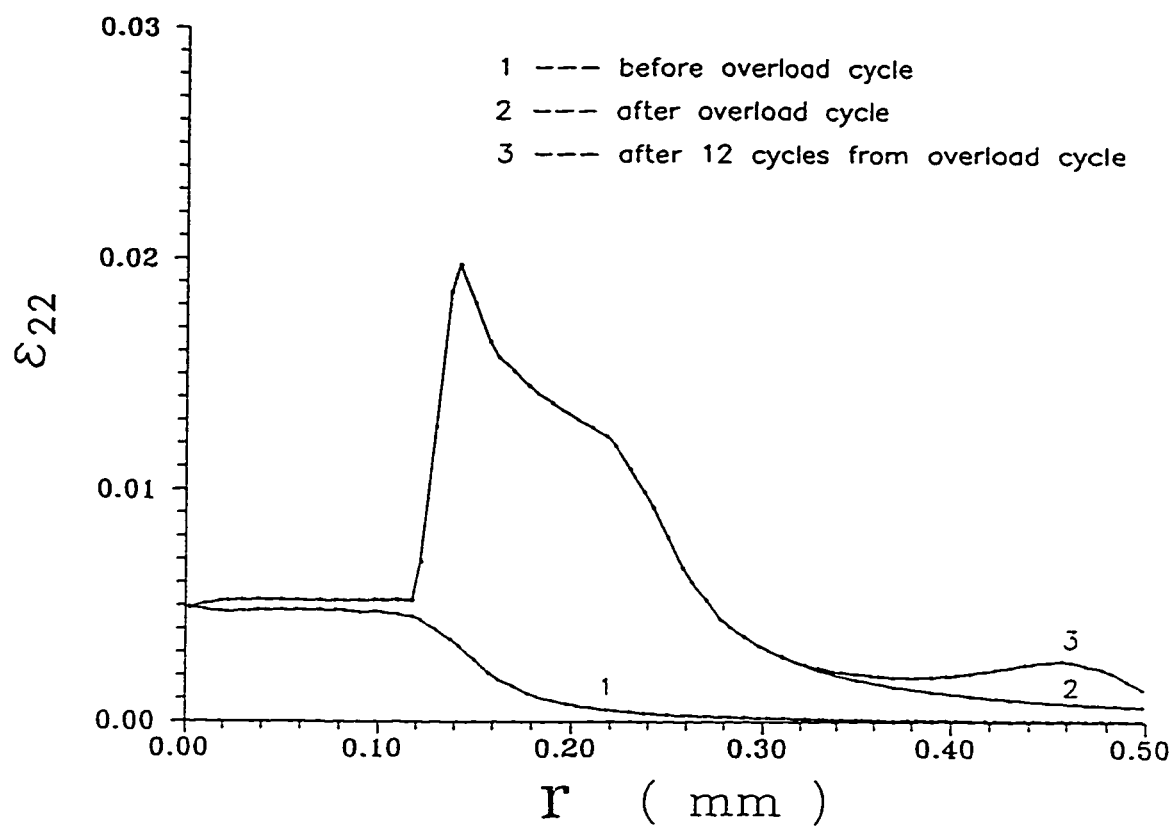


Fig.4-22b Residual strain distributions for the cycle before overload cycle, overload cycle and the cycle after 12 cycles from overload cycle.



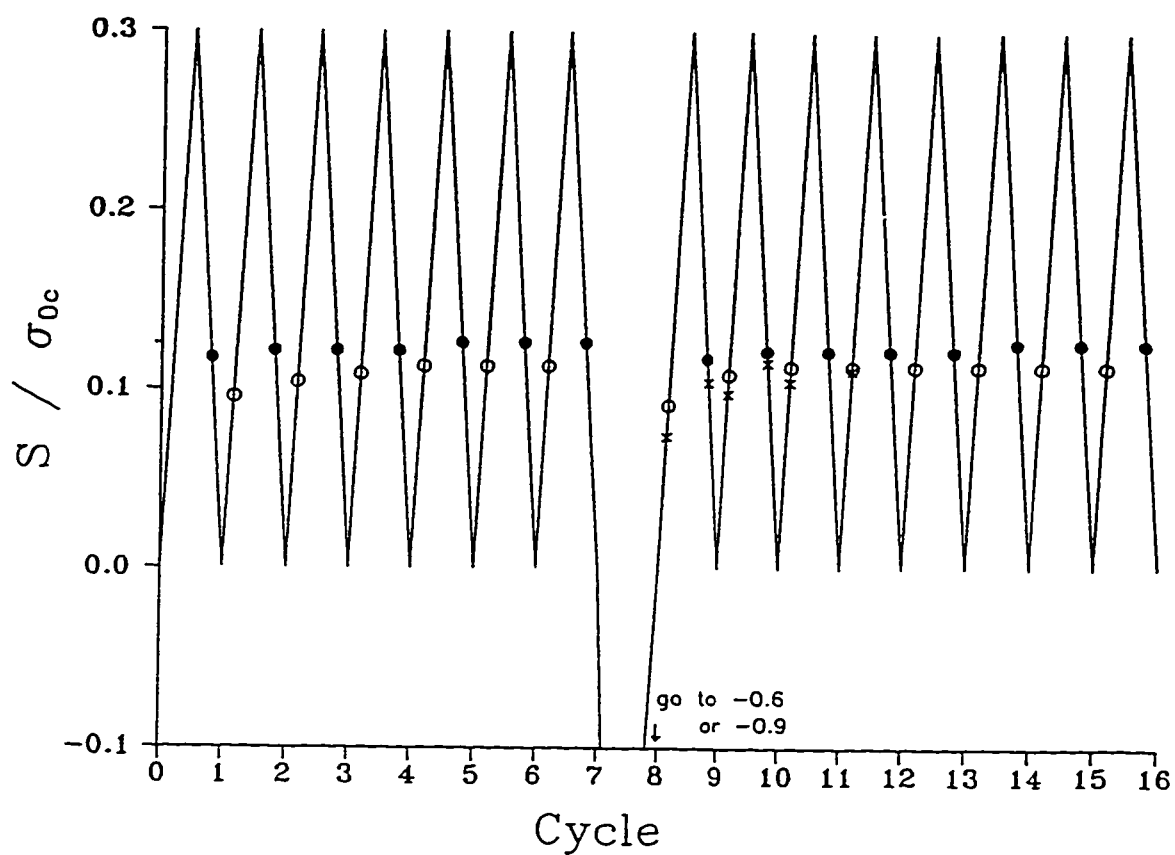


Fig.4-23 Crack opening stresses and closing stresses under constant-amplitude cyclic loading with a single 200% underload or 300% underload.

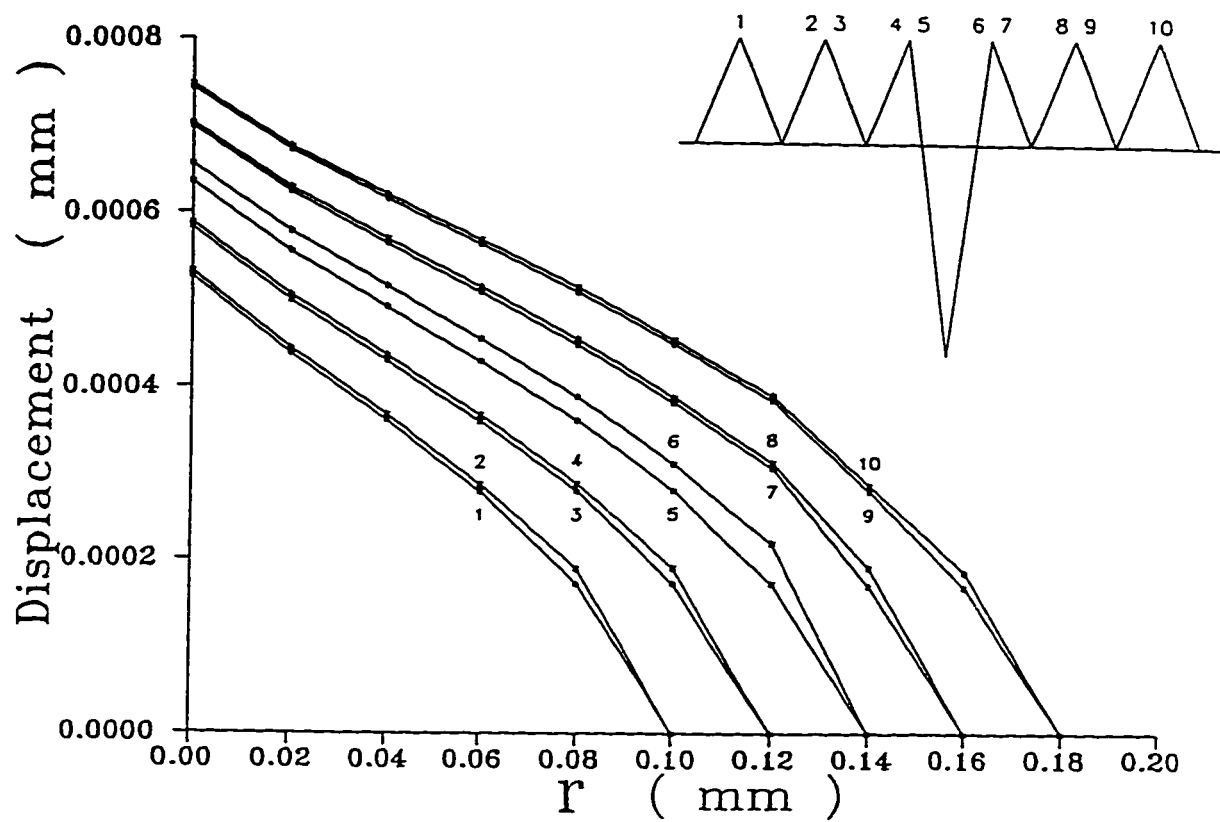


Fig.4-24 Crack profiles under constant-amplitude cyclic loading with a single 200% underload.

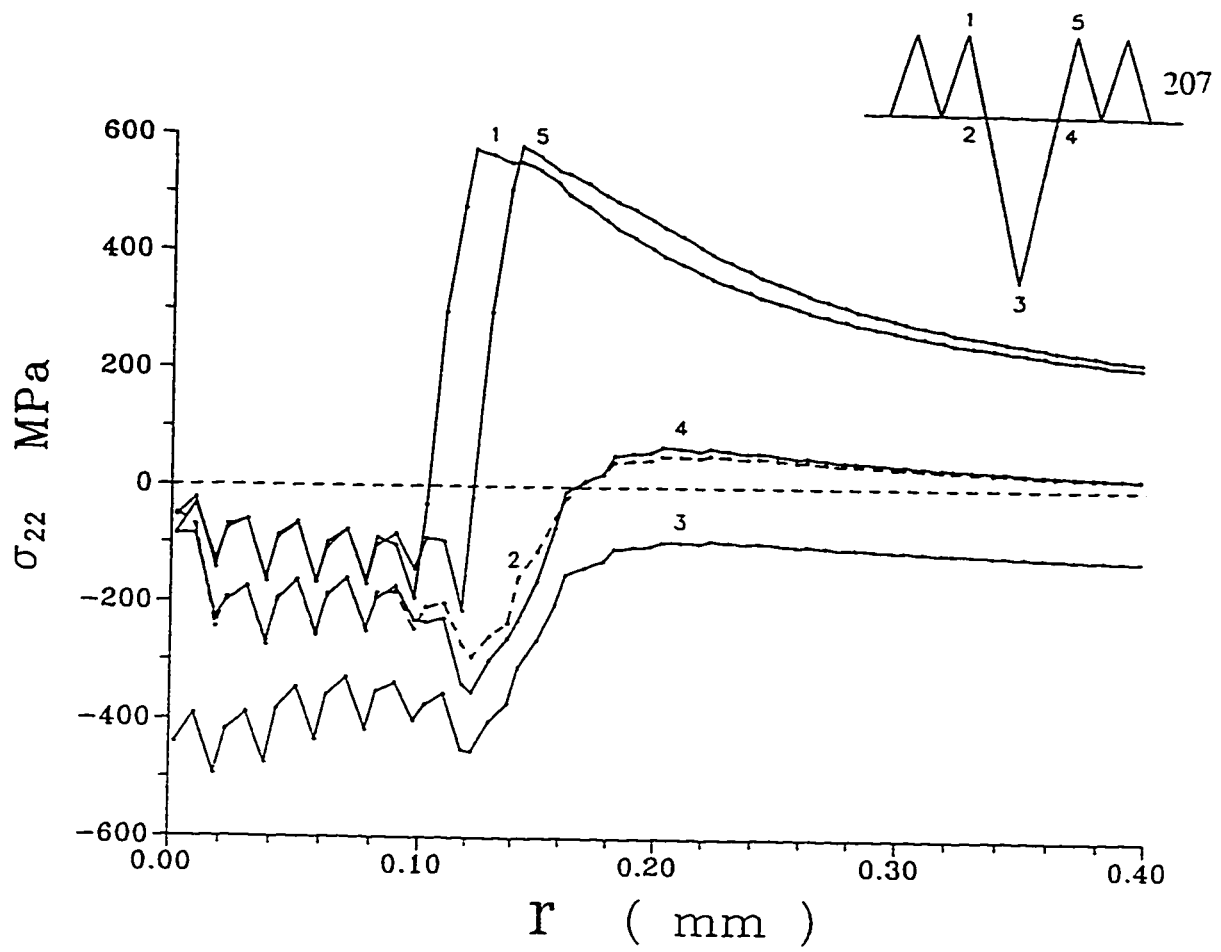


Fig.4-25 Stress distributions for special points near the underload.

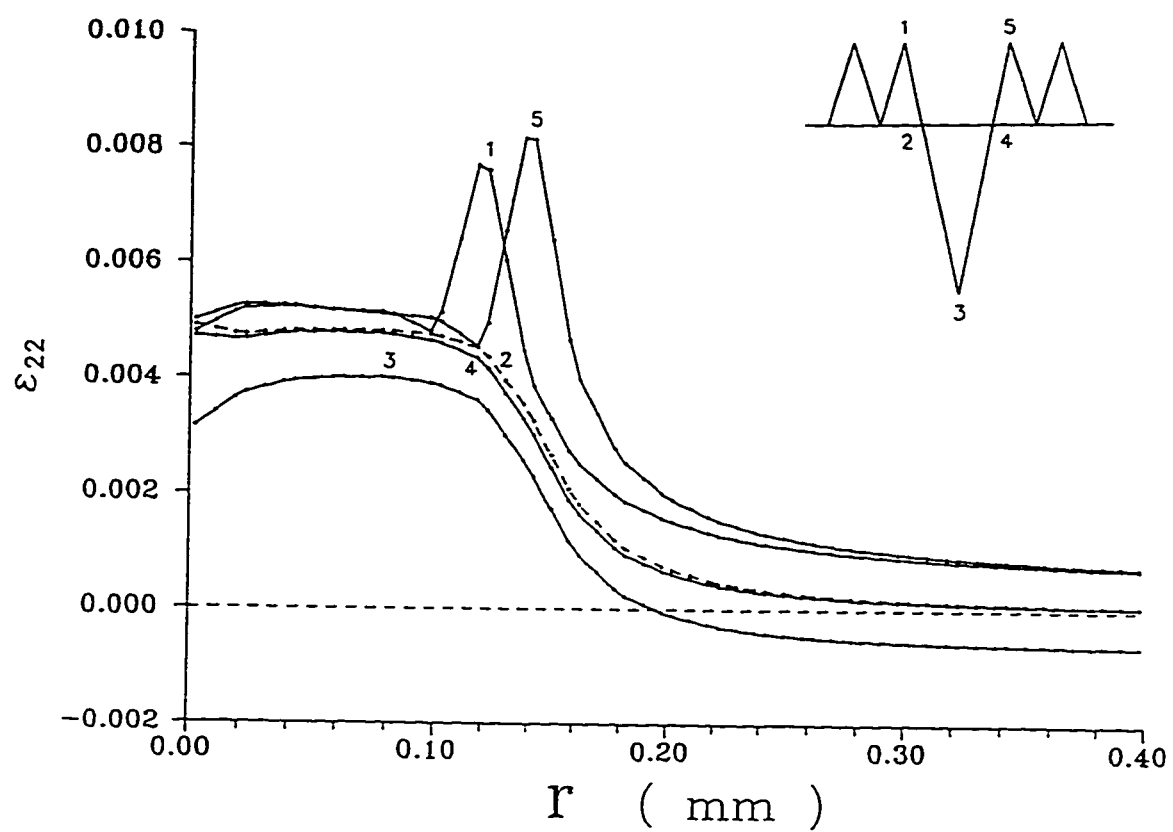


Fig.4-26 Strain distributions for special points near the underload.

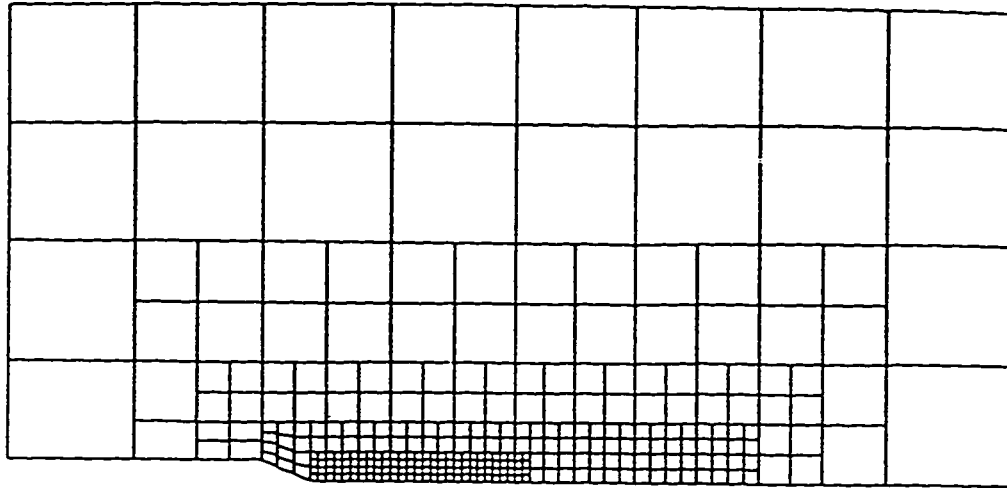


Fig.4-27 The mesh for a centre region near the notch root.

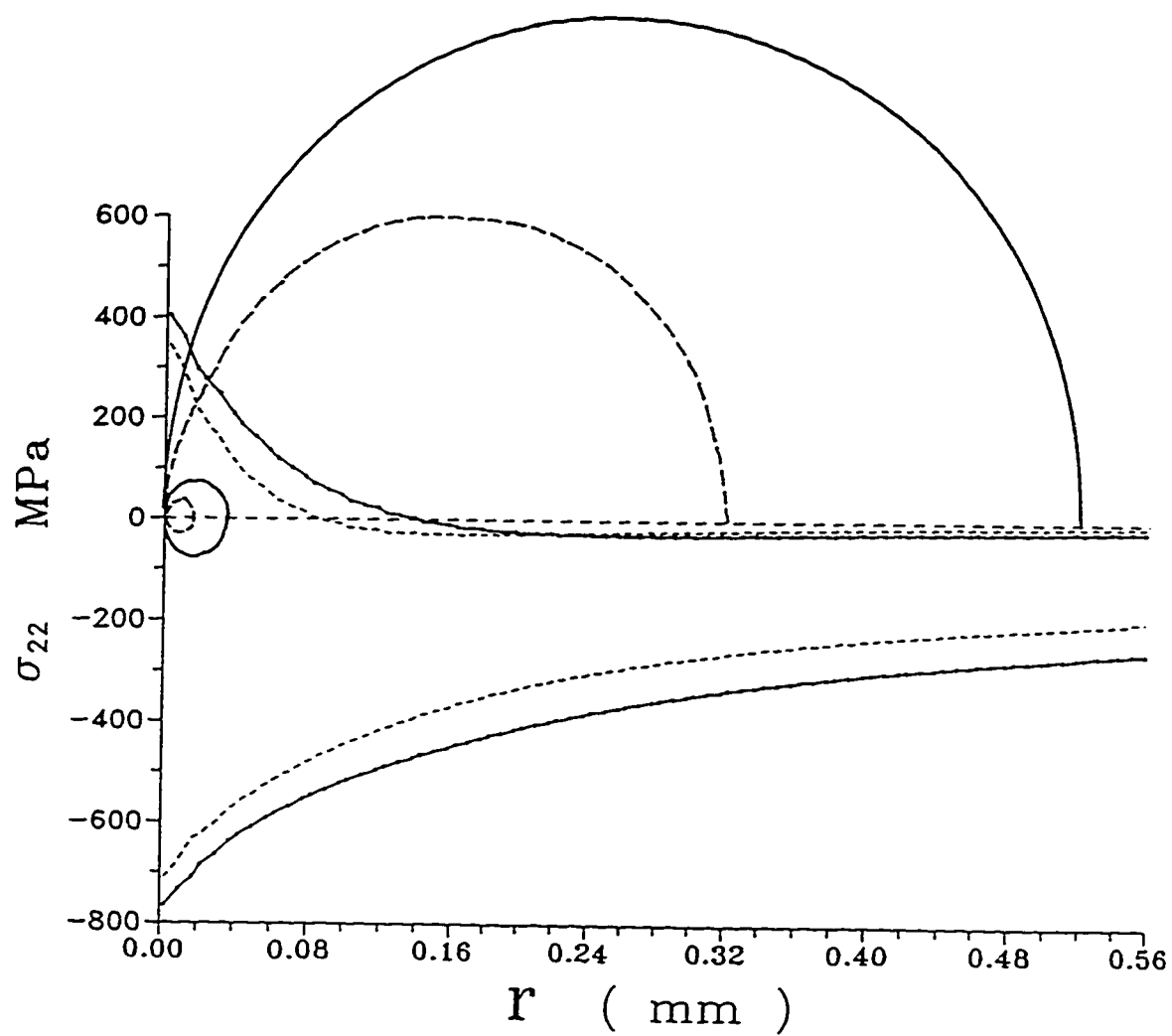


Fig.4-28 Normal stress distributions and plastic zones for the maximum compressive stress of  $0.4\sigma_{0c}$  (dashed lines) and  $0.5\sigma_{0c}$  (solid lines).

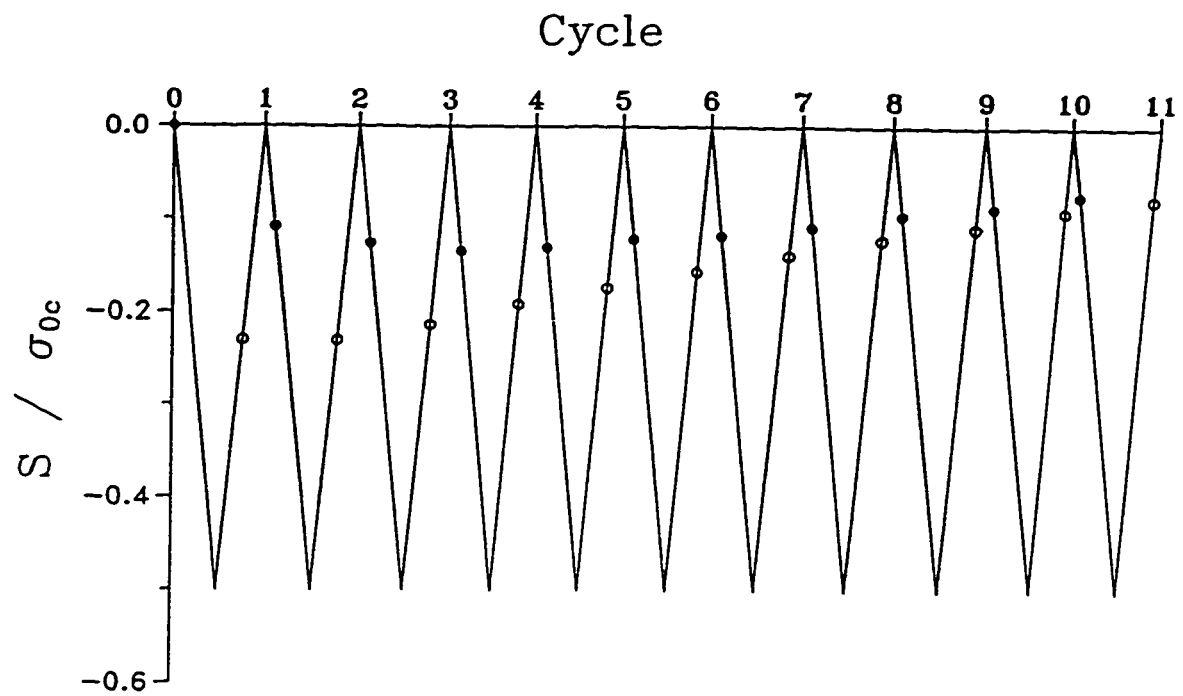


Fig.4-29 Crack opening and closing stresses during compressive cyclic loading using the proposed definition.

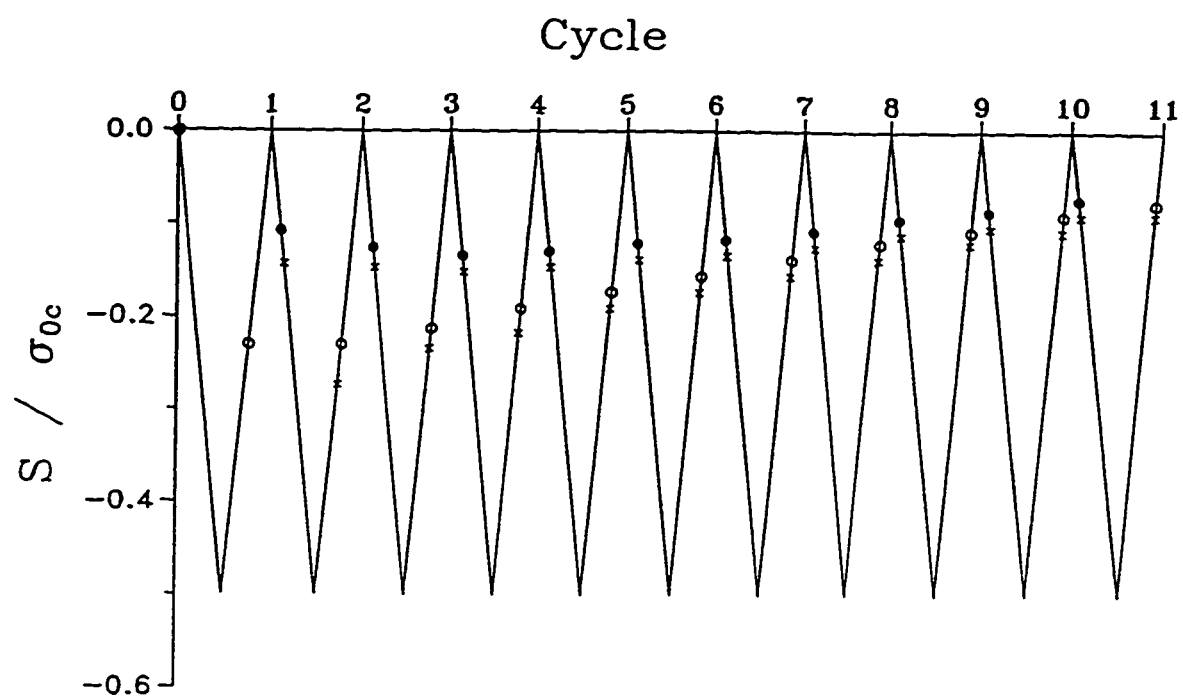


Fig.4-30 A comparison of the crack opening and closing stresses between the newly proposed and the old definition.



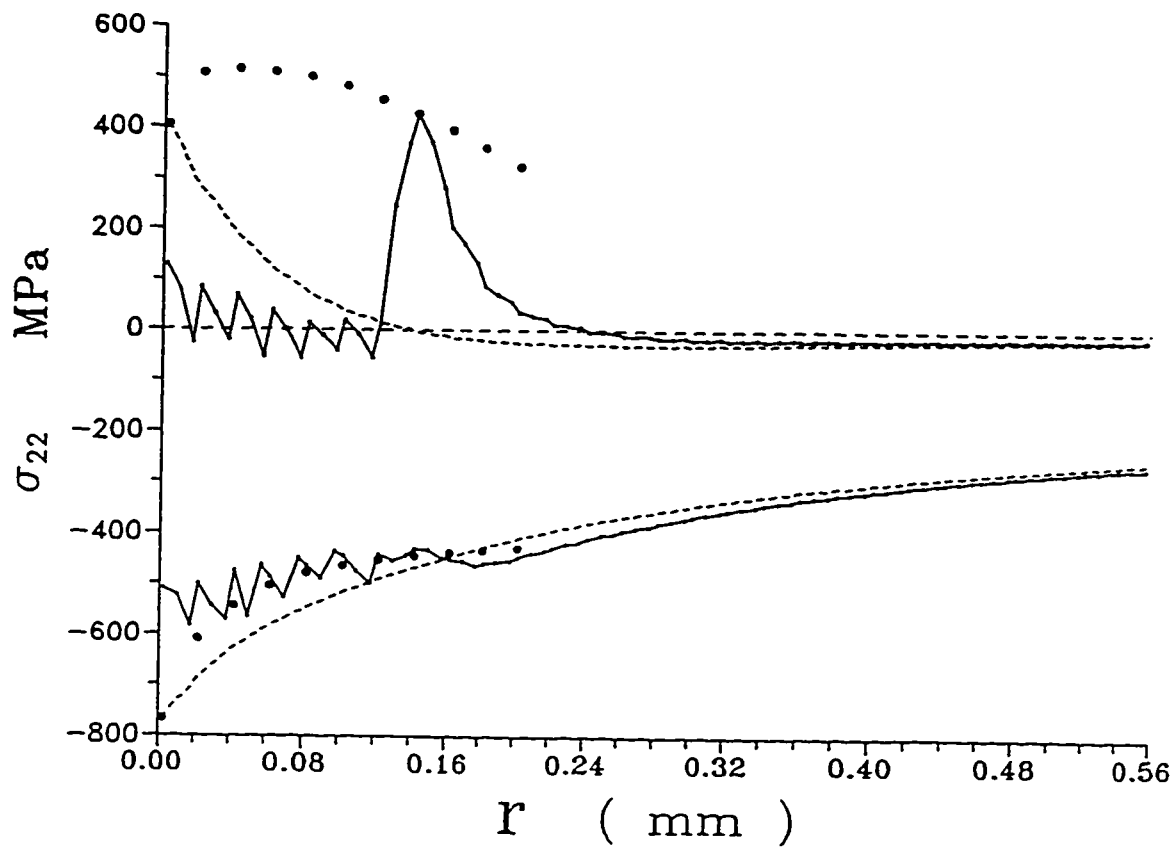


Fig.4-31 Normal stress distributions for the first cycle (dashed lines) and the 8<sup>th</sup> cycle (solid lines), and the stresses at the notch root and each advancing crack tip for each loading cycle (individual solid dots).

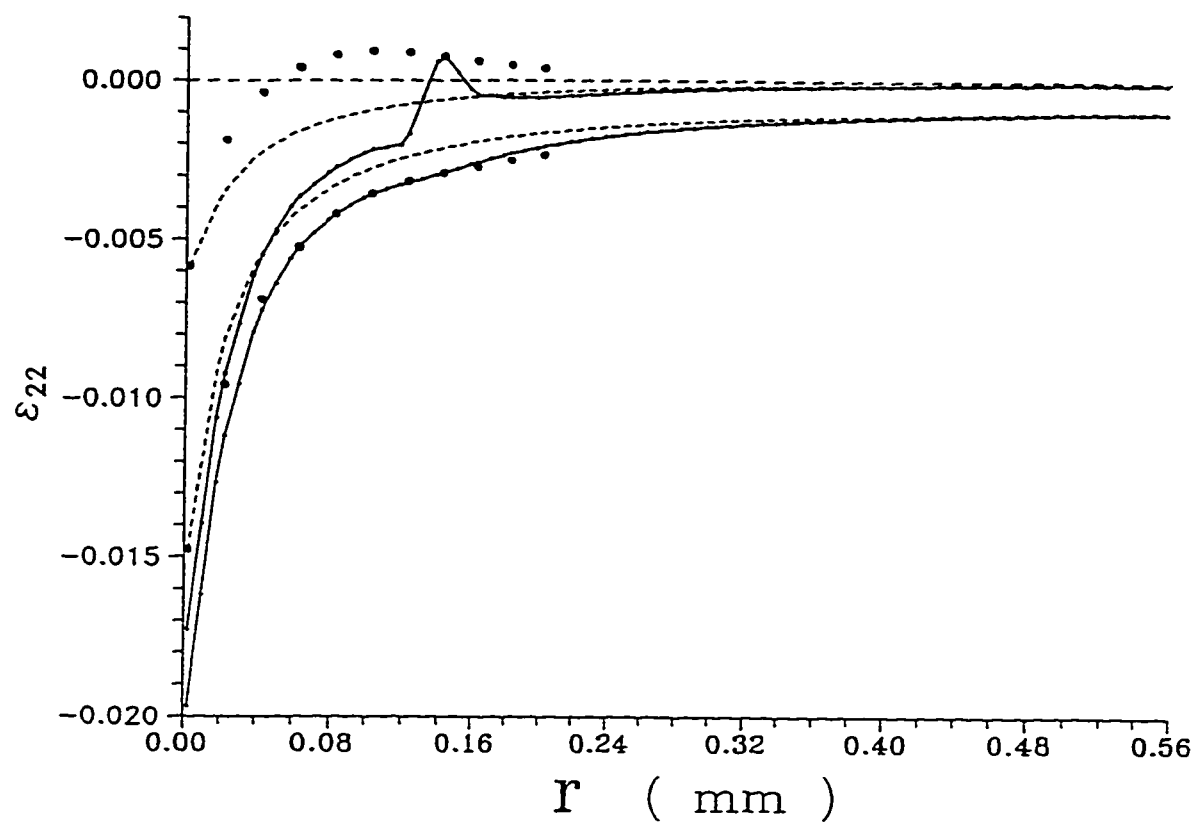


Fig.4-32 Normal strain distributions for the first cycle (dashed lines) and the 8<sup>th</sup> cycle (solid lines), and the strains at the notch root and each advancing crack tip for each loading cycle (individual solid dots).

Cycle	$S_{open}$ MPa	$\sigma_{max}$ MPa	$\epsilon_{max} \times 10^{-2}$	CTOD $\mu m$
1	0.0	682.74	0.79539	0.68649
2	21.0	591.17	0.79129	0.45382
3	23.0	578.06	0.76905	0.39901
4	24.0	576.94	0.75841	0.38268
5	25.0	575.22	0.75670	0.37933
6	25.0	575.02	0.75556	0.37948
7	25.0	574.71	0.75960	0.38079
8	25.0	574.75	0.76410	0.38062
9	25.0	574.88	0.76506	0.37989
10	26.0	575.19	0.76858	0.38016
11	26.0	577.35	0.77305	0.38119
12	26.0	578.13	0.77594	0.38128
13	26.0	578.83	0.77742	0.38154
14	26.0	578.95	0.77934	0.38170
15	27.0	579.19	0.78229	0.38254
16	27.0	579.44	0.78464	0.38312
17	27.0	579.70	0.78711	0.38342
18	27.0	579.87	0.78988	0.38397
19	27.0	579.94	0.79228	0.38451
20	28.0	580.19	0.79398	0.38498

Table 4-1 Crack opening stress, maximum stress, maximum strain and CTOD for each cycle during constant-amplitude cyclic loading.

## CHAPTER 5

### SUMMARY AND SUGGESTION FOR FURTHER RESEARCH

The major contribution of this thesis is implementation of a constitutive model of materials to perform non-linear analyses of cracked bodies.

In recent years numerical analysis has been playing an increasingly important role in solving technological problems. Fundamental to the numerical analysis is the constitutive relation which describes the material response. The constitutive relation proposed in this thesis is simple enough to be used effectively in computer programs and it matches the essential features of the time-independent elastic-plastic behaviour of materials fairly well for both monotonic and cyclic loading under complex loading paths.

The distinguishing feature of this constitutive relation is the manner in which it describes the hardening behaviour of materials. First, the evolution of the yield surface is based on the concepts of the yield surface, memory surface and limit memory surface. Unlike the surfaces proposed in some other constitutive relations, these surfaces can be obtained through experiments and they characterize certain properties of the material. Also, the motion of the yield surface determined by this rule is in better agreement with the experimental results compared to existing ones. Second, the change of radius of the yield surface is considered under a stable cyclic loading. For non-Masing behaviour which is exhibited by a wide range of structural metals, the shape of the steady hysteresis

loops reveal variation with respect to different strain ranges. Each material point of a cracked body is subjected to different strain ranges, and so should be treated in an appropriate manner. Third, an attempt is made to use the Ramberg-Osgood relation to fit the experimental curves of the material. These curves include monotonic, cyclic stress-strain curves and stable hysteresis loops for different strain ranges. The Ramberg-Osgood relation has three parameters, which allows for a better fit to the experimental curves, especially to the cyclic stress-strain curve and the stable hysteresis loops. In addition, when the Ramberg-Osgood relations representing the stable hysteresis loops are known, the current tangent modulus  $E_t$  for the reversed loading can be easily calculated.

A constitutive relation for small deformation can be successfully used to predict the stress and strain fields of cracked bodies up to a region of 2-3 CTOD from the crack tip. Within this region the magnitude of the experimentally measured strains becomes relatively large requiring a finite deformation constitutive relation. However, a finite deformation model with isotropic hardening, as used in Chapter 3, is not suitable for unloading because of the Bauschinger effect which takes place at the start of unloading. Therefore, establishing a finite deformation model with the kinematic hardening will be the next logical step in extending this research, though it will be challenging work.

Apart from a constitutive relation, some techniques are required to simulate the specific processes of material response in a numerical analysis. These modelling techniques which have a direct influence on the results, should reflect as much as possible the actual material response, so that the physical meaning can be retained. Also,

mathematical and computational simplicity should be considered.

A proposed loading procedure to study the delayed hydride cracking, is the second contribution of this thesis. This procedure successfully simulates the precipitation and expansion of hydride in an elastic-plastic stress field near a crack tip. After the precipitation and expansion of the hydride, the high stress gradient region is shifted from the crack tip to the front end of the hydride platelet. This then gives a clear explanation of why the hydride grows along the crack front.

From mechanical viewpoint, imposing displacements on the nodes ahead the crack tip under a tensile stress field places these nodes in a certain state between the free and fixed condition depending on the magnitude of the prescribed displacement. The stretch of the material is mitigated due to the appearance of the hydride platelet, while the hydride platelet itself bears compressive stresses. The decrease of the tensile stresses in the material restrains the thickness of the hydride platelet. When the hydride platelet extends to a certain length, the stress in the material at the rear end of the hydride platelet starts to increase. At this time, the rear end of the hydride platelet itself starts to bear tensile stress. When the length of the hydride platelet reaches a critical value, the hydride platelet cracks. The above explanation is consistent with the process of the delayed hydride cracking. For a compressive stress region appeared behind the front end of the hydride platelet, the shape of the assumed hydride platelet will influence the magnitude of the compressive stress. However, the compressive stress region must exist, which is necessary to satisfy the energy equilibrium. This may suggest that the effect of the tensile hydrostatic stress on the hydride is different from that of compressive hydrostatic stress.

The final contribution of this thesis is an improved node release scheme to simulate crack growth for studying crack closure under cyclic loading. Numerical modelling of crack growth has always been a great challenge to researchers. Significant here is the modelling of what really controls cracking as well as determining which one of the numerous theories of fracture criteria is most suitable for use in computer programs.

The proposed scheme which releases the crack-tip node at the top of each loading cycle, implies that maximum stress, or strain, or CTOD corresponding to one loading cycle is chosen as the critical parameter of failure. By such a node release scheme, the observed mechanisms of materials during cyclic loading can be displayed properly. In other words, the change of stress, strain and deformation in the region near the crack tip can be adequately described by this scheme. It is these factors including plastic deformation and residual stress that influence the crack opening stress. The use of a bundle of truss elements resolves the convergence problems experienced by other schemes. In addition, the energy release during crack growth can be calculated, which may be used as a practical fracture criterion in the numerical analysis.

It should be noted that using such a node release scheme to study crack growth rate is not appropriate, specially for variable amplitude loading. Experimental results have shown that a crack does not advance at each cycle but after application of several cycles. This fact implies that an energy fracture criterion should be considered in the numerical analyses of crack growth. Using the present work as a starting point, establishing an energy fracture criterion is an appropriate topic for further research work.

## REFERENCES

- [1-1] ADINAT, ADINA-IN and ADINA-PLOT Users Manuals, ADINA Engineering AB, MunKatan, s-722 Västerås, Sweden, a.d ADINA Engineering, Inc., 71 Elton Avenue, Watertown, MA 02172, U.S.A.
- [1-2] ANSYS, Engineering Analysis System User's Manual, Swanson Analysis systems, Inc., P.o. Box 65, Houston, Pennsylvania, 15342, U.S.A.
- [1-3] J.Wu, "Elasto-plastic material model and application", master thesis. University of Alberta. 1989.
- [1-4] F.Ellyin and J.Wu, " A description of elastoplastic behaviour based on memory and yield surface in plane stress state", in Constitutive Laws for Engineering Materials-Theory and Application, C.S. Desai et al.(eds). Elsevier, pp.531-538. New York. 1987.
- [1-5] F.Ellyin and Z.Xia. "Elastoplastic stress-strain relation based on a new anisotropic hardening model", Proc. IUTAM/ICM symp. on yielding damage and failure of anisotropic solids (Villard-de-Lans, France). 1988.
- [1-6] F.Ellyin and Z.Xia. "A rate-independent constitutive model for transient non-proportional loading", J.Mech.Phys.Solids, Vol.37, No.1 pp.71-91. 1989.
- [1-7] F.Ellyin and Z.Xia, "A rate-dependent inelastic constitutive model-part I: elastic-plastic flow",J.Engineering Material and Technology. Trans. ASME, Vol.113, 1991, pp.314-323, 1991.
- [1-8] Z.Xia and F.Ellyin, "A rate-dependent inelastic constitutive model-part II: creep deformation including prior plastic strain effects". J.Engng Materials and Technology, Vol.113, pp.324-328, 1991.
- [2-1] W.Prager, "The theory of plasticity: a survey of recent achievements". (James Clayton Lecture) proc. Instn. Mech. Engrs., Vol.169, pp.41-57,1955.
- [2-2] H.Ziegler, "A modification of prager's hardening rule", Quat. Appl. Math. Vol.17, pp.55-56, 1959.
- [2-3] D.C.Drucker and W.Prager. "Soil mechanics and plastic analysis or limit



- design", Quarterly Applied Mathematics, Vol.10, No.2, pp. 157-165, 1952.
- [2-4] Z.Mroz, " On the description of anisotropic work hardening", J. Mech. Phys. Solids, Vol.15, pp.163-175, 1967.
  - [2-5] Z.Mroz, " Hardening and degradation rule for metals under monotonic and cyclic loading", Journal of Engineering Material and Technology, Vol.105, pp.105-118, 1983.
  - [2-6] W.Trampczynski and Z.Mroz, " Anisotropic hardening model and its application to cyclic loading", International Journal of Plasticity, Vol.8, pp.925-946, 1992.
  - [2-7] Aris Phillips and Chong-won Lee, " Yield surface and loading surface. experiments and recommendations", Int. J. Solids Structures, Vol.15, pp.715-729, 1979.
  - [2-8] F.Ellyin, " On the concept of initial and subsequent yield loci". in: Failure Criteria of Structured Media, J.P. Boehler(ed), A.A. Balkema Publishers, Rotterdam, The Netherlands, 1983.
  - [2-9] F.Ellyin and J.Wu, " A description of elastoplastic behaviour based on memory and yield surface in plane stress state", in Constitutive Laws for Engineering Materials-Theory and Application, C.S. Desai et al.(eds), Elsevier, pp.531-538, New York, 1987.
  - [2-10] Von G Masing and Berlin-Siemensstadt, "Eigenspannungen und verfestigung beim messig", Proceedings 2nd Int. Congress of Appl. Mechanics, Zurich, pp.332-335, 1926.
  - [2-11] J. Morrow, "Internal friction, damping and cyclic plasticity", ASTM STP 378, pp.45-87, 1964.
  - [2-12] G. R. Halford and J. Morrow, "Low-cycle fatigue in torsion", in proceedings, ASTM, Vol.62, pp.695-707, 1962.
  - [2-13] H. Abdel-Raouf, T. H. Topper and A. Plumtree, "Cyclic plasticity and Masing behaviour in metals and alloys", Fracture 1977, Vol.2, ICF 4, Waterloo, Canada, pp.1207-1215, 1977.
  - [2-14] D.Lefebvre and F.Ellyin, " Cyclic response and inelastic strain energy in low cycle fatigue", International Journal of Fatigue, Vol.6, pp.9-15, 1984.

- [2-15] Walter Ramberg and William R. Osgood, "Description of stress-strain curves by three parameters", National advisory committee for aeronautics. Technical Note No.902, 1943.
  
- [3-1] D. Weinstein and F.C. Holtz, "Susceptibility of zirconium and zirconium alloys to delayed failure hydrogen embrittlement", Trans. ASM, **57**, 284, 1964.
  
- [3-2] J.C.M. Li, R.A. Oriani and L.S. Darken, "The thermodynamics of stressed solids", Zeitschrift für Physikalische Chemie Neue Folge, Vol.49, pp.271-290, 1966.
  
- [3-3] R. Dutton, K. Nuttall, M.P. Puls and L.A. Simpson, "Mechanisms of hydrogen induced delay cracking in hydride forming materials". Metall. Trans. **8A**, pp.1553, 1977.
  
- [3-4] C.E. Coleman and J.F.R. Ambler, "Delayed hydrogen cracking in Zr-2.5 wt% Nb alloy". Reviews on Coating and Corrosion, Vol.III, nos. 2 and 3, pp.105, 1979.
  
- [3-5] R. Dutton and M.P. Puls, " A theoretical model for hydrogen induced sub-critical crack growth", Effects of Hydrogen on the Behaviour of Materials, (edited by A.W. Thompson and I.M. Bernstein), Metallurgical Society of AIME, New York, pp.516, 1976.
  
- [3-6] L.A. Simpson and M.P. Puls, " The effects of stress, temperature and hydrogen content on hydride-induced crack growth in Zr-2.5 Pet Nb". Metall. Trans. A., Vol.10A, pp.1093-1105, 1979.
  
- [3-7] M.P. Puls, L.A. Simpson and R. Dutton, " Hydride-induced crack growth in zirconium alloys", Fracture Problems and Solutions in the Energy Industry (L.A. Simpson, ed.), Pergamon Press, Oxford/New York, pp.13 1981.
  
- [3-8] M.P. Puls, " The influence of hydride size and matrix strength on fracture initiation at hydrides in zirconium alloy", Metall. Trans. A., Vol.19A, pp.1507-1522, 1988.
  
- [3-9] M.P. Puls, " Effects of crack tip stress states and hydride-matrix interaction stresses on delayed hydride cracking", Metall. Trans. A, Vol.21A, pp.2905-2917 1990.
  
- [3-10] M.P. Puls, " Fracture initiation at hydrides in zirconium".Metall. Trans.

A. Vol.22A, pp.2327-2337, 1991.

- [3-11] R.L. Eadie and F. Ellyin, " The effect of hydride precipitation on the stresses near the crack tip in a delayed hydride crack in zirconium-2.5% Niobium", *Scripta Metallurgica*, Vol.23, pp.585-592, 1989.
- [3-12] B.A.Cheadle, C.E.Coleman, and H.Licht. " Candu-PHW pressure tubes: their manufacture, inspection, and properties", *Nuclear Technology*, Vol.57, pp.413-425, 1982.
- [3-13] Xin Quan Yuan and K.Tangri, " Metallographic observations on the developing hydride morphology at the crack tip during hydrogen induced delayed cracking in a Zr-2.5 Nb alloy", *Journal of Nuclear Materials*, Vol.105, pp.310-317, 1982.
- [3-14] G.R.Irwin. "Fracture. encyclopedia of physics", ed. S. Fluge. Springer Verlag, pp.551-89, 1958.
- [3-15] F. Ellyin. " Recent developments in predicting multiaxial fatigue failure". *Res Mechanica*. Vol.25, pp.1-25, 1988.
- [3-16] E.T.C. Ho. unpublished research, Ontario Hydro Research Division, 1988.
- [3-17] D.O. Northwood, I.M. London and L.E. Bahen. " Elastic constants of zirconium alloy", *J.Nucl. Mater.*, Vol. 55, pp.299-310, 1975.
- [3-18] J.R. Rice and M.A. Johnson, " The role of large crack tip geometry changes in plane strain fracture", *Inelastic Behaviour of Solids* (edited by M.F. Kanninen), McGraw-Hill, New York; pp.641-672, 1970.
- [3-19] R.M. McMeeking, " Finite deformation analysis of crack-tip opening in elastic-plastic material and implications of fracture", *J. Mech. Phys. Solids*, Vol.25, pp.357-381, 1977.
- [3-20] E.P.Sorensen, " A numerical investigation of plane strain stable crack growth under small-scale yielding conditions", *Elastic-Plastic Fracture*, ASTM STP 668, pp.151, 1979.
- [3-21] D.L.Davidson and J.Lankford, " Fatigue crack growth in metals and alloys: mechanisms and micromechanics", *International Materials Reviews*, Vol.37, No.2, pp.45-76, 1992.
- [3-22] L. G. Luo, A. Ryks and J. D. Embury, "On the development of a

metallographic method to determine the strain distribution ahead of a crack tip", *Metallography*, Vol.23, pp.101-117, 1989.

- [4-1] W. Elber, "Fatigue crack closure under cyclic tension", *Engng Fracture Mech.* Vol.2, No.1, pp.37-45, 1970.
- [4-2] W. Elber, "The significance of fatigue crack closure", *Damage Tolerance in Aircraft Structures*, ASTM STP 486, pp.230-242, 1971.
- [4-3] P. C. Paris and F. Erdogan, "A critical analysis of crack propagation laws", *J. Bas. Engng.* 55, pp.528-534, 1963.
- [4-4] Raghuvir Kumar, "Review on crack closure for constant amplitude loading in fatigue", *Engng Fracture Mech.* Vol.42, No.2, pp.389-400, 1992.
- [4-5] B. Budiansky and J. W. Hutchinson, "Analysis of closure in fatigue crack growth", *Journal of Applied Mechanics*, Vol.45, pp.267-276, 1978.
- [4-6] J. C. Newman, Jr., "A crack-closure model for predicting fatigue crack growth under aircraft spectrum loading", *ASTM STP 748*, Philadelphia, pp.53-84, 1981.
- [4-7] J. C. Newman, Jr. and Harry Armen, Jr., "Elastic-plastic analysis of a propagating crack under cyclic loading", *AIAA Journal* Vol.13, No.8, pp.1017-1023, 1975.
- [4-8] J. C. Newman, Jr., "Finite-element analysis of fatigue crack closure", *ASTM STP 590*, pp.281-301, 1976.
- [4-9] J. C. Newman, Jr., "Finite element analysis of crack growth under monotonic and cyclic loading", *ASTM STP 637*, pp.56-80, 1977.
- [4-10] Norman A. Fleck and J. C. Newman, Jr., "Analysis of crack closure under plane strain conditions", *ASTM STP 982*, pp.319-341, 1988.
- [4-11] R. G. Chermahini, K. N. Shivakumar and J. C. Newman, Jr., "Three-Dimensional finite-element simulation of fatigue crack growth and closure", *ASTM STP 982*, Philadelphia, pp.398-413, 1988.
- [4-12] R. C. McClung and H. Sehitoglu, "On the finite element analysis of fatigue crack closure-1. basic modelling issues", *Engng Fracture Mech.* Vol.3, No.2, pp.237-252, 1989.

- [4-13] R. C. McClung and H. Sehitoglu, "On the finite element analysis of fatigue crack closure-2. numerical results", *Engng Fracture Mech.* Vol.33, No.2, pp.253-272, 1989
- [4-14] R. C. McClung, "Application of a finite element analysis of fatigue crack closure", 7th. International conference on fracture, Houston, Texas, pp.1257-1264, 1989.
- [4-15] R. C. McClung, "Crack closure and plastic zone sizes in fatigue". *Fatigue Fract. Engng Mater. Struct.* Vol.14, No.4, pp.455-468, 1991.
- [4-16] R. C. McClung, B. H. Thacker and S. Roy, "Finite element visualization of fatigue crack plane stress and plane strain". *International Journal Fracture*, 50: 27-49, 1991.
- [4-17] T. Nishioka and S. N. Atluri, "Numerical modelling of dynamic crack propagation in finite bodies, by moving singular elements". *Journal of Applied Mechanics*, Vol.47, pp.570-582, 1980.
- [4-18] M. Nakagaki and S. N. Atluri, "Elastic-plastic analysis of fatigue crack closure in modes I and II". *Aiaa journal*, Vol.18, No.9, pp.1110-1117, 1980.
- [4-19] J. Y. Zhang, T. R. Hsu and I. Q. Wang, "Numerical modelling of crack propagation using multi-variable and breakable finite elements". *Communications in Applied Numerical Methods*, Vol.6, pp.215-222, 1990.
- [4-20] C. L. Ho, O. Buck and H. L. Marcus, "Application of strip model to crack tip resistance and crack closure phenomena". *Progress in Flaw Growth and Fracture Toughness Testing*, ASTM STP 536, pp.5-21, 1973.
- [4-21] Noel E. Ashbaugh, "Effects of load history and specimen geometry on fatigue crack closure measurements", *Mechanics of Fatigue Crack Closure*, ASTM STP 982, pp.186-196, 1988.
- [4-22] S. K. Ray and A. F. Grandt, "Comparison of methods for measuring fatigue crack closure in a thick specimen", *Mechanics of Fatigue Crack Closure*, ASTM STP 982, pp.197-213, 1988.
- [4-23] D. L. Davidson, "Plasticity induced fatigue crack closure", *Mechanics of Fatigue Crack Closure*, ASTM 982, pp.44-61, 1988.
- [4-24] D. L. Davidson, "Observing growing crack in the scanning electron

- microscope and measurement of crack tip parameters by stereoimaging". Fatigue Crack Measurement: Techniques and Applications, EMAS Edited by K. J. Marsh, R. A. Smith and R. O. Ritchie, pp.315-334.
- [4-25] A. A. Wells, "Unstable crack propagation in metals: damage and fast fracture", Proceedings of the Crack Propagation Symposium Cranfield. The College of Aeronautics, Vol.1, pp.210-230, 1962.
  - [4-26] F. M. Burdekin and D. E. W. Stone, "The crack opening displacement approach to fracture mechanics in yielding", Journal of Strain Analysis. Vol.1, pp.145-153, 1966.
  - [4-27] D. M. Tracey, "Finite element solutions for crack-tip behaviour in small-scale fielding", Journal of engineering materials and technology. April. pp.146-151, 1976.
  - [4-28] J. R. Rice and E. P. Sorensen, "Continuing crack-tip deformation and fracture for plane-strain crack growth in elastic-plastic solids". J. Meck. Phys. Solids, Vol.26, pp.163-186, 1978.
  - [4-29] J.C.Newman, "An elastic-plastic finite element analysis of crack initiation, stable crack growth, and instability", Fracture Mechanics: Fifteenth Symposium. ASTM STP 833, pp.93-117, 1984.
  - [4-30] D. C. Drucker and J. R. Rice, "Plastic deformation in brittle and ductile fracture", Engineering Fracture Mechanics, Vol.1, pp.577-602, 1970.
  - [4-31] H. Adersson, "A finite-element representation of stable crack-growth". J. Mech. Phys. Solids, Vol.21, pp.337-356, 1972.
  - [4-32] Dai Yao and Hwang Keh-Chih, "A finite element investigation of unsteady crack growth in power-law hardening materials under small-scale yielding conditions", Engng Fracture Mechanics, Vol.34, No.3, pp.531-546, 1989.
  - [4-33] Keui Ogura and Kiyotsugu Ohji, "Fem analysis of crack closure and delay effect in fatigue crack growth under variable amplitude loading", Engineering Fracture Mechanics, Vol.9, pp.471-480, 1977.
  - [4-34] A. N. Palazotto and J. G. Mercer, "A finite element coparison between short and long cracks within a plastic zone due to a notch", Engineering Fracture Mechanics, Vol.35, No.6, pp.967-986, 1990.
  - [4-35] P. L. Lalor and H Sehitoglu, "Fatigue crack closure outside a small-scale yielding regime", Mechanics of Fatigue crack Closure, ASTM STP 982,

pp.342-360, 1987.

- [4-36] H. Sehitoglu and W. Sun, "The significance of crack closure under high temperature fatigue crack growth with hold periods", *Engineering Fracture Mechanics*, Vol.33, No.3, pp.371-388, 1989.
- [4-37] H. Sehitoglu and W. Sun, "Modelling of plane strain fatigue crack closure", *Journal of Engineering Mechanics and Technology*, Vol.113, pp.31-40, 1991.
- [4-38] N. A. Fleck, "Compliance methods for measurement of crack length". *Fatigue Crack Measurement: Techniques and Applications*, EMAS edited by K. J. Marsh, R. A. Smith and R. O. Ritchie, pp 69-93.
- [4-39] J. Schijve, "Fatigue crack closure: observations and technical significance". *Mechanics of Fatigue Crack Closure*, ASTM STP 982, pp.5-34, 1988.
- [4-40] J. R. Rice, "Mechanics of crack tip deformation and extension by fatigue". *Fatigue Crack Propagation*, ASTM STP 415, pp.247, 1967.
- [4-41] F. Ellyin and J. Wu, "Elastic-plastic analysis of a stationary under cyclic loading and effect of overload", *International Journal of Fracture* Vol.56, pp.189-208, 1992.
- [4-42] J. Schijve, "Fatigue crack propagation in light alloy sheet materials and structures", *NRL Report MP 195 National Aeronautical and Astronautical Research Institute*, Amsterdam, Holland, 1960.
- [4-43] E. F. J. von Euw, R. W. Hertzberg and R. Roberts, "Delay effects in fatigue crack propagation", *Stress Analysis and Growth of cracks. Proceedings of the 1971 National Symposium on Fracture Mechanics, Part 1*, ASTM STP 513, American Society for Testing and Materials, pp.230-259, 1972.
- [4-44] P. C. Paris and L. Hermann, "Twenty years of reflection on questions involving fatigue crack growth part 11: some observations of crack closure", *Fatigue Thresholds, Fundamentals and Engineering Applications*, Vol.1, EMAS, pp.11-32, 1982.
- [4-45] C. M. Ward-Close and R. O. Ritchie, "On the role of crack closure mechanisms in influencing fatigue crack growth following tensile overloads in a titanium alloy: near threshold versus higher  $\Delta K$  behaviour". *Mechanics of Fatigue Crack Closure*, ASTM STP 982, J. C. Newman, Jr

and W. Elber, Eds., pp.93-111. 1988.

- [4-46] C. M. Ward-Close, A. F. Blom and R. O. Ritchie. "Mechanisms associated with transient fatigue crack growth under variable-amplitude loading: an experimental and numerical study", *Engineering Fracture Mechanics*, Vol.32, No.4, pp.613-638, 1989.
- [4-47] R. L. Carlson, G. A. Kardomateas and P. R. Bates, "The effects of overloads in fatigue crack growth", *Int J Fatigue*, Vol.13, No.6, pp.453-460, 1991.
- [4-48] R. Kumar, "Prediction of delay cycles due to instant of single overload cycles". *Engng Fracture Mechanics*, Vol.42, No.3, pp.563-571, 1992.
- [4-49] H. S Goel and S. Chand, "A fatigue crack growth model for single overload tests". *Journal of Engineering Materials and Technology*. Vol.116, pp.168-172, 1994.
- [4-50] T. H. Topper and M. T. Yu, "The effect of overloads on threshold and crack closure". *Int. J. Fatigue*. Vol.7, No.3. pp.159-164. 1985.
- [4-51] F. J. Zwerneman and K. H. Frank, "Crack opening under variable amplitude loads", *Fracture Mechanics: Perspectives and Directions [Twentieth Symposium] ASTM STP 1020*, R. P. Wei and R. P. Gangloff, Eds., pp.548-565. 1989.
- [4-52] E. Zaiken and R. O. Ritchie, "On the role of compression overloads in influencing crack closure and the threshold condition for fatigue crack growth in 7150 aluminum alloy", *Engineering Fracture Mechanics*. Vol.22, No.1, pp.35-48, 1985.